DOE/ER/12900--T1

BREAKUP OF METAL JETS PENETRATING A VOLATILE LIQUID

BY

JEFFREY P. SCHNEIDER

B.S., University of Nebraska, 1982
M.S., University of Illinois, 1989

THESIS

Submitted in partial fulfillment of the requirements
for the degree of Doctor of Philosophy in Nuclear Engineering
in the Graduate College of the
University of Illinois at Urbana-Champaign, 1993

Urbana, Illinois

DISCLAIMER

Portions of this document may be illegible in electronic image products. Images are produced from the best available original document.

TABLE OF CONTENTS

REFERENCES

APPENDICES -

A. MFSBS Procedure Checklist
B. HYCAM Sequences
C. Jet Leading Edge Penetration Data
D. Radiograph Stills
E. Selected Pressure Data
F. Debris Sifting Data

ACKNOWLEDGEMENTS

This work was funded by U. S. Department of Energy contract DE-FG07-89ER12900. It was performed in cooperation with B. W. Spencer, Manager, Engineering Development Laboratories (EDL), Reactor Engineering Division, Argonne National Laboratory (ANL). ANL has provided technical assistance and laboratory facilities, including X-ray, motion picture, and other equipment. Useful advice and assistance were provided by many of the EDL staff; Dr. R. P. Anderson, Dr. D. R. Armstrong, Dr. J. L. Binder, J. C. Cassulo, Dr. J. D. Gabor, L. M. McUmber, and R. T. Purviance were especially helpful. B. Bonomo assisted in the preparation of a number of figures.

The academic advisor for this work was Dr. B. G. Jones. His patient encouragement is gratefully acknowledged.

NOMENCLATURE

A = flow area

a = jet radius

Bo = Bond number $\equiv \frac{D^2 \rho_c g}{\sigma}$

c_d = drag coefficient

c_f = friction coefficient

d = drop diameter

D = jet diameter (initial)

Fr = Froude number $\equiv \frac{V^2}{gD}$

g = acceleration of gravity

h = melt furnace pool height

I_m = Bessel function of the first kind, order m

j = superficial velocity

k = wave number or ratio of specific heats

k_s = roughness element height

K = Hopkins and Robertson parameter $\equiv \frac{V_j}{V_p}\sqrt{\frac{\rho_j}{\rho_a}}$, or flow resistance coefficient

K_i = Interaction Parameter

K_m = Bessel function of the second kind, order m

l = depth

L = melt fall distance, nozzle to liquid free surface

L = jet breakup or penetration length

m = mass

M = momentum flow

M = momentum

$N_{\mu F}$ = viscosity number $\equiv \frac{\mu_f}{\sqrt{\rho_f \sqrt{\frac{\sigma}{g\Delta\rho}}}}$

$\dot{m}$ = mass flow rate

Oh = Ohnesorge number $\equiv \frac{\mu_d}{\sqrt{\rho_j d_0 \sigma}}$

P = pressure

Re = Reynolds number $\equiv \frac{\rho V D}{\mu}$

S = sieve screen size

t = time

V = velocity or jet velocity (initial)

W = weight of fluid in the jet column

We = Weber number $\equiv \frac{\rho_j V^2 D}{\sigma}$

We_a = Ambient Weber number $\equiv \frac{\rho_a V^2 D}{\sigma}$

α = void fraction, wave amplitude time constant, or nozzle contraction coefficient

Δ = difference

$\varepsilon = \frac{\rho_j}{\rho_c}, \frac{\rho_j}{\rho_a}$, or nozzle to liquid free surface fall time

εFr = densitometric Froude number $\equiv \frac{\rho_j}{\rho_c} \frac{V^2}{gD}$

η = interfacial perturbation wave or ULLN distribution variable

κ = penetration rate constant

λ = wavelength or latent heat of vaporization

μ = dynamic viscosity or mean value

ρ = density

σ = jet surface tension or standard deviation

τ = shear stress or dummy variable of integration

φ = velocity potential

Subscripts

a = ambient fluid

avg = average

c= liquid coolant or continuous phase

d = drop or dispersed phase

e = equivalent

eff = effective

f = liquid

g = gas

j = jet

n = nozzle

p = penetration

r = relative

s = liquid free surface

v = vapor

vc = vapor chimney

0 = initial

Superscripts

+ = dimensionless variable

1.0 INTRODUCTION

1.1 Background-

In the two types of nuclear power reactors operating in the United States, Pressurized Water Reactors (PWRs) and Boiling Water Reactor (BWRs), the reactor pressure vessel (RPV) contains a large plenum below the reactor core (i.e., the nuclear fuel bundles). In the event of a loss of coolant accident (LOCA), the core may become uncovered, causing the fuel pins to melt. The molten fuel would pour into the plenum and collect on the RPV lower head. The following is a brief description of the fuel relocation mechanics its consequences (For an overview of the thermo-fluid science issues in core-melt accidents, see Theofanous (ref. 1).).

The RPV internal structure includes one or more perforated plates in the lower plenum (Figure 1).[2] These plates are expected to divide the molten fuel flow into small diameter streams or jets,[3] which would break up as they penetrate the coolant in the lower plenum. The breakup of these jets would occur in two phases, each dominated by a distinct fragmentation mechanism. As a fuel jet first penetrates the coolant, a stagnation flow develops at its leading edge, causing the column to spread radially and eject molten fuel into the coolant (Figure 2). Because of this removal of fluid from the jet leading edge, the rate at which the jet leading edge penetrates the coolant is less than the jet velocity. If the jet column were not affected by the presence of the ambient fluid, the jet would continue to penetrate deeper into the coolant as long as the jet flow continued. However, the jet fluid in the column is fragmented by pressure fluctuations due to the jet/ambient fluid relative motion, so that a steady jet is reduced to a field of falling drops below a critical depth called the *breakup length*.

The temperature of the molten fuel is much greater than the minimum film boiling temperature of the water coolant. The jet column and the coolant will be separated by, at a minimum, a thin vapor film. However, vapor generation from the quenching of fuel drops dispersed in the coolant, if sufficiently great, could cause significant voiding of the coolant surrounding the jet column, so that the jet essentially penetrates a highly voided counterflowing two-phase mixture.

When molten fuel fragments are dispersed into the coolant, an energetic fuel-coolant interaction, i.e., a steam explosion, may result. A steam explosion could produce missiles capable of penetrating the containment structure.[4] The strength of the explosion would depend on the mass of fuel available to participate, i.e., the mass 'properly' mixed (*premixed*) with the coolant. If the jet breakup length is less than the depth of coolant in

the RPV, the entire mass of relocated fuel might become premixed. On the other hand, if the jet can penetrate coherently to the RPV lower head, the mass of fuel premixed is limited by the rate of ejection of fuel fragments from the jet leading edge.

Coherent penetration of fuel jets to the RPV lower head may cause ablation and breach of the RPV.[5] Molten fuel ejected at high pressure from the RPV could cause direct heating of the containment atmosphere sufficient to overpressurize the containment structure.[6]

Another concern is the quenchability of molten fuel ejected from a breached RPV into the reactor cavity. One strategy to ensure quenchability is the use of a wet cavity,[7] which is intended to cause the fuel jets to be fragmented into a quenchable debris bed.

In order to address the concerns described above, a fundamental understanding of the jet breakup phenomena must be obtained. The breakup length of a fuel jet penetrating the volatile coolant must be estimated. The rate of melt ejection from the leading edge of the fuel jet during its initial penetration of the coolant is also of interest. To date, no analytical or computational model predictions of either of these behaviors have been validated by comparison with relevant experiments.

1.2 Scope of the Present Work

A few authors have attempted, using analytical models, to estimate the breakup length of molten fuel jets penetrating water. Several computational models of fuel-coolant mixing have also been developed. Some of these model fuel fragmentation, making them nominally capable of predicting jet breakup lengths. However, such predictions could not be validated. Evaluation of the very different assumptions about the hydrodynamic fragmentation of the molten fuel has also been impossible, due to the paucity of relevant experimental data.

The fragmentation behavior of a hot jet in a volatile liquid determines the ambient flow conditions (i.e., two-phase flow regimes and velocity fields). These in turn determine the jet fragmentation behavior. In other words, the hydrodynamics and thermodynamics are coupled. Therefore, the computational models can only be validated by comparison of code predictions with data from experiments with hot jets penetrating volatile liquids.

Ideally, computational models would be validated by experiments with prototype materials. Since prototype material experiments are relatively difficult to conduct, it is reasonable as a first step in their validation to compare their predictions with data from experiments conducted with more easily handled simulant materials.

In the present work, simulant material experiments have been conducted which

contribute to the base of relevant experimental data. The breakup of metal (Cerrobend®) jets penetrating a volatile liquid CFC (Freon®-11) has been observed using high speed motion pictures and X-radiography (both flash and cine). These experiments have been designated MFSBS (*Molten Fuel Stream Breakup Simulation*). The data obtained include *Breakup Length, Jet Leading Edge Penetration Rate, Net Vapor Generation,* and *Jet Debris Size Distribution.*

The present work was also initiated to determine whether the excellent correlation of jet *penetration length* (defined as the length of the vapor chimney surrounding the jet) with the jet/volatile liquid density ratio and Froude number, obtained by Saito et. al.,[8] would predict jet breakup lengths when the jet density ratio is much greater than that of the volatile liquid. In their experiments with water jets penetrating volatile liquids of comparable density (Freon-11 and liquid nitrogen) the interactions were photographed using a high speed video camera. The shadow of the backlit vapor chimney always obscured the jet, making it impossible to observe the mechanisms determining the penetration length. In the MFSBS experiments, *X-radiography has been used to visualize the jet,* so that the operative fragmentation mechanisms could be observed.

In addition to presentation and discussion of the experiment data, this work includes analyses yielding simple correlations for jet breakup length and jet leading edge penetration rate.

2.0 LITERATURE REVIEW

The literature review begins with introductory remarks about the physics of jet breakup. Then, linear analysis of jet instability is discussed in detail. The balance of the relevant literature is discussed in the following order: analyses and experiments related to liquid jet breakup in gases, liquid jet breakup in quiescent liquids, liquid jet breakup in volatile liquids, liquid jet penetration of liquids. The literature review concludes with a discussion of analytical and computational models of molten fuel jet breakup and fuel-coolant mixing.

2.1 Remarks on the Physics of Jet Breakup

Two types of *hydrodynamic* instability may cause the breakup of a steady *laminar* jet: *Rayleigh* and *Kelvin-Helmholtz*.

If an initially cylindrical jet is deformed slightly so that its diameter is nonuniform, the surface curvature, and with it, the internal pressure due to capillarity, will be greater where the diameter is smaller. Then, fluid will flow from the smaller to the larger diameter regions, magnifying the diameter variations; until the jet breaks into large drops. Breakup due to capillarity is usually called *Rayleigh* breakup (for Lord Rayleigh, who first analyzed this type of instability).

Aerodynamic forces may also cause jet instability. Due to the Bernoulli effect, the pressure at the crest of a small deformation on the jet surface will be lower than at its base, causing it to grow. This type of instability is called *Kelvin-Helmholtz* (or, occasionally, Aerodynamic). If the wavelength of the deformation is on the order of the jet diameter, the jet will become segmented. If the deformation wavelength is much smaller than the jet diameter, the deformation may grow until a drop is formed and ejected from its crest. It has usually been presumed that this instability is responsible for jet *atomization*, i.e., the breakup of a jet into a fine spray almost immediately as it issues from the nozzle. However, other mechanisms, such as cavitation, have also been proposed to explain atomization.

Deformation of the jet surface is resisted by the inertia of the jet fluid and by viscous stresses. Deformations having curvatures larger than that of the jet column are also opposed by capillarity.

The hydrodynamic breakup of a *turbulent* jet can also be affected by nozzle geometry and jet turbulence intensity,[9] with which jet breakup lengths have been correlated.[10] Jets may also break up due to *thermo-mechanical* instability; i.e., flashing (if

the jet is a superheated liquid) or cavitation (caused large turbulent pressure fluctuations in the jet when its surface is subjected to extremely high shear stress). These breakup mechanisms are not relevant to fuel jet breakup in core-melt accidents and are not discussed here.

2.2 Linear Analysis of Jet Instability

2.2.1 Derivation of the Dispersion Relation

Many of the salient features of jet breakup can be predicted qualitatively by examining the stability of a fluid interface subjected to a small perturbation. If it is assumed that the perturbation amplitude is small enough that powers of the perturbation amplitude and velocity potential greater than one may be neglected, linearized forms of the governing equations may be used. This was the basis for the jet breakup length relations derived by Weber, Taylor, and Levich.[11,12,13,14]

An alternative approach, which is restricted to long wavelength, but not necessarily infinitesimally small perturbations, is based on the assumption that the jet cross-section remains circular even as the jet column develops sinuosities (which is a good approximation for perturbation wavelengths much greater than the jet diameter). Viscous jets in gases have been shown with this assumption to be subject to long wavelength transverse instability caused by dynamic pressure forces.[15,16,17] This approach is not relevant to fine fragmentation of a jet, and so will not be discussed here.

Lamb[18] and Chandrasekhar[19] have given general introductions to linear instability analysis. Its application to jets is discussed extensively by Levich. The present discussion is, for simplicity, limited to inviscid fluids.

Consider an initially undisturbed cylindrical jet, subjected to a surface deformation of arbitrary waveform. Any waveform can be expanded (by Fourier integral) as the superposition of sinusoidal waves; thus only sinusoidal deformations of the interface need be considered. Let:

$$\eta = \eta_0 e^{(i(kx+m\theta)+\alpha t)}$$

where k is the wave number and α is the wave amplitude time constant. Here, m is the azimuthal mode of the deformation; for example, m = 0 corresponds to an axisymmetric or varicose deformation, while m = 1 represents a sinuous or 'snake' deformation.

The velocity potentials due to the perturbations of the interfaces must satisfy Laplace's equation, which in cylindrical coordinates is:

$$\frac{d^2\varphi}{dx^2} + \left[\frac{1}{r^2}\right]\frac{d^2\varphi}{d\theta^2} + \left[\frac{1}{r}\right]\frac{d}{dr}\left[r\frac{d\varphi}{dr}\right] = 0$$

The perturbation velocity potentials must have the same exponential form as the perturbations:

$\varphi = R(r)e^{(i(kx+ m\theta)+ \alpha t)}$

Solutions for R(r) that satisfy Laplace's equation are the modified Bessel functions of the first and second kind, of order m:

$R(r) = AI_m(kr) + BK_m(kr)$

where A and B are constants, and m may take any non-negative integer value.

The boundary conditions for the perturbation velocity potentials are φ_j remains finite at r = 0, and $\varphi_a \rightarrow 0$ as $r \rightarrow \infty$.

Subordinating to the boundary conditions gives the following expressions for the perturbation velocity potentials:

$\varphi_j = c_1 I_m(kr)e^{(i(kx+ m\theta)+ \alpha t)}$

and

$\varphi_a = c_2 K_m(kr)e^{(i(kx+ m\theta)+ \alpha t)}$

The linearized kinematical matching conditions, which match the normal velocity components on either side of the interface, are:

$$-\frac{d\varphi_i}{dr} = \frac{d\eta}{dt} + V_i\frac{d\eta}{dx},\ i=a,j$$

at r = a.

The dynamic matching condition, which equates pressures on both sides of the interface is:

$$p_j - p_a = -\frac{\sigma}{a^2}\left[\eta + a^2\frac{d^2\eta}{dx^2} + \frac{d^2\eta}{d\theta^2}\right]$$

at r = a.

The final boundary condition is derived from Bernoulli's equation:

$$p_i = \rho_i\frac{d\varphi_i}{dt} + \rho_i V_i\frac{d\varphi_i}{dx} \quad i = a, j$$

When the expressions for the velocity potentials and pressures are substituted into the kinematical and dynamic matching conditions the following system of algebraic equations is obtained:

$$c_1 I_m(ka)\rho_j(\alpha + ikV_j) - c_2 K_m(ka)\rho_a(\alpha - ikV_a) = -\frac{\sigma\eta_0}{a^2}(1 - (ka)^2 - m^2)$$

$$-c_1\frac{dI_m(ka)}{dr} = \eta_0(\alpha + ikV_j)$$

$$- c_2 \frac{dK_m(ka)}{dr} = \eta_0(\alpha + ikV_a)$$

This set of equations is homogeneous in the arbitrary constants c_1, c_2, and η_0.

Let M be the matrix of the coefficients of these constants. A unique solution exists only when:

$|M| = f(\varepsilon, We_a, k^+, \alpha^+) = 0$

The solution for the real part of α is:

$$(\alpha^+)^2 = \frac{\varepsilon\gamma_m\beta_m(k^+)^2}{(\gamma_m\varepsilon + \beta_m)^2} + \frac{[1 - m^2 - (k^+)^2]}{We_a(\gamma_m\varepsilon + \beta_m)}$$

where

$$\alpha^+ = \frac{aRe(\alpha)}{(V_j - V_a)}$$

$$\varepsilon = \frac{\rho_j}{\rho_a}$$

$$\gamma_m = \frac{k^+ I_m(k^+)}{\left[\frac{dI_m(k^+r^+)}{dr^+}\right]_{r^+=1}}$$

$$\beta_m = \frac{- k^+ K_m(k^+)}{\left[\frac{dK_m(k^+r^+)}{dr^+}\right]_{r^+=1}}$$

$$We_a = \frac{a\rho_a(V_j - V_a)^2}{\sigma}$$

$$k^+ = ka$$

$$r^+ = \frac{r}{a}$$

2.2.2 Analysis of the Dispersion Relation

Equation XXX is the called the *dispersion relation*. Usually this term refers to the relation between wave velocity and wavelength; however, here the term refers to the relation between wave amplitude e-folding time and wavelength. It is an algebraic equation quadratic in the complex quantity α. When α^+ is positive, the wave is unstable and will grow.

The limit as $We_a \rightarrow 0$ (or $\rho_a \rightarrow 0$) of the dispersion relation is the equation for breakup of a stationary liquid thread in a vacuum due to capillarity. Equation XXX then reduces to:

$$(\alpha^+)^2 = \frac{[1 - m^2 - (k^+)^2]}{We_a\gamma_m\varepsilon}$$

This equation was first derived by Lord Rayleigh.[20] Note that the growth rate is positive only for $m = 0$ and $k^+ < 1$. That is, the liquid thread is unstable only for varicose deformations, and only for deformation wavelengths somewhat greater than the jet diameter. The most rapidly growing deformation is one for which $k^+ = 0.7$. More generally, for liquid jets in gases, with $We_a << 1$:

$k^+ \sim 1$ with:

$$a^+_{max} \sim \frac{V}{(V - V_a)\sqrt{We}}$$

The dispersion relation shows that as We_a increases (with a finite ε), the wavelength of the most unstable deformation decreases. For $We_a \gg 1$:

$$k^+_{max} \sim \frac{1}{We_a}$$

with

$$a^+_{max} \sim We_a \sqrt{\frac{\rho_a}{\rho_j}}$$

Yang has analyzed the dispersion relation with regard to the azimuthal mode of the most rapidly growing deformations.[21] For $k^+ << 1$ (i.e., short waves), sinuous ($m = 1$) deformations will be more rapidly growing than varicose disturbances when:

$$We_a \geq 1 + \frac{1}{\varepsilon}$$

while for $k^+ \gg 1$, sinuous deformations will become dominant when:

$$We_a \geq k^+\left(1 + \frac{1}{\varepsilon}\right)$$

When We_a is large, all azimuthal modes m have essentially equal growth rates.

2.2.2.1 Summary

This analysis indicates the existence of at least three types or *regimes* of jet breakup, each corresponding to a particular range of We_a for a given jet-ambient gas pair.

When We_a is small, capillary breakup is dominant; the jet develops long wavelength ($k^+ < 1$) varicosities, and breaks into large drops. At a moderate value of We_a, sinuous, rather than varicose deformation becomes predominant. When We_a is very large, the jet develops very short wavelength ($k^+ \gg 1$) deformations of all azimuthal modes. Presumably, these deformations grow to eject small drops, as is observed in jet atomization.

2.2.3 Jet Breakup Length Relations

Linear -instability analysis is strictly valid only for infinitesimally small deformations. However, it has nevertheless been used to estimate jet breakup length.

It is usually assumed that the jet will break up due to the growth of deformations of the most unstable wavelength, i.e., the one for which α^+ is greatest. When this wavelength is on the order of the jet diameter, i.e., when k^+ is small, the jet is presumed to divide into large drops.

Levich assumed that the time required for the jet to break into drops is roughly the e-folding time of the wave amplitude. It follows that the jet breakup length is:

$$\frac{L}{D} \sim \frac{V}{Re(\alpha)_{max} D} \sim \frac{V}{V_r \alpha^+_{max}}$$

When the most unstable wavelength is much smaller than the jet diameter, i.e., when k^+ is large, the jet is presumed to be eroded by the ejection of drops. Taylor, and later Levich, assumed that the maximum amplitude reached by the small wave before it ejects a drop is proportional to its wavelength. Then, the entrainment rate, also called *erosion velocity*, is given roughly by:

$$E \sim \frac{Re(\alpha)_{max}}{k_{max}} \sim V_r \sqrt{\frac{\rho_a}{\rho_j}}$$

The continuity relation for the jet, assuming constant jet and erosion velocities, is:

$$D^2 V \sim LDE \text{ or } \frac{L}{D} \sim \frac{V}{E}$$

Combining these relations gives the jet breakup length:

$$\frac{L}{D} \sim \frac{V k_{max}}{Re(\alpha)_{max}} = \frac{V k^+_{max}}{V_r \alpha^+_{max}}$$

Thus, the breakup length expressions for high and low We_a are

$$\frac{L}{D} \sim \sqrt{\frac{\rho_j V^2 D}{\sigma}} = \sqrt{We}$$

and

$$\frac{L}{D} \sim \sqrt{\frac{\rho_j V^2}{\rho_a V_r^2}} = \sqrt{\frac{\rho_j}{\rho_a}} \frac{V}{V_r} = \sqrt{\frac{We}{We_a}}$$

respectively.

These relations identify the functional relation between jet breakup length and what are assumed to be the most important independent variables: V, D, ρ_j, and ρ_a. Constants of proportionality must be determined by experiment.

2.3 Jet Breakup in Quiescent Fluids

There exists a very extensive experimental literature on the breakup of liquid jets in gases (typically atmospheric air). Distinct breakup regimes have been noted; unfortunately, the various workers have used a variety of nomenclatures.

Breakup lengths have also been defined and measured in a variety of ways. Unless otherwise noted, breakup length here refers to the length of the contiguous jet column.

2.3.1 Breakup Regimes

Reitz proposed that the experimentally observed behaviors could be categorized by four breakup regimes: *Rayleigh*, *First Wind-Induced*, *Second Wind-Induce*, and *Atomization*.[22] Their characteristics are as follows:

1) RAYLEIGH-In the absence of aerodynamic forces (e.g., low velocity jets), varicose deformations due to capillary instability break the jet into drops having diameters larger than the jet.
2) FIRST WIND INDUCED-Capillarity is augmented by Kelvin-Helmholtz instability, breaking the jet into drops having diameters comparable to the jet.
3) SECOND WIND INDUCED-Large aerodynamic forces due to the jet-gas relative motion make the Kelvin-Helmholtz instability predominant. Both long wavelength deformations, such as sinuous and helical, and erosion of small drops from the jet surface are observed.
4) ATOMIZATION-The jet is fragmented into drops very much smaller than its diameter almost immediately as it issues from the nozzle. The mechanism of atomization has not been definitely established. The most developed theory is that of aerodynamic breakup. However, other explanations of the atomization phenomena have been proposed; namely, rearrangement of the jet velocity profile, jet supply pressure oscillations, wall-boundary layer velocity profile relaxation, nozzle turbulence, and cavitation.

Jet breakup regime maps have been constructed in terms of Ohnesorge (or Weber) and Reynolds numbers. These dimensionless groups include all the relevant variables for liquid jets issuing into atmospheric air. An example of such a map is shown in Figure XXX, with regime boundaries as given by Brodkey.[23] The extant experimental results have been mapped in this way most recently by Windquist.[24]

A comprehensive review of liquid jet breakup literature relevant to core melt accidents has been made by Ginsberg.[25] He constructed a qualitative plot of jet breakup

length as a function of the jet velocity. In this plot, the breakup length exhibits two local maxima, with a constant value above a threshold velocity. The ascent to the first local maximum corresponds to the *Rayleigh* regime. The descent from it is due to the onset of Kelvin-Helmholtz (or aerodynamic) instability. This breakup regime is designated *Transition*. With increasing jet velocity, the breakup length ascends to the second local maximum. The breakup regime corresponding to this ascent is termed *Turbulent*. As the jet velocity is further increased, the breakup length falls to a constant value, corresponding to the *Atomization* regime.

Ginsberg concluded from this plot that breakup length and breakup regime are primarily determined by the ambient Weber number. The regime boundaries suggested by Ginsberg are Rayleigh for $0 \lesssim We_a \lesssim 1$, and Atomization for $We_a \gtrsim 10^2$. He noted, however, that the atomization regime had been observed only for very small diameter jets ($\lesssim$ 1 mm diameter).

2.3.2 Jet Breakup Experiments, Analyses, and Breakup Length Relations

The following discussion reviews breakup length relations in the literature, for clarity *categorized by the present author* using the regime nomenclature proposed by Reitz:

2.3.2.1 Rayleigh Regime

Weber derived the relation:

$$\frac{L}{D} \sim \left[\sqrt{We} + \frac{3We}{Re}\right]$$

for the capillary breakup of jets of low viscosity.

Grant and Middleman later correlated their experimental data for laminar jet breakup with a similar expression:[26]

$$\frac{L}{D} = 19.5\left[\sqrt{We} + \frac{3We}{Re}\right]^{0.85}$$

For cold water jets issuing from a sharp-edged orifice into air, Lienhard and Day found:[27]

$$\frac{L}{D} = 11.5\sqrt{We}$$

In the water-gas cocurrent inverted annular flow experiments of De Jarlais et. al., the breakup length of turbulent jets in the Rayleigh regime was correlated by:[28]

$$\frac{L}{D} = 480(Re)^{-0.53}\sqrt{We}$$

The bulk of the literature on liquid jet breakup in *liquids* is concerned with the Rayleigh regime. A comprehensive review of this literature is given by Kitamura and Takahashi.[29]

The behavior of *highly viscous* liquid threads in liquids was analyzed by Tomotika.[30] In his analysis, the liquid inertia is neglected, so that only viscous forces oppose the action of capillarity. The diameter of the drops produced by this breakup increases with the ambient fluid/jet viscosity ratio; for a value near unity, the drop diameter is predicted to be about six times that of the jet. Experimental data are in good agreement with the theory.[31]

2.3.2.2 First Wind-Induced Regime

In experiments conducted by Ivanov, as the velocity of a liquid jet in air was increased, sinuous, rather than varicose deformations were observed.[32] His review of experimental data in the literature indicated that this change typically occurred at $We_a \sim 1$.

De Jarlais et. observed a transition from varicose to sinuous breakup for $\frac{We_a}{\alpha^2} \sim 2$. Note that $\frac{We_a}{\alpha^2}$ is an effective ambient Weber number for a jet in a confined gas flow area (For a free jet, $\alpha \rightarrow 1$).

The instability of jets submerged in the same fluid was studied by Batchelor and Gill.[33] They found that a laminar submerged jet is subject only to sinuous instability. They noted that a type of asymmetric instability had been seen in the experiments of Reynolds with water jets in water.[34] Reynolds observed a repeated lateral deflection of the jet as it penetrated the water, which he termed *Pedal Breakdown*. Pedal Breakdown also appears to have occurred in experiments with molten uranium alloy jets in liquid sodium.[35]

Recent experiments with pours of aluminum into water also evidenced a first wind-induced breakup.[36] Rayleigh breakup began as the jet flowed through the gas space above the water. In the water, the breakup of the jet into very large drops was more rapid. Although the jet Weber numbers were much greater than unity, one can speculate that the cooling of the aluminum surface caused a large increase in melt viscosity (the viscosity increases by orders of magnitude as the melting point is approached). According to the regime map of Ohnesorge, the Rayleigh breakup may occur for even very large values of We if the Reynolds number is sufficiently low.

2.3.2.3 Second Wind-Induced Regime

The experiments of Hoyt and Taylor on the breakup of water jets in a coaxial air flow fall into this regime.[37] In their experiments, some atomization occurred very near the nozzle, but did not cause the loss of a significant part of the jet fluid. Further from the nozzle, the jet developed helical waves, whose crests were eroded by the ejection of small drops. The eventual segmentation of the jets was shown to be due to form drag on these waves.

Breakup length correlations for turbulent jets in this regime have been obtained by Miesse, and Lienhard and Day. Miesse correlated breakup length for jets issuing from diesel injector nozzles by:[38]

$$\frac{L}{D} = 540 Re^{\frac{5}{8}} \sqrt{We}$$

For jets issuing from sharp edged orifices with Re > 48,000, Lienhard and Day found:

$$\frac{L}{D} = 2.75 \times 10^{10} Re^{-2} \sqrt{We}$$

In the *cocurrent* inverted annular flow experiments of De Jarlais et. al., the jets developed sinuous waves at $\frac{We_a}{\alpha^2} \approx 1$, while at higher values (on the order of tens), drop-ejecting roll waves appeared. This they termed *roll wave entrainment*. The onset of roll wave entrainment was in fair agreement with the prediction of the inception criteria for entrainment in annular two-phase flow proposed by Ishii and Grolmes.[39]:

$$\frac{j_g \mu_f}{\sigma} \sqrt{\frac{\rho_g}{\rho_f}} \geqq N_{\mu F}^{0.8}, \text{ for } N_{\mu F} < \frac{1}{15}$$

Breakup lengths for the entire range of wind induced breakup, i.e., for $\frac{We_a}{\alpha^2} \geq$, were correlated by:

$$\frac{L}{D} = \left(\frac{L}{D}\right)_{Rayleigh} f\left(\frac{We_a}{\alpha^2}\right)$$

where:

$$f\left(\frac{We_a}{\alpha^2}\right) = 1.43 \left(\frac{We_a}{\alpha^2}\right)^{-0.645}$$

De Jarlais et. al. conjectured that an expression for the wind-induced breakup of a laminar jet in cocurrent inverted annular flow could be obtained by using the Rayleigh breakup relation of Weber, with a constant of proportionality of ≈12 (as indicated by the

data of Grant and Middleman). This conjecture yields:

$$\frac{L}{D} \approx 17\left[\sqrt{We} + \frac{3We}{Re}\right]\left[\frac{We_a}{\alpha^2}\right]^{-0.645}$$

For a free jet (= 1) at high Re, this relation is similar to the proportionality derived from linear instability analysis in section XXX.

2.3.2.4 Atomization Regime

G. I. Taylor studied wind-generated ripples on the surface of a viscous fluid, using a linear instability analysis. As discussed above, the predicted entrainment rate for an inviscid jet is:

$$E \sim \frac{V_r}{\sqrt{\varepsilon}}$$

According to Taylor's analysis, increasing the liquid viscosity leads to a decrease in the rate of droplet ejection, but also to an increase in the size of the ejected drops, so that the entrainment rate is not greatly affected. Recalling that the mass balance for the steady jet is:

$$\frac{L}{D} \sim \frac{V}{E}$$

the corresponding jet breakup length for a jet issuing into a stagnant fluid (where $V_r = V$) is:

$$\frac{L}{D} \sim \sqrt{\varepsilon}$$

Taylor suggested a constant of proportionality of 5, based on his interpretation of the extant experimental literature on water jet breakup in air. Reitz's experiments with atomizing jets showed spray angle to increase (corresponding to a decrease in jet breakup length) with the ambient gas density, and to be insensitive to jet velocity, as predicted by Taylor's analysis. However, Reitz found that nozzle geometry had a strong effect on spray angle, and hence on the constant of proportionality in Taylor's breakup length relation.

More recently, the governing equations for the linear instability of viscous jets have been solved numerically. Lin and Kang assumed spatially, rather than temporally growing surface waves (for the relation between these, see ref. 40); their results differ slightly from Taylor's analysis. For example, Taylor's theory predicts a single spay angle, while Lin and Kang predict that this varies along the length of the jet core.[41] Lin and Ibrahim later considered the effect of ambient gas viscosity in their study of the instability of a viscous liquid jet in a vertical pipe.[42]

Although the aerodynamic theory is well developed, it cannot alone explain experimental observations, since the 'constant' of proportionality in equation XXX determined from atomizing jet experiments has varied from ~3 to 27. Recently, a cavitation model of atomization has been proposed which predicts:[43]

$$\frac{L}{D} \sim \frac{1}{We^3}\left[\frac{6V\mu_j}{\tau D}\right]^{\frac{7}{2}}$$

where τ is the shear stress at the nozzle or free jet surface. According to this model, high surface shear produces turbulent pressure fluctuations that induce cavitation. The authors claim that the parametric variations predicted by this relation are supported by all of the experimental studies of atomizing jets.

2.3.3 Summary

Jet breakup has been characterized by regimes, and these have been mapped as suggested by Ohnesorge. However, it is important to note that the atomization regime has been observed only for very small diameter jets.

Typical breakup length relations for low viscosity jets can be summarized as follows:

For Rayleigh breakup. it has been observed that:

$$\frac{L}{D} \sim \sqrt{We}$$

For turbulent jets, there is a Reynolds number dependence:

$$\frac{L}{D} \sim \frac{\sqrt{We}}{Re^n}$$

where $n > 0$.

When the jets break up due to the action of aerodynamic forces, there is a dependence on ambient Weber number:

$$\frac{L}{D} \sim \frac{\sqrt{We}}{We_a^m Re^n}$$

where $m > 0$ (and $n > 0$ if the jet is turbulent).

It is important to note the definition of breakup length associated with each of the above expressions. In general, breakup length denotes the distance over which the initially contiguous jet becomes broken into separate drops or segments which have characteristic dimensions comparable to the jet diameter. For the atomization regime, however, the breakup length denotes the length of the contiguous jet core, which is eroded by the ejection of drops having dimensions much smaller than the jet diameter.

2.4 Jet Breakup in Volatile Liquids

A number of experiments have been conducted in which *corium* (prototype reactor core material mixtures of UO_2, zirconium, and steel) or iron-alumina thermite melt streams were poured into water.[44,XXX,45,46,47] However, jet breakup length correlations have not been obtained from these experiments.

Sandia National Laboratories (SNL) has carried out numerous drops of 'slugs' of iron/alumina melt into water in the FITS experiments. These were intended to provide data regarding steam explosions, debris formation and hydrogen generation (from oxidization of the melt). SNL has also conducted experiments with iron/alumina jets issuing at low velocity (< 1 m/s) into water. The experimentalists reported immediate jet breakup on contact with the water.

Prototypic materials experiments at ANL (CWTI and CCM series) have used corium thermite (UO_2-ZrO_2-Steel) melts in water. The CWTI series of experiments modeled corium discharge into the reactor cavity of the Zion PWR. In experiment CWTI-9, the corium jet penetrated the 14 jet diameters (31 cm) to the vessel base without substantial breakup.

In the later CCM series experiments, corium was poured into a deep (~1 m) pool of water; however, in most experiments, the available melt mass was probably too small to establish a steady jet breakup. Motion picture photography of the melt stream breakup was not possible. X- ray radiographic motion pictures were obtained in one experiment; however, the field of view was too limited for breakup length to be determined. Breakup lengths (or dispersal lengths) had to be estimated from thermocouple responses; i.e., thermocouples along the jet axis were burnt out as the leading edge of the corium jet contacted them. These data suggested that breakup lengths of tens of stream diameters are possible. However, the interpretation of the raw data was very subjective, so these data must be considered to be approximate.

The CCM debris beds consisted largely of re-agglomerated melt; however, there were also many clearly identifiable spheroidal debris fragments. Even though the melt temperature was only about 160 °C above liquidus, drops torn from the corium stream apparently became hydrodynamically stable before solidifying.

In two of the CCM experiments, the water level rise in the pool was photographed by a motion picture camera. The pool swell data, in conjunction with the thermocouple data (from which the boundaries of the melt mixture at various times may be estimated), indicate that a corium jet penetrating water at one atmosphere is surrounded by a very

large diameter, highly voided mixture region, i.e., a vapor chimney.

The experimental difficulties associated with the use of these very high temperature melts (the melting point of UO_2 is about 3100 K) has motivated experiments using relatively low temperature fluids in both isothermal and boiling jet experiments. The penetration of large diameter immiscible Freon-TF jets into water was observed in experiments at Sandia National Laboratories (SNL).[48] The breakup length was defined as the depth at which the jet leading edge penetration velocity slowed from an initial value comparable to the jet velocity, to a much lower, fairly constant value. It was well predicted by Taylor's suggested relation for atomizing jets:

$$\frac{L}{D} = 5\sqrt{\varepsilon}$$

The authors interpreted the measured breakup length as being the length of the non-buoyant region of a turbulent buoyant jet. However, this relation is not in agreement with data for turbulent jets in the literature reviewed by Chen and Rodi. They correlated centerline velocity, density, and species concentration data for turbulent, buoyant jets in the literature (all of which were *miscible* gas and liquid pairs with $\varepsilon \approx 1$).[49] They noted that the jet could be characterized as consisting of non-buoyant (near the nozzle), intermediate, and plume (in the far field) regions. Near the nozzle, the jet momentum flux dominates the behavior, while in the far field, the buoyant force is dominant. They correlated the length of the non-buoyant region by:

$$\frac{L_{\text{non-buoyant}}}{D} \sim 0.5\sqrt{\frac{Fr\sqrt{\varepsilon}}{\varepsilon - 1}}$$

This correlation was derived from similarity arguments, i.e., it is applicable only for a self-similar flow. In a fully developed turbulent jet, the mean velocity and density profiles are Gaussian and self-similar. Near the nozzle, where these profiles are not yet developed, the jet has a potential core with a flat velocity profile, where the jet fluid and ambient fluids are not intermixed. Chen and Rodi noted that the length of the potential core for gas jets in comparable density gases is roughly 5 jet diameters. Although Marshall et. al. supposed that their measured breakup lengths (equation XXX) corresponded to the non-buoyant region of a turbulent buoyant jet, it may be more accurately interpreted as the length of the jet *core*; the breakup lengths observed were comparable to the typical jet core length noted by Chen and Rodi.

Spencer et. al. conducted pours of Wood's metal and Cerrotru into water.[50] They defined the jet breakup length as the depth at which the mixture penetration velocity fell to a nearly constant value, characteristic of the terminal velocity of small drops. The breakup length was interpreted as the length of the substantially contiguous jet column, i.e., the

depth at which fragmentation was complete. This interpretation implicitly equates the jet breakup length with the length over which the jet's initial momentum is transferred to the ambient liquid. That is, it assumes that fragments torn from the jet lose their initial momentum over a negligibly short distance which does not extend beyond the end of the contiguous jet column.

The melt temperature and water subcooling in these experiments were varied to create conditions ranging from no boiling to transition boiling at the melt-water interface. In the experiments with little boiling and no *net* steam generation, the jet breakup lengths were 18-20 jet diameters. High speed motion pictures showed the jet to be undergoing both long and short wavelength deformations, with filaments being drawn from the wave crests into the water. Fitting the breakup length data to relation XXX indicates a proportionality constant of ≈ 6. Interfacial boiling led to breakup lengths more than double those in experiments with no net vapor generation. It is especially interesting to note that the greatest breakup length was observed for transition boiling, where the vapor generation rate was relatively low.

In order to investigate the fundamental phenomena of boiling jet breakup, Saito et. al. conducted experiments with water jets penetrating Freon-11 and liquid nitrogen. The experiments were photographed with a high-speed video camera. The jets themselves were always obscured by the shadow of a very large diameter vapor chimney.

Because the jet and volatile liquid densities were similar, the dispersed jet fluid did not fall to the bottom of the pool, but was swept upward by the vapor flow/and or buoyancy. The length of the vapor column beneath the pool surface, termed *penetration length* by the experimenters, was correlated extremely well by:

$$\frac{L}{D} = 2.1\sqrt{\varepsilon Fr}$$

for $0.7 < \varepsilon < 1.2$

They proposed the following relation, apparently considering the jet to be a streamline along which Bernoulli's equation could be applied:

$$\frac{1}{2}\rho_j V^2 = (\rho_c - \rho_j)gL + \left[\frac{\Delta P}{\Delta l}\right]_f L$$

According to this relation, the penetration length corresponds to the depth at which the entire velocity head of the jet flow has been converted to static pressure head. The static pressure in the vapor chimney was assumed to be the sum of the hydrostatic pressure gradient in the coolant pool and a pressure gradient due to the interaction of the jet with the liquid coolant. A rearrangement of this relation yielded:

$$\frac{L}{D} = \frac{1}{2}\left(\frac{\varepsilon}{1-\varepsilon}\right) Fr \left(\frac{1}{1-K_i}\right)$$

where K_i, the *Interaction Parameter*, "...indicates the relative strength of the resistant force due to the thermal and hydrodynamic interactions between the jet and coolant, compared with the buoyancy due to the density difference," where K_i is defined by:

$$K_i \equiv \frac{\left(\frac{\Delta P}{\Delta l}\right)_f}{(\rho_c - \rho_j)g}$$

From their empirical penetration length correlation, it was inferred that:

$$K_i = 1 + \frac{1}{4.2}\left(\frac{\sqrt{\varepsilon}}{\varepsilon - 1}\right)\sqrt{\frac{We}{Bo}}$$

Saito et. al. asserted that We is related to Kelvin-Helmholtz breakup along the jet column, while Bo is related to breakup at the jet leading edge. They conjectured that an increase in We causes a stronger hydrodynamic interaction between the jet and liquid coolant, decreasing the penetration length. On the other hand, an increase in Bo increases jet fragmentation, and hence vapor generation, at the jet leading edge, which produces a thicker vapor blanket; this decreases the jet-coolant interaction and therefore increases the penetration length.

The jets could not be seen in the video, so the physical process determining the penetration length could not be observed. It was therefore not clear that this relation would be applicable for large ε, e.g., for corium in water. However, the authors noted that two of the *breakup lengths* of Wood's metal jets in water (when there was net steam generation) reported by Spencer et. al were also in agreement with their correlation.

It is notable that penetration length was dependent on the *liquid* coolant density, even though there was apparently little contact between the vertical jet column and the liquid coolant. This suggests that the penetration length may be a function of the hydrostatic pressure gradient in the coolant pool.

2.5 Fuel-Coolant Mixing and Jet Breakup Analyses

It has generally been assumed that in order to be considered 'premixed' for participation in a steam explosion, molten fuel must be fragmented to some optimal size, and be surrounded by a two phase mixture of sufficiently low void fraction.[51] One of the objectives of the current computational models of fuel coolant mixing is, of course, to allow estimation of the maximum premixed fuel mass. Prior to the development of these models, various criteria were proposed based on simple analyses. A good review of these

was given by Corradini and Moses.[52]

Cho et. al. proposed that premixing would be limited by the energy required for the hydrodynamic fragmentation of the fuel, and noted that for LWRs this is much less than the internal energy of the molten fuel.[53] Henry and Fauske assumed that the mixing process would be limited by fluidization of the water by the generated steam at the critical heat flux.[54] Their analysis predicts a very small premixed fuel mass. Corradini and Moses pointed out that this result is a consequence of their assumption that water can reach the fuel only from above by falling through the steam flow.

Theofanous and Saito briefly speculated about the breakup of a corium jet in water.[55] They considered Rayleigh breakup the most likely fragmentation mechanism. However, they concluded that, for the available fall distances in core-melt accidents, only jets of ~10 cm or less in diameter would have time to break up. They presumed that jet breakup (other than Rayleigh breakup) would occur only if Steen's criteria[56] for entrainment in parallel flow were met:

$$\frac{V_r \mu_a}{\sigma_j}\sqrt{\frac{\rho_a}{\rho_j}} > 2.46\ 10^{-4}$$

They noted that although a relative velocity of only ~1 m/s is needed for entrainment for water as the ambient fluid, for the more likely event of the jet being blanketed by steam, the minimum entrainment velocity is ~1000 m/s. They also briefly mentioned that mixing would also occur at the leading edge of a penetrating fuel jet, but concluded that a significant mass of fuel would not be mixed with the coolant in this way.

Ginsberg estimated corium jet breakup length based on his review of the literature on liquid jet breakup in gases. He assumed a 5 m/s corium jet with a 20 m/s countercurrent steam flow; for these conditions, Ginsberg expected an atomizing jet. Using Taylor's relation for jet breakup length in a *stagnant* ambient fluid (equation XXX), he estimated the breakup length to be on the order of 100 jet diameters.

The effect of a vapor film or blanket surrounding the corium jet was also taken into consideration by Epstein and Fauske in their linear analysis of Kelvin-Helmholtz instability for a two-interface (i.e., corium/steam and steam/water) plane geometry.[57] They concluded that the vapor blanket around the corium jet would be so thick that the jet would be affected only by the steam flow. Implicitly assuming the vapor to be stagnant, the breakup length relation they derived for this case is:

$$\frac{L}{D} = \frac{\sqrt{3}}{2}\left(1 + \frac{\rho_s}{\rho_j}\right)\left(\frac{\rho_j}{\rho_s}\right)^{\frac{1}{2}}$$

This relation is essentially that of Taylor (proportionality XXX). The significance of the

constant of proportionality is doubtful, since this equation was derived using relations having only order-of-magnitude accuracy. Nevertheless, the authors used this relation, taking $\frac{\rho_j}{\rho_s} \approx 10^4$, to estimate a fuel jet breakup length on the order of 90 jet diameters.

Bürger et. al. have suggested that the vapor velocity in this case would be much greater than the jet velocity, so that the vapor and jet-vapor relative velocities would be comparable.[58] They correlated breakup length from the the literature with proportionality XXX derived above, with the vapor velocity estimated by equating the vapor kinetic energy with the hydrostatic head of the coolant pool, i.e.:

$$V_v \sim \sqrt{\frac{\rho_c g L}{\rho_v}}$$

The resulting breakup length expression is:

$$\frac{L}{D} \sim (\varepsilon Fr)^{\frac{1}{3}}$$

which differs from the empirical correlation of Saito et. al. in the exponent of the densitometric Froude number.

2.6 Computational Models of Fuel-Coolant Mixing

A complete list and brief description of the extant computational models of fuel-coolant mixing is given by Fletcher and Thyagaraja.[59] Only the four codes that have included modeling of fuel fragmentation are discussed here.[60] Both IFCI[61] and CHYMES are two-dimensional finite difference Eulerian codes for three fluids, i.e., molten fuel, liquid coolant, and vapor. In the CHYMES code it is assumed that the fuel is configured as dispersed spherical drops, while IFCI employs in addition a surface tracking algorithm to calculate surface erosion due Kelvin-Helmholtz instability.[62] Both use drop fragmentation rates derived from the Lagrangian relation:

$$\frac{d}{dt}(d) = -0.245|V_r|\sqrt{\frac{\rho_a}{\rho_d}}$$

obtained from a detailed model of the splitting of drops due to Rayleigh-Taylor instability developed by Pilch.[63]

The physical basis for this relation may be explained simply. Pilch noted that, although the real breakup times reported in the literature for liquid drops in gas streams varied by orders of magnitude, the dimensionless breakup time:

$$t^+ = \sqrt{\frac{\rho_a}{\rho_d}}\left(\frac{t|V_r|}{d_0}\right)$$

ranged only from 3 to 6.[64] It is notable that over this range of Weber numbers, roughly 10-10^6, a number of different drop breakup regimes are observed.[65] An order-of-magnitude approximation for the rate of drop fragmentation is therefore:

$$\frac{d}{dt}(d) \approx \frac{d}{t} \approx \frac{1}{t^+}|V_r|\sqrt{\frac{\rho_a}{\rho_d}}$$

Another related drop fragmentation model, developed by Chu, has also been used in the TEXAS code to model fragmentation of a jet.[66] There the jet was idealized as a train of sequentially fragmenting drops, on the assumption that significant fragmentation would occur only at the jet leading edge, as suggested by the analysis of Epstein and Fauske.

THIRMAL is a quasi-one-dimensional model of the fragmentation of a *single jet*. Various assumptions are made to estimate the characteristics of the vapor counterflow in the two-dimensional mixing zone surrounding the jet. It is assumed that the jet column is eroded, due to Kelvin-Helmholtz instability, by the entrainment of small drops into the vapor counterflow. As in the analysis of Epstein and Fauske, the expression for erosion velocity, and hence the breakup length, is obtained directly from analysis, without an experimentally determined proportionality constant.

2.6.1 Comparison with Experimental Observations

Although equation XXX was derived from a drop breakup model, it has the same form as the relation for entrainment rate derived by Taylor; it *may* therefore predict reasonably well the rate of atomization of a jet column due to Kelvin-Helmholtz instability, using an appropriate constant of proportionality. The appropriate value for liquid jet breakup in liquids (where entrainment is occurred over the entire jet surface, as for atomizing jets) can be estimated by comparison with the experimentally determined proportionality constants in relations XXX and XXX:

$$\frac{d}{dt}(d) = \frac{d}{dx}(d)\frac{dx}{dt} \approx \frac{D}{L}V \approx \frac{1}{5}\frac{|V_r|}{\sqrt{\varepsilon}}$$

This value is roughly the same as is used by CHYMES and IFCI, indicating that their predictions of jet breakup length for jets in the *atomization regime* may be reasonable.

The jet breakup model developed by Chu and Corradini using a similar drop breakup model with the TEXAS code has been compared with observations from FITS

experiments (iron-alumina pours into water) conducted at SNL. The predicted leading edge penetration rate was in good agreement with the experiments. However, the debris sizes predicted were much larger than observed.

CHYMES code predictions have been compared with observations of uranium dioxide-molybdenum drop fields penetrating water.[67] The steam generation rate was well predicted. However, in the experiments the drop field was momentarily fluidized upon entering the water; this was not predicted by CHYMES. The mixture front then developed Rayleigh-Taylor instability, and penetration resumed. CHYMES predicted well the later, steady penetration rate.

2.6.2 Summary

In the extant computational models of fuel-coolant mixing, fuel fragmentation is modeled, if at all, very simply. In all models, the local drop fragmentation rate or jet column erosion velocity is proportional to $\frac{|V_r|}{\sqrt{\varepsilon}}$, which experiments have shown to be at least a good first approximation for fragmenting drops or completely atomizing jets. Local fragmentation rate predictions then depend on what constant of proportionality is selected, and on the method used to calculate $|V_r|$.

The comparisons of the models with experiments have been very limited; none have been shown to accurately predict the breakup length of any jet penetrating a volatile liquid. To quote Fletcher and Thyagaraja, "Needless to say each set of workers defends the assumptions they have made. In general, the models have become more complex with time...It is not, however, evident that such complexity is warranted by the existing experimental data base against which the models can be validated."

2.7 Summary

Although there is a large body of literature on the breakup of liquid jets in gases and quiescent liquids, there has been little investigation of the breakup of hot jets directed into volatile liquids.

Analyses of fuel jet breakup in coolant have equated the jet breakup length with the depth at which the jet column has been completely eroded by entrainment of the melt into the vapor flow, and have simply combined Taylor's idea that:

$$E \sim \frac{V_r}{\sqrt{\varepsilon}}$$

with assumptions about the jet-vapor relative velocity and constants of proportionality from the literature on atomizing jet experiments. Computational models have either neglected fuel fragmentation, or applied a similar fragmentation rate relation to each computational cell. There has been little comparison of the predictions of the computational models with relevant experimental data, primarily due to the lack of the latter.

Experiments with corium or iron-alumina thermite pours into water have not yielded jet breakup length correlations. Only in the simulant experiments of Saito et. al. with water jets in Freon-11 and liquid nitrogen has a correlation (albeit a ***penetration length*** correlation) been obtained. The physical mechanisms determining penetration length could not be observed. However, the dependence of the penetration length upon the density of the penetrated *liquid* (even though the jet was shielded from contact with the liquid by a large diameter vapor chimney) suggests that the hydrostatic pressure gradient in the pool plays an important rôle.

3.0 EXPERIMENT OBJECTIVES

One of the objectives of the present experiments was to contribute *jet breakup length, jet leading edge penetration rate*, and *vapor generation* data to the existing simulant material experiment data base available for the evaluation of computational models.

In addition, these experiments were conducted to address specific questions about the applicablility of the jet *penetration length* correlation obtained by Saito et. al. Namely, 1) Is the correlation a good predictor of *breakup length* for high jet-coolant density ratio systems (e.g., molten reactor fuel penetrating water), and if so, 2) What type of fragmentation mechanisms are operative? The latter question has been addressed by obtaining visual images of the jet breakup process using X-radiography. These images can also be used for the evaluation of the conceptual pictures of fuel fragmentation utilized by the computational models.

To satisfy the experiment objectives, it was necessary to select appropriate simulant fluids, and construct an apparatus that would 1) Allow variation of the jet Froude number, 2) Allow both photographic and radiographic images of the jet breakup process to be obtained, and 3) Maintain a hydrostatic pressure gradient in the coolant pool, which the form of the Saito et. al. correlation suggests played an important rôle in determining jet penetration length. A hydrostatic pressure gradient is also necessary to test the breakup length correlation proposed by Bürger et. al., which is based in part on the assumption of a hydrostatic pressure gradient in the coolant pool.

4.0 EXPERIMENT DESCRIPTION

4.1 Introduction

The present experiments, single dense metal (Cerrobend®) jets have been directed into nearly saturated Freon-11. Cerrobend® is a low melting point alloy (wt. %: 50.0 Bi, 26.7 Pb, 13.3 Sn, 10.0 Cd) whose generic name is Lipowitz's metal. Freon-11 is the DuPont Co. trade name for trichlorofluoromethane (CCl_3F).

Jet leading edge penetration rates have been measured, and jet breakup lengths have been inferred, from high-speed motion pictures. The motion pictures also provide a record of the extent of the melt/vapor/liquid mixture region. Flash and cine X-radiography has been used to visualize the jet column and surrounding mixture. The two X-ray systems are complementary; the flash system could be used without obstructing the motion picture camera view of the apparatus, and provides high resolution images, while the cine system could record the dynamic fragmentation of the jet and the motions of entrained fragments, albeit with lower resolution. The jet debris fragments have been sifted, and the data have been correlated and compared with those from related experiments. Finally, the net vapor generated by the melt quenching has been measured from the apparatus pressurization or by condensation.

Experiments with three collinear jets at various spacings have also been conducted using the same apparatus (with the additon of a multiple nozzle assembly) and procedure. For a description of these experiments, see Marciniak.[68]

4.2 Simulant Material Selection

The jet Froude number can be controlled by varying the jet diameter and entry velocity. The jet/coolant liquid density ratio can be varied only by using different simulant fluids. Simulant experiments with density ratio values near unity have already been conducted by Saito et. al.; therefore, the highest possible jet density was desirable for the MFSBS experiments. A large jet/coolant liquid density ratio is also needed so that the melt can be differentiated from the ambient liquid in radiographs. Finally, it was desired to obtain a density ratio as close as possible to that of corium/water.

The necessary jet density could be obtained only by using a dense metal (i.e., Pb) or dense metal alloy. Cerrobend® was chosen as the jet fluid because its low melting point makes it convenient to use. It is also relatively inexpensive and widely available.

The apparatus had to include large transparent panels for photography, and so

could not easily be designed to withstand high pressures or vacuum. The coolant was therefore selected to allow the experiments to be conducted with the apparatus at approximately atmospheric pressure. The boiling point of Freon-11 is only 23.8 °C at 1 atm; even a relatively low temperature metal jet directed into Freon-11 at 1 atm. creates a large vapor chimney.

Relevant physical properties of these materials are given in Table XXX.[69,70,71] Cerrobend® surface tension has been estimated from the surface tensions of its constituent elements,[72] weighting by volume fraction.

Property	Cerrobend® (70 °C)	Freon-11 (sat. liquid @ 1 atm.)	Freon-11 (sat. vapor @ 1 atm.)
Density (kg/m^3)	9,229	1,477	5.87
Surface Tension (N/m)	0.4	0.019	---
Dynamic Viscosity (Pa·s)	1.6×10^{-3}	4.39×10^{-4}	1.05×10^{-5}
Melting Point (°C)	70	---	---
Boiling Point (°C) (1 atm.)	---	23.8	---
Heat of Vaporization (kJ/kg)	---	180.2	---
Heat of Fusion (kJ/kg)	33	---	---
Heat Capacity (kJ/kg °C)	0.17	0.87	0.50

Ideally, the coolant should be in film boiling on all melt surfaces (as obviously occurs when corium is quenched in water) to ensure that melt fragmentation is not caused by nucleate boiling; such a breakup mechanism would not be important for corium breakup in water, and so is not of interest here.. However, the maximum melt temperature is limited by the need to ensure that a vapor explosion (which the experiment apparatus might not withstand) does not occur.

Fauske proposed that a necessary condition for a vapor explosion is an instantaneous melt/ambient liquid contact temperature above the homogeneous nucleation

temperature of the ambient liquid.[73] For a metal in Freon-11, Fauske's vapor explosion criteria requires a jet temperature above approximately 130 °C. Accordingly, to allow a margin of safety, the maximum melt temperature in the MFSBS experiments has been limited to 110 °C.

The possibility of chemical reactions was also a concern. Violent molten metal-CFC chemical reactions have been observed;[74] however, these occurred at temperatures much higher than the melt temperatures in the present experiments.

Hosler and Westwater measured the minimum film boiling temperature of Freon-11 to be 111 °C,[75] so it is conceivable that even with a melt temperature of ≈110 °C, film boiling will occur at least momentarily on the melt as it first contacts Freon-11 liquid. Once established, the film boiling of Freon-11 on molten Wood's metal (a bismuth, lead, tin and cadmium eutectic having a composition almost identical to Lipowitz's metal) has been observed to be extremely stable.[76]

4.3 Apparatus

The major components of the experiment apparatus (shown in Figure XXX) are the melt furnace, the interaction vessel (in which jet breakup occurs), and the vapor expansion volume. See the apparatus flow diagram (Figure XXX). The jet diameter and velocity were controlled via interchangeable nozzles, and pressurization of the melt furnace, respectively, while both were affected by the fall distance between the nozzle and the Freon-11 liquid surface.

Three different melt furnaces have been used. All are basically spool pieces wrapped with heating elements. Furnace #1 has an inside diameter of 5 cm, with a melt capacity of about 2 kg. Furnace #2 has an I.D. of 58 mm, with a melt capacity of about 12 kg. Furnace #3 is described by Marciniak; it has upper and lower sections of different diameter (178 mm and 51 mm, respectively).

Melt flow is initiated by cutting a diaphragm at the base of the furnace. The diaphragm cutter is a hollow stainless steel cylinder with a sharpened edge, which cuts a circular flap in the diaphragm and pushes it out of the flow path. Melt flows through the center of the cutter. Immediately below the diaphragm was a short interchangeable nozzle. The diaphragm cutter is connected to a pneumatic piston, which is driven by an 80 psi argon reservoir via a normally closed solenoid valve.

The interaction vessel is a rectangular aluminum channel frame, fitted front and back with transparent acrylic panels. It can withstand a pressurization of about 10 psi. The frame interior height is 137.5 cm. Its width is 51.8 cm, which is intended to be

sufficiently greater than the mixture diameter that the hydrostatic pressure gradient in the Freon-11 pool is maintained during the interaction. The front to back width is only 10 cm (on the order of the expected vapor chimney diameter), so that the X-ray beam passing front to back through the vessel ideally suffers little attenuation by liquid Freon-11.

The apparatus was fitted with several type K thermocouples with Omega electronic cold junctions. Three pressure transducers (Omega model PX102, strain gage type, 0-25 psia) were also fitted; in the interaction vessel gas space, expansion volume, and melt furnace gas space. Each gage was wired into a Wheatstone Bridge. An exitation voltage of 5 VDC was applied across two corners of the bridge, producing a signal voltage proportional to the pressure across the other corners of 0-100 mV. The bridge and electronic cold junction signal voltages were recorded by a CRT Oscillograph (Honeywell Visicorder model 1858).

Each experiment was photographed by two RedLake HYCAM 16 mm cameras, operated at 500 frames/second. One camera viewed the entire interaction vessel; the other viewed the jet in free fall above the Freon-11 surface. Kodak 7250 tungsten balanced color reversal film was used in all cameras (HYCAMs and X-ray cine).

A standard video camera and VCR were also used to provide immediately available photographs of the experiment.

Two X-ray systems were used. High resolution still images were made by exposing a single 8 x 10 inch sheet of Kodak Ortho H or T-Mat H X-ray film to a 100 kV X-ray pulse (≈2000 amp., 40 ns) from a Hewlett Packard Flash X-Ray System, Model 43731A. The film was placed in a Kodak X-Omatic cassette with Lanex Fast Screens, positioned against the back acrylic panel of the interaction vessel. A stationary X-ray grid was placed in front of the film cassette to prevent fogging of the image by scattered X-rays. The X-ray tube was positioned about 32 inches in front of the grid. This system required only a small X-ray tubehead to be placed near the interaction vessel; it could therefore be used concurrently with the HYCAMs.

X-ray motion pictures were obtained using a Hewlett Packard model 760/273 high speed X-ray cine system. The system provides 10 Joule, 50 ns pulses at 350 KV and 250 Hz, synchronized with a motion picture camera. The X-ray beam is received by an image intensifier (Varian VXI-145), which displays the image on a one inch diameter green phosphorous screen. The screen image is photographed at 250 frames per second by a Photosonics model 1P 16mm motion picture camera. The X-ray tube was placed about 56 inches away from the image intensifier; with the installed collimator, this provides an X-ray beam approximately nine inches in diameter at the intensifier. The tube is mounted in a large X-ray generator cabinet, which blocked the line of sight from the HYCAMs. A

stationary X-ray grid was also used with the cine system.

4.4 Experimental Procedure

The interaction vessel was filled and drained by gravity flow; the Freon-11 supply barrels being raised and lowered as necessary. The barrels and the interaction vessel were pressurized to about 5 psig with argon during filling and draining operations, to prevent boiling of the Freon-11.

The apparatus was either isolated or vented to a fume hood (either directly or bubbled through a small container of chilled Freon-11). When isolated, a pressure equalization line connected the apparatus interior with the furnace gas space above the melt.

The melt furnace was either vented to the apparatus interior or pressurized with argon (usually a 5 psig regulated supply). After the furnace had drained, the argon flowed into and pressurized the apparatus interior (when isolated) or displaced the Freon-11 vapor (when vented to the fume hood). In some experiments, the furnace pressurization was increased to about 10 psi, with the argon supply isolated prior to the test to avoid overpressurization of the apparatus after completion of the melt injection.

The experiments were conducted from the room adjacent to that in which the apparatus was located, as a safety precaution against both inadvertent X-ray exposure and possible injury in the event of a vapor explosion.

The HYCAMs and Viscorder were started manually. Melt injection was initiated by manually energizing a timer. The timer immediately closed the 110 VAC circuit to the solenoid operated isolation valve on the 80 psig argon supply to the diaphragm cutter piston actuator. The Flash X-ray pulse was initiated when the timer (after the preset time had elapsed) closed the 50 VDC Flash X-ray trigger circuit. An LED driver was actuated when the timer was first energized, and when the Flash X-ray was triggered. This powered the synchronization mark LED in one of the HYCAMs.

The X-ray cine system operation was initiated manually.

Figure XXX is the instrumentation and control schematic for the apparatus when this X-ray system was used. The instrumentation and control schematic for the apparatus when the X-ray cine system was operated is shown in Figure XXX.

The interlock system was a safety precaution (only) to prevent accidental exposure to X-rays. The limit switch on valve MV-1 was another safety precaution; the solenoid valve that initiated melt injection (by supplying 80 psig argon to the diaphragm cutter piston actuator) could only be energized if MV-1 was open, i.e., if the interaction vessel

was vented to the expansion volume, to prevent accidental overpressurization of the apparatus.

Appendix XXX shows a typical procedure checklist.

4.5 Test Matrix

The first two experiments were scoping tests to check experiment procedures.

Experiments 3-8 did not utilize X-radiography. A wide range of jet diameters was used to check the agreement between measured breakup lengths and the Saito et. al. correlation.

Experiments 9-11 were scoping tests using the Flash X-ray system, to evaluate its efficacy.

In experiments 12 and 13, the HYCAM view of the jet leading edge was obscured by the shadow of the X-ray film cassette (the interaction vessel was backlit), so that breakup lengths could not be determined.

In experiments 14-26, the jet diameter and entry velocity were varied to obtain more data for breakup length correlation. In addition, in experiments 16-21, the jet diameters and velocities were similar, but the X-ray film cassette position was varied to obtain images from all sections (upper, middle, lower) of the vapor chimneys produced by comparable jets.

In experiment 27, in an attempt to obtain video images of the interior of the vapor chimney, a 90° field of view boroscope was placed with the lens (looking downward) about one inch from the centerline of the jet.

Experiments 28-31 were conducted to provide breakup length data for much smaller diameter jets, where, unlike the experiments with larger jets, Rayleigh breakup could be expected to play a much more important rôle in jet breakup, in order to determine if their breakup lengths showed the same trends as the larger jets.. Since the diameters of the vapor chimneys produced by these jets were small compared to the 10 cm front-to-back width of the interaction vessel, attenuation of the X-ray beam by liquid Freon-11 precluded X-radiography.

Experiments 32-34 used the X-ray cine system (only) to view the *dynamics* of the penetration and fragmentation processes.

The experiment parameters and objectives are tabulated below (Table XXX). X-ray depth is the depth of the beam centerline below the pretest Freon-11 liquid surface level.

Test #	Furnace #	Melt Mass (g)	D_{nozzle} (mm)	Freon Depth (cm)	X-ray Depth (cm)	Objectives
1	1	≈ 500	19	32	na	Scoping
2	1	1176.2	12.7	64	na	Scoping
3	2	4818	12.7	91.5	na	Breakup Length (B.L.)
4	2	6665	25.4	109.5	na	Breakup Length
5	2	6772.3	19	110	na	Breakup Length
6	2	6906.8	6.4	114	na	Breakup Length
7	2	6970.6	12.7	113	na	Breakup Length
8	2	5246.5	6.4	107.5	na	Breakup Length
9	2	7169.5	19	108	28.5	Flash X-ray Scoping
10	2	7073.4	6.4	107.3	27.8	Flash X-ray Scoping
11	2	6847.1	19.0	109	58.5	Flash X-ray Scoping
12	2	7090.5	19.0	111.5	32	Flash X-ray
13	2	7027.1	19.0	111.5	32	Flash X-ray
14	2	7228.8	19.0	111.5	32	B.L. and Flash X-ray
15	2	7538.7	19.0	110.5	63.5	B.L. and Flash X-ray
16	2	7006.2	12.7	103.5	24	B.L. and Flash X-ray
17	2	7057.3	12.7	107	60	B.L. and Flash X-ray
18	2	6766.5	12.7	107.5	28	B.L. and Flash X-ray
19	2	7008.7	12.7	107	27.5	B.L. and Flash X-ray
20	2	6885.3	12.7	99	11	B.L. and Flash X-ray
21	2	6917.4	12.7	110.5	22.5	B.L. and Flash X-ray
22	2	5983.2	6.4	105.5	na	B.L. and Flash X-ray

23	2	6801.3	6.4	103.5	15.5	B.L. and Flash X-ray
24	3	12955.9	25.4	100	20.5	B.L. and Flash X-ray
25	3	16067.9	6.4	105.8	26.3	B.L. and Flash X-ray
26	3	na	25.4	110	30.5	B.L. and Flash X-ray
27	3	12493.9	12.7	103.5	na	B.L., Boroscope Video, and Flash X-ray
28	3	9722.2	3.2	105	na	Breakup Length
29	3	9901.8	3.2	91.5	na	Breakup Length
30	3	na	3.2	93	na	Breakup Length
31	3	9121	3.2	98.5	na	Breakup Length
32	3	≈15500	12.7	93.5	14	X-ray Cine
33	3	≈15500	12.7	88.5	39	X-ray Cine
34	3	≈15500	3.2	84.5	35	X-ray Cine

5.0 EXPERIMENT RESULTS

5.1 Introduction-

Thirty-three experiments were conducted by the present author using single jets. Breakup lengths were determined for 22 of these. Flash X-ray stills were obtained in 14 experiments; X-ray cine film in three. The experiments were designated MFSBS- for *Molten Fuel Stream Breakup Simulation*. Experiments with three collinear (i.e., side-by-side) jets at various spacings were later conducted by Marciniak using the MFSBS apparatus; these which yielded 16 breakup length estimates and 12 flash X-ray stills.

5.2 Motion Pictures

5.2.1 General Observations

Above the Freon-11 liquid surface, the motion pictures show that the jet develops small amplitude varicose deformations due to capillarity (Figure XXX shows an extreme example of this).

Below the surface, the vapor chimney obscures the jet. Large liquid waves protruding into the vapor chimney are often visible. These are pushed upward by the vapor flow. Some of the smaller melt drops are entrained in these waves, and fall down along the walls of the vessel after reaching the surface. However, most of the jet debris fall near the jet axis.

Figures XXX through XXX are sequences of four stills from the HYCAM film. For each experiment (in which the HYCAM film quality was adequate for reproduction), the jet is shown as it first entered the Freon-11 liquid, when it had penetrated roughly half the way to the breakup length, near the time that it reached the breakup length, and at a (usually much later) time.

5.2.2 Breakup Length

5.2.2.1 Definition

In the idealized conceptual picture of jet breakup discusses in section XXX, the depth of complete jet fragmentation is just the length of the contiguous jet core. Ideally, then, the steady state jet breakup length could be defined as the average of many observed

core lengths over a sufficiently long time.

Saito et. al. averaged the length of the vapor chimney over a relatively long (~3 seconds) time to obtain a steady state *penetration length*. This is essentially the steady state jet breakup length *if* the vapor chimney length corresponds roughly to the length of the jet core. In these experiments, $\varepsilon \sim 1$; the jet debris were swept upward out of the coolant pool by the vapor flow and/or buoyancy, so the lower edge of the vapor chimney was clearly delineated.

In the present experiments, where $\varepsilon \gg 1$, the jet debris continue to fall beyond the end of the contiguous jet and/or vapor chimney. When the field of falling debris is dense, it is difficult to determine by inspection the depth at which there is clearly no longer a jet core.

Spencer et. al. overcame this difficulty by noting that, the debris field extending beyond the jet core falls at a terminal velocity much lower than the penetration rate of the coherent jet. They then assumed that the jet asymptotically approaches its steady state breakup length during its initial penetration of the coolant. With this assumption, the jet breakup length may be determined by measuring the rate at which the jet initially penetrates the coolant pool; the breakup length being defined as the depth at which the jet leading edge penetration rate has fallen to the terminal velocity of the debris. The criterion for determining jet breakup length used for this analysis is based on that idea.

Here, the variation of jet leading edge depth with time was obtained by manual measurement from the high speed motion picture film. These data were then manipulated using the *TechPlot* technical plotting and data processing software.[77] Leading edge penetration rate values were obtained by numerical differentiation, using a natural spline interpolation with two nodes. The curve fitted to the calculated penetration rates was obtained from a Savitzky-Golay smoothing routine with left and right window sizes less than 1/6th of the total number of data points. Figures XXX through XXX show the jet leading edge depth and penetration rate curves. Both the calculated penetration rate values and the smoothed curves are shown.

Jet breakup length is defined here as the depth at which the leading edge penetration rate has fallen to the highest possible value for debris falling at their terminal velocities. Jet breakup is assumed to be complete at or before the time that the leading edge penetration rate falls to the highest possible terminal velocity of a hydrodynamically stable debris fragment. To obtain an upper bound for this velocity, the drop is assumed to be a solid sphere (the drag coefficient, c_d, is lower for a solid sphere than for other solid objects or deforming drops). Interactions between nearby drops are neglected, since these reduce the terminal velocity.[78] For simplicity, the effects of boiling

(e.g., the presence of a vapor film at the drop surface) are neglected also.

At the terminal velocity, the body and drag forces acting on the drop are balanced. The terminal velocity of a spherical debris fragment is:

$$V_d = \sqrt{\frac{4gd}{3c_d}\left(\frac{\rho_i}{\rho_c} - 1\right)}$$

with the drag coefficient taken to be ≈ 0.45. (a reasonable value for a solid drop in Newton's regime, i.e., where drop Reynolds numbers are between 10^3 and $2x10^5$).

In order to use this relation, an appropriate debris fragment diameter must be selected. Here, the diameter of the largest molten metal drop that is stable in free-fall through the liquid coolant is used. The equivalent diameter of the largest stable drops may be estimated as:[79]

$$d_e \approx 4\sqrt{\frac{\sigma}{g(\rho_j - \rho_c)}}$$

These relations yield $d_e \approx 9.2$ mm, for which the maximum debris free fall velocity is $V_d \approx 1.2$ m/s. Therefore, *the jet breakup length is here taken as the depth at which the leading edge penetration rate has fallen to 1.2 m/s*, with certain exceptions. Note that 9.2mm is considerably larger than the initial jet diameter in several experiments. It would be expected that the largest debris fragments produced in those experiments would be no larger than about twice the jet diameter (i.e., as is produced by Rayleigh breakup of a low viscosity jet). Therefore, this definition may somewhat underestimate the breakup lengths of the smallest diameter jets.

This criterion was not useful for some experiments. In experiments 20, 21, 24 and 25, the jet leading edge penetration velocity did not fall to the value given by equation 3. In experiment 24, the base of the center section of the debris bed was flat (i.e., conformed to the vessel base), and a large mass of debris was melded together. Apparently the molten jet impinged on the vessel base. The jet breakup length is therefore indeterminate, although it obviously must be greater than the ≈1 m depth of the Freon-11 pool. For the other experiments, where no impingement was indicated by the debris characteristics, the breakup length has somewhat arbitrarily been taken to be 1 cm less than the pool depth.

Finally, in experiment 31 the HYCAMs did not operate. Breakup length was estimated from inspection of the videotape.

5.2.2.2 Breakup Length Data

The initial jet velocities and diameters (at the Freon-11 surface) for these

experiments, along with the measured breakup lengths, are given in Table XXX. The jet velocity given is that at the initial jet-liquid contact. This was calculated from the average jet leading edge velocity in the gas space, as measured from the motion pictures, assuming gravitational acceleration. The motion of the diaphragm cutter normally propelled some melt drops ahead of the main body of the jet; these were ignored. The leading edge of the melt stream was in all but one experiment only slightly larger than the diameter of the stream behind it, indicating that the leading edge and stream velocities were essentially the same. In MFSBS-26, however, the diaphram was not cut completely. In this experiment, the partially cut diaphragm acted as a throttle, reducing the jet leading edge velocity. It also introduced substantial swirling at the jet leading edge (although the column visible in the gas space just behind the leading appeared undisturbed).

However, when small diameter nozzles (3.0 or 6.4 mm) were used, the melt propelled by the diaphragm cutter could not easily be distinguished in the HYCAM film from the main body of the jet, resulting in measured jet velocities greater than was consistent with the initial furnace head. In such cases the latter was used to calculate the jet velocity; nozzle losses were neglected.

The entry diameter is of course always somewhat smaller than the nozzle diameter, because of the stretching due to acceleration during the fall through the gas space. The jet diameter given is that at the liquid surface, *calculated* from the steady state continuity relation $VD^2 = \text{constant}$. Breakup length was measured from the initial Freon-11 level, neglecting the level rise in the liquid pool after initial contact, which was usually several centimeters.

Test #	Melt Mass (grams)	D_{nozzle} (mm)	V(0) (m/s)	$V(t_L)$ (calculated) (m/s)	D(0) (calculated) (mm)	$D(t_L)$ (calculated) (mm)
1	≈500	19	na	na	na	na
2	1176.2	12.7	na	na	na	na
3	4818	12.7	4.4	4.4	6.6	5.6
4	6665	25.4	na	na	na	na
5	6772.3	19	3.9	3.9	12.0	11.9
6	6906.8	6.4	3.8	3.8	4.2	4.1
7	6970.6	12.7	5.0	5.0	11.0	10.7
8	5246.5	6.4	5.8	5.8	5.7	5.7
9	7169.5	19	na	na	na	na
10	7073.4	6.4	na	na	na	na
11	6847.1	19.0	na	na	na	na
12	7090.5	19.0	na	na	na	na
13	7027.1	19.0	na	na	na	na
14	7228.8	19.0	3.6	3.6	10.0	8.0
15	7538.7	19.0	4.3	4.2	14.0	14.0
16	7006.2	12.7	5.2	5.2	11.0	10.6
17	7057.3	12.7	5.2	5.2	11.0	10.7
18	6766.5	12.7	4.0	4.0	11.0	8.1
19	7008.7	12.7	4.9	4.9	10.0	10.0
20	6885.3	12.7	5.2	5.2	10.0	10.0
21	6917.4	12.7	4.5	4.5	10.0	9.9
22	5983.2	6.4	5.3	5.3	6.0	5.4
23	6801.3	6.4	5.4	5.4	5.9	5.4
24	12955.9	25.4	3.1	3.1	21.0	21.0
25	16067.9	6.4	5.2	5.2	6.2	6.2
26	na	25.4	2.2	2.0	20.0	18.1
27	12493.9	12.7	5.1	5.1	12.0	12.0
28	9722.2	3.2	4.2	4.2	3.0	3.0
29	9901.8	3.2	4.7	4.7	3.0	2.9
30	na	3.2	6.0	6.0	3.0	3.0
31	9121	3.2	5.6	5.6	3.0	3.0
32	≈15500	12.7	na	na	≈12	na
33	≈15500	12.7	na	na	≈12	na
34	≈15500	3.2	na	na	≈3	na

The jet entry velocity is not constant over the entire flow, of course, because the melt depth in the furnace decreases as it drains. The melt furnace-interaction vessel pressure differential does not decrease significantly over the time Δt during which the jet leading edge penetrates to the breakup length (see Figures XXX through XXX), so the

velocity of the melt exiting the nozzle at the base of the melt furnace can easily be estimated from the Bernoulli equation:

$$V_n(t) = \sqrt{\frac{2(\rho_j g h(t) + \Delta P)}{\rho_j(1+K)}}$$

with ΔP taken as constant.

The height of the melt pool in the furnace is:

$$h(t) = h_0 - \left[\frac{\alpha D_n}{D_f}\right]^2 \int_0^t V_n(\tau)d\tau$$

Differentiating this relation shows that:

$$\frac{V_n(t)}{V_n(0)} = 1 - \left[\frac{\alpha D_n}{D_f}\right]^2 \frac{gt}{(1+K)V_n(0)}$$

The jet fluid undergoes gravitational acceleration as it falls from the nozzle to the liquid free surface, so the entry and nozzle velocities are related by:

$$V(t+\varepsilon(t)) = \sqrt{V_n(t)^2 + 2Lg}$$

The entry diameter can be calculated from the continuity relation:

$$\int_0^t V_n(\tau)\alpha D_n^2 d\tau = \int_{\varepsilon(0)}^{t+\varepsilon(t)} V(\tau)D^2 d\tau$$

where ε is the nozzle to liquid free surface fall time for a cross-sectional element of the jet column. Differentiating yields:

$$V_n(t)aD_n^2(t) = \left[1 + \frac{de}{dt}\right] V(t+e(t))D^2(t+e(t))$$

Noting that:

$$\varepsilon = \frac{V(t+\varepsilon(t)) - V_n(t)}{g}$$

and differentiating shows that:

$$\frac{d\varepsilon}{dt} = \frac{1}{g}\left[\frac{2V_n(t)}{\sqrt{V_n(t)^2 + 2Lg}} - \frac{dV_n(t)}{dt}\right]$$

Assuming that $\frac{dV_n(t)}{dt}$ is negligible, the entry diameter is given by:

$$D(t+\varepsilon(t)) = \alpha D_n(t)\left[1 + \frac{2Lg}{V_n(t)^2}\right]^{\frac{1}{4}}$$

However, the jet velocity and diameter at the liquid free surface at the time the jet leading edge reaches the breakup length can be conservatively (i.e., under-) estimated by assuming that the furnace head loss is equal to the furnace melt height reduction caused by a volumetric flow rate of $\frac{\pi}{4}V(0)D^2(0)$ over the time between initial contact and penetration

to the breakup length, Δt. That is:

$$V(t_L) \approx \sqrt{V^2 - 2g\left[\frac{D(0)}{D_f}\right]^2 \Delta t}$$

The corresponding diameter can be estimated from the continuity relation:

$$D(t_L) \approx D_n\left[1 - \frac{2gl}{V^2(t_L)}\right]^{\frac{1}{4}}$$

Jet velocities and diameters estimated for $t = t_L$ are also listed in Table XXX. In every experiment, the variations in jet velocity and diameter over the time Δt is negligible, considering the uncertainties involved in breakup length determination.

The breakup length data are tabulated below (Table XXX). The reference event which was chosen as $t = 0$ is listed for each test. In early experiments, t_0 was taken as the time that the melt first entered the Freon-11 liquid (determined from HYCAM film with an accuracy of ± 2 ms). In later experiments, t_0 corresponds to the timing mark made on the HYCAM film at the time the diaphragm cutter piston actuator solenoid valve was energized.

Test #	V_{entry} (m/s)	D_{entry} (calc'd) (mm)	L (cm)	Method	t_0 ref'nce	t_{entry} (ms)	$t_{breakup}$ (ms)
1	na	na	na	na	na	0	na
2	4.8	6.4	≈53	visual (vis) from film (mp)	entry	0	≈496
3	4.4	6.6	59	penetrat'n curve (pc)	entry	0	215
4	na	na	na	na	entry	0	na
5	3.9	12.0	84	pc	entry	0	315
6	3.8	4.2	61	pc	entry	0	335
7	5.0	11.0	78	pc	entry	0	375
8	5.8	5.7	70	pc	entry	0	445
9-13	na	na	na	na	na	na	na
14	3.6	10.0	83	pc	solenoid	538	875
15	4.3	14.0	87	pc	solenoid	468	915
16	5.2	11.0	91	pc	solenoid	420	765
17	5.2	11.0	78	pc	solenoid	416	720
18	4.0	11.0	98	pc	solenoid	406	850
19	4.9	10.0	74	pc	solenoid	406	630
20	5.2	10.0	99	vis (mp)	solenoid	458	870
21	4.5	10.0	104	vis (mp)	solenoid	816	1190
22	5.3 (est.)	6.0	78	pc	solenoid	368	760
23	5.4 (est.)	5.9	81	pc	solenoid	386	790
24	3.1	21.0	>100	na	solenoid	462	na
25	5.2	6.2	106	vis (mp)	solenoid	368	855
26	2.2	20.0	67	pc	solenoid	442	760
27	5.1	12.0	82	pc	solenoid	416	700
28	4.2	3.0	38	pc	solenoid	400	495
29	4.7 (est.)	3.0	31	pc	solenoid	410	495
30	6.0 (est.)	3.0	47	vis (video)	na	0	na
31	5.6 (est.)	3.0	36	pc	solenoid	302	420
32	na	≈12	na	na	na	na	na
33	na	≈12	na	na	na	na	na
34	na	≈3	na	na	na	na	na

Clearly, the MFSBS breakup length data show the same trends as the Saito et.al.

penetration length data, namely, that the dimensionless breakup (or penetration) length increases with increasing jet velocity and decreases with increasing jet diameter. These trends were also found in the later multiple jet experiments conducted by Marciniak. For the 23 breakup length data points (not including the indeterminate value for MFSBS-24), the best power curve correlation of breakup length with jet entry velocity and diameter is:

$$\frac{L}{D} \sim \frac{V^{0.6}}{D^{0.4}}$$

for which the correlation coefficient is 0.72. These trends are in fair agreement with both the emprical correlation of Saito et. al. and that proposed by Bürger et. al. In Figure XXX, the data are correlated with the penetration length function of Saito et. al., viz $2.1\sqrt{\varepsilon Fr}$; Figure XXX shows the correlation with $7.9(\varepsilon Fr)^{\frac{1}{3}}$ (the constant of proportionality being chosen to provide the best fit of the data). The correlation coefficients are 0.43 and 0.55, respectively; one correlation is not clearly preferable to the other. Although these correlations are only fair, the probabilities that breakup length is independent of $\sqrt{\varepsilon Fr}$ or $(\varepsilon Fr)^{\frac{1}{3}}$ are less than 0.05 and 0.02, respectively, for this set of 23 observations.[80]

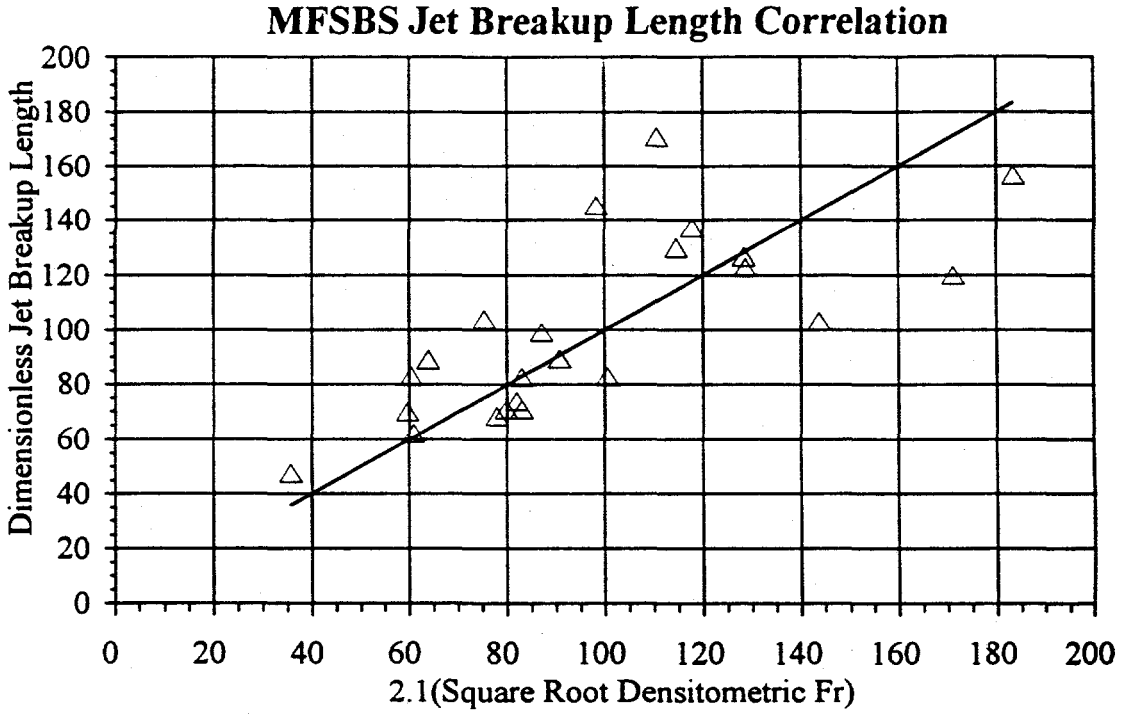
MFSBS Jet Breakup Length Correlation
Dimensionless Jet Breakup Length
200
180
160
140
120
100
80
60
40
20
0
0
20
40
60
80
100
120
140
160
180
200
2.1(Square Root Densitometric Fr)

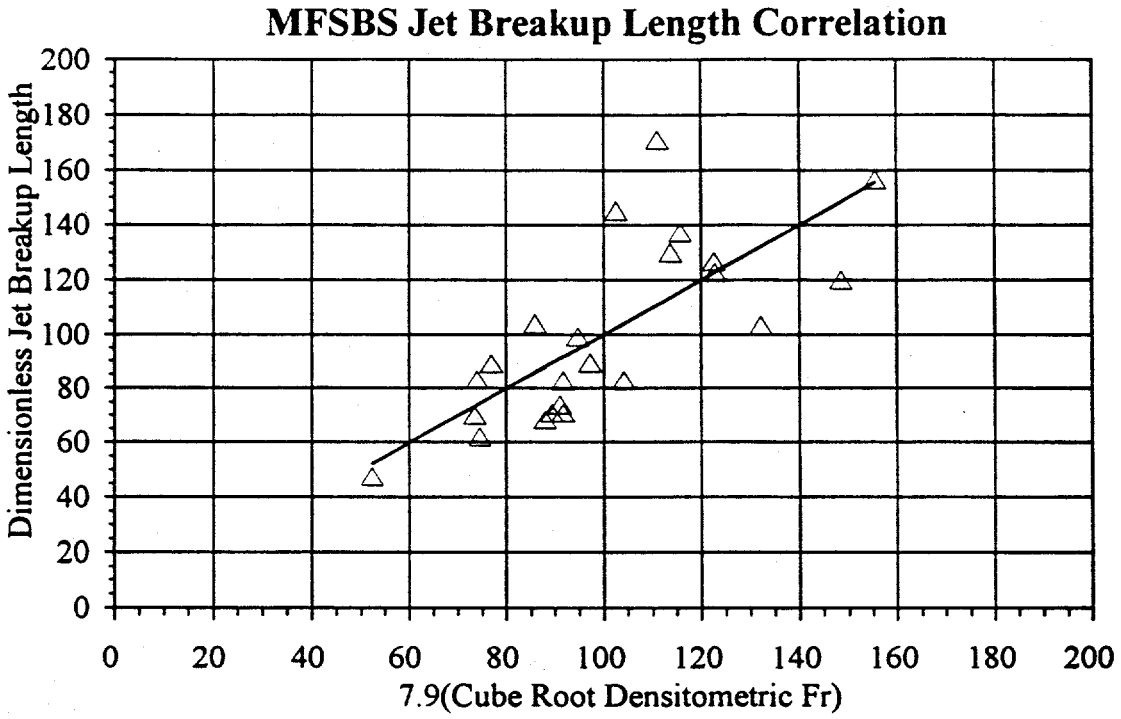

5.2.3 Leading Edge Penetration Rate

The dimensionless penetration velocity, V^+, was estimated from the jet leading edge penetration data (Figures XXX through XXX), a task made more difficult by the fact that the leading edge penetration rate often varies considerably during the penetration to the breakup length. This may be due to segmentation of the jet, which the radiographs (discussed below) show can occur at a depth much less than the breakup length.

However, in all experiments the jet *initially* penetrated the coolant at a fairly constant rate. Below, the elapsed times (beginning with the initial jet-coolant contact) and corresponding depths over which this occurred are listed in Table XXX (Admittedly, the choice of the elapsed time is somewhat subjective) From these data, the penetration velocities, V_p, were calculated. The velocity in the jet column, V_{avg}, is taken as the average velocity over the elapsed time, assuming gravitational acceleration. The values calculated for V_{avg}, V_p, and V^+ are also listed in Table XXX. The arithmetic mean of the

V^+ values is 0.71; the standard deviation is 0.16. The median value is 0.68.

Exp. No.	V_{entry}	Depth Penetrated	Elapsed Time	V_{avg}	V_p	V^+ (V_p/V_{avg})
3	4.4	0.45	0.150	5.1	3.0	0.59
5	3.9	0.67	0.222	5.0	3.0	0.60
6	3.8	0.21	0.100	4.3	2.1	0.48
7	5.0	0.41	0.120	5.6	3.4	0.62
8	5.8	0.30	0.100	6.3	3.0	0.48
14	3.6	0.60	0.212	4.6	2.8	0.60
15	4.3	0.48	0.156	5.1	3.1	0.61
16	5.2	0.42	0.108	5.7	3.9	0.68
17	5.2	0.40	0.102	5.7	3.9	0.69
18	4.0	0.34	0.096	4.5	3.5	0.79
19	4.9	0.53	0.132	5.5	4.0	0.73
20	5.2	0.44	0.114	5.8	3.8	0.67
21	4.5	0.34	0.114	5.1	3.0	0.58
22	5.3 (est.)	0.17	0.030	5.4	5.5	1.01
23	5.4 (est.)	0.14	0.030	5.5	4.6	0.84
24	3.1	0.52	0.168	3.9	3.1	0.78
25	5.2	0.60	0.162	6.0	3.7	0.61
26	2.2	0.40	0.150	2.9	2.6	0.90
27	5.1	0.33	0.084	5.5	3.9	0.71
28	4.2	0.23	0.048	4.4	4.8	1.09
29	4.7 (est.)	0.19	0.042	4.9	4.6	0.94
31	5.6 (est.)	0.31	0.090	6.0	3.5	0.58

5.3 Radiographic Images

5.31 Introduction

The vapor chimney surrounding the metal jet has a very rough, opaque surface. In order to view the configuration of the fragmenting jet column, X-radiography has been used.

The X-ray beam was placed at one of four heights above the bottom of the interaction vessel. These heights are listed below (Table XXX).

X-ray Beam Location #	X-ray Beam ℄ Height Above Vessel Bottom (cm)
1	88.0
2	79.5
3	50.5
4	47.0

The Flash X-ray pulse time was intended to coincide roughly with the time that the jet reached the breakup length, so that the observed flow would be quasi-steady. Table XXX lists for each experiment the time that the Flash X-ray pulse was fired, along with the times that the jet first entered the liquid, and the time that the jet reached the breakup length. The depth of the X-ray beam below the liquid surface is also listed, along with the total depth of the liquid and the jet breakup length.

Test #	t_{entry} (ms)	$t_{breakup}$ (ms)	$t_{X\text{-}ray}$ (ms)	L (cm)	Freon Depth (cm)	X-ray Location #	X-ray Depth (cm)
1	0	na	na	na	32	na	na
2	0	na	na	na	64	na	na
3	0	215	na	59	91.5	na	na
4	0	na	na	na	109.5	na	na
5	0	315	na	84	110	na	na
6	0	335	na	61	114	na	na
7	0	375	na	78	113	na	na
8	0	445	na	70	107.5	na	na
9	na	na	Timer set for 900	na	108	2	28.5
10	na	na	Timer set for 1500	na	107.3	2	27.8
11	na	na	Timer set for 1200	na	109	3	58.5
12	na	na	Timer set for 1200	na	111.5	2	32
13	na	na	Timer set for 1200	na	111.5	2	32
14	538	875	2102	83	111.5	2	32
15	468	915	1044	87	110.5	4	63.5
16	420	765	1052	91	103.5	2	24
17	416	720	1048	78	107	4	60
18	406	850	1564	98	107.5	2	28
19	406	630	1346	74	107	2	27.5
20	458	870	1260	99	99	1	11
21	816	1190	1248	104	110.5	1	22.5
22	368	760	na	78	105.5	failed	na
23	386	790	954	81	103.5	1	15.5
24	462	na	na	>100	100	failed	20.5
25	368	855	1082	106	105.8	2	26.3
26	442	760	866	67	110	2	30.5
27	416	700	na	82	103.5	failed	na
28	400	495	na	38	105	na	na
29	410	495	na	31	91.5	na	na
30	0	na	na	47	93	na	na

31	302	420	na	36	98.5	na	na
32	na	na	Cine	na	93.5	2	14
33	na	na	Cine	na	88.5	3	39
34	na	na	Cine	na	84.5	3	35

Brief descriptions of the radiographs (still and cine) are given in Table XXX.

Test #	Image Description
1-8	X-ray not used
9	Contiguous Jet Column (partial image, perhaps due to damage in development)
10	Excessive Attenuation by Freon Liquid
11	Unusable (ruined in development)
12	Segmented Jet Column
13	Segmented Jet Column
14	Segmented Jet Column
15	Radially Dispersed Melt Fragments
16	Segmented Jet Column
17	Radially Dispersed Melt Fragments
18	Contiguous Jet Column
19	Segmented Jet Column
20	Contiguous Jet Column
21	Contiguous Jet Column
22	X-ray did not trigger; no image
23	Contiguous Jet Column
24	X-ray did not trigger; no image
25	Jet Column Obscured by Entrained Melt Fragments
26	Contiguous Jet Column
27	X-ray did not trigger; no image
28-31	X-ray not used
32	X-ray cine, Contiguous Jet Column
33	X-ray cine, Segmented Jet Column
34	X-ray cine, Deceleration of Large Segments

5.3.2 Radiograph Stills

The X-ray stills are shown in figures XXX through XXX. Nearly contiguous jet columns appear in several of the radiographs of the upper portions of the vapor chimney (MFSBS-20, 21, and 23). In the central section of the vapor chimney, the jet column was always broken into segments (MFSBS-12, 13, 14, 16, 18, and 19).

The upper sections of the jets often show varicose deformations, which were

probably already present when the jet entered the pool. However, in the MFSBS-20 and 23 radiographs, there also appear to be large sinuous or helical deformations (called roll waves by De Jarlais et. al.). There appears to be some entrainment of melt at the crests of the large waves, and the filaments connecting the large waves also occasionally appear to be shattering. The large jet segments observed in the central section of the vapor chimney appear to have a greater number of protruding filaments than the waves on the contiguous jet column just below the liquid surface. The radiograph from MFSBS-17 appears to show the lower end of the vapor chimney, where there are only smaller melt masses visible. These have spread radially several jet diameters from the jet axis.

In general, the radiographs show the vapor chimney to have a width an order of magnitude larger than that of the jet. However, liquid waves occasionally protrude into the chimney almost to the jet surface.

In all of the radiographs, a field of small fragments appears to surround the jet column/segments. Since the X-radiograph is a two-dimensional projection of a three-dimensional distribution of melt, coolant, and vapor, fragments that appear to be adjacent to the jet inside the vapor chimney may in fact be entrained in liquid in front of or behind it. However, in the radiograph cine film, the debris entrained in the coolant liquid can be distinguished from the jet column by their much lower velocities.

5.3.3 Radiographic Motion Pictures

The X-ray cine system was used in three experiments. In experiment 32, the cine film shows the upper part of a ≈12mm jet column; in experiment 33 it shows the central region of a ≈12mm jet column. In experiment 34, the cine film shows roughly the lower half of a ≈3mm jet.

Below, a brief description of the events recorded is given for each film.

5.3.3.1 MFSBS-32

The cine film begins before the appearance of the jet leading edge. The leading edge of the jet column is slightly blunted (Figure XXX). It leaves a trail of small drops and filaments in its wake. Only a few diameters behind the leading edge, the vapor chimney width is several jet diameters. At 100 ms after the appearance of the jet, its column has become thinner. At 150 ms, the melt drops entrained in the liquid around the vapor chimney are moving upward, as are liquid/vapor interfacial waves. A large roll wave or sheet protruding from the jet column also appears at this time; its outer edges

appear to extend and eject drops and filaments into the liquid. After the roll wave passes out of view (224 ms), the jet column behind it is shattered into small segments (from about one to a few diameters long). A nearly contiguous jet column again comes into view at 368 ms. From this time until the end of the film at 568 ms, entrained melt drops in the liquid increasingly obscure the view. Many of these drops are moving upward with the liquid.

5.3.3.2 MFSBS-33

The cine film begins before the appearance of the jet leading edge. Initially, the jet column and leading edge have a much smaller diameter than seen in experiment 32; the jet leading edge is trailed by a contiguous column a few diameters long (Figure XXX). This is followed by a series of irregular shaped roll waves connected at most by thin ligaments. At 100 ms, a liquid bridge across the vapor chimney appears at the lower edge of the cine view. As it moves upward, the jet appears to develop a leading edge stagnation flow about three to four jet diameters wide that breaks through the liquid bridge. After the roll wave passes out of view, the jet column immediately behind it is completely shattered. A nearly contiguous and full diameter jet column enters the view at 288 ms. This flow continues, with the column frequently broken into segments a few diameters long, until the end of the film at 844 ms. By that time, entrained melt drops have obscured much of the view.

5.3.3.3 MFSBS-34

The cine film begins before the appearance of the jet leading edge. The 3 mm diameter jet column is too small to be distinguished; only the intermittent flow of larger (up to about 6 mm) width segments can be seen. Excessive attenuation of the X-ray beam by liquid Freon-11 makes identification of the vapor chimney boundaries difficult.

The visible large segments appear to be decelerated without significant fragmentation. Below the end of the vapor chimney they are clearly falling at roughly their terminal velocity. The film records 764 ms of the jet flow.

5.34 Interpretation of Radiograph Results

The jet is typically surrounded by a very large diameter vapor chimney, although a liquid bridge across the vapor chimney may occasionally be formed and move upwards

along the jet column, creating a leading edge type stagnation flow that ejects melt into the liquid. The jet is also clearly deformed by Kelvin-Helmholtz instability in the vapor flow, developing sinuous or "roll" waves. Sinuous or helical deformation of the jets is consistent with observations from previous experiments, and is predicted by the linear analysis of Kelvin-Helmholtz instability.

The jet is often broken into segments just below the liquid surface, and is always segmented in the lower part of the vapor chimney. There is significant entrainment of melt filaments from the jet column/segments, particularly from the crests of large waves. Segments also occasionally appear to be rapidly shattered by the vapor flow. However, many or perhaps most of the small melt fragments entrained in the coolant liquid surrounding the vapor chimney appear to originate near its base (i.e., lower end) and move with the liquid as it is pulled upward by the vapor flow.

Finally, it is interesting to note that the relatively large jet segments in the ~3mm diameter jet experiment were not finely fragmented until entering the liquid at the chimney base. Some of the fragments fell, while others were entrained in the upward moving liquid near the vapor chimney.

5.4 Net Vapor Generation

A secondary objective of the present experiments was to collect data on net vapor generation which could be used by code developers for model comparison.

The vapor generated by the melt quench was retained in the apparatus (tests 1-18, 24), vented to a fume hood (tests 19, 32-34), or condensed in a container of chilled Freon-11 (tests 20-23, 25, 31).

For the experiments in which the apparatus was closed, the net vapor generation has been estimated from the pressure rise, using the ideal gas law:

$$\Delta m\ (kg) = \frac{\Delta p\ (kPa)\ Vol.\ (m^3)}{17.91 \left[\frac{(kPa)(m^3)}{(kg)}\right]}$$

The net changes in interaction vessel pressures were read from oscillograph charts, with an accuracy of $\pm$ 0.8 kPa. The volumes of condensed vapor were measured in a graduated cylinder, from which the condensed masses were determined with an accuracy of $\pm$ 0.007 kg.

Pressure data for selected experiments are shown in Figures XXX through XXX. The vapor generation data is summarized in Table XXX.

Test #	Melt Temp. (°C) /Enthalpy (kJ)	Apparatus Δp (kPa) /Calculated Generated Vapor Mass (kg) /Latent Heat (kJ)	Mass (kg) /Latent Heat of Condensed Vapor (kJ)	Percent of Melt Enthalpy Contributed to Net Vapor Generation
1	106/≈24	na	na	na
2	107/55	8.5/0.034/6.2	na	11.3
3	94/224	na	na	na
4	102/313	19.1/0.077/13.8	na	4.4
5	105/319	20.8/0.084/15.1	na	4.7
6	108/326	24.6/0.096/17.3	na	5.3
7	109/329	na	na	na
8	107/247	na	na	na
9	102/337	32.2/0.131/23.6	na	7.0
10	107/333	29.7/0.123/22.1	na	6.6
11	110/323	36.1/0.147/26.5	na	8.2
12	108/334	33.1/0.131/23.6	na	7.1
13	110/331	31.4/0.125/22.4	na	6.8
14	89/337	30.5/0.121/21.8	na	6.5
15	109/355	na	na	na
16	108/330	na	na	na
17	108/3[illegible]3	na	na	na
18	108/319	na	na	na
19	109/330	na	na	na
20	100/323	na	na	na
21	101/324	na	0.059/10.6	3.3
22	109/282	na	na	na
23	109/321	na	0.110/19.8	6.2
24	102/610	na	na	na
25	102/755	na	0.117/21.1	2.8
26	103/na	na	na	na
27	95/586	na	na	na
28	109/458	na	na	na
29	104/466	na	na	na
30	103/na	na	na	na
31	104/429	na	0.205/36.9	8.6
32	103/≈729	na	na	na
33	106/≈731	na	na	na
34	107/≈731	na	na	na

The net vapor generation may include some vapor originating in the jet debris bed on the vessel base, though this contribution is probably small. As the debris collects on the vessel base, it does not appear to generate significant vapor. After a few seconds, extensive boiling is usually visible in the videotapes. However, most of the vapor bubbles appear to be condensed as they rise through the ~1 meter of liquid.

The only obvious trend in the data above is that the percent of melt enthalpy contributed to net vapor generation tended to increase with decreasing breakup length (at least for the six tests having both breakup length and vapor generation data). This is possibly the result of there being less melt-liquid contact when the breakup length is greater.

5.5 Mixing Zone Global Void Fraction

In theory, the *global* void fraction of the melt/vapor/liquid mixing zone can be easily estimated from the motion pictures. In practice, splashing on the coolant surface usually makes it difficult to accurately locate the free surface. However, for MFSBS-8 a global void fraction estimate has been made for t = 492 ms (about the time that the jet leading edge has penetrated to the breakup length).

From the motion pictures, the frontal area of the coolant pool swell is 73.4 cm^2. The width of the vessel is 10.0 cm, giving a displaced coolant volume of 734 cm^3. The projected area of the backlit mixing zone is 571 cm^2; its length is 71.8 cm. Assuming that the horizontal cross-section of the mixing zone is everywhere circular, its average diameter is 7.95 cm, and its volume is 3563 cm^3. The void fraction is the ratio of displaced coolant volume to mixture volume. These data indicate $\alpha \approx 0.21$ over the entire mixture.

The global void fraction for this test may be underestimated, because the projected area of the backlit mixture may be much larger than the vapor chimney. The radiographs typically show melt fragments entrained in the liquid well outside the vapor chimney; the mixture shown by the backlighting may be delineated by the melt drop field, not by the vapor chimney.

An attempt was made in one experiment to photograph the interior of the vapor chimney. In MFSBS-27, a boroscope (with a 90° angle of view), attached to a standard video camera, was inserted ≈2.5 cm from the jet centerline, a few cm below the Freon-11 liquid surface. Before the melt injection, the entire vessel, from its base up to a few cm below the boroscope, was clearly visible. During the melt injection, the boroscope view was completely blurred, the standard video speed of 30 frames per second evidently being

much too low to capture the motions of the two-phase mixture. The jet column, although very near the boroscope, was only partially visible, short sections appearing in only a few video frames.

Unfortunately, the light level in the interaction vessel was too low to allow the boroscope to be used with a HYCAM.

5.6 Jet Debris Characteristics

5.6.1 Debris Bed

Due to the geometry of the interaction vessel, the melt debris beds were two-dimensional. The debris were distributed very roughly normally across the vessel, with the maximum depth near the vessel centerline. This spatial distribution has been observed previously in particle settling experiments.[81]

Typically, little vapor appeared to be generated by the debris bed until some time (on the order of a second) after the end of the melt flow. Then, vapor flowed up through narrow, tortuous channels in the debris bed, being discharged as bubbles at its upper surface. This formation of vapor channels has also been observed previously in particulate bed dryout experiments conducted by Gabor et. al.[82]

Figure XXX is a photograph of a typical debris bed (MFSBS-17) , viewed from the front of the vessel. Figure XXX shows its cross-section at the center of the vessel. Note the large voids.

In the central region of the debris bed, particles of all sizes were present. Near the edges there was typically a higher concentration of small (~1-2 mm) particles. The latter had probably been entrained in liquid which was pulled to the surface by the vapor flow; and, after reaching the surface, had fallen down along the vessel walls (This particle flow path is visible in the motion pictures). Large numbers of fragments were often intertwined.

The spatial variation of debris bed depth for MFSBS-17 is plotted in Figure XXX. From this plot, the overall void fraction is found to be 0.61, much higher than those of packed beds of uniform spheres (0.2595-0.43), sand (0.37-0.50), or granular crushed rock (0.44-0.45).[83] Note that the void fraction may have been affected fluidization of particles by vapor generated within the bed, as has been observed in experiments with debris bed pool boiling.[84] However, in the present experiments, large motions of the debris bed were not visible in the videos.

5.6.2 Debris Particle Characteristics

In general, the smallest ($\lesssim$1mm) fragments were nearly spherical; larger fragments were elongated drops or short filaments. The largest fragments ($\gtrsim$9.5mm) were predominantly re-agglomerations of partially solidified drops and filaments. Photographs of random samples of fragments from MFSBS-16 retained by the different sieve screens are shown in Figures XXX through XXX. In these figures, the fragments are shown resting on ruled graph paper with large and small divisions of 1 cm and 1 mm, respectively.

5.6.2.1 Debris Sifting Data

The solidified jet debris were sifted through screens having mesh spacings of 9.5, 4.75, 2.36, 1.19, 0.85, and 0.59 mm using a Ro-Tap mechanical shaker (W. S. Tyler Co., Cleveland, OH). The raw data have been plotted as the percent of the total debris mass retained by (i.e., larger than) a sieve screen versus the screen size. The mass distribution of particles produced by the fragmentation and quenching of a melt mass in liquid is typically upper limit log normal (ULLN);[85] it was reasonable to expect this distribution in the present experiments. Therefore, upper limit log normal distributions have been fitted to the data. Both the sifting data and the fitted distributions are plotted in Figures XXX through XXX.

In the ULLN distribution, the distribution of the smaller particles is log normal; however, the probability density function is zero for particle sizes above a limit determined by hydrodynamic stability criteria. That is, the ULLN distribution is the normal distribution:

$$P(Z) = \frac{100}{\sqrt{2\pi}} \int_{-\infty}^{Z} e^{\frac{-\zeta^2}{2}} d\zeta$$

with

$$\zeta = \frac{\log\eta - \log\mu}{\log\sigma}$$

where

$$\eta(d, S_m) = \frac{(S_m)(d)}{(S_m - d)}$$

and Sm is the upper limit sieve screen size, i.e., the smallest screen through which all debris will pass.

Note that ζ = Z corresponds to d = S, the sieve screen size that retains the mass

percent P(Z) of the debris. Thus:

$$Z = \frac{\log\eta(S, S_m) - \log\mu}{\log\sigma}$$

which is the equation for a line on a plot of Z versus $\log\eta(S, S_m)$.

The debris sifting data were fitted to equation XXX. To do this, the Z values corresponding to P(S) were obtained from a table of the Normal distribution function, then, the values of the parameters μ, σ, and S_m were determined using a Simplex method nonlinear curve fitting routine in *TechPlot*.

Note that the unit of Z is the normal distribution standard deviation σ; thus, 68% of the debris mass is retained by sieve screen sizes corresponding to Z=-1 through Z=+1, 95% by Z=-2 through Z=+2, etc. The sieve screen size which retains a given percent of the debris mass is shown by rearrangement of equation XXX:

$$S(Z) = \frac{\mu}{\sigma^{-Z} + \left(\frac{\mu}{S_m}\right)}$$

Particularly:

$$S(Z=0) = S_{50\%} = \frac{\mu}{1 + \left(\frac{\mu}{S_m}\right)}$$

$$S(Z=-1) = S_{16\%} = \frac{\mu}{\left(\frac{1}{\sigma}\right) + \left(\frac{\mu}{S_m}\right)}$$

and

$$S(Z=+1) = S_{84\%} = \frac{\mu}{\sigma + \left(\frac{\mu}{S_m}\right)}$$

The surface (also called Sauter) distribution can also be obtained from sifting data. Log normal surface and mass means are related by:[86]

$$\log\mu^* = \log\mu - (1.151)\log^2\sigma$$

Of course, this relation is strictly valid only if the debris particles can be characterized by a single dimension. Then, assuming that Sm is actually the diameter of the largest debris particle, the surface distribution is given by equation XXX, with μ replaced by μ^*, and P(Z) being the percent of the debris surface area retained by the sieve screen size S. Similarly, equations XXX through XXX also apply for the surface distributions, with μ and $S_{XX\%}$ replaced by μ^* and $S^*_{XX\%}$, respectively.

The statistical data are summarized in Table XXX.

Exp. No.	μ (mm)	σ	Sm (mm)	$S_{84\%}$ (mm)	$S_{50\%}$ (mm)	$S_{16\%}$ (mm)	μ* (mm)	$S^*_{84\%}$ (mm)	$S^*_{50\%}$ (mm)	$S^*_{16\%}$ (mm)
3	3.3	0.4	14.9	5.0	2.7	1.3	1.4	2.7	1.3	0.6
4	3.9	0.4	14.7	5.8	3.1	1.4	1.5	2.9	1.3	0.6
5	4.2	0.4	17.6	6.5	3.4	1.6	1.7	3.3	1.5	0.7
6	3.5	0.4	16.0	5.8	2.9	1.3	1.3	2.7	1.2	0.5
7	3.8	0.4	16.9	6.0	3.1	1.4	1.4	2.9	1.3	0.6
8	3.4	0.4	15.3	5.6	2.8	1.2	1.1	2.5	1.1	0.4
9	4.8	0.4	13.8	6.7	3.6	1.6	1.5	3.2	1.4	0.5
10	3.3	0.4	14.9	5.4	2.7	1.2	1.2	2.5	1.1	0.5
11	4.1	0.4	15.3	6.2	3.2	1.4	1.5	3.0	1.3	0.6
12	4.4	0.4	16.9	6.9	3.5	1.5	1.5	3.2	1.4	0.6
13	4.2	0.4	13.4	6.1	3.2	1.4	1.3	2.8	1.2	0.5
14	4.1	0.4	14.6	6.1	3.2	1.4	1.5	3.0	1.3	0.5
15	5.5	0.4	23.1	8.8	4.4	2.0	2.0	4.2	1.8	0.7
16	3.2	0.4	13.8	5.3	2.6	1.1	1.1	2.4	1.0	0.4
17	3.6	0.4	13.0	5.7	2.8	1.2	1.1	2.4	1.0	0.4
18	3.1	0.4	14.8	5.3	2.6	1.1	1.1	2.3	1.0	0.4
19	3.2	0.4	15.8	5.4	2.6	1.1	1.1	2.5	1.1	0.4
20	2.8	0.4	13.8	4.7	2.4	1.0	1.1	2.3	1.0	0.4
21	3.2	0.4	13.9	5.1	2.6	1.1	1.1	2.4	1.1	0.4
22	2.8	0.4	13.8	4.7	2.3	1.0	1.0	2.2	0.9	0.4
23	2.8	0.4	12.7	4.5	2.3	1.0	1.0	2.1	0.9	0.4
25	5.6	0.3	14.1	7.7	4.0	1.6	1.4	3.2	1.2	0.4
27	7.0	0.3	14.9	8.7	4.8	2.0	1.7	3.8	1.5	0.5
28	5.7	0.4	12.6	7.1	3.9	1.7	1.6	3.4	1.4	0.5
29	4.3	0.3	12.8	6.6	3.2	1.2	1.0	2.5	0.9	0.3
31	2.3	0.3	27.3	6.0	2.1	0.7	0.4	1.4	0.4	0.1

5.6.2.2 Conclusions

The debris sizes do not appear to depend strongly upon the initial jet diameter or velocity. The fitted parameter S_m, presumably the best estimate of the largest debris fragment size, is consistently ~1-2 cm. Since these data have been affected to some extent by reagglomeration on the vessel base, the largest debris fragments produced by hydrodynamic fragmentation were presumably somewhat smaller. A maximum fragment of ~1 cm diameter is consistent with breakup in free-fall through liquid Freon-11.

Freezing of the debris apparently did not occur until hydrodynamic fragmentation was well advanced. The debris generally have smooth, rounded surfaces, formed by the action of surface tension; these are very different from the sheet-like fragments

characteristic of rapid surface freezing. However, the elongated shapes of the debris may indicate that the melt became very viscous (i.e., cooled to near the melting point) before the drop had fragmented to a hydrodynamically stable size, since for sufficiently high Ohnesorge number, drops tend to become deformed into cylindrical threads rather than break apart.

It is interesting to note that the mean fragment sizes and shapes in the present experiments are comparable to those from experiments with Wood's metal jets in subcooled water (i.e., where there was little boiling and no net vapor generation) conducted by Spencer et. al.

6.0 ANALYSIS AND INTERPRETATION

6.1 Introduction

Here, a simple explanation is given for the observed jet breakup length correlation. A correlation for estimating the jet leading edge penetration rate is also proposed. These are compared with data from the present experiments and from the literature.

6.2 Jet Leading Edge Penetration Rate Correlation

If the fuel jet breakup length is expected to be much greater than the depth of the coolant pool, ejection of melt from the leading edge of a fuel jet during its initial penetration of the coolant may be the most important mechanism by which molten fuel is 'premixed'.

During the initial penetration, the flow of mass into the jet column at the coolant free surface is balanced by the rate of growth of the column mass (i.e., length) and the rate at which jet fluid is dispersed from the jet leading edge. Assuming constant diameter and velocity along the jet column, continuity requires:

$$\frac{\pi}{4}D^2V_j \approx \frac{\pi}{4}D^2V_p + \frac{\dot{m}_e}{\rho_j}$$

where $\dot{m}_e$ is the rate at which melt mass is ejected from the jet leading edge. Integrating over the time required for the jet to penetrate to the bottom of the coolant pool of depth l gives:

$$m_e \approx \frac{\pi}{4}D^2\rho_j(1 - V^+)l$$

where V^+ is the *dimensionless penetration rate*:

$$V^+ = \frac{V_p}{V_j}$$

Thus, the jet leading edge penetration rate is a measure of the mass of jet fluid dispersed into the coolant during the initial penetration. If the depth of the coolant pool is much less than the jet breakup length, equation XXX could be used as a rough estimate of the mass of fuel that may be pre-mixed for participation in a steam explosion, given a means to predict V^+.

Chu and Corradini modeled this mixing process by modifying the TEXAS code to apply a drop fragmentation model developed by Chu at the jet leading edge. However,

their computational model was not compared with observations of penetrating jets, and it is not clear that jet leading edge vortex flow is equivalent to that of a fragmenting drop.

As a first approximation, the rate at which melt is ejected from the leading edge of a molten fuel jet during its initial penetration of the coolant may be estimated more simply, and perhaps at least as accurately, from a simple force balance.

Consider a frame of reference moving with the leading edge of the penetrating jet directed into a counterflowing continuous phase, with the fluid velocities adjusted so that the jet (Figure XXX).

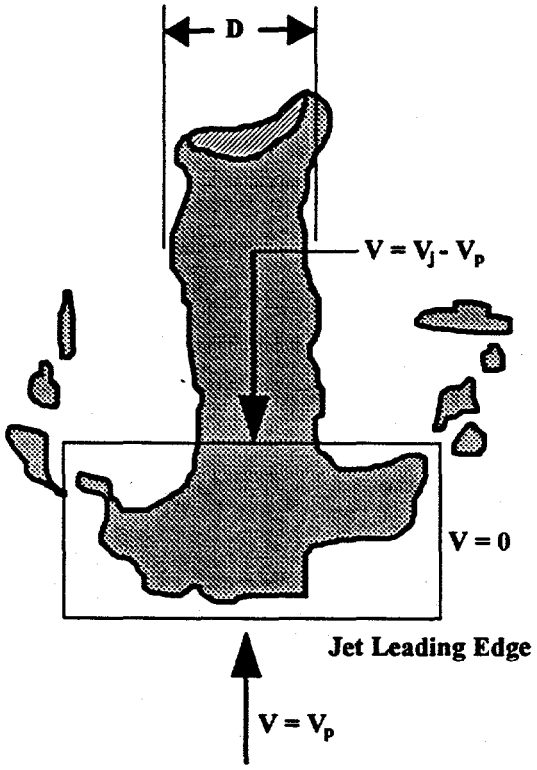

The jet penetration rate will stabilize (i.e., the leading edge position in this reference frame will become fixed) when the drag force on the leading edge is balanced by the momentum flow into the leading edge from the jet column. As a first approximation, the jet leading edge is considered to be analogous to a deforming, fragmenting drop. A fragmenting drop, which initially has a drag coefficient of roughly 0.5, flattens to a diameter about twice its original value; and, when deformed in this way, has a drag coefficient of about 1.5. Assuming that the leading edge diameter fluctuates from 1-2 times its original value as material is torn away, the jet leading edge force balance is:

$$\frac{(c_D \approx 1)}{2} \rho_c V_p^{\,2} \frac{\pi}{4} (\approx 1.5D)^2 = \rho_j (V_j - V_p) \frac{\pi}{4} D^2$$

Rearranging to solve for V^+:

$$V^+ \approx \frac{1}{1 + \frac{1}{\sqrt{\varepsilon}}}$$

where $\varepsilon \equiv \frac{\rho_j}{\rho_c}$.

There are several sets of experiments reported in the literature from which approximate jet leading edge penetration rates may be obtained for comparison with the simple relation above.

Hopkins and Robertson conducted experiments with *plane* water jets penetrating gasoline, castor oil, water, brine, glycerine, and carbon tetrachloride (for which ε varied from 0.626 to 1.42, and V^+ varied from 0.3 to 0.5).[87] Their data were well correlated by:

$$V^+ = \frac{1}{1 + \frac{1.4}{\varepsilon}}$$

Equation XXX gives values of V^+ for these ε of 0.4 to 0.5.

The dependence of V^+ on variables other than the jet-ambient fluid density ratio was not examined. However, they did note that order of magnitude variations of ambient fluid viscosity had no effect.

A few approximate data are also available for cylindrical jets, from the experiments of Saito et. al. (water jets in Freon-11 and liquid nitrogen (boiling)), Marshall et. al. (Freon-TF jets in water (quiescent)), Spencer et. al. (Wood's metal jets in water (quiescent), and the present MFSBS experiments, discussed in section XXX. These penetration rate data are given in Table XXX.

For the Saito et. al. experiments, V^+ has been estimated as the penetration length divided by the penetration time (read from plots of jet leading edge position vs. time) and the initial (i.e., entry) jet velocity. The values given here are from two experiments in which the penetration rate was fairly constant (i.e., where the jet column was probably contiguous). The jet diameter and entry velocity were 5 mm and 9 m/s, respectively, in both experiments. Marshall et. al. included a plot of jet leading edge position vs. time for only one of their experiments, for which the jet diameter was 3.81 cm, the initial velocity was 1.4 m/s, and the penetration rate was 1.02 m/s. Spencer et. al. reported the relevant data for one experiment, for which the entry velocity and penetration rate were given as 2.7 m/s 2.1 m/s, respectively.

Jet	Ambient Liquid	ε	V^+	Eqn. XXX
Water (Saito)	Freon-11	0.7	0.3	0.5
Water (Saito)	Liquid Nitrogen	1.2	0.4	0.5
Freon-TF (Marshall)	Water	1.6	0.7	0.6
Cerrobend® (Schneider)	Freon-11	6.3	0.7	0.7
Wood's Metal (Spencer)	Water	9.2	0.8	0.8

These rough data indicate that penetration rate increases with increasing jet-ambient liquid density ratio. Equation XXX gives a fair first estimate of penetration rates for these experiments.

6.3 Interpretation of Quasi-Steady Jet Breakup Process

In attempting to explain the observed velocity and jet diameter dependence of the measured jet breakup lengths, one must first answer the question, "What physical process limits the steady jet's penetration of the volatile liquid?"

In the analyses of Ginsberg and Epstein and Fauske, it was assumed that the jet penetrates to the depth where it has been completely eroded (i.e., finely fragmented) by entrainment of melt into the surrounding vapor flow. The assumption that the jet is ejecting drops (i.e., atomizing) over its entire surface leads to the continuity relation:

$$\frac{L}{D} \sim \sqrt{\frac{\rho_j}{\rho_c}} \frac{V}{V_r}$$

derived in section XXX. Bürger et. al. has proposed using this relation with the assumption that the vapor kinetic energy is proportional to the hydrostatic head of the vapor chimney:

$$\rho_v V_v^2 \sim \rho_c g L$$

Bürger also assumes that:

$$V_v \gg V_j$$

so that:

$$V_r \approx V_v$$

With these assumptions, Bürger proposed the breakup length relation:

$$\frac{L}{D} \sim (\varepsilon Fr)^{\frac{1}{3}}$$

Note that the above correlation might also be applicable to long-wavelength (segmentation) breakup of the jet, for which relation XXX was also derived. Thus, this

correlation could be expected to be applicable for jet breakup due to Kelvin-Helmholtz instability, regardless of the dominant wavelength of the instability.

The breakup length data for the present experiments are in fair agreement with this relation. In the present experiments, some entrainment of melt into the vapor flow is apparent, although the complete atomization of the jet envisioned by Ginsberg, Epstein and Fauske, and Bürger was not evident; relatively large jet fluid masses are seen even in the lower section of the vapor chimney. And, in MFSBS-34, relatively large jet segments (i.e., having diameters larger than the 3 mm jet diameter) were observed to be decelerated without being finely fragmented.

The radiographs of the present experiments, the breakup regime appears to generally correspond to Reitz's second wind-induced regime. Unfortunately, breakup regime maps such as Figure XXX are applicable only for stagnant ambient gas, and only for one particular jet/ambient gas density ratio (i.e., water or liquids of similar density in air, for which $\varepsilon \sim 10^3$), so it is not possible to compare the observed breakup regime with that predicted for the vapor velocities assumed by the above breakup length correlation (which would be on the order of tens of meters per second).

However, other jet breakup regime determination criteria, discussed in the literature review, can be applied. Ginsberg's criteria for atomization of low viscosity jets, viz:

$We_a \sim 100$

would be met for vapor velocities on the order of 20 m/s. Linear instability analysis would also predict that for $We_a \gg 1$, the most rapidly growing deformation of the jet surface would have a wavelength much smaller than the jet diameter, as in atomization. However, it is notable that the atomization regime has been observed experimentally only for very small diameter (~1 mm) jets. The larger diameter jets used by Hoyt and Taylor, and De Jarlais et.al., underwent breakup in which the growth of long wavelenth deformations played an important rôle, with entrainment of jet fluid drops into the gas flow occuring only at the crests of the large waves, for We_a on the order of hundreds.

For larger diameter jets, entrainment criteria determined from annular two-phase flow have also been used to predict the onset of droplet entrainment from the jet surface. The entrainment inception criterion proposed by Ishii and Grolmes for two-phase annular flow was developed from a model of the shearing off of roll wave crests. Using the model to correlate their and other data in the literature, they obtained the criterion:

$$\frac{\mu_f j_g}{\sigma}\sqrt{\frac{\rho_g}{\rho_f}} \geqq N_{\mu F}^{0.8}, \text{ for } N_{\mu F} < \frac{1}{15}$$

For the inverted annular flow experiments of De Jarlais et. al., the Ishii-Grolmes correlation was shown to predict the miminum gas velocity for roll wave entrainment breakup within roughly a factor of two. This relation indicates that a jet-vapor relative velocity (assumed to be analogous to j_g) of ≈25 m/s would be required for entrainment of melt drops from waves on the jet in the present experiments.

Theofanous and Saito proposed proposed using the empirical correlation for the inception of entrainment (when the annular film is very thick) obtained by Steen and Wallis, viz:

$$\frac{\mu_g j_g}{\sigma}\sqrt{\frac{\rho_g}{\rho_f}} > 2.46\ 10^{-4}$$

to predict the vapor velocity required for atomization of a jet. This relation was obtained by plotting the linear increase of the percent of the liquid entrained with the gas velocity, and extending the line to zero entrainment percent to determine the corresponding gas velocity. This considerably overestimates the gas velocity at which the first entrainment occurs in annular two-phase flow. For Cerrobend® entrainment by Freon-11 vapor, their correlation predicts that the vapor velocity must exceed 370 m/s.

Finally, the criterion fo the onset of flooding in gas-liquid annular flow obtained by Pushkina and Sorokin is:[88]

$$Ku \equiv \frac{j_g\sqrt{\rho_g}}{(g\sigma(\rho_l-\rho_g))^{0.25}} = 3.2$$

might be used to predict jet atomization. The Kutateladze number has been interpreted by Whalley as the dimensionless minimum gas velocity for levitation of liquid drops;[89] it may therefore also be a reasonable criterion for the onset of entrainment. For the MFSBS experiments, this criterion predicts a Freon-11 vapor velocity of ≈18 m/s would be required for Cerrobend® droplet entrainment.

Based on these criteria, it appears that in the present experiments the vapor velocities could have been of the magnitude assumed by Bürger et. al. In addition, the observed substantial entrainment and upward flow of liquid around the vapor chimney would also be consistent with very high vapor velocities in the center of the chimney.

However, while the correlation proposed by Bürger may have applied to the present experiments, the penetration length data of Saito et. al. are correlated much better (i.e., extremely well, with a correlation coefficient of 0.99) by a different relation, viz:

$$\frac{L}{D} = 2.1\sqrt{\varepsilon Fr}$$

Saito et. al. supposed that the jet penetration length in their experiments was the depths at which the jet's velocity head had been completely converted to static pressure head or had

been expended doing work against the coolant (although they did not show how this conceptual picture would lead to their penetration length correlation). They supposed that an increase in the rate of vapor generation, i.e., an increase in the vapor blanket thickness, would increase the penetration length by shielding the jet from contact with the liquid coolant.

However, in a large diameter vapor chimney, very high vapor velocities could be produced, which would not act as a shield for the jet column, but rather would lead to breakup of the jet column due to Kelvin-Helmholtz instability. If breakup of the jet due to Kelvin-Helmholtz instability limited its penetration in the experiments of Saito et. al., their correlation should be equivalent to proportionality XXX, which would imply that:

$V_r \sim \sqrt{\rho_c g D}$

This relation would be difficult to justify.

An alternative explanation of their correlation can be proposed. In a vapor chimney in which the vapor is accelerated by the hydrostatic pressure gradient, it is possible that the drag forces on the elements of a deformed/segmented jet 'column' could decelerate the jet fluid so that it is levitated above the base of the chimney. If this occurred, melt-coolant mixing and vapor generation would momentarily cease, and the vapor chimney would shorten. The vapor velocity would then be reduced, again allowing the melt to penetrate into the liquid coolant at the base of the chimney and generate vapor. The vapor chimney would therefore, at steady state, have to stabilize at an average length comparable to the depth at which the jet fluid drops/segments could be decelerated/levitated. Any relatively large, low velocity jet segments entering the liquid at the base of the chimney would presumably be fragmented by Rayleigh-Taylor instability over a short distance free-fall through the liquid, so that the vapor chimney length (i.e., the jet penetration length measured by Saito et. al.) and jet breakup length would be comparable.

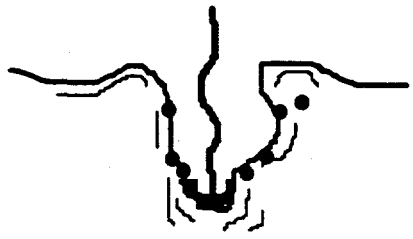

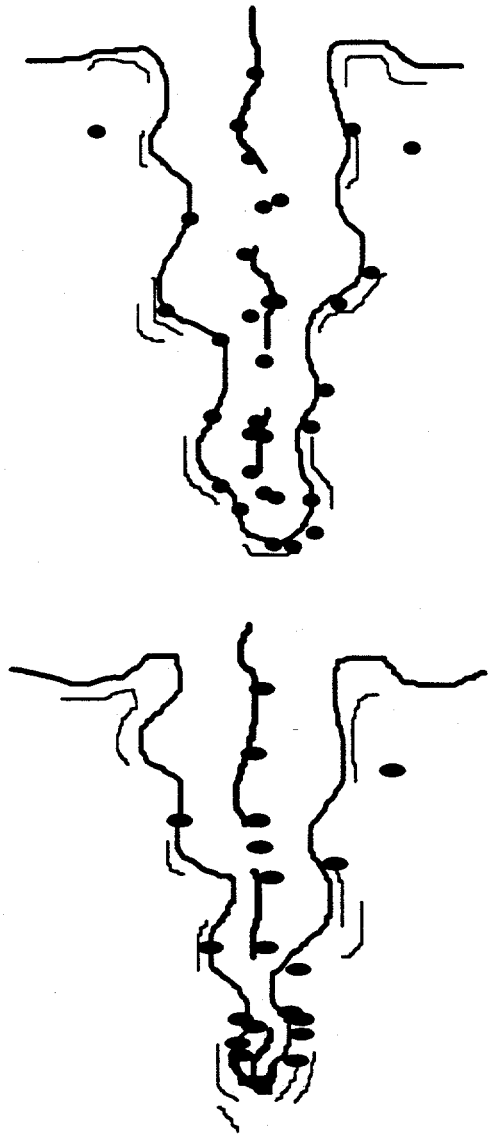

In order to momentarily levitate jet fluid above the base of the vapor chimney, the drag force acting on the jet surface must balance the jet initial momentum and the gravitational force acting on the jet column:

$c_f \rho_v V_v^2 DL \sim [\rho_j V^2 D^2] + [\rho_j D^2 Lg]$

where the brackets denote order of magnitude.

The gravitational force can be neglected when:

$\frac{L}{D} \ll [Fr]$

If this condition is satisfied, the force balance yields:

$$\frac{L}{D} \sim \sqrt{\frac{\rho_j V^2}{\rho_c g D}}$$

when it is assumed, as in the derivation of the correlation suggested by Bürger, that:

$\rho_v V_v^2 \sim \rho_c g L$

The breakup length relation above has the same form as the empirical jet penetration length correlation of Saito et. al.

It may seem to be a contradiction to assume that the jet fluid is levitated by the vapor flow without becoming finely fragmented, when the criteria above suggest that the vapor velocities postulated are clearly capable of inducing fragmentation. However, there is not necessarily a contradiction when the time scale of deceleration to levitation and that of fragmentation are compared.

When a drop is placed in a 'high velocity' gas flow, it is not instantaneously fragmented. During its deformation and fragmentation, it is also being accelerated by the gas flow, so that the drop-gas relative velocity is constantly decreasing during the breakup process.

Consider a drop initally traveling with a velocity V in a counterflowing gas with velocity V_g, where $V_g \gg V$. It is well established that, over the entire range of drop breakup regimes, the time required for complete fragmentation of a drop (when Oh is small, i.e., when the liquid viscosity is low) is:

$$t_{frag} \sim \frac{d}{V_r}\sqrt{\frac{\rho_d}{\rho_g}}$$

where the constant of proportionality has a value of about 5. This relation can be explained simply by noting that over the fragmentation time, a mass of fluid $\sim \rho_d d^3$ is moved a distance $\sim d$. Balancing the dynamic pressure force acting on the drop with the product of its mass and an acceleration $\sim \frac{d}{t_{frag}^2}$ yields the relation above.

The time required for the drop to be decelerated to levitation (i.e., $V \approx 0$) can be estimated from a simple force balance:

$$c_D d^2 \rho_g V_r^2 \sim d^3 \rho_j \frac{V}{t_{decel}}$$

which when rearranged is:

$$t_{decel} \sim \frac{\rho_d V d}{c_D \rho_g V_r^2}$$

For deceleration of the drop to occur before it is completely fragmented:

$t_{decel} \leq t_{frag}$

That is:

$$\frac{V}{V_r} \leq c_D \sqrt{\frac{\rho_g}{\rho_d}}$$

Assuming that the jet can be thought of as a train of segments (with comparable drag coefficients), and further assuming, as before, that the vapor in the chimney is accelerated by the hydrostatic pressure gradient, the above criterion becomes:

$$\frac{L}{D\varepsilon Fr} > \eta$$

where η is an undefined constant. When levitation precedes complete breakup, the breakup length would presumably be predicted by the Saito et.al. correlation; therefore, the criterion can be written as:

$\varepsilon Fr < \eta$

The values of εFr in the present experiments and in those of Saito et. al. were similar, spanning two orders of magnitude in both sets of experiments. This would suggest that if levitation limited jet penetration in one set of experiments, it would have in the other as well.

Thus far use has been made of the assumption that the kinetic energy of the vapor in the chimney balances the hydrostatic pressure in the coolant pool. Some discussion of this assumption is in order.

The mixing of melt and coolant, i.e., the vapor generation, appears to accur primarily at the base of the vapor chimney. The mean vapor flow is parallel to the jet axis; therefore, there cannot be on average a radial pressure gradient, and the pressure gradient in the vapor chimney must be roughly the hydrostatic pressure gradient of the pool.

As the vapor flow develops from the chimney base, a vapor boundary layer is formed adjacent to the vapor-liquid interface (Figure XXX). The potential core of the vapor chimney, however, would be accelerated by the pressure gradient. If the vapor chimney were sufficiently long, the vapor velocity profile would become fully developed, so that the hydrostatic pressure force could be balanced by shear at the vapor-liquid coolant interface, so that the vapor velocity would no longer depend on L.

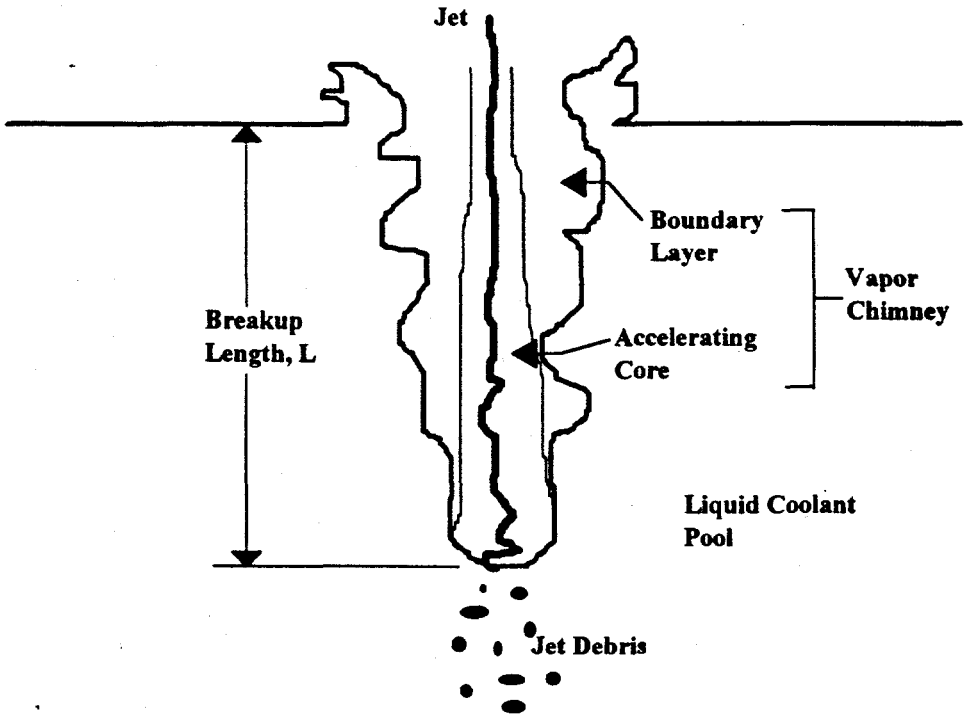

Apparently, in most or all of the present experiments, *the vapor chimney was too short for the vapor velocity profile to become fully developed.* In the potential core of the vapor flow, assuming the vapor velocity at the base of the chimney is negligible, the vapor velocity along the jet will be, from the Bernoulli equation:

$$V_v \approx \sqrt{\frac{2\rho_c g(L-x)}{\rho_v}}$$

where x the the depth below the liquid free surface. For Freon-11 coolant, this relation indicates that a vapor chimney having a depth of one meter could generate a vapor velocity at the surface on the order of 70 m/s near the jet.

There are clearly some limits to the length of the potential core of the vapor chimney. First, the potential core must have a flow area much larger than the jet in order for the core vapor velocity to be considered the ambient fluid velocity. The flow area of the potential core of the vapor chimney decreases as the free surface is approached, due to the growth of the boundary layer caused by interfacial shear, and due to the acceleration of the core flow.

First, continuity requires that the diameter of the potential core decrease with decreasing depth (i.e., with increasing vapor velocity). Te rate of vapor generation must obviously be sufficient to create a vapor channel so large that the vapor velocity profile

does not become fully developed. The second possible limitation would be choking of the vapor flow. A high quality two-phase flow has a critical velocity comparable to the velocity of sound of the vapor:

$$V = \sqrt{\frac{k_v p}{\rho_v}}$$

Estimating the maximum vapor velocity (i.e., at the free surface) from:

$$\rho_v V^2 \approx 2\rho_c g L$$

choking would be expected when:

$$L \approx \frac{k_v p}{2\rho_c g}$$

For Freon-11, $k_v \approx 1.1$, corresponding to choking when L exceeds roughly 4 m, which is much greater than the ~1 m depth of the coolant pool in the present experiments.

6.4 Conclusions

The MFSBS jet leading edge penetration rate data, with those of the other extant simulant material experiments, show increasing jet leading edge penetration rate with increasing jet-ambient liquid density ratio. A simple physical argument has been used to yield an expression for the dimensionless penetration rate which explains this trend. The relation obtained is similar to one obtained empririically by Hopkins and Robertson for plane water jets penetrating various liquids.

The MFSBS breakup length data show (dimensionless) breakup length to increase with jet velocity and decrease with jet diameter. However, it is not possible to determine from these data whether the correlation proposed by Bürger et. al., or the excellent empirical correlation of Saito et. al., is a better predictor, the correlation of the present data with both relations being only fair.

The physical process envisioned by Bürger et. al. (who were interested primarily in jets larger than those used in the present experiments) is one in which an undisturbed jet core extends to the breakup length, while the entire surface of the jet is ejecting small drops. In contrast to this view, Saito et. al. envisioned (for their experiments) a contiguous jet column extending to the base of the vapor chimney. The radiographs (both still and cine) from the present experiments show neither of these jet configurations. Melt is observed to be entrained from the jet column into the vapor flow, but only at the crests of large waves. The jet column itself is rarely contiguous, but rather is broken into segments just below the liquid surface, with large segments (i.e., on the order of the jet diameter) being observed even near the base of the vapor chimney. These images support

the proposed explantation of the jet breakup (or penetration) length as the depth at which the jet segments are completely decelerated by the vapor flow.

It is also notable that the debris data from the present experiments and those from Spencer's experiments with Wood's metal jets in water (with essentially no boiling) are similar. The observed preponderance of filaments (rather than spheroids) in the debris suggests rapid quenching of the debris fragments, as would occur during breakup in the coolant liquid. This would be expected in the latter experiments, but would not in the former unless most of the fragmentation had occurred in the liquid at the base of the vapor chimney rather than in the vapor flow.

7.0 CONCLUSIONS

7.1 Effect of Ambient Liquid Boiling on Jet Breakup Length

The breakup length data show that the dimensionless breakup length increases with jet velocity and decreases with jet diameter. This trend observed in the experiments of Saito et. al. with water jets in Freon-11 and liquid nitrogen, and is also predicted by the breakup length correlation proposed by Bürger et. al. Both relations show the dimensionless breakup length to be a function of the jet Froude number. Both relations are fair predictors of breakup lengths in the present experiments.

Both Ginsberg and Epstein and Fauske had suggested that Taylor's breakup length relation for jet breakup in a stagnant fluid, in which the dimensionless breakup length depends only on the jet and ambient fluid (in this case, a highly voided two-phase mixture), would be a good predictor of corium jet breakup lengths in water. Experiments with liquid jet breakup in liquids have established that the Taylor relation provides a good estimate of breakup length; therefore, the dependence on jet diameter and velocity observed in the present experiments, and those of Saito et. al., shows that the vapor velocity in the chimney surrounding the jet must not have been negligible.

The excellent correlation obtained by Saito et. al. indicates that the vapor velocity, which has an important effect on both jet fragmentation and jet segment deceleration/levitation, was determined solely by the hydrostatic pressure gradient in the coolant pool. This could only occur when the vapor chimney is wide enough for a potential core to extend over its entire length, i.e., when the vapor velocity profile is not fully developed. Using this vapor velocity with the well established breakup length relation from linear instability analysis yields the correlation proposed by Bürger et. al. This correlation is a poor predictor of the penetration length observations of Saito et. al. However, an alternative conceptual picture, in which the jet is segmented, and the segments are periodically decelerated and levitated above the base of the vapor chimney, provides a plausible explanation for the correlation obtained by Saito et. al.

The radiographs from the present experiments show jets that are segmented, and somewhat eroded by the countercurrent vapor flow. The X-ray cine films also show occasional penetration of liquid waves deep into the vapor chimney with jet-liquid contact. The observation of relatively large jet fluid masses deep into the vapor chimney supports the notion that these may be decelerated and levitated above the base of the vapor chimney by the vapor flow. The predominance of filaments in the jet debris also suggests that final fragmentation of the jet fluid occurs primarily in the liquid at the base of vapor

chimney, where the fragments are rapidly quenched. **Compare convective heat flux in vapor flow with nucleate boiling heat flux.**

7.2 Recommendations for Future Work

From the simulant experiments conducted to date, some conclusions can be drawn about the effect of boiling of the ambient liquid.

The isothermal liquid-jet-in-liquid experiments conducted at SNL showed Taylor's jet breakup relation to be a good predictor. The experiments with Wood's metal in water at ANL yielded breakup lengths that were also in fair agreement with the same relation, when there was little boiling of the water.

The present experiments and those of Saito et. al. show that the vapor velocity near the jet in a large diameter vapor chimney can be large enough to have an important effect on breakup length, at least when the vapor velocity profile is not fully developed. It is not clear that the deceleration/levitation-limited jet penetration proposed as an explanation of the Saito et. al. penetration length correlation could be applicable for 'large' diameter jets, where long wavelength deformation and segmentation of the jet column may not occur. However, such large diameter jets could not fragment significantly over the ~1 m to ~3 m coolant depths encountered in-vessel or ex-vessel in the reactor cavity.

The correlation of Saito et. al. should give a good estimate of the shortest possible breakup length for corium jets in water. If the vapor generation rate near the jet is small enough that the vapor velocity profile becomes developed, vapor velocities would be decreased, and breakup lengths (due either to deceleration/levitation or fragmentation in the vapor flow) would be increased. For example, in one of the ANL Wood's metal-in-water experiments in which the melt temperature was high enough to produce transition boiling on the jet surface (and therefore reduce the vapor generation rate relative to lower melt temperature experiments), the breakup length was significantly increased. At high ambient pressures and coolant subcoolings, a molten fuel jet penetrating water may be blanketed by a thin vapor film, rather than a large diameter vapor chimney. Experiments in which the vapor generation rate relatively low would be useful, in order to provide quantitative jet breakup length data for this 'regime'. Characterization of developed vapor chimney flows through the use of instrumentation capable of measuring local velocities and void fractions would also provide important data for comparison with the predictions of the computational models.

Marciniak has already carried out experiments (using the MFSBS apparatus) with three collinear jets directed into nearly saturated Freon-11. No significant difference

between breakup length correlations for single and three jet experiments was found. Presumably, this indicates that the vapor boundary layers along the jets were thin compared to the space between the jets, so that the vapor velocity near a jet was not much affected by the presence of the others. However, *three-dimensional* arrays of jets would probably be produced in a core melt accident; at present there is no breakup length or other data for such arrays to be used for code comparison.

REFERENCES

1. T. G. Theofanous, *Thermo-Fluid Science in Severe Nuclear Accidents*, ANS Proc. 1989 National Heat Transfer Conf., Philadelphia, PA, August 6-9, 1989, p. 3.

2. **Nuclear Engineering International**, **15**, No. 167, p. 344 (1970).

3. M. A. Abolfadl and T. G. Theofanous, *An Assessment of Steam Explosion Induced Containment Failure. Part II: Premixing Limits*, **Nuclear Science and Engineering**, **97**, p. 282 (1987).

4. G. E. Lucas, W. H. Amarasooriya, and T. G. Theofanous, *An Assessment of Steam Explosion Induced Containment Failure. Part I: Probabalistic Aspects*, **Nuclear Science and Engineering**, **97**, p. 259 (1987).

5. J. L. Rempe, G. L. Thinnes, and C. M. Allison, *Light Water Reactor Lower Head Failure Analysis (Draft)*, NUREG/CR-5642, EGG-2618 (Draft, December 1990).

6. G. Wilson et. al., *An Integrated Structure and Scaling Methodology for Severe Accident Technical Issue Resolution*, NUREG/CR-5809, EGG-2659 (1991).

7. K. Becker and J. Engstrom, *A Method for Protecting Containments from Thermal Attack During Severe Light Water Reactor Accidents*, KTH-NEL-49, Department of Nuclear Reactor Engineering, Royal Institute of Technology, Stockholm, Sweden (1989)

8. M. Saito et. al., *Experimental Study on Penetration Behaviors of Water Jet into Freon-11 and Liquid Nitrogen*, ANS Proc. 1988 National Heat Transfer Conf., Houston, TX, July 24-27, 1988.

9. M. J. McCarthy and N. A. Molloy, *Review of the Stability of Liquid Jets and the Influence of Nozzle Design*, **Chem. Eng. Journal**, 7, p. 1 (1974).

10. E. J. McKeogh and D. A. Ervine, *Air Entrainment Rate and Diffusion Pattern of Plunging Liquid Jets*, **Chem. Engng. Sci.**, **36**, p. 1161 (1981).

11. C. Weber, *On the Breakdown of a Fluid Jet*, **Zeitschrift fur angewandte Mathematik und Mechanik**, **11**, p.136 (1931); Cited by Ginsberg (ref.).

12. G. I. Taylor, *Generation of Ripples by Wind Blowing Over a Viscous Fluid* (1940), in G. K. Batchelor, **The Scientific Papers of G. I. Taylor**, **3**, Cambridge University Press, Cambridge, MA (1963).

13. G. I. Taylor, *The Dispersion of Jets of Metals at Low Melting Point in Water* (1942), in G. K. Batchelor, **The Scientific Papers of G. I. Taylor**, **3**, Cambridge University

Press, Cambridge, MA (1963).

14. V. C. Levich, **Physicochemical Hydrodynamics**, Prentice-Hall, Inc., Englewood Cliffs, NJ (1962).

15. V. M. Entov and A. L. Yarin, *Dynamical Equations for a Liquid Jet*, **Fluid Dynamics, 15**, No. 5, p. 644 (1980).

16. A. L. Yarin, *On the Dynamical Equations for Liquid Jets*, **Fluid Dynamics, 18**, No. 1, p. 134 (1983)

17. V. M. Entov and A. L. Yarin, *Transverse Stability of a Liquid Jet in a Counterflowing Air Stream*, **J. Engineering Physics, 38**, No. 5, p. 495 (1980).

18. H. Lamb, **Hydrodynamics** (5th ed.), Cambridge University Press, New York (1924).

19. S. Chandrasekhar, **Hydrodynamic and Hydromagnetic Stability**, Dover Publications, Inc., New York (1981).

20. W. S. Rayleigh, *On the Destability of Jets*, **Proc. Lond. Math. Soc., 1**, p. 10 (1878); Cited by Ginsberg (ref.).

21. H. Q. Yang, *Asymmetric Instability of a Liquid Jet*, **Phys. Fluids A, 4** (4), p. 681, (1992)

22. R. D. Reitz, **Atomization and Other Breakup Regimes of a Liquid Jet**, Ph.D. Thesis, Department of Mechanical and Aerospace Engineering, Princeton University, October, 1978.

23. R. S. Brodkey, **The Phenomena of Fluid Motions**, Addison-Wesley Publishing Co., Reading, MA (1967).

24. S. C. Windquist and M. L. Corradini, **Modeling the Atomization of a Liquid Jet and Application of the Model to Large Diameter Molten Corium Jets**, Masters Thesis, University of Wisconsin, August 1986.

25. T. Ginsberg, *Liquid Jet Breakup Characterization with Application to Melt-Water Mixing*, Proc. International ANS/ENS Topical Meeting on Thermal Reactor Safety, San Diego, CA, Feb. 2-6, 1986, Vol. 5, p. II.4-1.

26. R. P. Grant and S. Middleman, *Newtonian Jet Stability*, **AIChE Journal, 12**, No. 4, p. 669 (1966).

27. J. H. Lienhard and J. B. Day, *The Breakup of Superheated Liquid Jets*, **ASME Trans., *Journal of Basic Engineering*, 92**, p. 515 (September, 1970)

28. G. De Jarlais, M. Ishii, and J. Linehan, *Hydrodynamic Stability of Inverted Annular*

Flow in an Adiabatic Simulation, **ASME Trans., 108**, p. 84 (1986).

29. Y. Kitamura and T. Takahashi, *Stability of Jets in Liquid-Liquid Systems*, Chapter 19, **Encyclopedia of Fluid Mechanics, 2**, Gulf Publishing Co., Houston, TX (1986).

30. S. Tomotika, *On the Instability of a Cylindrical Thread of a Viscous Liquid surrounded by Another Viscous Fluid*, **Proc. Roy. Soc., 150**, p. 322 (1935).

31. F. D. Rumscheidt and S. G. Mason, *Break-Up of Stationary Liquid Threads*, **J. Colloid Sci., 17**, p. 260 (1962).

32. V. A. Ivanov, *Disintegration of a Liquid Jet*, **J. Appl. Mech. Tech. Phys. USSR, 7**, p. 19 (1966).

33. G. K. Batchelor and A. E. Gill, *Analysis of the Stability of Axisymmetric Jets*, **J. Fluid Mech., 14**, p. 529 (1962).

34. A. J. Reynolds, *Observations of a Liquid-into-Liquid Jet*, **J. Fluid Mech., 14**, p. 552 (1962).

35. J. D. Gabor, R. T. Purviance, R. W. Aeschlimann, and B. W. Spencer, *Characterization of Metal Fuel Fragmentation*, ANL-IFR-52, Argonne National Lab. (1986).

36. J. D. Gabor, R. T. Purviance, J. C. Cassulo, and B. W. Spencer, *Molten Aluminum Alloy Fuel Fragmentation Experiments*, Proc. of the Fifth International Topical Meeting on Reactor Thermal Hydraulics (NURETH5), September 21-24, 1992, **III**, p. 898.

37. H. J. Hoyt and J. J. Taylor, *Waves on Water Jets*, **J. Fluid Mechanics, 83**, Part 1, p. 119 (1977).

38. C. C. Miesse, *Correlation of Experimental Data on the Disintegration of Liquid Jets*, **Ind. and Engr. Chem., 47**, p. 1690 (1955).

39. M. Ishii and M. A. Grolmes, *Inception Criteria for Droplet Entrainment in Two-Phase Concurrent Film Flow*, **AIChE Journal, 21**, No. 2, p. 308 (1975).

40. M. Gaster, *A Note on the Relation Between Temporally-Increasing and Spatially Increasing Disturbances in Hydrodynamic Stability*, **J. Fluid Mech., 14**, p. 222 (1962).

41. S. P. Lin and D. J. Kang, *Atomization of a Liquid Jet*, **Physics of Fluids, 30**, No. 7, p. 2000 (1987).

42. S. P. Lin and E. A. Ibrahim, *Instability of a Viscous Liquid Jet Surrounded by a*

Viscous Gas in a Vertical Pipe, **J. Fluid Mech., 218**, p. 641 (1990).

43 S. Siry, G. Anand, and R. N. Christensen, *The Study of Jet Breakup Mechanisms in Condensing Injectors*, Proc. of the Fifth International Topical Meeting on Reactor Thermal Hydraulics (NURETH-5), Salt Lake City, UT, September 21-24, 1992, I, p. 87.

44. B. W Marshall, Jr., and M. Berman, *An Experimental Study of Isothermal and Boiling Liquid Jets*, 14th Water Reactor Safety Research Information Meeting, Gaithersburg, MD, October 27-31, 1986.

45. B. W. Marshall, Jr., *Recent Fuel-Coolant Interaction Experiments Conducted in the FITS Vessel*, ANS Proc. 1988 National Heat Transfer Conference, Houston, TX, July 24-27, 1988, p. 265.

46. B. W. Spencer, J. J. Sienicki, and L. M. McUmber, *Hydrodynamics and Heat Transfer Aspects of Corium-Water Interactions*, EPRI NP-5127, (1987).

47. S. K. Wang, C. A. Blomquist, B. W. Spencer, L. M. McUmber, and J. P. Schneider, *Experimental Study of the Fragmentation and Quench Behavior of Corium Melt Streams in Water*, 5th Proc. of Nuclear Thermal Hydraulics, ANS Winter Mtg., San Francisco, CA, November 26-30, 1989.

48. B. W. Marshall, Jr., D. F. Beck, and M. Berman, *Mixing of Isothermal and Boiling Molten-Core Jets with Water: The Initial Conditions for Energetic FCIs*,, Proc. International ENS/ANS Conf. on Thermal Rea tor Safety, Avignon, France, Oct. 2-7, 1988, p. 117.

49. C. J. Chen and W. Rodi, **Vertical Turbulent Buoyant Jets-A Review of Experimental Data**, Pergamon Press, Inc., New York, NY, 1980.

50. B. W. Spencer, J. D. Gabor, and J. C. Cassulo, *Effect of Boiling Regime on Melt Stream Breakup in Water*, 4th Miami International Symposium on Multi-Phase Transport and Particulate Phenomena, Miami Beach, FL, December 15-17, 1986.

51. D. F. Fletcher and R. P. Anderson, *A Review of Pressure-Induced Propagation Models of the Vapour Explosion Process*, **Progress in Nuclear Energy, 23**, No. 2, p. 137 (1990).

52. M. L. Corradini and G. A. Moses, *Limits to Fuel/Coolant Mixing*, **Nuclear Science and Engineering, 90**, p. 19 (1985).

53. D. H. Cho, H. K. Fauske, and M. A. Grolmes, *Some Aspects of Mixing in Large-Mass, Energetic Fuel-Coolant Interactions*, Proc. Int. Mtg. Fast Reactor Safety and Related Physics, Chicago, IL, October 5-8, 1976, Vol. 4, p. 1852 (referenced by XXX).

54. R. E. Henry and H. K. Fauske, *Required Initial Conditions for Energetic Steam Explosions, Fuel-Coolant Interactions*, HTD-19, ASME (1981).

55. T. G. Theofanous and M. Saito, *An Assessment of Class-9 (Core-Melt) Accidents for PWR Dry-Containment Systems*, **Nuclear Engineering and Design, 66**, p. 301 (1981).

56. D. A. Steen and G. B. Wallis, *The Transition from Annular to Annular Mist Co-Current Two-Phase Down Flow*, NYO-3114-2 (D. A. Steen, M.Sc.thesis, Dartmouth College, 1964). Cited by G. F. Hewitt and N. S. Hall-Taylor, **Annular Two-Phase Flow**, Pergamon Press, New York, 1970.

57. M. Epstein and H. K. Fauske, *Steam Film Instability and the Mixing of Core-Melt Jets and Water*, ANS Proc. 1985 National Heat Transfer Conf., Denver, Co, August 1985.

58 M Bürger, E. v.Berg, S.H. Cho, and A. Shatz, *Modeling of Jet Breakup as a Key Process in Premixing*, Proc. of the Sixth International Topical Meeting on Reactor Thermal Hydraulics (NURETH-6), Grenoble, France, October 5-8, 1993.

59. D. F. Fletcher and A. Thyagaraja, *The CHYMES Coarse Mixing Model*, **Progress in Nuclear Energy, 26**, p. 31 (1991).

60. J. J. Sienicki, S. K. Wang, and B. W. Spencer, *Analysis of Melt Arrival Conditions on the Lower Head in U. S. LWR Configurations*, Proc. of the Fifth International Topical Meeting on Reactor Thermal Hydraulics (NURETH-5), Salt L ke City, UT, September 21-24, 1992, II, p. 450.

61. M. F. Young, *IFCI: An Integrated Code for Calculation of All Phases of Fuel-Coolant Interactions*, NUREG/CR-5084 (1987).

62. M. F. Young, *Application of the IFCI Integrated Fuel-Coolant Interaction Code to a FITS-Type Pouring Mode Experiment*, SAND89-1692C (1989).

63. M. Pilch, **Acceleration Induced Fragmentation of Liquid Drops**, Ph.D. Thesis, University of Virginia (1981).

64. M. Pilch and C. A. Erdman, *Consideration of Liquid Drop Fragmentation in Safety Analysis*, **Trans. Am. Nuc. Soc., 38**, p. 403 (1981).

65. L. P. Hsiang and G. M. Faeth, *Near Limit Drop Deformation and Secondary Breakup*, **Int. J. Multiphase Flow, 18**, p. 635 (1992).

66. C. C. Chu and M. L. Corradini, *One-Dimensional Transient Fluid Model for Fuel/Coolant Interaction Analysis*, **Nuclear Science and Engineering, 101**, p. 48 (1989).

67. M. K. Denham, A. P. Tyler, and D. F. Fletcher, *Experiments on the Mixing of Molten Uranium Dioxide with Water and Initial Comparisons with CHYMES Code Calculations*; Proc. of the Fifth International Topical Meeting on Reactor Thermal Hydraulics (NURETH5), September 21-24, 1992, **VI**, p. 1667.

68. M. J. Marciniak, **Experimental Observations of the Breakup of Multiple Metal Jets in a Volatile Liquid**, Masters Thesis, Department of Nuclear Engineering, University of Illinois at Urbana-Champaign (January 1993).

69. Cerro Copper and Brass Co., Bellefonte, PA 16823.

70. *Thermodynamic Properties of Freon-11*, E. I. DuPont De Nemours & Co. (Inc.), "Freon" Products Division, Wilmington, DL 19898 (1965).

71. J. D. Gabor, B. W. Spencer, and J. C. Cassulo, *Simulant Material Pour Stream Breakup Tests and Model Implications*, ANL-IFR-77, August, 1987.

72. **CRC Handbook of Chemistry and Physics** (61st ed.), R. C. Weast, Ed., CRC Press, Inc., Boca Raton, FL, 1980.

73. H. K. Fauske, *On the Mechanism of Uranium Dioxide-Sodium Explosive Interactions*, **Nuclear Science and Engineering, 51**, p. 95 (1973).

74. B. J. Eiseman, *Reactions of Chlorofluorohydrocarbons with Metals*, DuPont Freon Technical Bulletin RT-33. Reprinted from **ASHRAE Journal, 5**, No. 5, p.63 (1963).

75. E. R. Hosler and J. W. Westwater, *Film Boiling on a Horizontal Plate*, **J. American Rocket Society, 32**, p. 553 (1962).

76. G. A. Greene, J. Klein, J. Klages, E. Schwarz, and Y. Sanborn, *Some Observations on Simulated Molten Debris-Coolant Layer Dynamics*, BNL-NUREG-32951 (April 1983)

77. **TechPlot Technical Plotting and Data Processing User's Handbook**, Polysoft Ltd., Salt Lake City UT (1992).

78. M. Ishii and N. Zuber, *Drag Coefficient and Relative Velocity in Bubbly, Droplet or Particulate Flows*, **AIChE Journal, 25**, No. 5, p. 843 (1979).

79. R. Clift, J. R. Grace, and M. E. Weber, **Bubbles, Drops, and Particles**, Academic Press, New York (1978).

80. H. D. Young, **Statistical Treatment of Experimental Data**, McGraw-Hill Book Company, Inc., New York, 1962.

81. M. S. El-Genk and S. H. Kim, *Experimental Studies of Lateral Distribution and Composition of Sediments of Single and Binary Particle Mixtures*, **AIChE**

Symposium Series, 80, No. 236, p.372 (1984).

82. J. D. Gabor, E. S. Sowa, L. Baker, Jr., and J. C. Cassulo, *Studies and Experiemnts on Heat Removal from Fuel Debris in Sodium*, ANS Fast Reactor Safety Mtg., Los Angeles (April 1974).

83. W. M. Rohsenow (Ed.), **Handbook of Heat Transfer Applications**, McGraw-Hill, Inc., New York (1985).

84. I. Catton, V. K. Dhir, and C. W. Somerton, *An Experimental Study of Debris Bed Coolability Under Pool Boiling Conditions*, EPRI NP-3094 (May 1983).

85. D. F. Fletcher, *The Particle Size Distribution of Solidified Melt Debris from Molten Fuel-Coolant Interaction Experiments*, **Nuclear Engineering and Design, 105**, p. 313 (1988).

86. R. D. Cadle, **Particle Size Determination**, Interscience Publishers, Inc., New York (1955).

87. D. F. Hopkins and J. M. Robertson, *Two-Dimensional Incompressible Fluid Jet Penetration*, **J. Fluid Mech., 28**, Part 2, p. 273 (1967).

88. O. L. Pushkina and Y. L. Sorokin, *Breakdown of Liquid Film Motion in Vertical Tubes*, **Heat Trans. Soviet Research, 1**, No. 5, p.56. Cited by J. M. Delhaye et. al., **Thermalhydraulics of Two-Phase Systems for Industrial Design and Nuclear Engineering**, McGraw-Hill Book Co., New York, 1981.

89. P. B. Whalley, **Boiling, Condensation, and Gas-Liquid Flow**, Oxford University Press, New York, 1987.

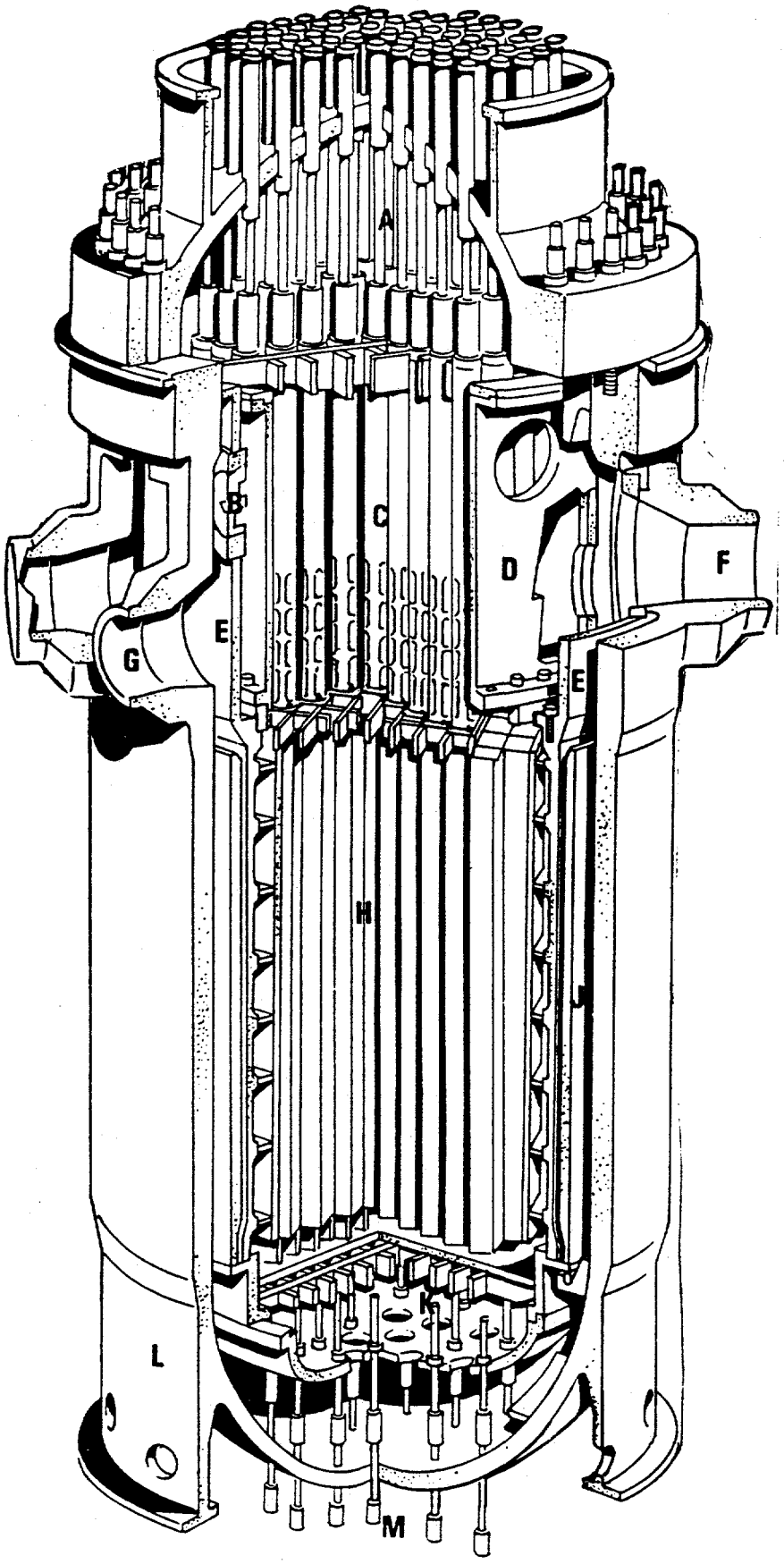

Key to reactor

A. Control rod drive actuators
B. Internals vent valve
C. Control rod guide tubes
D. Upper plenum
E. Core support shield
F. Outlet nozzle
G. Inlet nozzle
H. Fuel assembly
J. Thermal shield
K. Flow baffle
L. Support skirt
M. In-core instrumentation nozzles

Figure 1. Babcock & Wilcox Pressurized Water Reactor (1970), Onconee Nuclear Power Station (1)

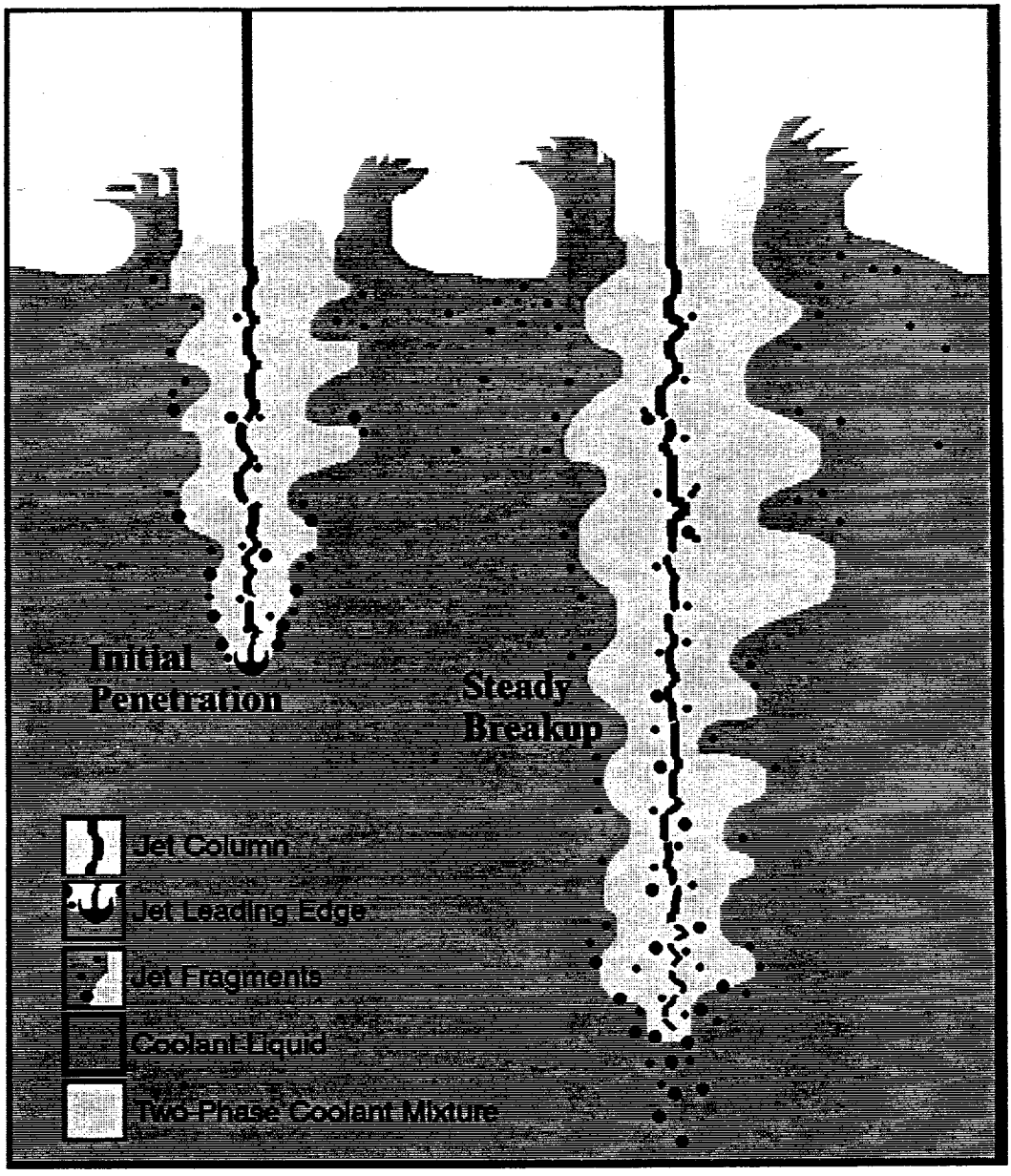

FIGURE 2. PHASES OF JET PENETRATION

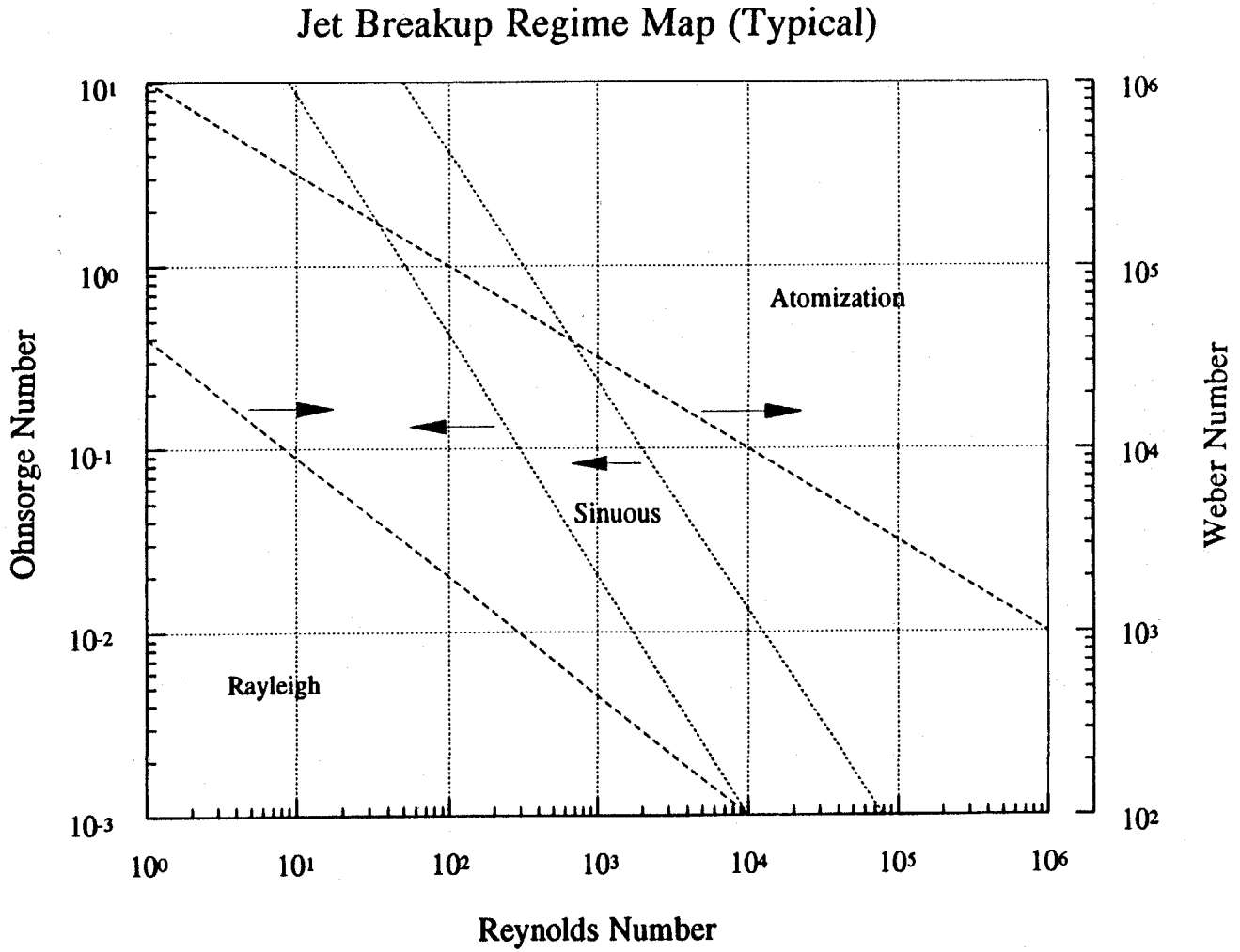
Jet Breakup Regime Map (Typical)
Ohnsorge Number
Weber Number
Reynolds Number
Atomization
Sinuous
Rayleigh
10¹
10⁰
10-1
10-2
10-3
10⁶
10⁵
10⁴
10³
10²
10⁰
10¹
10²
10³
10⁴
10⁵
10⁶

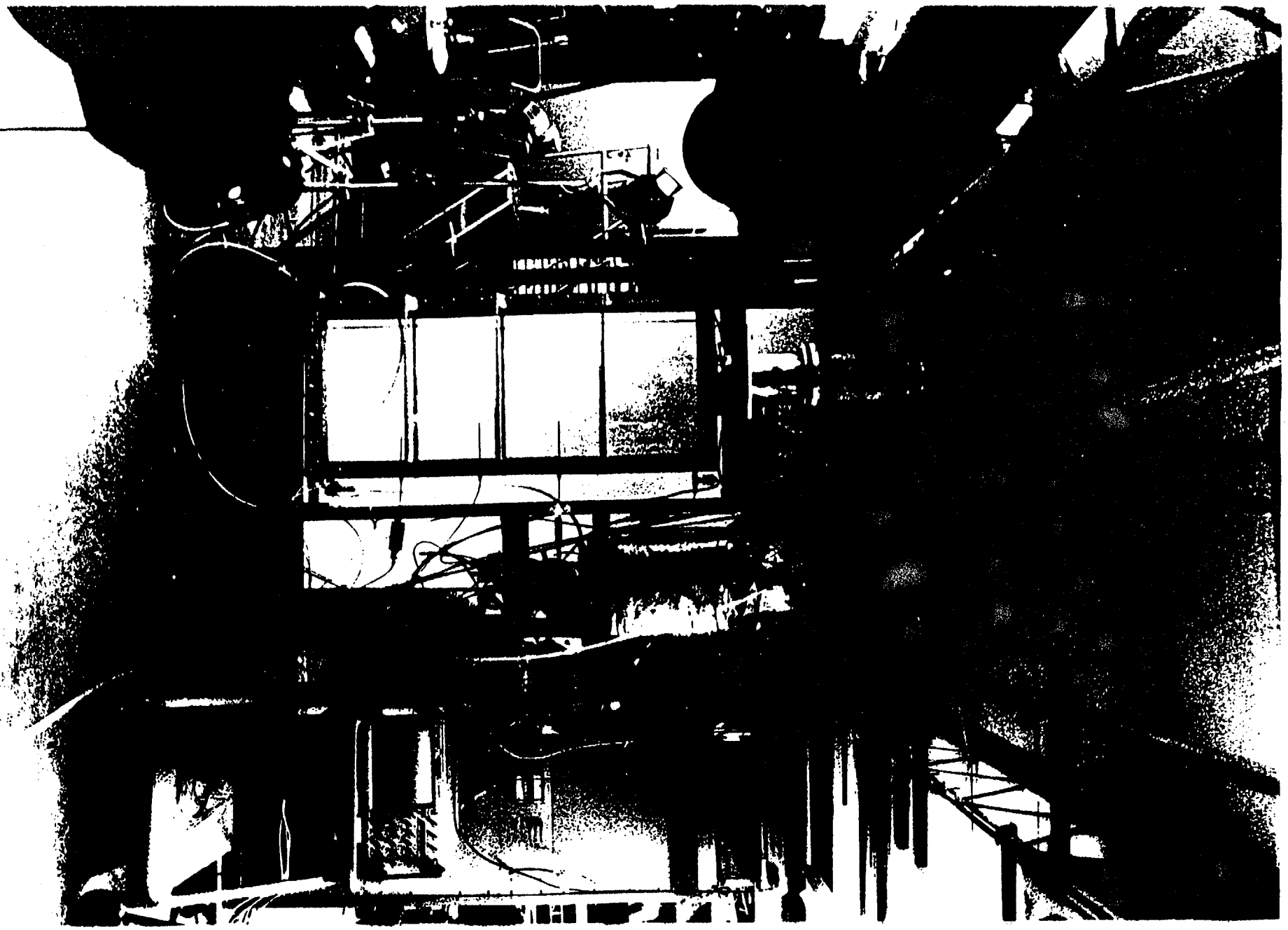

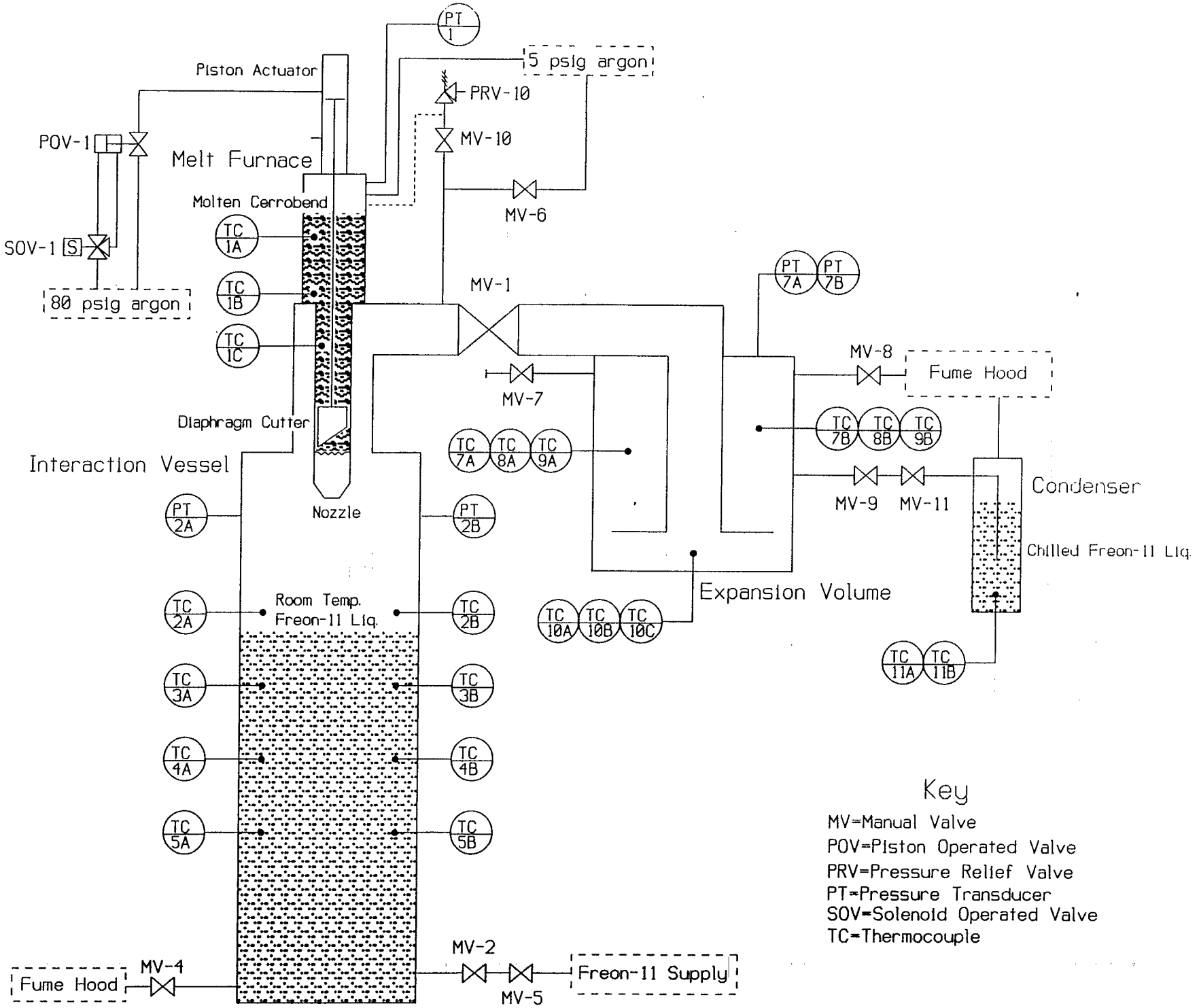
PT 1
5 psig argon
Piston Actuator
PRV-10
MV-10
POV-1
Melt Furnace
MV-6
Molten Cerrobend
TC 1A
SOV-1 S
TC 1B
MV-1
80 psig argon
TC 1C
PT 7A
PT 7B
MV-8
Fume Hood
MV-7
Diaphragm Cutter
TC 7B
TC 8B
TC 9B
TC 7A
TC 8A
TC 9A
Interaction Vessel
MV-9
MV-11
Condenser
Nozzle
PT 2A
PT 2B
Chilled Freon-11 Liq.
Room Temp.
Freon-11 Liq.
TC 2A
TC 2B
Expansion Volume
TC 10A
TC 10B
TC 10C
TC 11A
TC 11B
TC 3A
TC 3B
TC 4A
TC 4B
TC 5A
TC 5B
MV-2
MV-4
Fume Hood
Freon-11 Supply
MV-5
Key
MV=Manual Valve
POV=Piston Operated Valve
PRV=Pressure Relief Valve
PT=Pressure Transducer
SOV=Solenoid Operated Valve
TC=Thermocouple

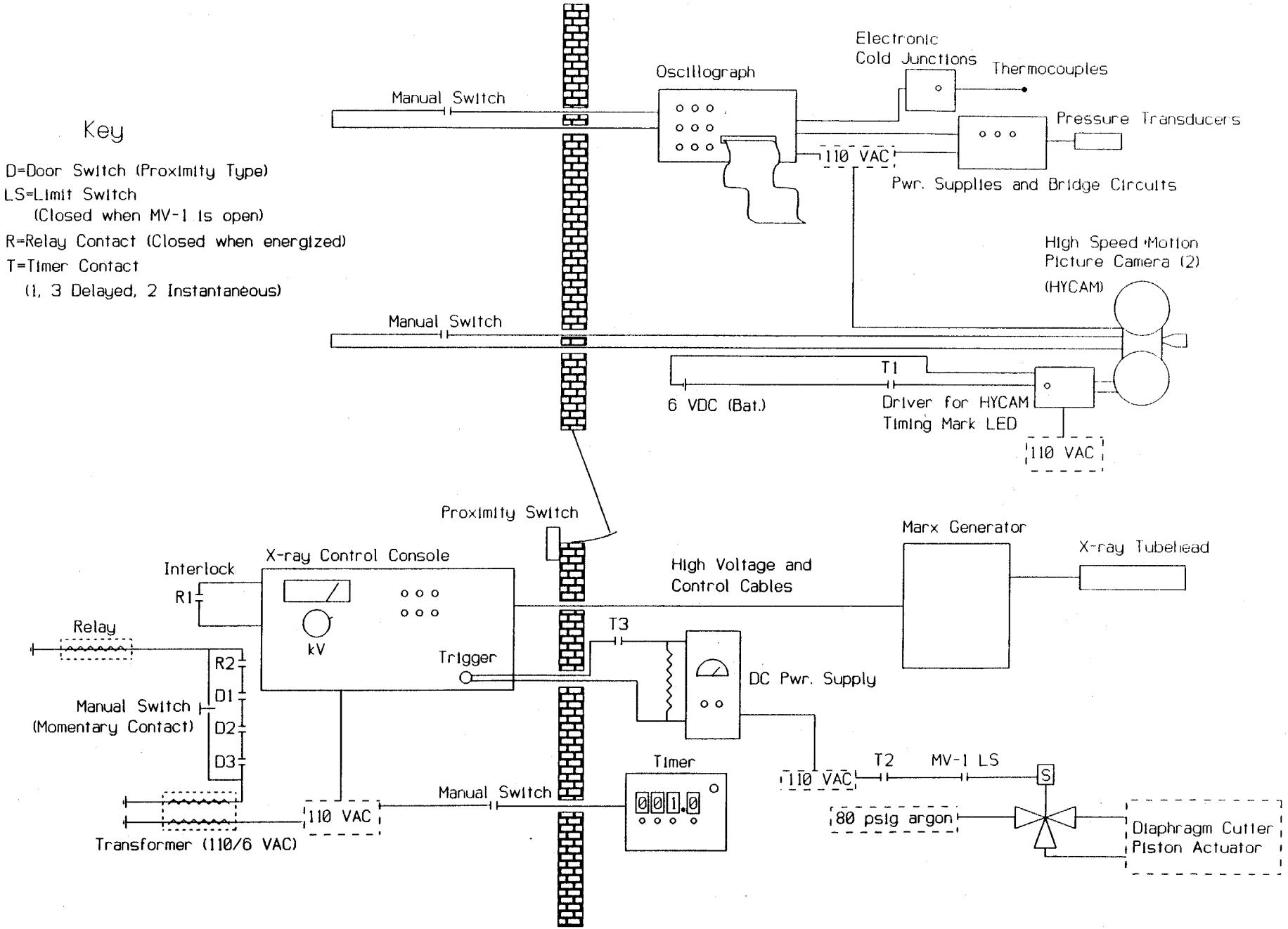
Key
D=Door Switch (Proximity Type)
LS=Limit Switch
(Closed when MV-1 is open)
R=Relay Contact (Closed when energized)
T=Timer Contact
(1, 3 Delayed, 2 Instantaneous)
Manual Switch
Oscillograph
Electronic
Cold Junctions
Thermocouples
Pressure Transducers
110 VAC
Pwr. Supplies and Bridge Circuits
High Speed Motion
Picture Camera (2)
(HYCAM)
Manual Switch
T1
6 VDC (Bat.)
Driver for HYCAM
Timing Mark LED
110 VAC
Proximity Switch
Marx Generator
X-ray Tubehead
X-ray Control Console
Interlock
R1
High Voltage and
Control Cables
Relay
kV
T3
Trigger
DC Pwr. Supply
R2
D1
Manual Switch
(Momentary Contact)
D2
D3
Timer
T2
MV-1 LS
S
110 VAC
Manual Switch
0010
80 psig argon
Diaphragm Cutter
Piston Actuator
110 VAC
Transformer (110/6 VAC)

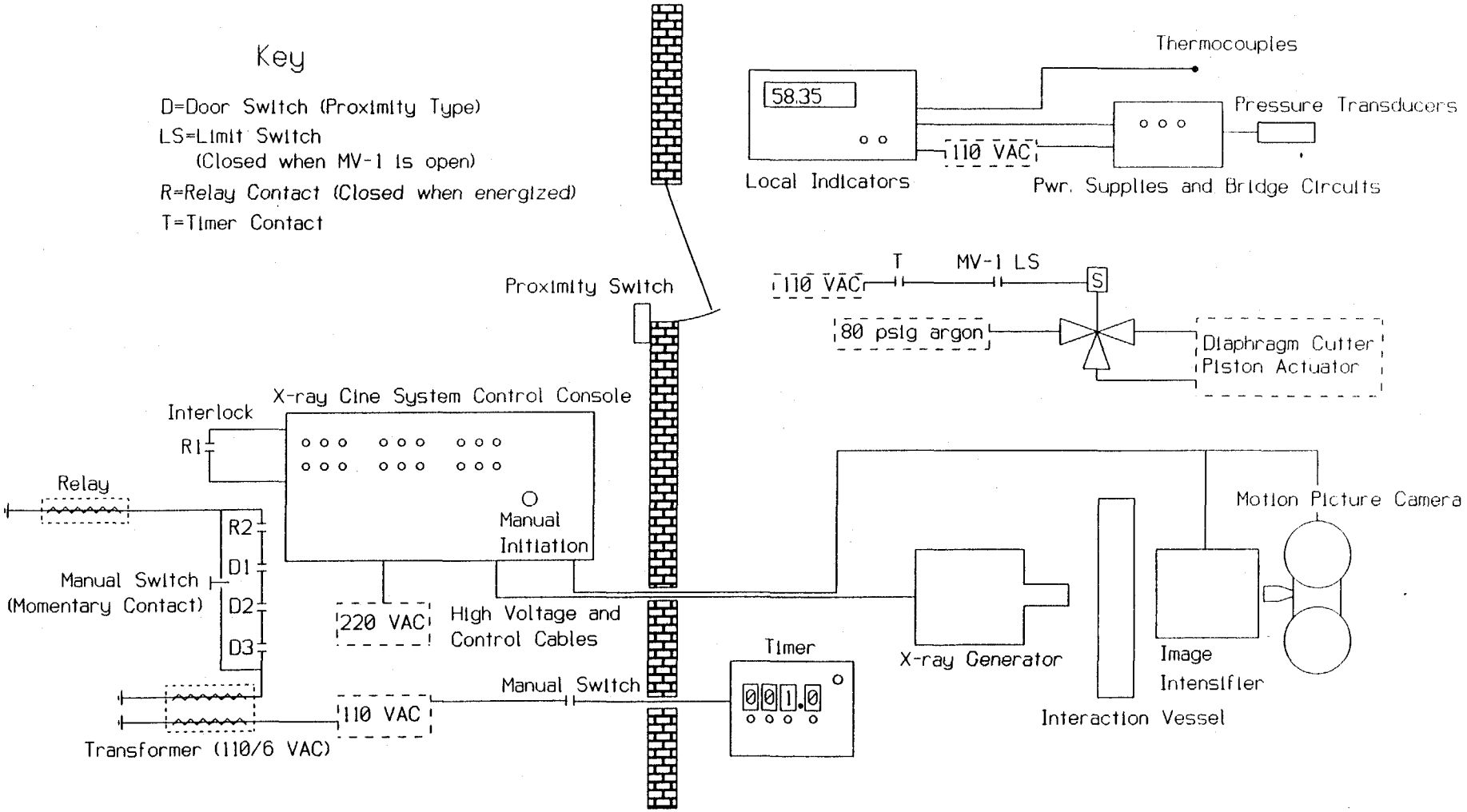
Key
D=Door Switch (Proximity Type)
LS=Limit Switch
(Closed when MV-1 is open)
R=Relay Contact (Closed when energized)
T=Timer Contact
Thermocouples
58.35
Pressure Transducers
110 VAC
Local Indicators
Pwr. Supplies and Bridge Circuits
T
MV-1 LS
S
110 VAC
80 psig argon
Diaphragm Cutter
Piston Actuator
Proximity Switch
X-ray Cine System Control Console
Interlock
R1
Relay
R2
D1
D2
D3
Manual Switch
(Momentary Contact)
Manual
Initiation
220 VAC
High Voltage and
Control Cables
Timer
Manual Switch
X-ray Generator
Motion Picture Camera
Image
Intensifier
Interaction Vessel
110 VAC
Transformer (110/6 VAC)

Test Designation: MFSBS-_____
Date: __-__-__

MFSBS PROCEDURE CHECKLIST

Pre-Test Apparatus Preparations

_____ Switch on electronic cold junctions and check batteries.
_____ Energize furnace heaters.
_____ Cue videotape.
_____ Set up Visicorder
_____ Fill Argon reservoir to 80 psig.
_____ Open low pressure Argon isolation valves.
_____ Verify that MV-1 and 10 are open.
_____ Load furnace with solid particulate metal. When full, spoon out oxide layer. Mount diaphragm cutter. Connect Argon supply hose.
_____ Check that power cords to timer, HYCAMs, Solenoid Valve, and sync. to HYCAM #1 are in place.

Pre-Test X-Ray System Preparations

_____ Open Nitrogen gas cylinder valve.
_____ Set Marx Generator Nitrogen pressure to 25 psig.
_____ Set X-ray time delay as specified in the Test Spec.
_____ Place film cassette on Interaction Vessel and align Xray tube.
_____ Turn on X-ray contr ol cabinet and high voltage power (do not insert key). Check X-ray interlocks. Open each of the three interlocked doors, and verify that the interlock circuit opens. De-energize X-ray cabinet.

Interaction Vessel Fill

_____ Turn on local ventilation blower and fume hood fan.
_____ Raise Freon-11 barrel.
_____ Align valves as follows: MV-2, 4, 8, 9 and 11 closed, others open.
_____ Connect fill/drain and Argon hoses to Freon-11 barrel.
_____ Fill Interaction Vessel, throttling Freon-11 flow into the Interaction Vessel with MV-2.
_____ Close MV-2, 5 and 6.
_____ Lower Freon-11 barrel.

Melt Injection

_____ **Verify TC-1A and B trendicator readings are between 100 and 110 °C and stable or falling.**
_____ Record TC-1A, B and ambient temperatures on Test Spec.
_____ Open MV-8.

_____ Record Interaction Vessel coolant depth (137.5 cm -distance from top of Interaction Vessel) on Test Spec.
_____ Close MV-8.
_____ Attach chilled Freon container and open MV-9 and 11.
_____ Energize floodlights. Check positioning.
_____ De-energize furnace heaters.
_____ **Evacuate Room C-111.**
_____ Start video recording.
_____ Close interlock circuit.
_____ Turn on X-ray cabinet power.
_____ Insert key.
_____ Turn on key switch.
_____ Turn on POWER switch.
_____ Turn the HIGH VOLTAGE CONTROL to zero.
_____ Press the HIGH VOLTAGE ON button on the high voltage power supply and advance the HIGH VOLTAGE CONTROL until the meter reads 30 kV.
_____ Manually start Visicorder.
_____ Manually start HYCAMs.
_____ Manually energize timer for melt injection and X-ray delay generator start.
_____ Turn off POWER switch.
_____ Turn off key switch and remove key.
_____ Turn X-ray control cabinet power off.
_____ Re-enter Rm. C-111. De-energize floodlights.
_____ Close MV-11 and remove chilled Freon container.

Interaction Vessel Drain

_____ Open MV-5 and 6.
_____ Open MV-2 to drain Interaction Vessel
_____ Close MV-2, 5 and 6.
_____ Disconnect hoses from Freon-11 barrel.
_____ Isolate low pressure Argon supply.
_____ Open MV-4 and 8.
_____ Turn off local ventilation blower and fume hood fan.
_____ Close X-ray Nitrogen cylinder valve.

Test Specification

Nozzle diameter: ____ 0.25" ____ 0.50" ____ 0.75" ____ 1.0" ____ "
X-ray time delay (seconds): ____
X-ray cassette location:

Freon-11 liquid depth (cm): ____
Melt temperature (°C): TC-1A ____ TC-1B ____ TC-1C ____
Ambient temperature (°C): ____

Special Test Objectives
1. _____
2. _____

Configuration Changes Since Previous Test
1. _____
2. _____

Selected Test Results

Melt entry velocity (from HYCAM film) (m/s): ____
Breakup Length (from HYCAM film) (cm): ____

Debris sifting data (mass, g / %)
> 9.50 mm: ____/____
> 4.75: ____/____
> 2.36: ____/____
> 1.19: ____/____
> 0.85: ____/____
> 0.59: ____/____
< 0.59: ____/____
Total: ____/____

Comments

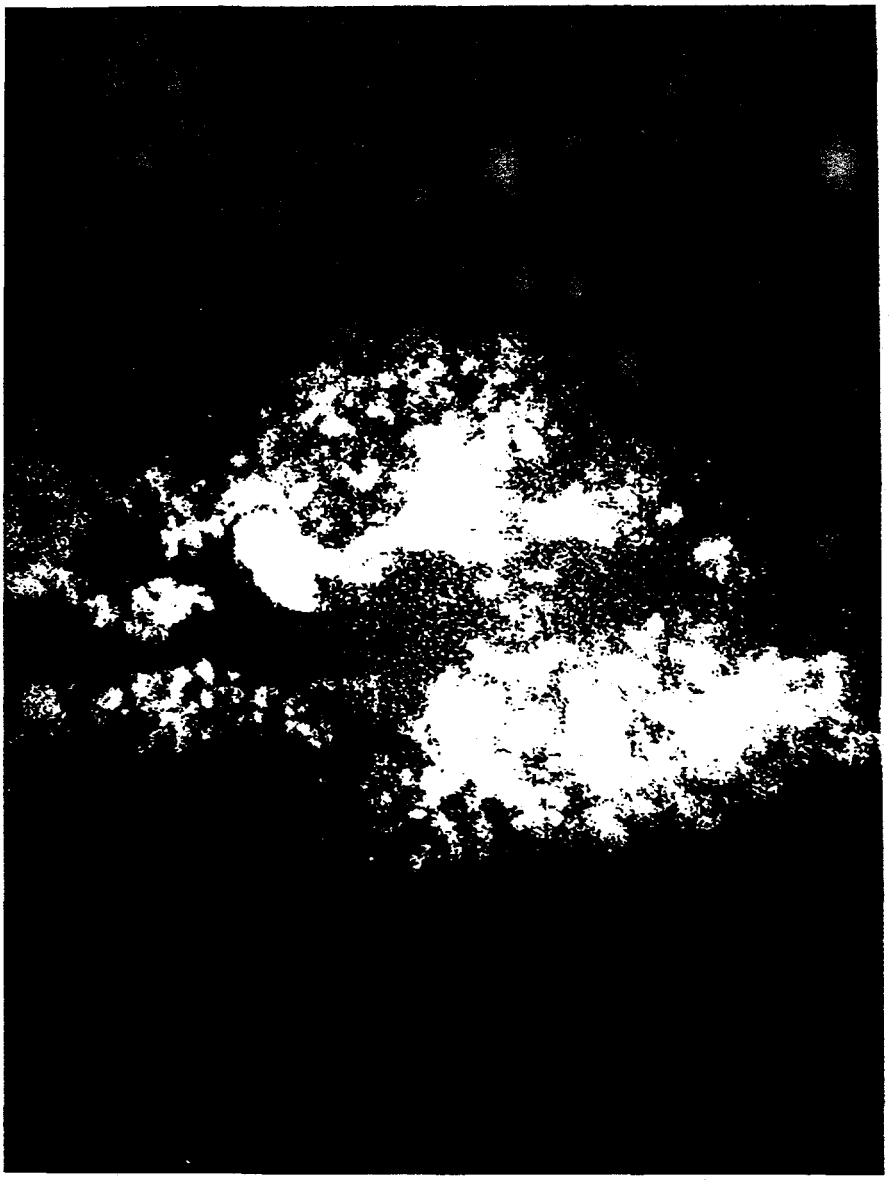

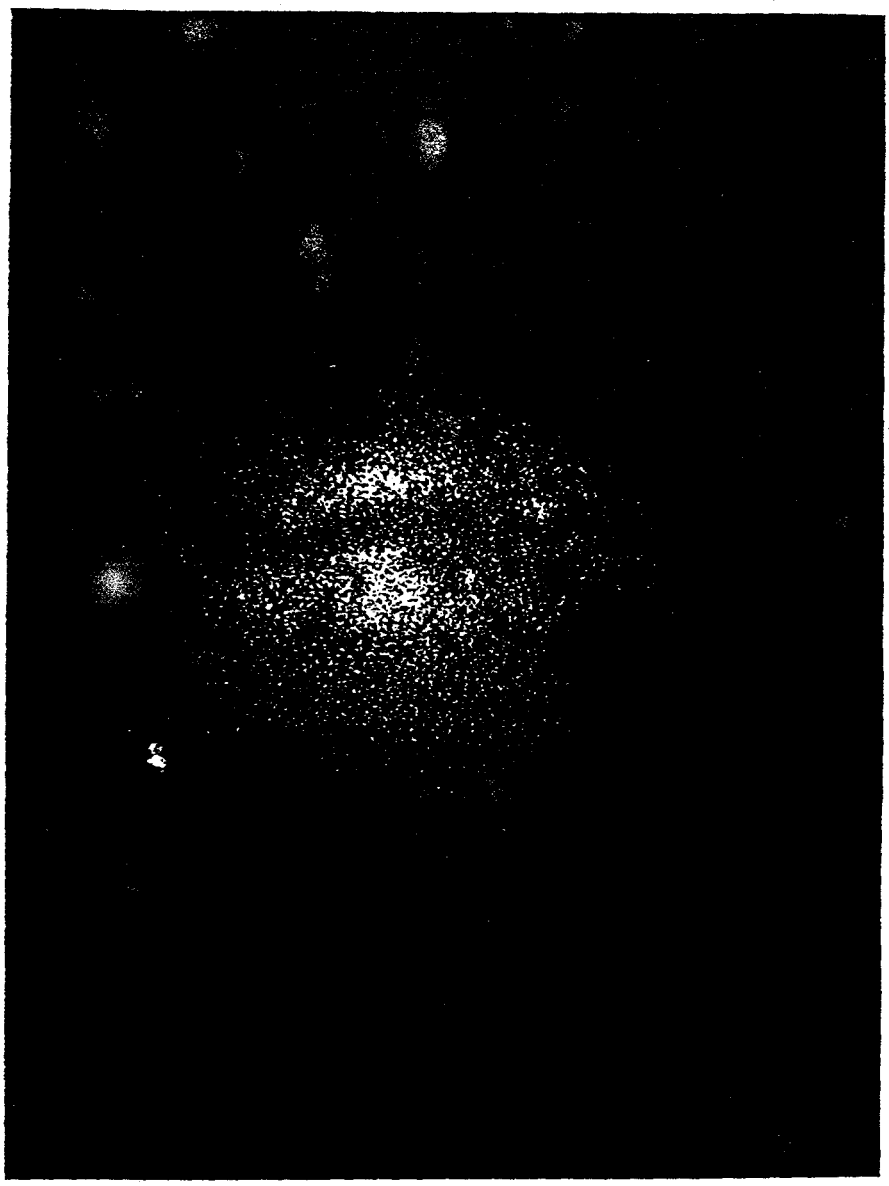

BED17, PSG
PSD

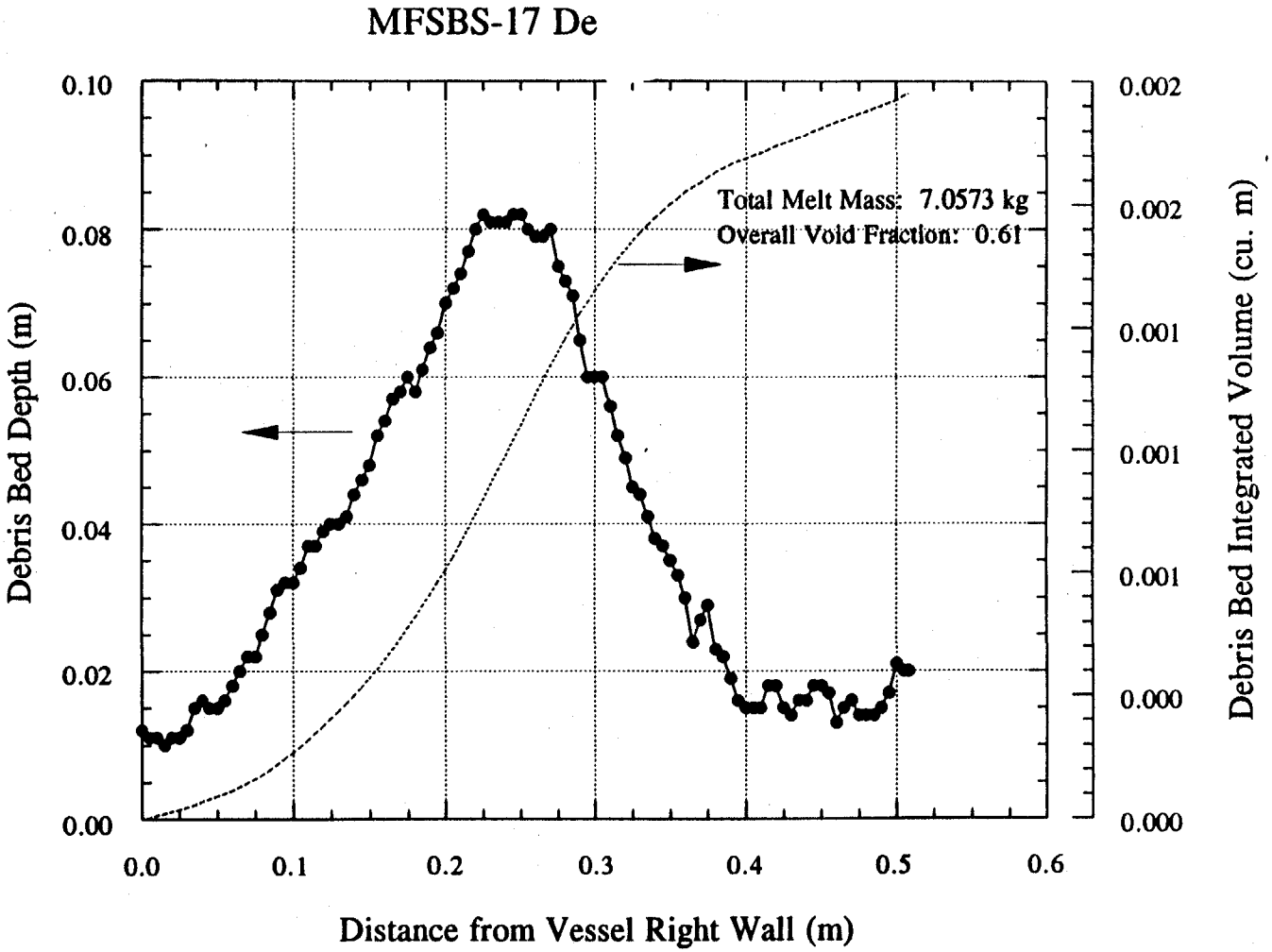

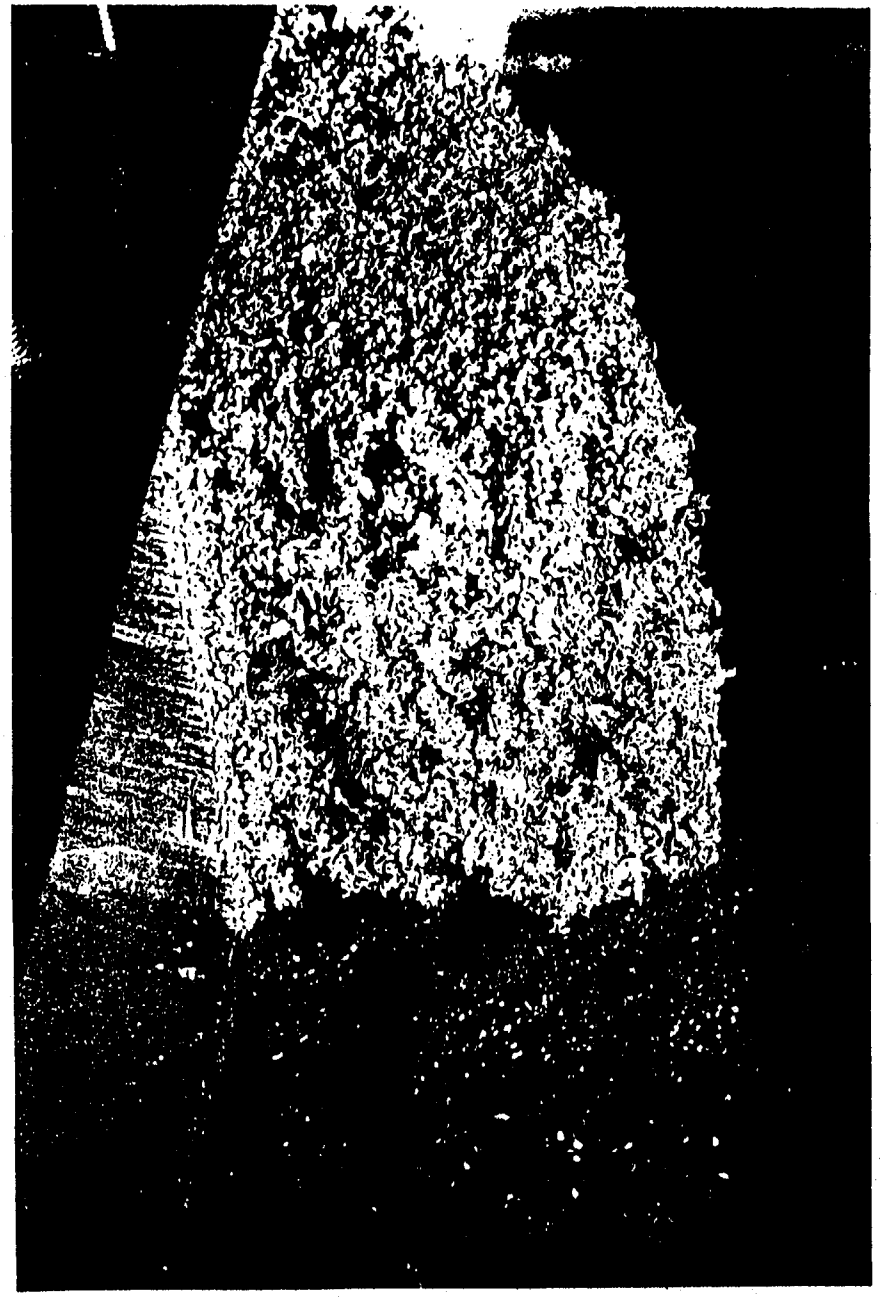

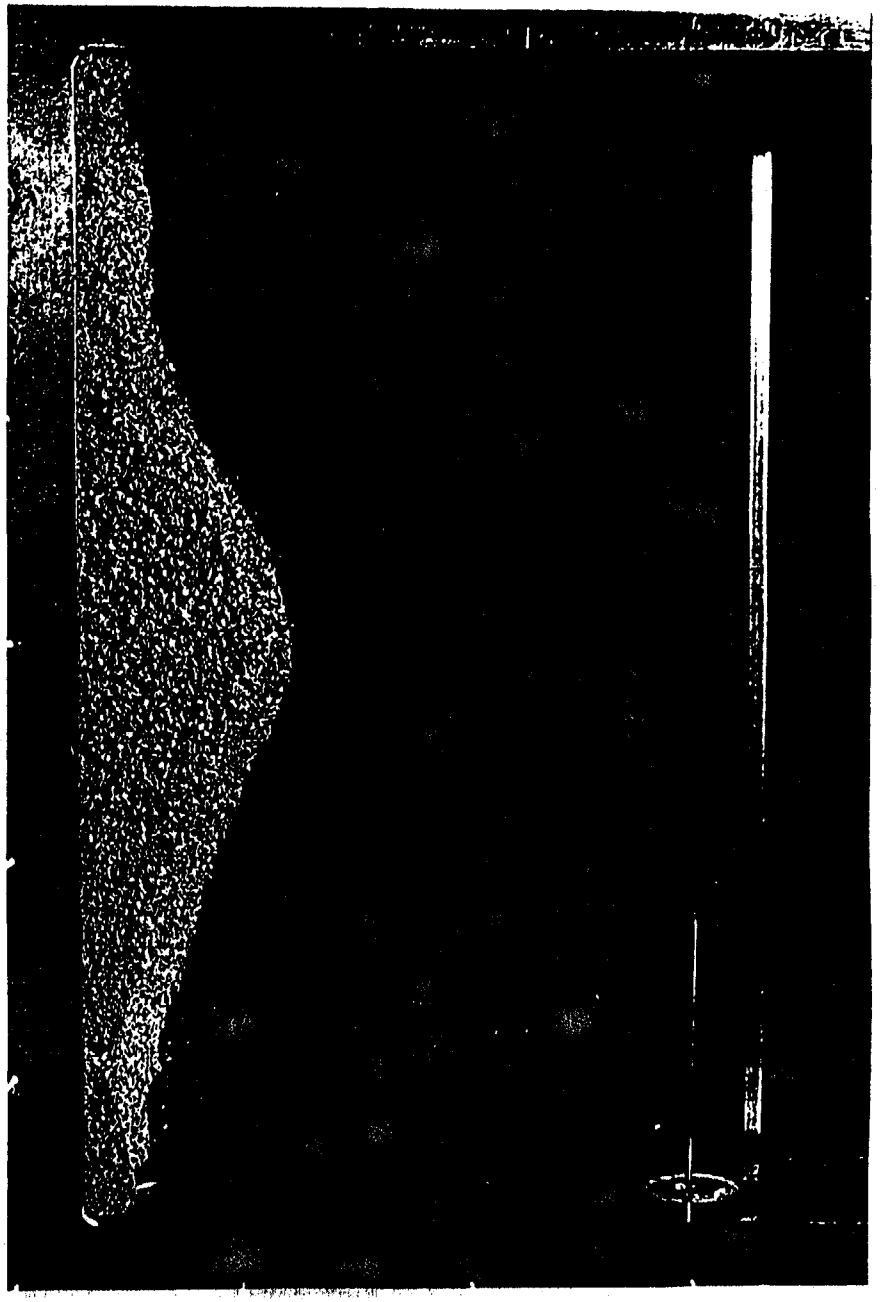

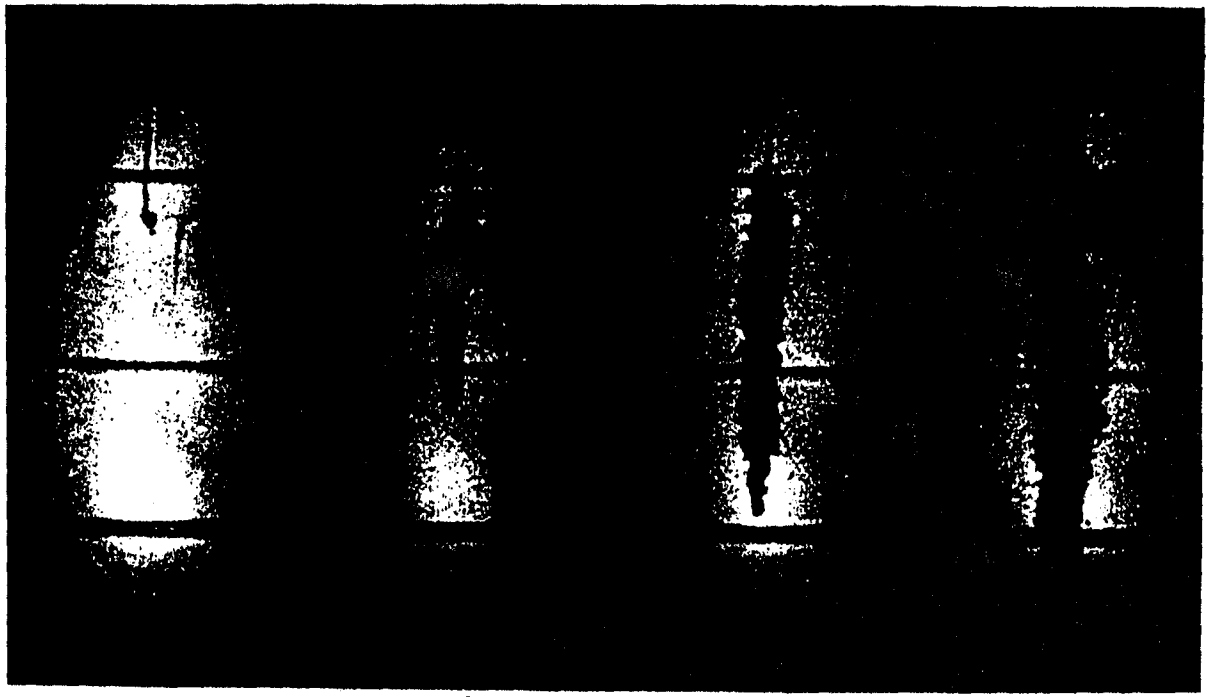

0 ms 126 ms 215 ms 1212 ms

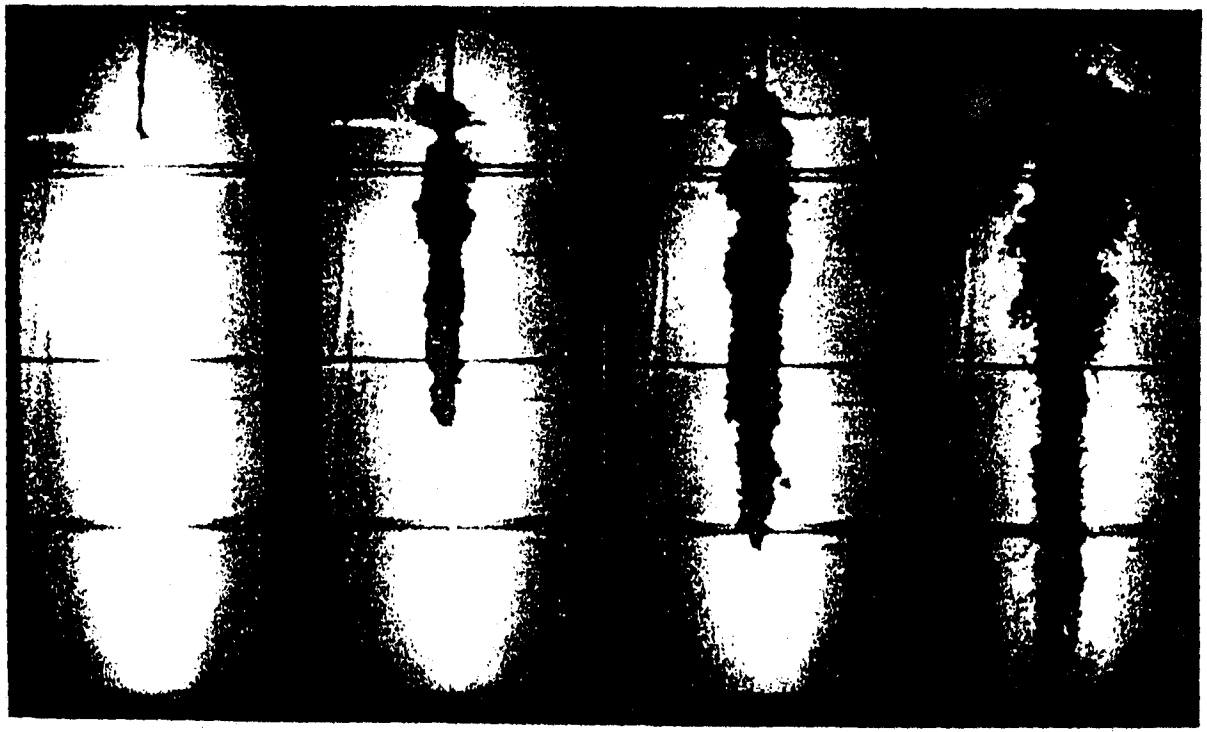

0 ms 200 ms 315 ms 1084 ms

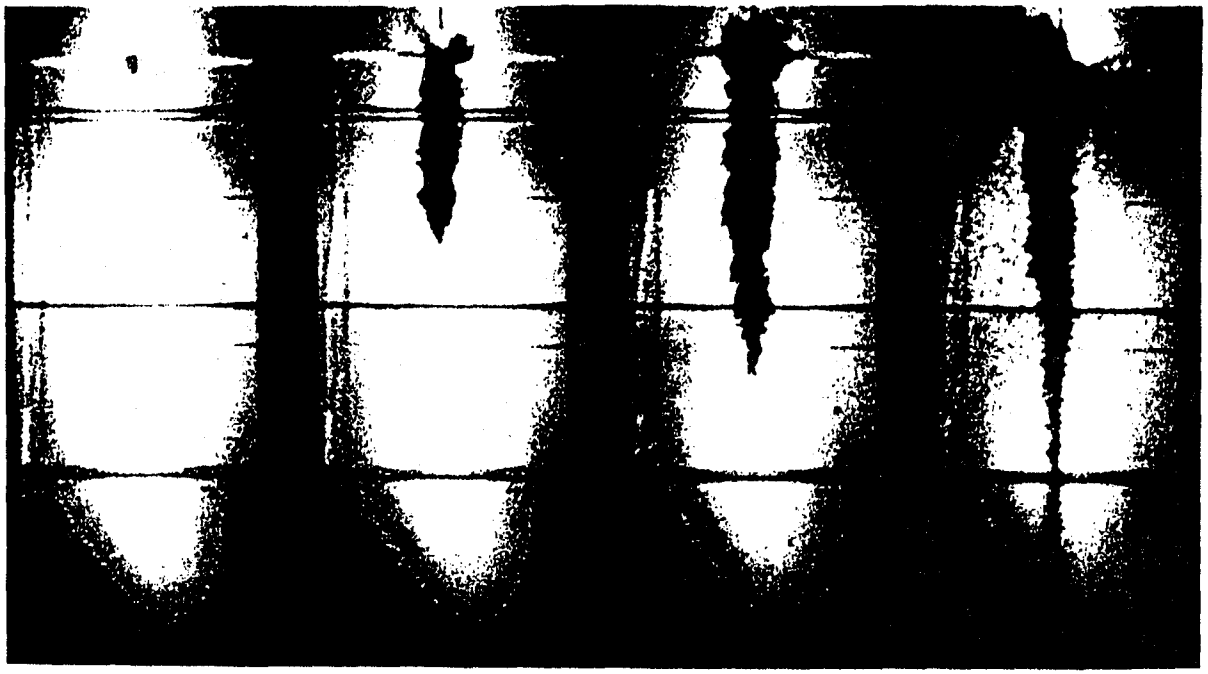

0 ms 198 ms 335 ms 2540 ms

0 ms 206 ms 375 ms 2026 ms

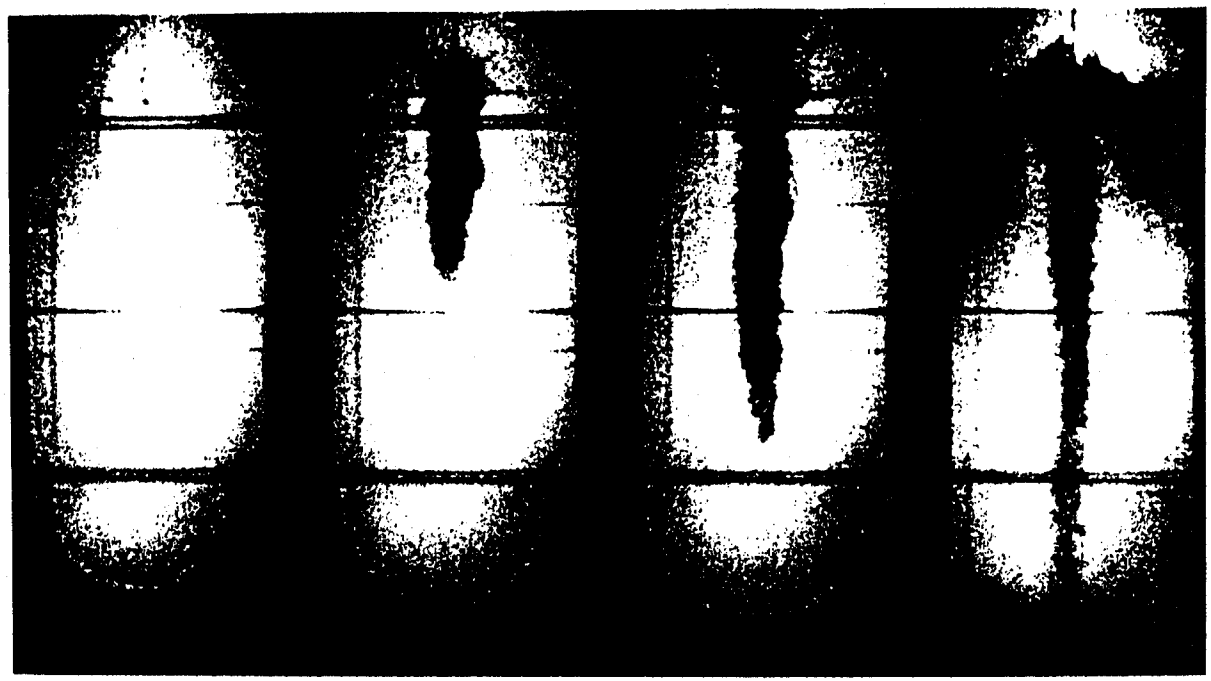

0 ms 254 ms 445 ms 2120 ms

538 ms 760 ms 875 ms 2090 ms

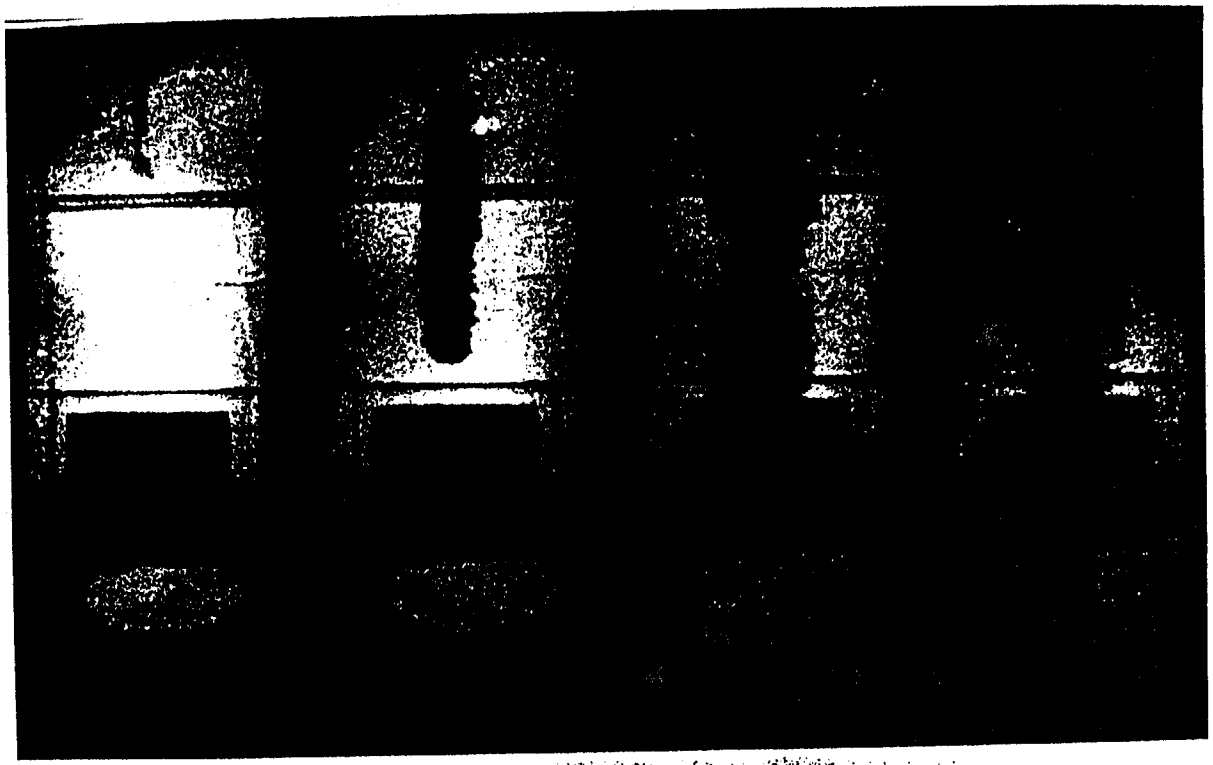

434 ms 604 ms 915 ms 1580 ms

420 ms 600 ms 765 ms 1918 ms

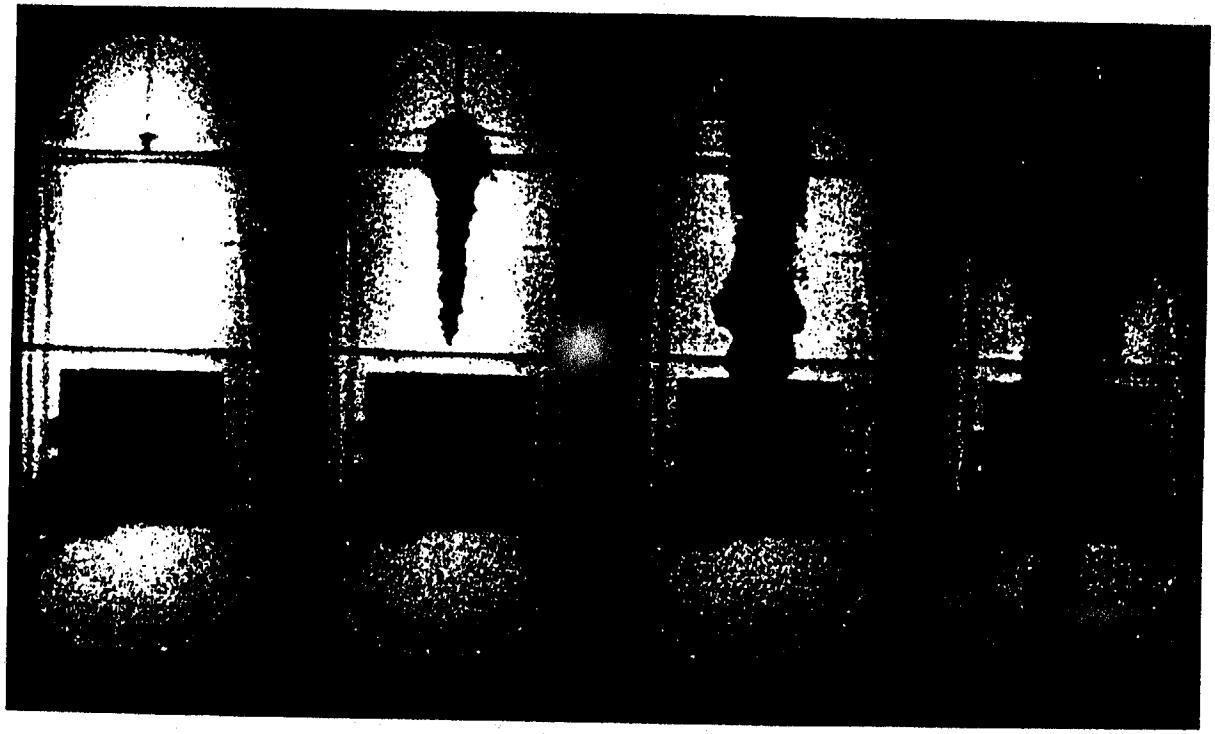

416 ms 518 ms 720 ms 1344 ms

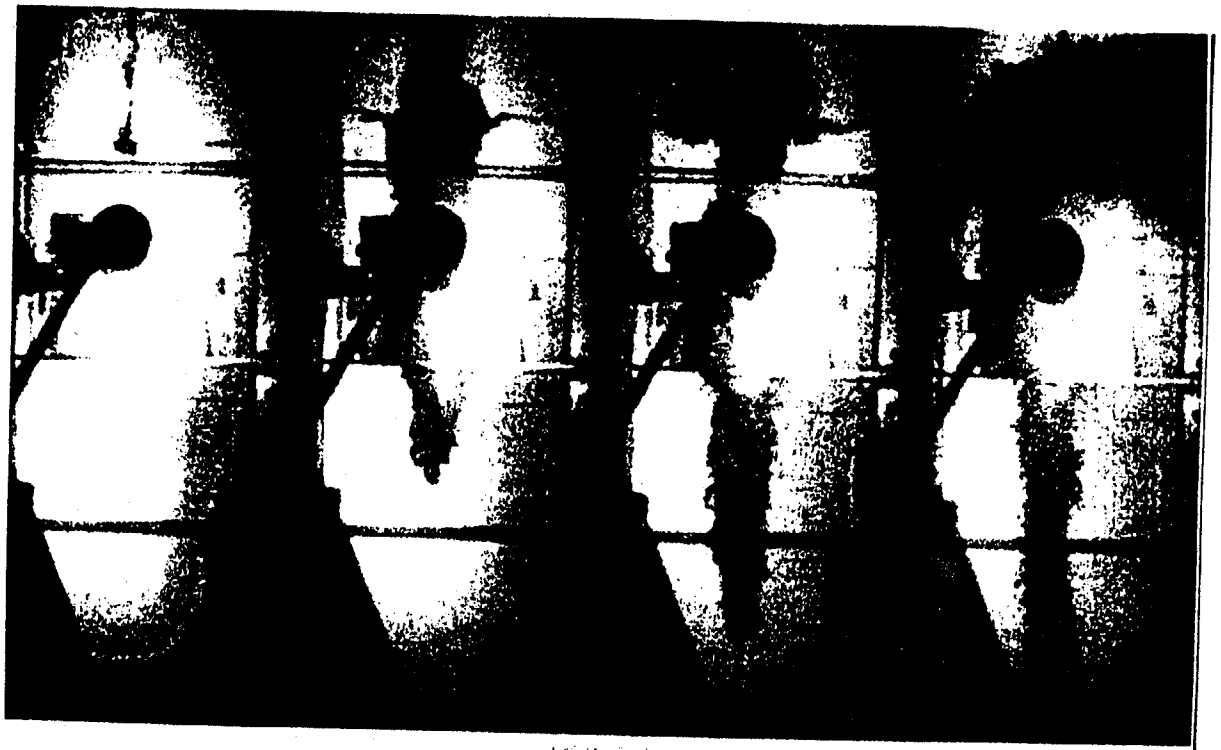

448 ms 666 ms 895 ms 1286 ms

406 ms 540 ms 630 ms 1932 ms

458 ms 650 ms 870 ms 1394 ms

816 ms 1020 ms 1190 ms 2222 ms

462 ms 620 ms 796 ms 1496 ms

368 ms 524 ms 855 ms 1998 ms

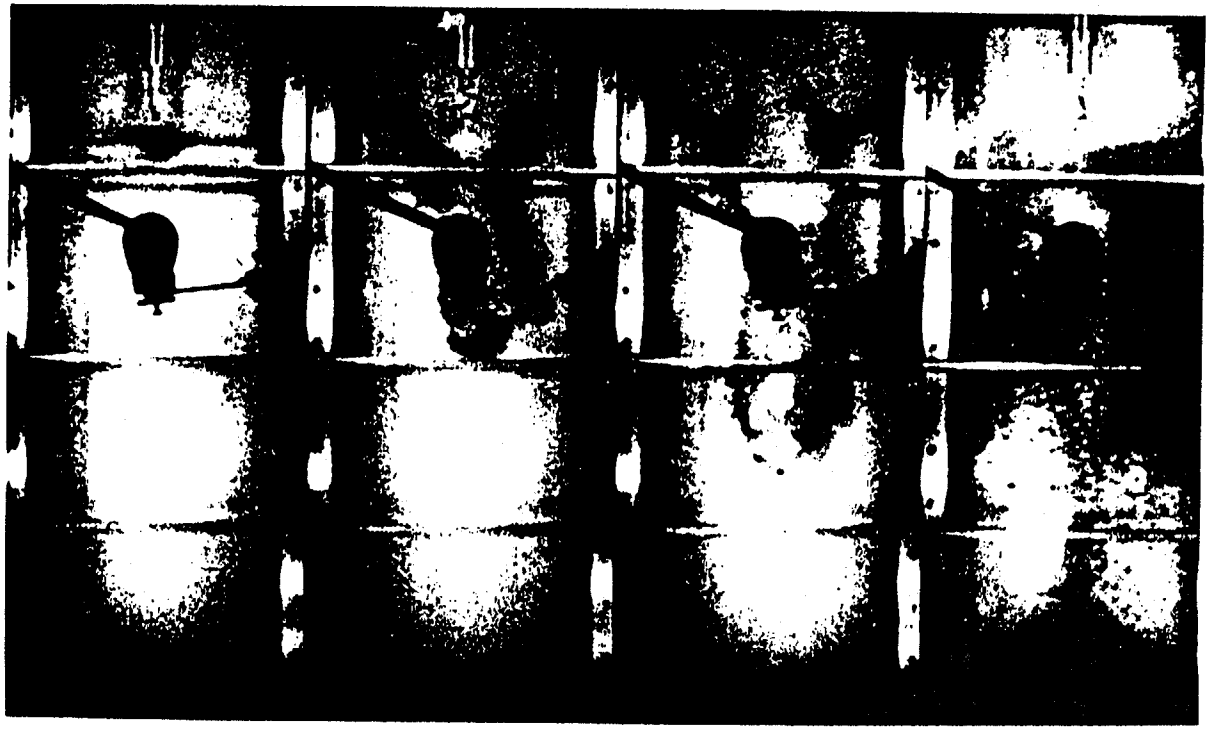

442 ms 610 ms 760 ms 2026 ms

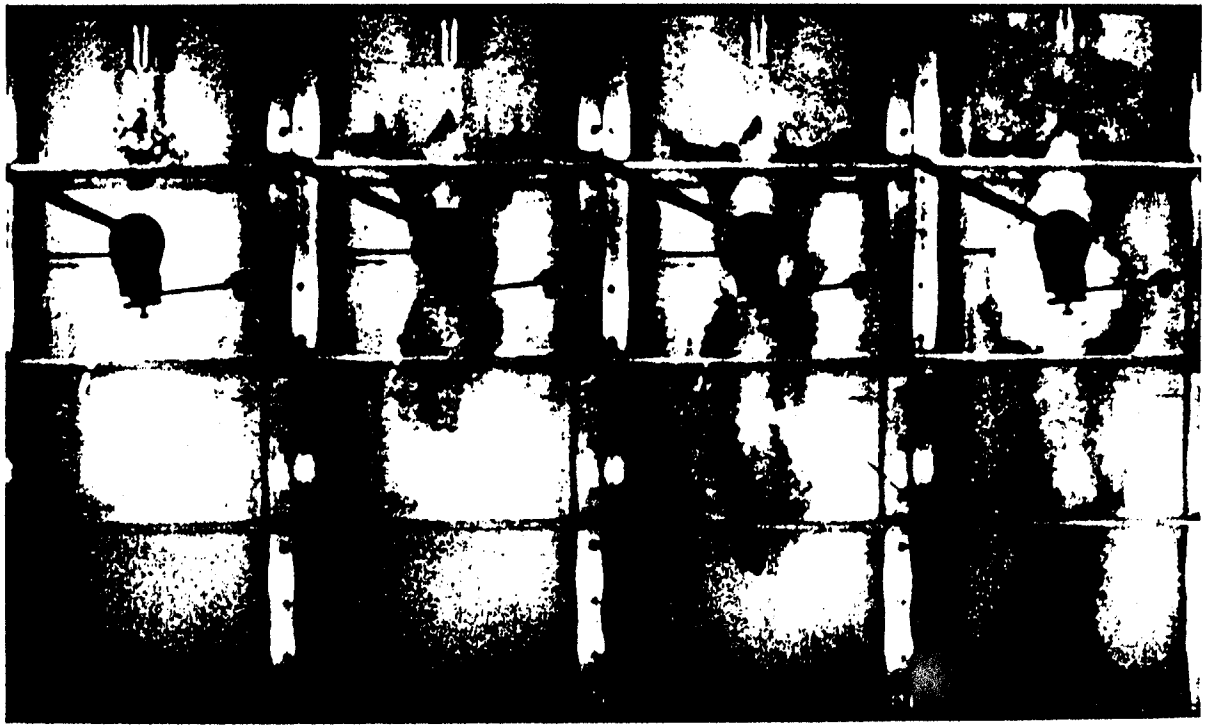

416 ms 588 ms 700 ms 1116 ms

400 ms 460 ms 495 ms 968 ms

410 ms 460 ms 495 ms 1398 ms

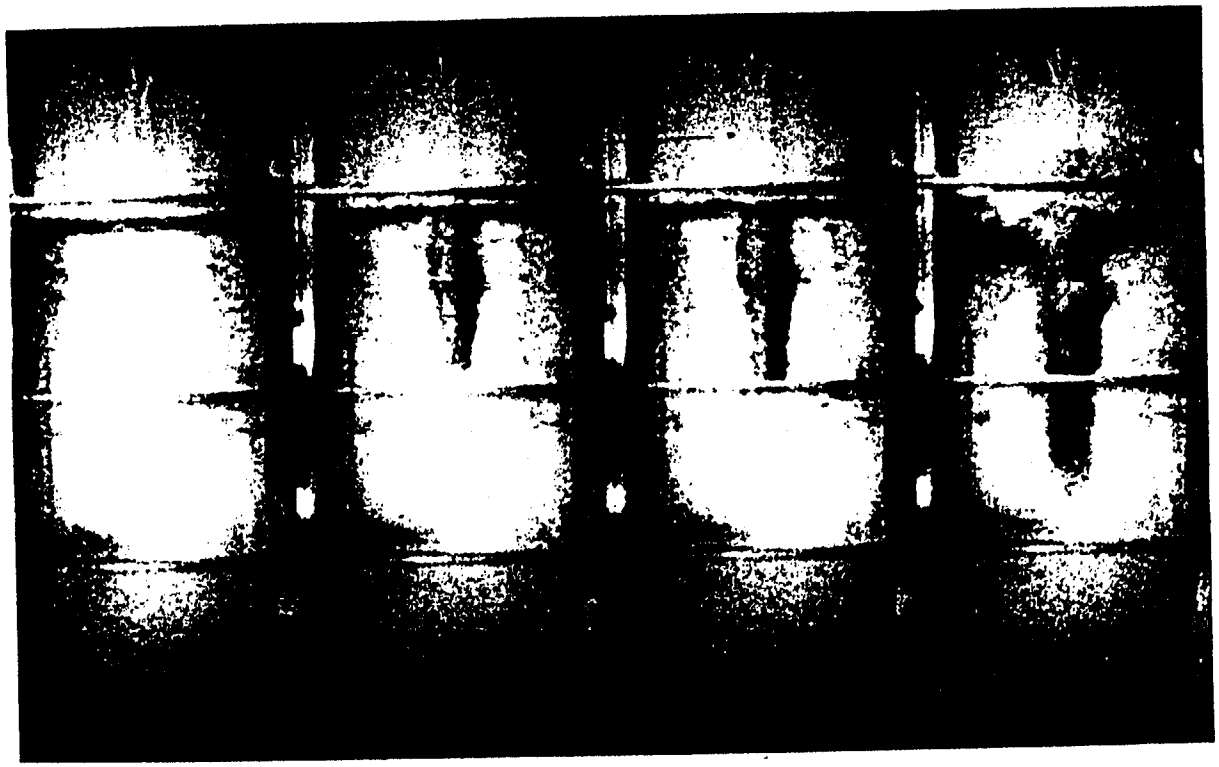

302 ms 386 ms 420 ms 1158 ms

NSMHDXX.PSG

FILENAME

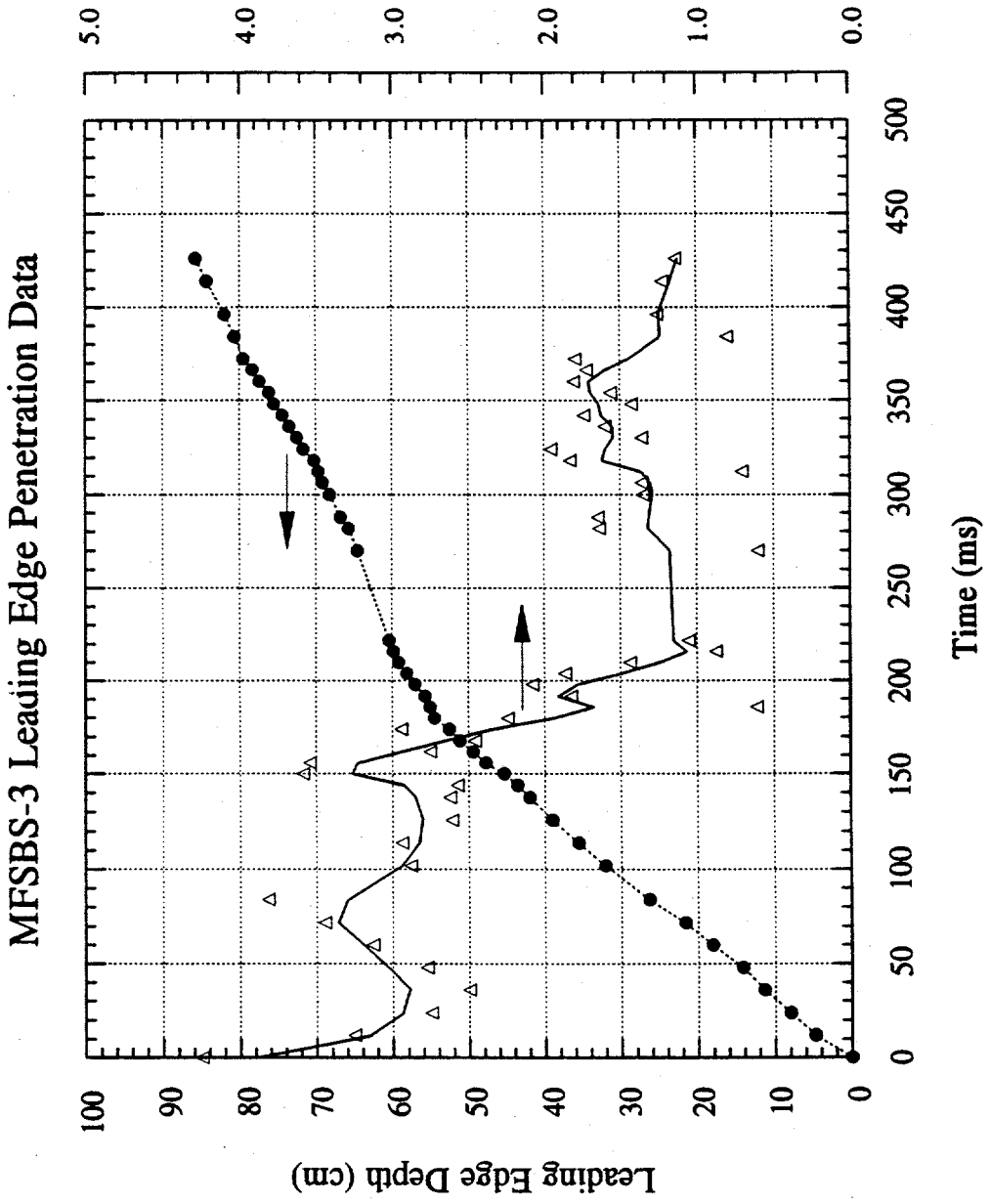

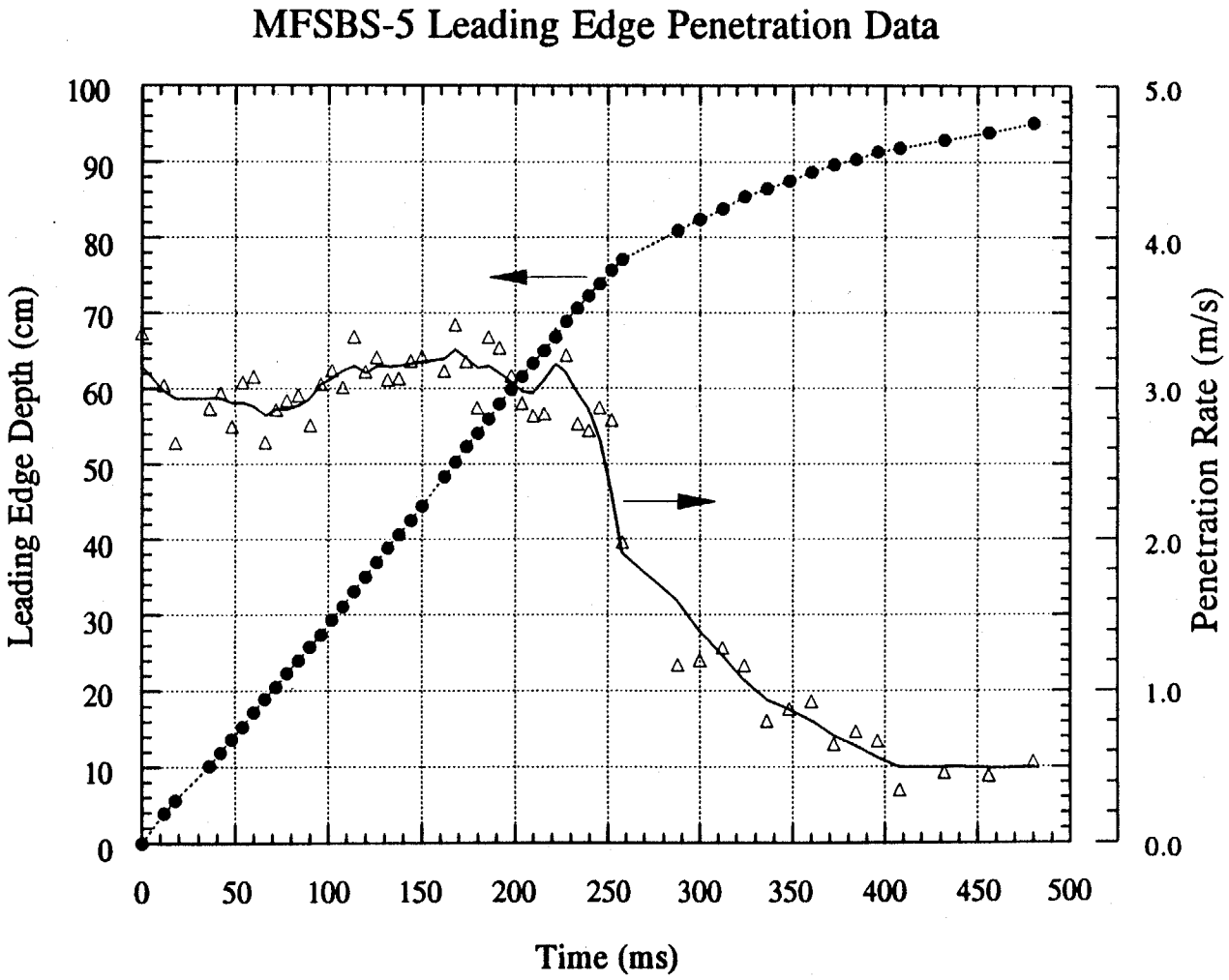
MFSBS-5 Leading Edge Penetration Data
Leading Edge Depth (cm)
Penetration Rate (m/s)
Time (ms)
0
10
20
30
40
50
60
70
80
90
100
0.0
1.0
2.0
3.0
4.0
5.0
0
50
100
150
200
250
300
350
400
450
500

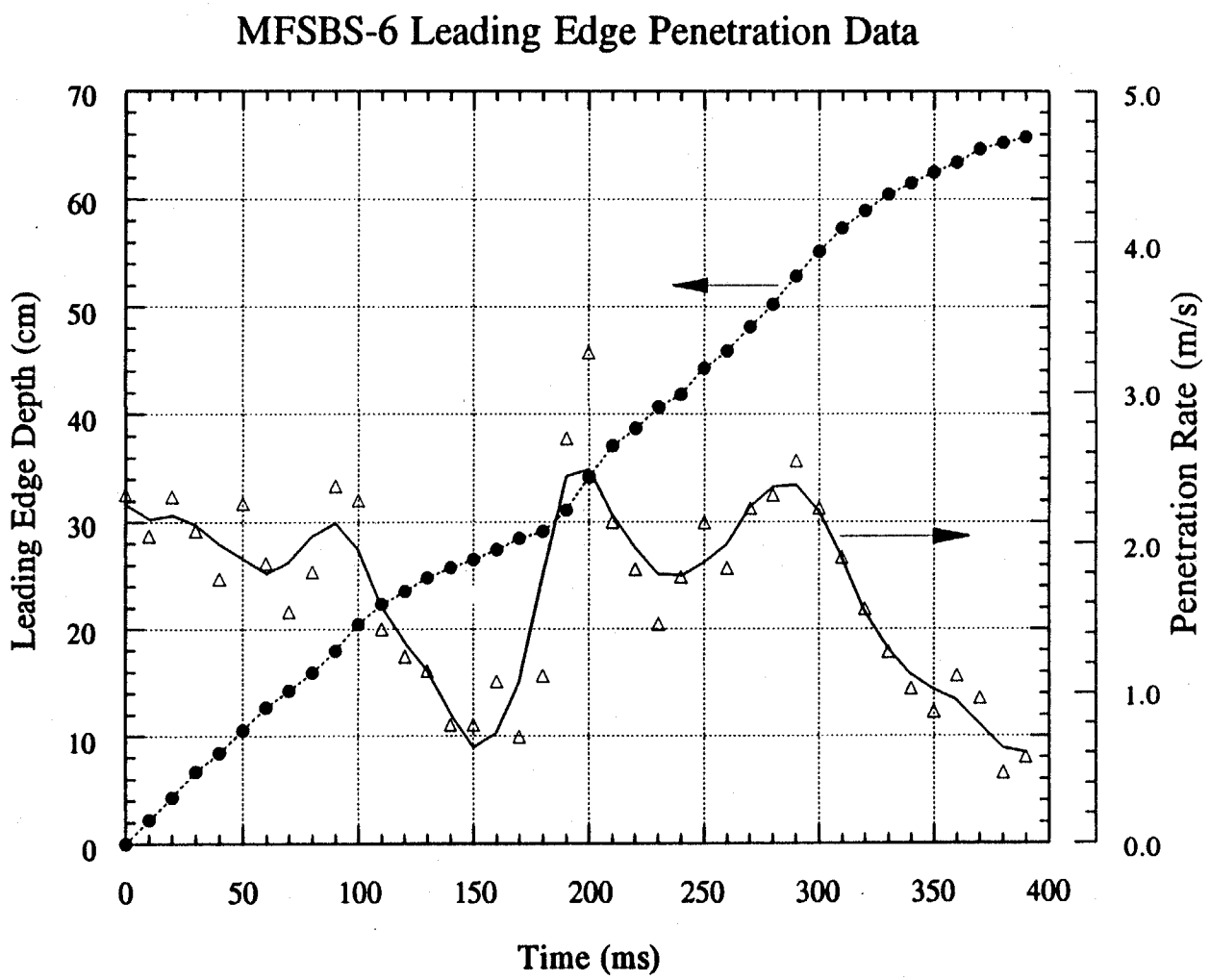
MFSBS-6 Leading Edge Penetration Data
Leading Edge Depth (cm)
Penetration Rate (m/s)
Time (ms)
0
10
20
30
40
50
60
70
0.0
1.0
2.0
3.0
4.0
5.0
0
50
100
150
200
250
300
350
400

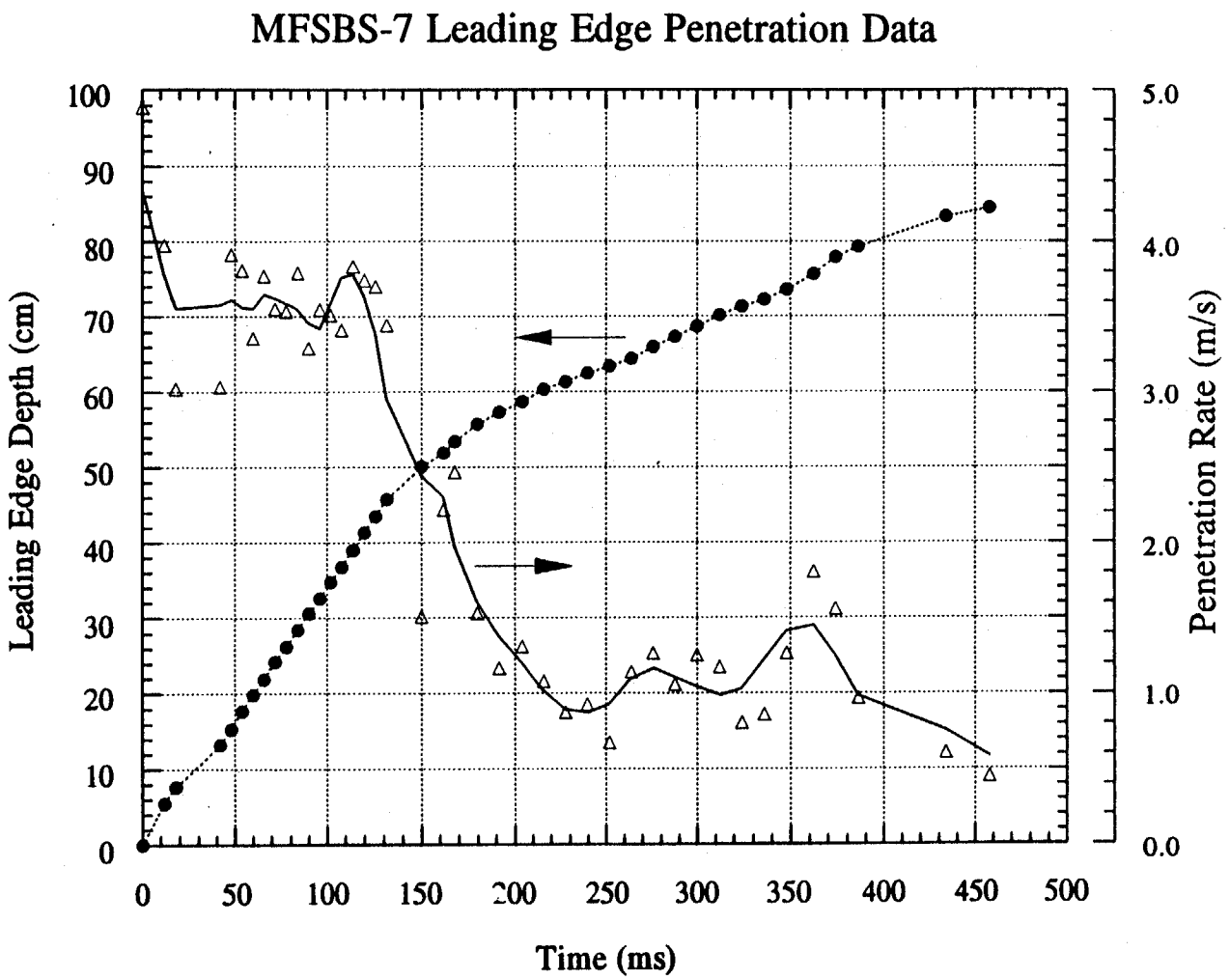
MFSBS-7 Leading Edge Penetration Data
Leading Edge Depth (cm)
Penetration Rate (m/s)
Time (ms)
0
10
20
30
40
50
60
70
80
90
100
0.0
1.0
2.0
3.0
4.0
5.0
0
50
100
150
200
250
300
350
400
450
500

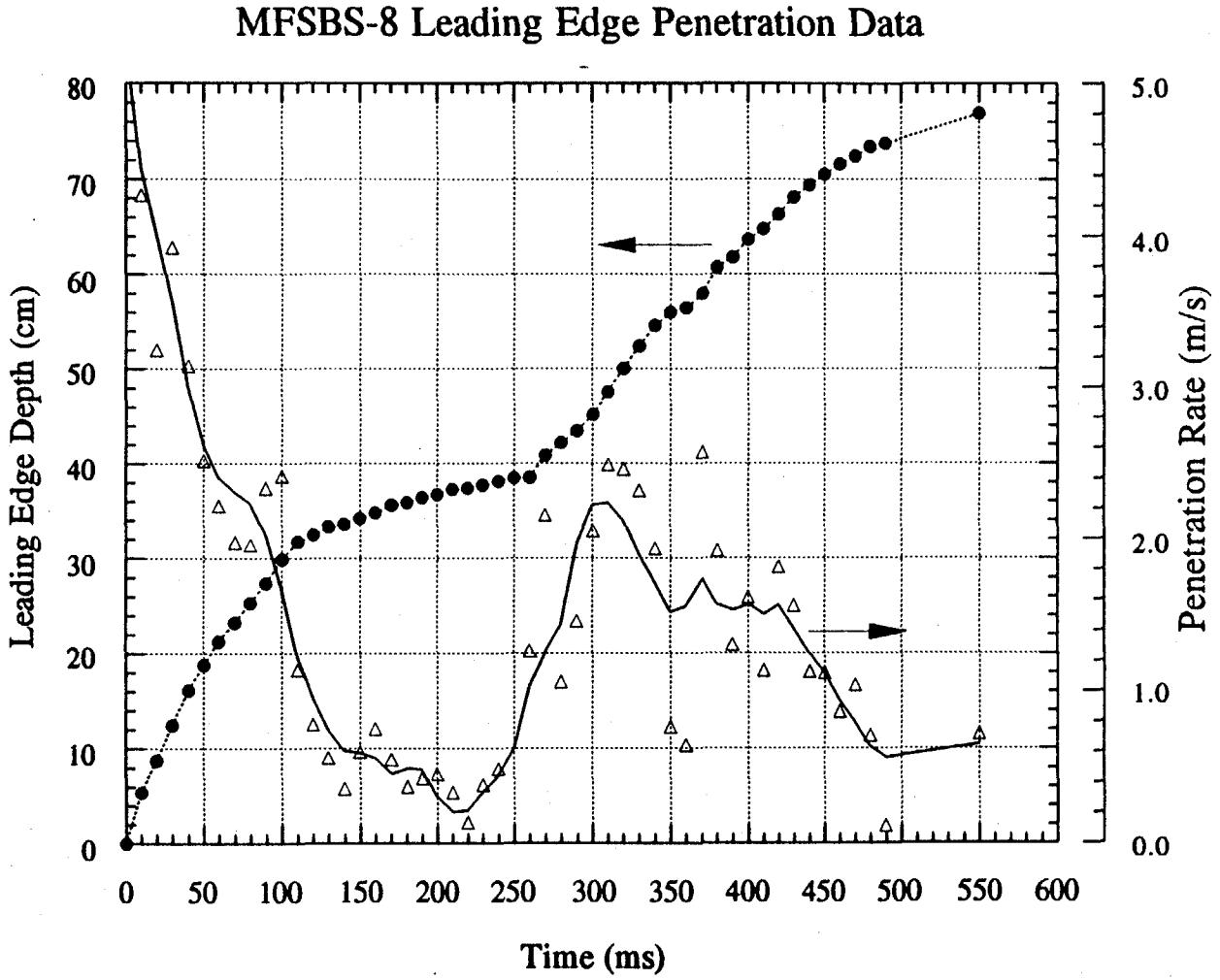
MFSBS-8 Leading Edge Penetration Data
Leading Edge Depth (cm)
Penetration Rate (m/s)
Time (ms)
0
10
20
30
40
50
60
70
80
0.0
1.0
2.0
3.0
4.0
5.0
0
50
100
150
200
250
300
350
400
450
500
550
600

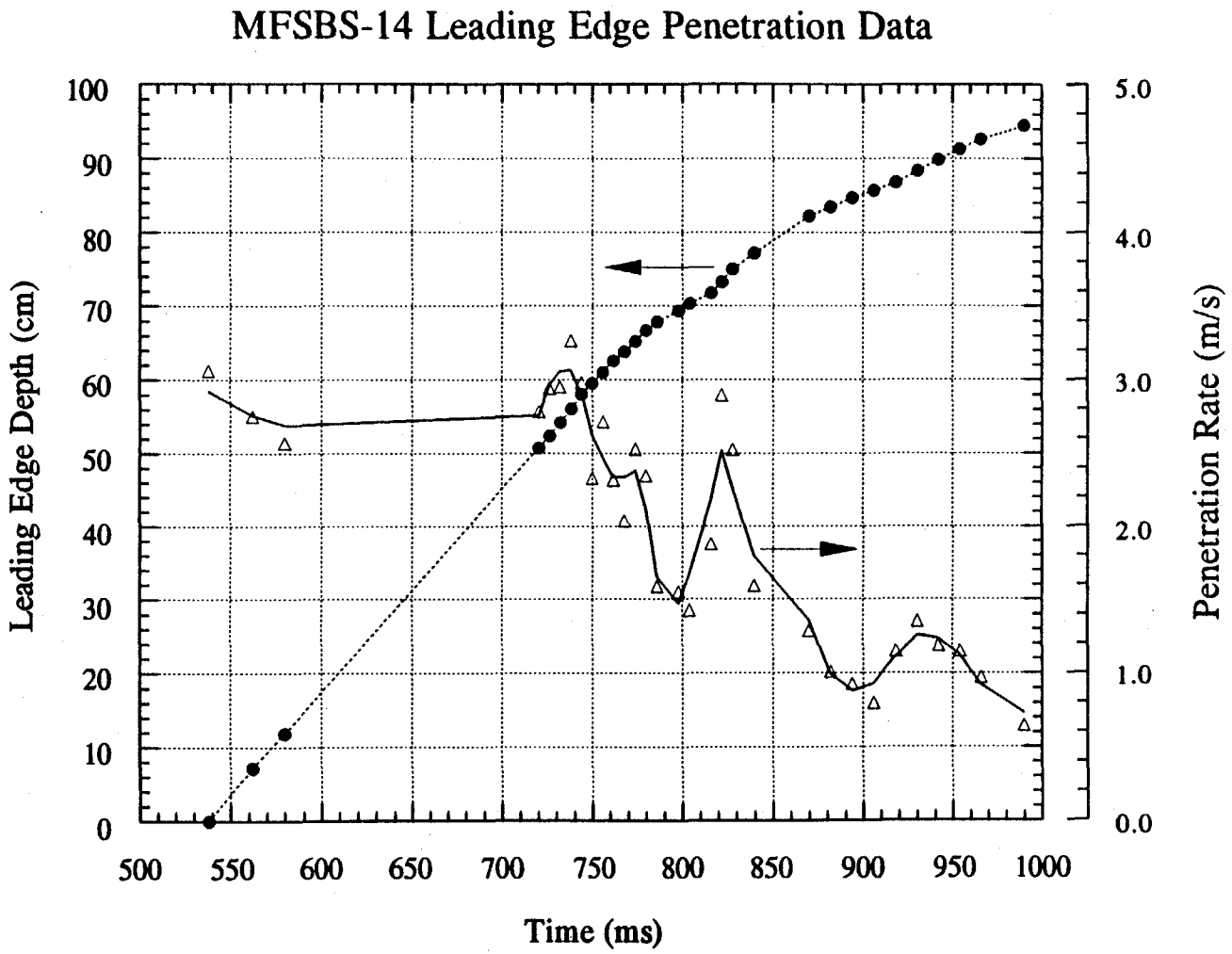
MFSBS-14 Leading Edge Penetration Data
Leading Edge Depth (cm)
Penetration Rate (m/s)
Time (ms)
100
90
80
70
60
50
40
30
20
10
0
5.0
4.0
3.0
2.0
1.0
0.0
500
550
600
650
700
750
800
850
900
950
1000

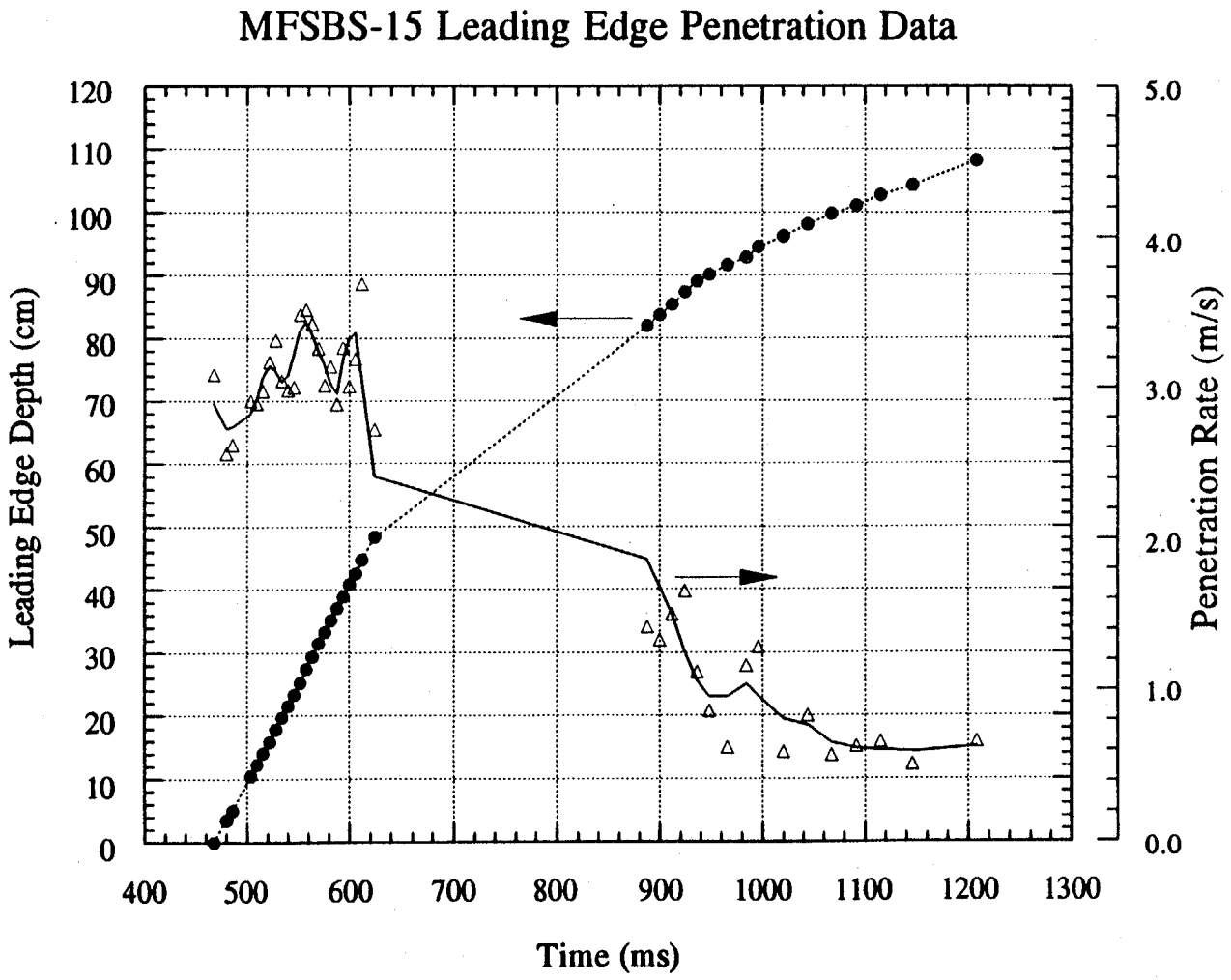
MFSBS-15 Leading Edge Penetration Data
Leading Edge Depth (cm)
Penetration Rate (m/s)
Time (ms)
0
10
20
30
40
50
60
70
80
90
100
110
120
0.0
1.0
2.0
3.0
4.0
5.0
400
500
600
700
800
900
1000
1100
1200
1300

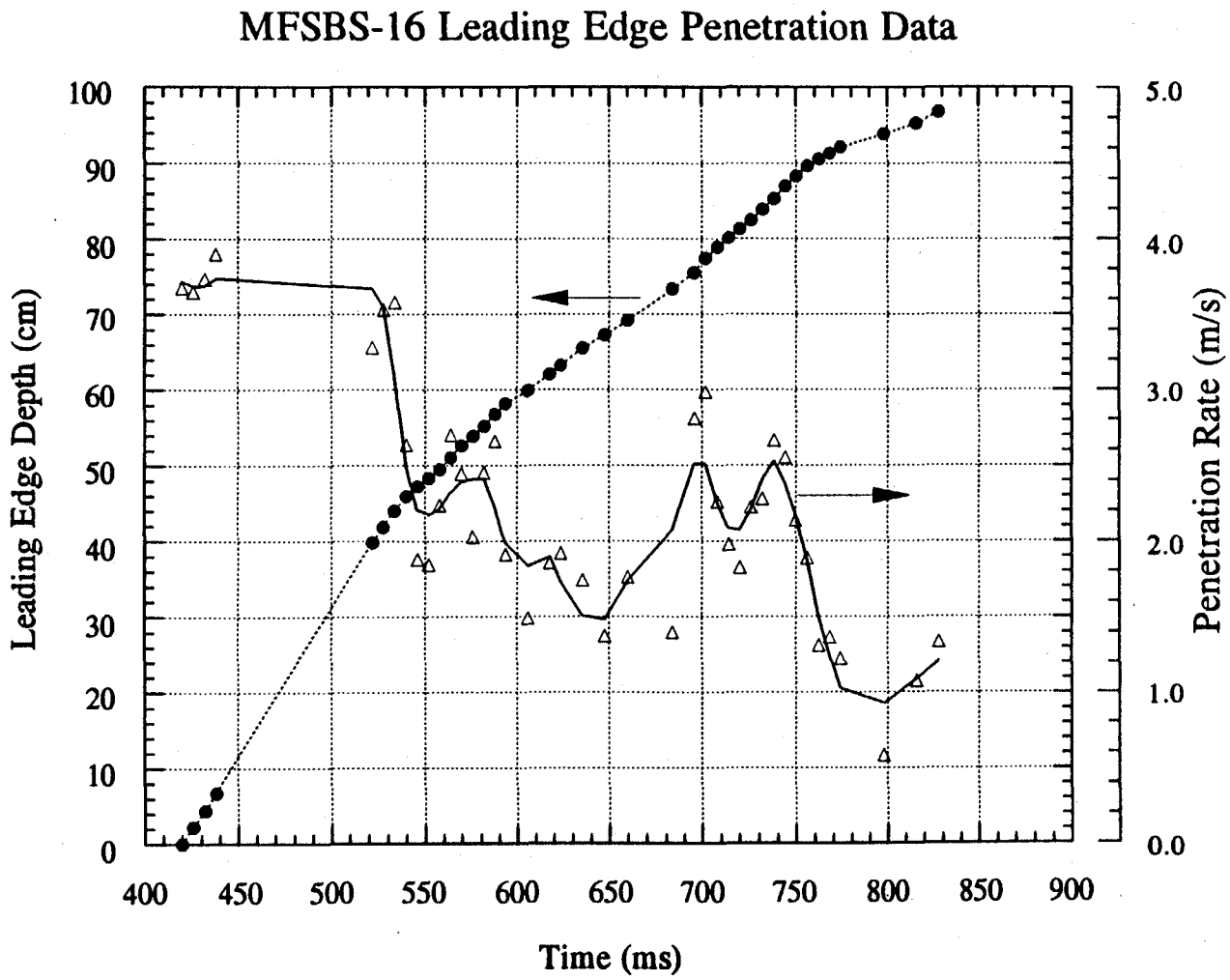
MFSBS-16 Leading Edge Penetration Data
Leading Edge Depth (cm)
Penetration Rate (m/s)
Time (ms)
0
10
20
30
40
50
60
70
80
90
100
0.0
1.0
2.0
3.0
4.0
5.0
400
450
500
550
600
650
700
750
800
850
900

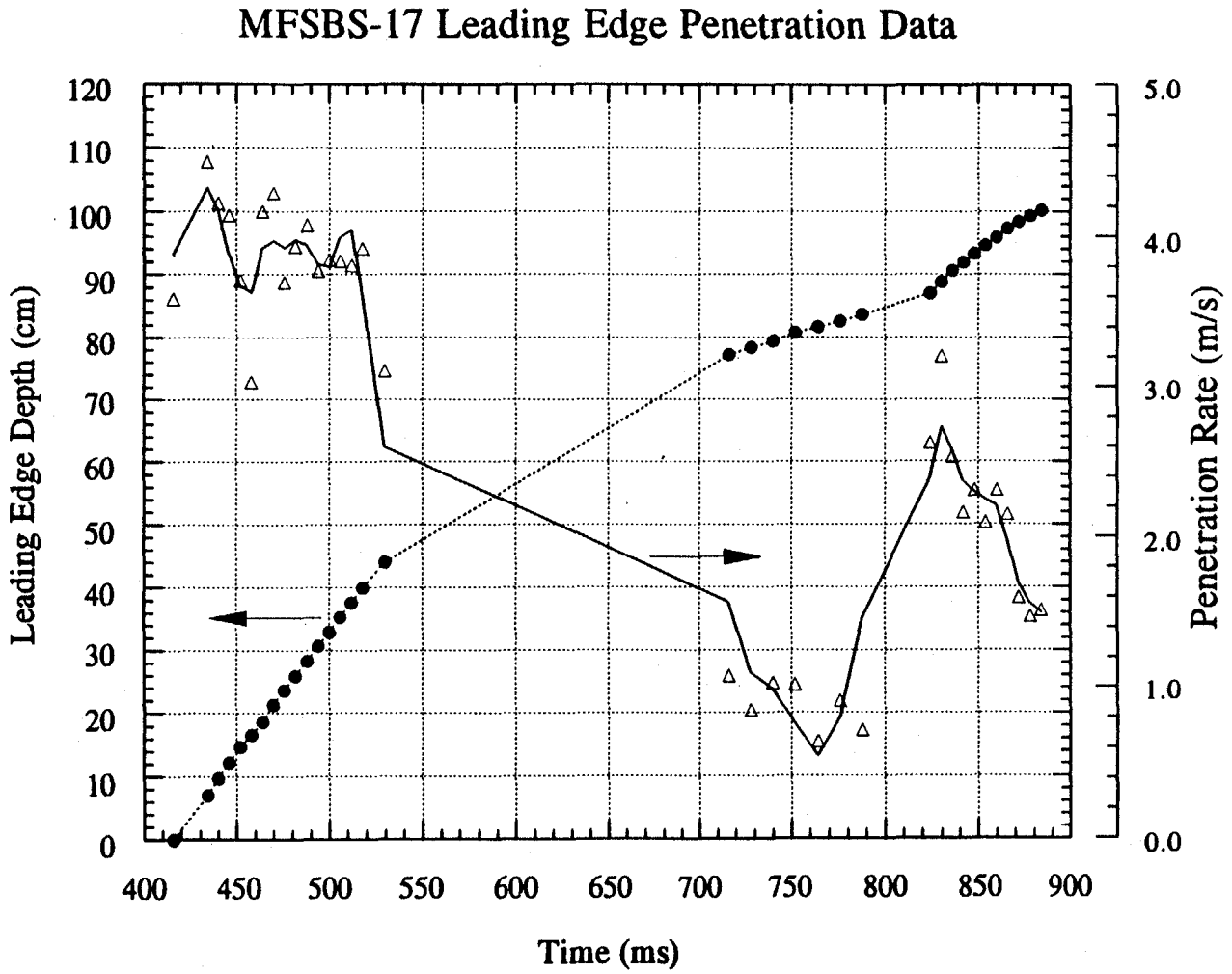
MFSBS-17 Leading Edge Penetration Data
Leading Edge Depth (cm)
Penetration Rate (m/s)
Time (ms)
0
10
20
30
40
50
60
70
80
90
100
110
120
0.0
1.0
2.0
3.0
4.0
5.0
400
450
500
550
600
650
700
750
800
850
900

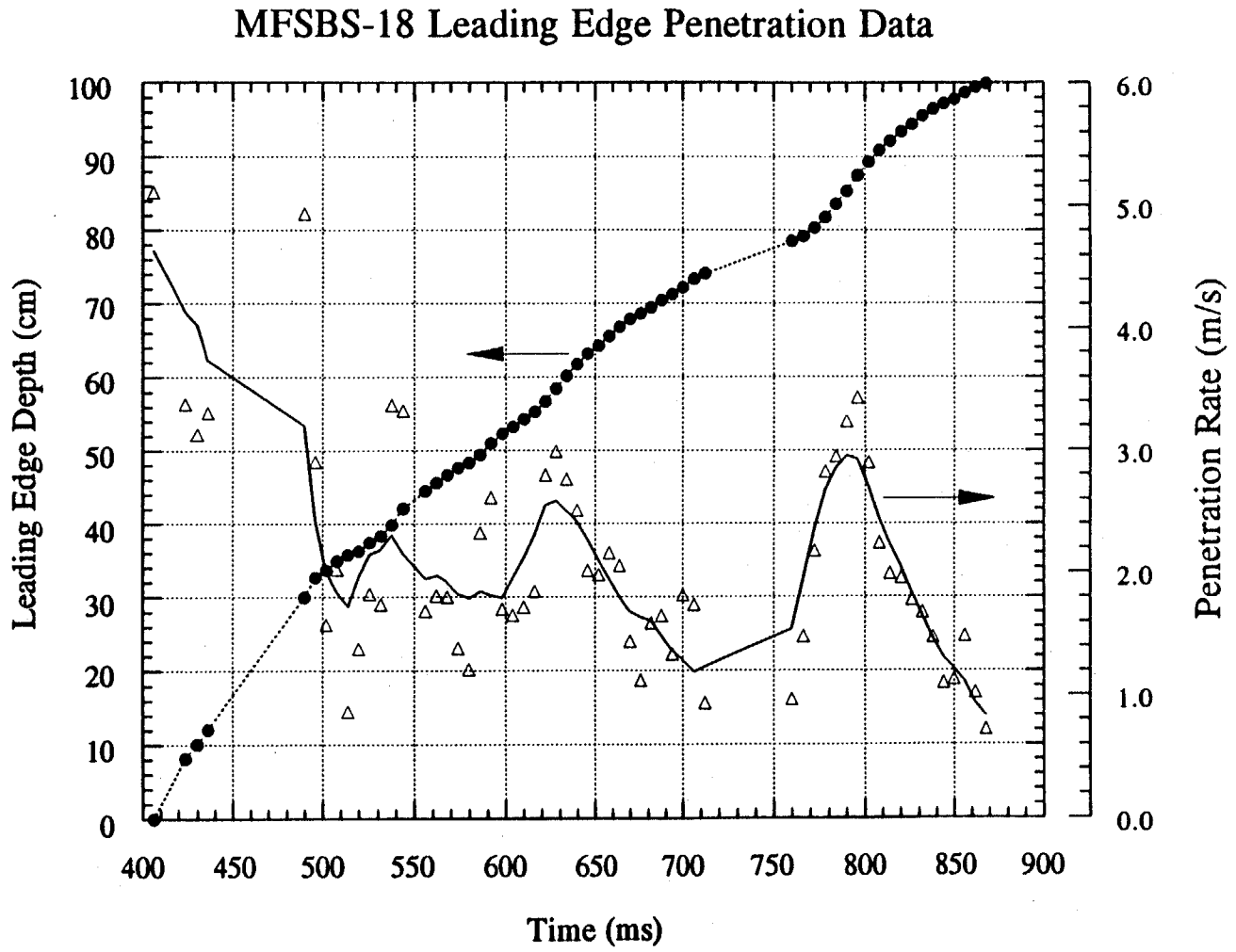
MFSBS-18 Leading Edge Penetration Data
Leading Edge Depth (cm)
Penetration Rate (m/s)
Time (ms)
100
90
80
70
60
50
40
30
20
10
0
6.0
5.0
4.0
3.0
2.0
1.0
0.0
400
450
500
550
600
650
700
750
800
850
900

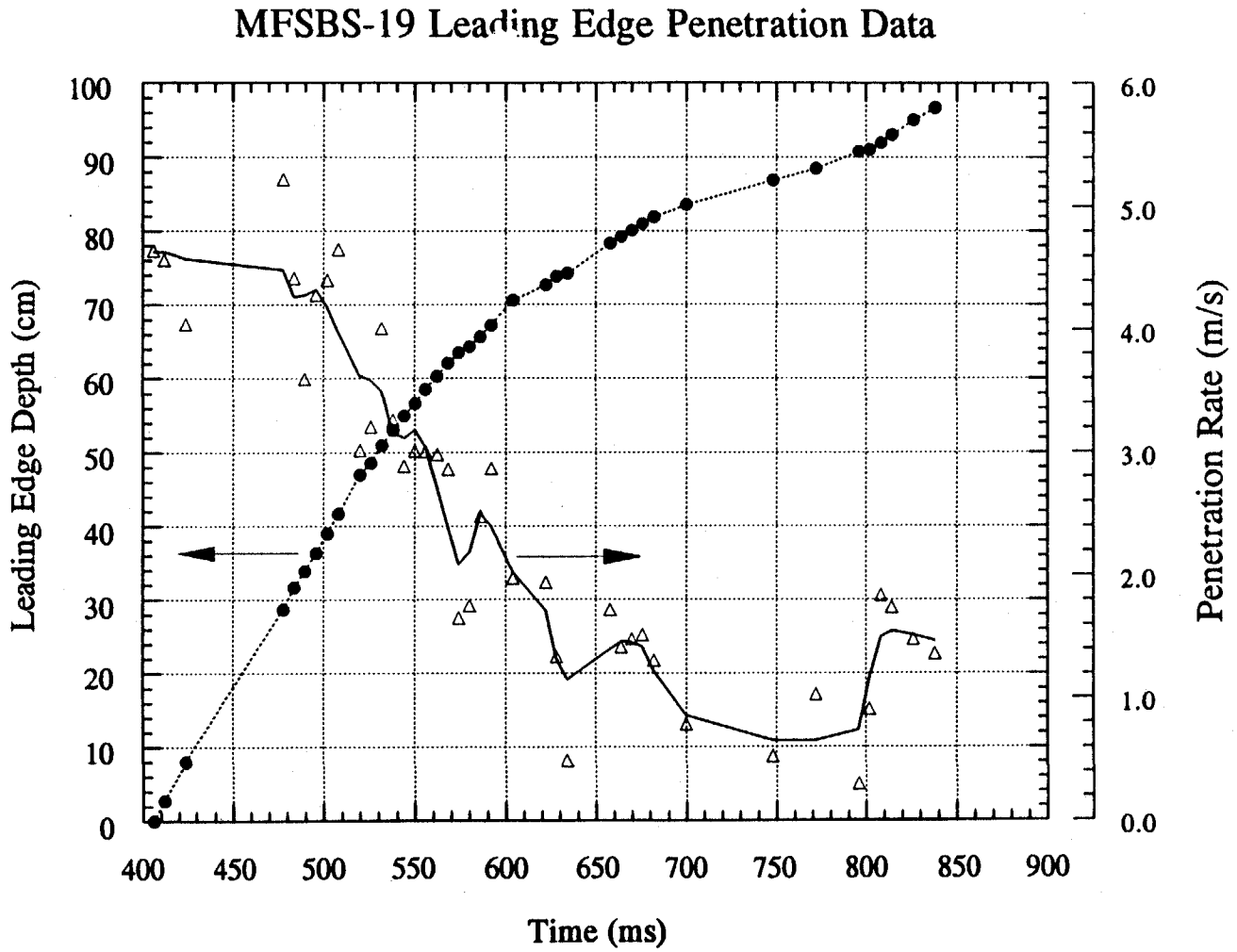
MFSBS-19 Leading Edge Penetration Data
Leading Edge Depth (cm)
Penetration Rate (m/s)
Time (ms)
0
10
20
30
40
50
60
70
80
90
100
0.0
1.0
2.0
3.0
4.0
5.0
6.0
400
450
500
550
600
650
700
750
800
850
900

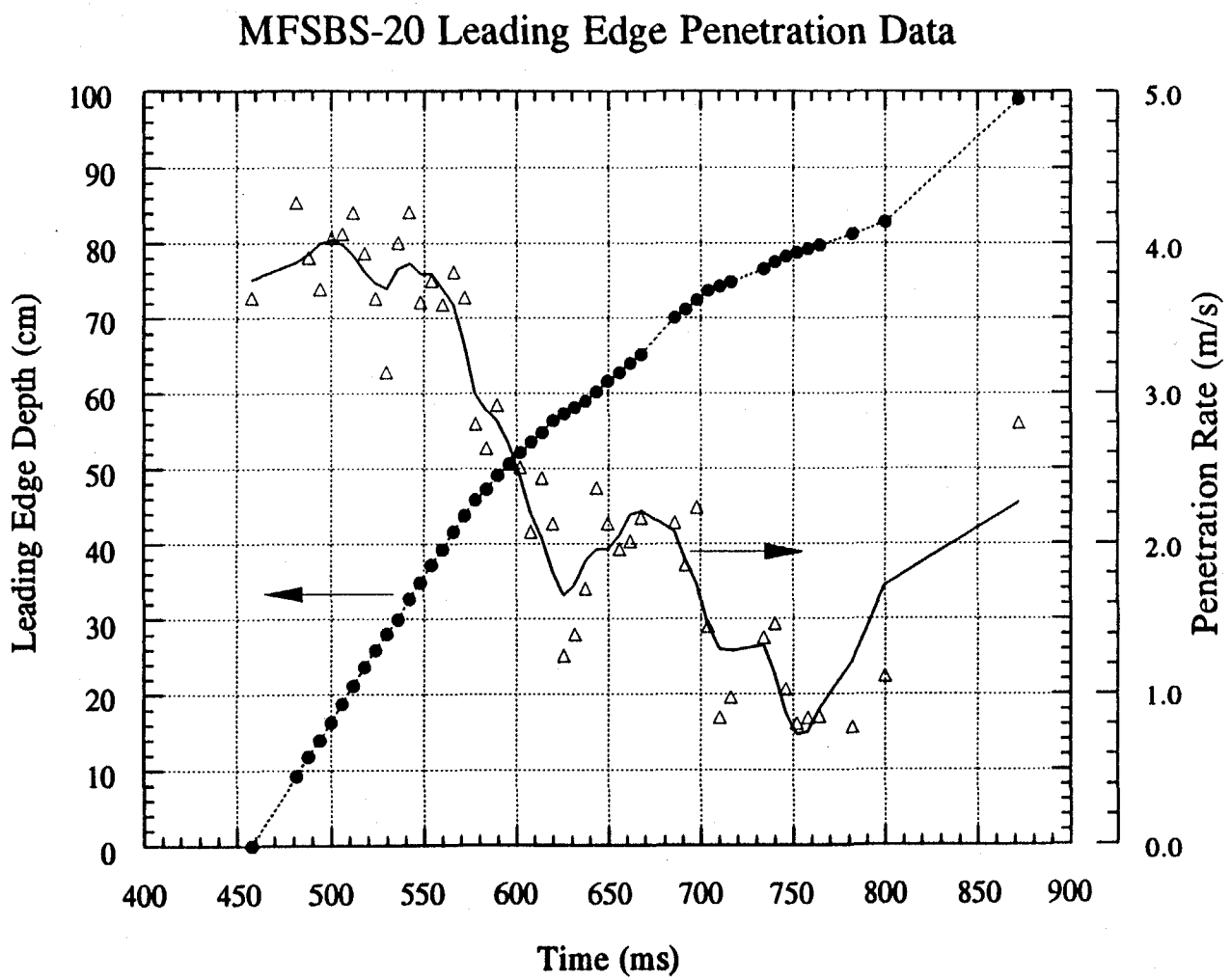
MFSBS-20 Leading Edge Penetration Data
Leading Edge Depth (cm)
Penetration Rate (m/s)
Time (ms)
100
90
80
70
60
50
40
30
20
10
0
5.0
4.0
3.0
2.0
1.0
0.0
400
450
500
550
600
650
700
750
800
850
900

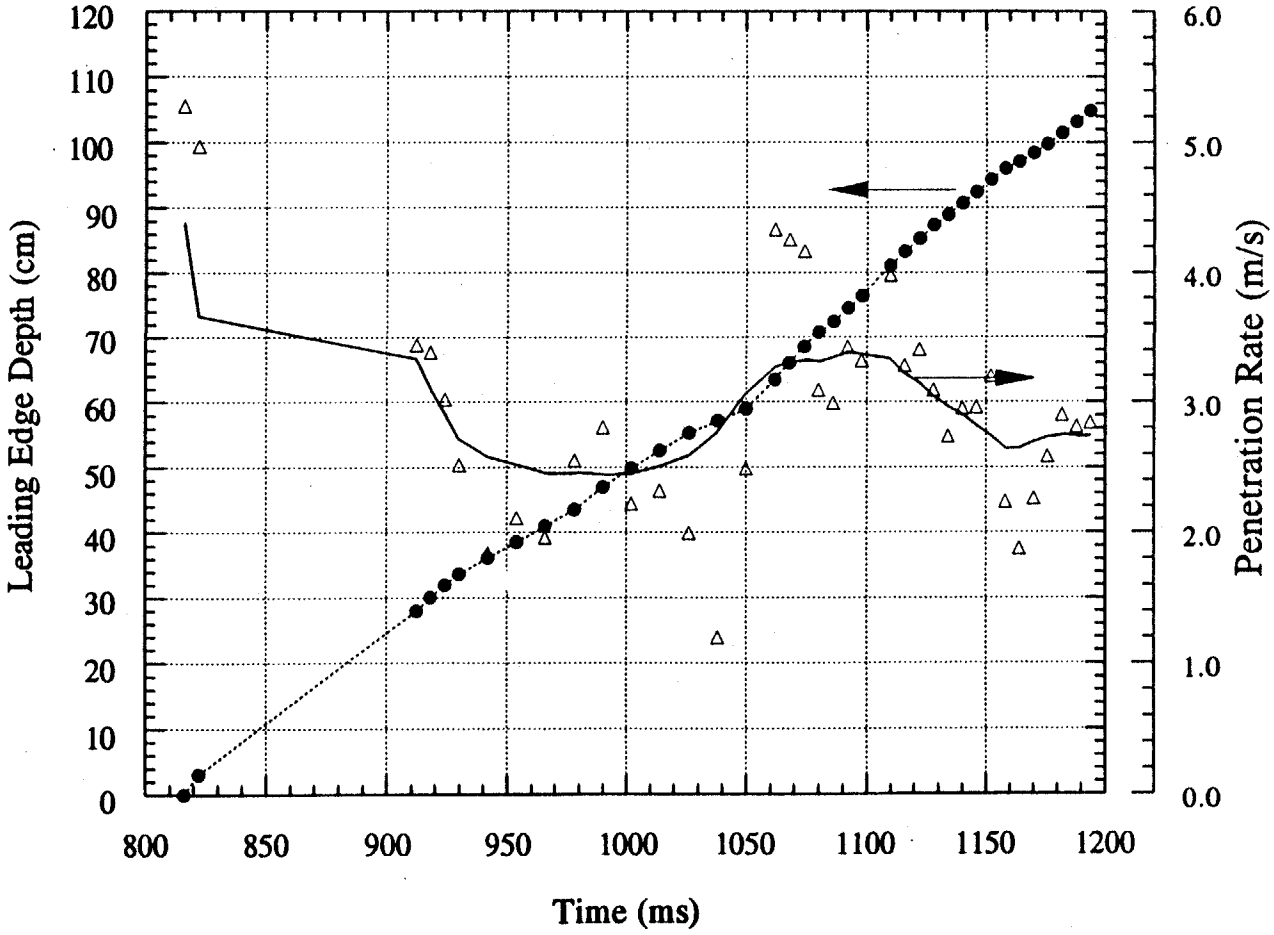
MFSBS-21 Leading Edge Penetration Data
Leading Edge Depth (cm)
Penetration Rate (m/s)
Time (ms)
120
110
100
90
80
70
60
50
40
30
20
10
0
6.0
5.0
4.0
3.0
2.0
1.0
0.0
800
850
900
950
1000
1050
1100
1150
1200

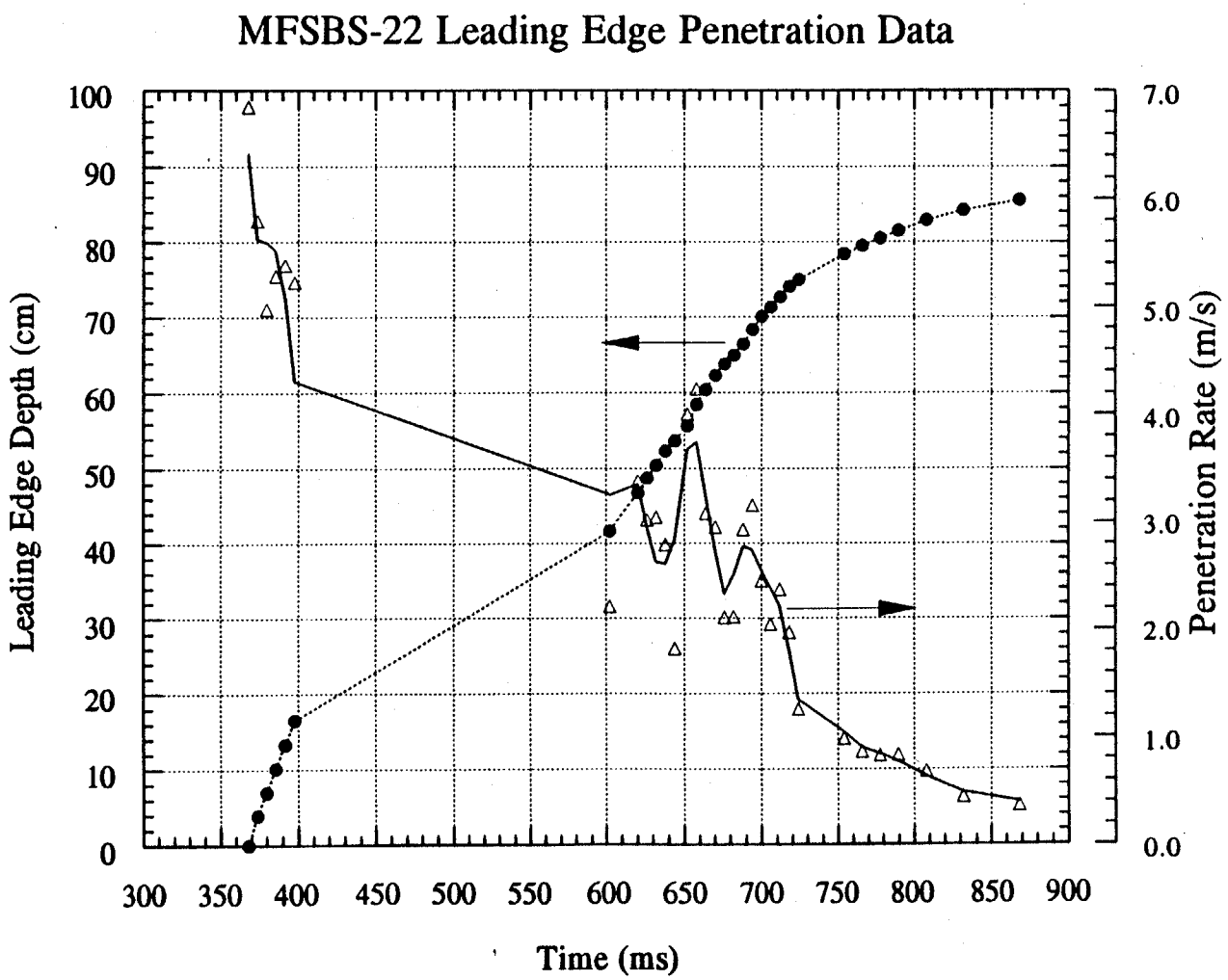
MFSBS-22 Leading Edge Penetration Data
Leading Edge Depth (cm)
Penetration Rate (m/s)
Time (ms)
0
10
20
30
40
50
60
70
80
90
100
0.0
1.0
2.0
3.0
4.0
5.0
6.0
7.0
300
350
400
450
500
550
600
650
700
750
800
850
900

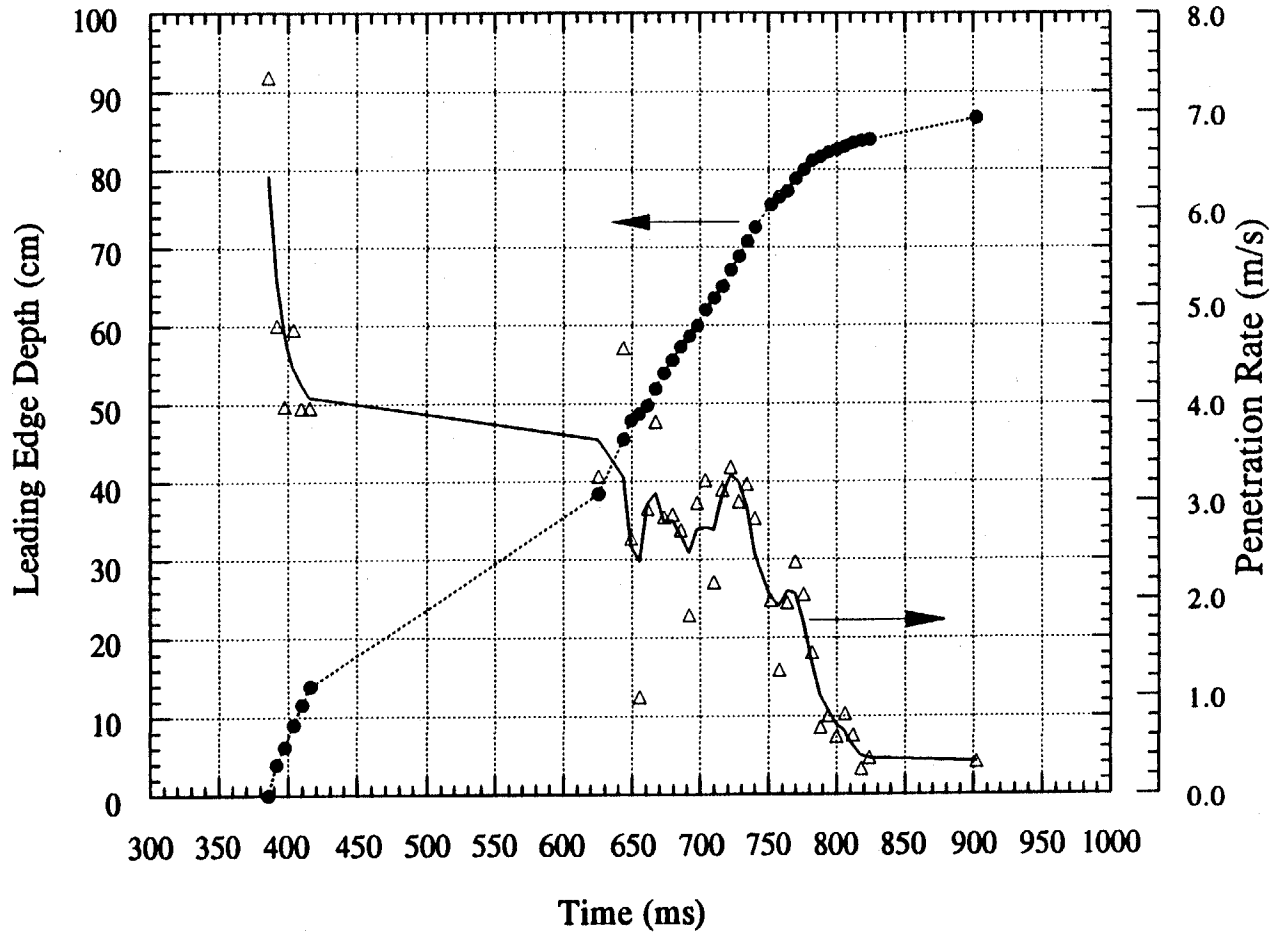
MFSBS-23 Leading Edge Penetration Data
Leading Edge Depth (cm)
Penetration Rate (m/s)
Time (ms)
0
10
20
30
40
50
60
70
80
90
100
0.0
1.0
2.0
3.0
4.0
5.0
6.0
7.0
8.0
300 350 400 450 500 550 600 650 700 750 800 850 900 950 1000

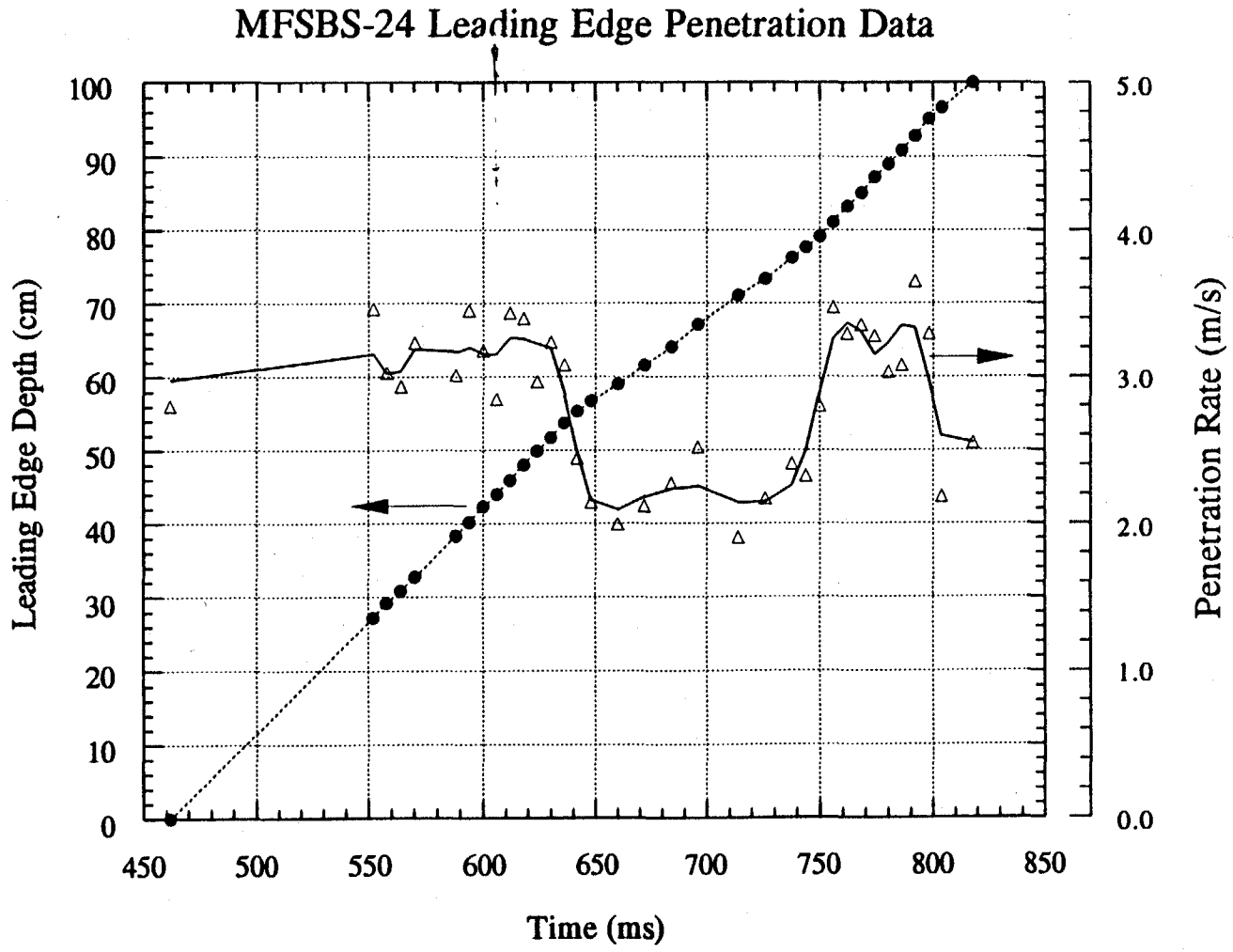
MFSBS-24 Leading Edge Penetration Data
Leading Edge Depth (cm)
Penetration Rate (m/s)
Time (ms)
100
90
80
70
60
50
40
30
20
10
0
5.0
4.0
3.0
2.0
1.0
0.0
450
500
550
600
650
700
750
800
850

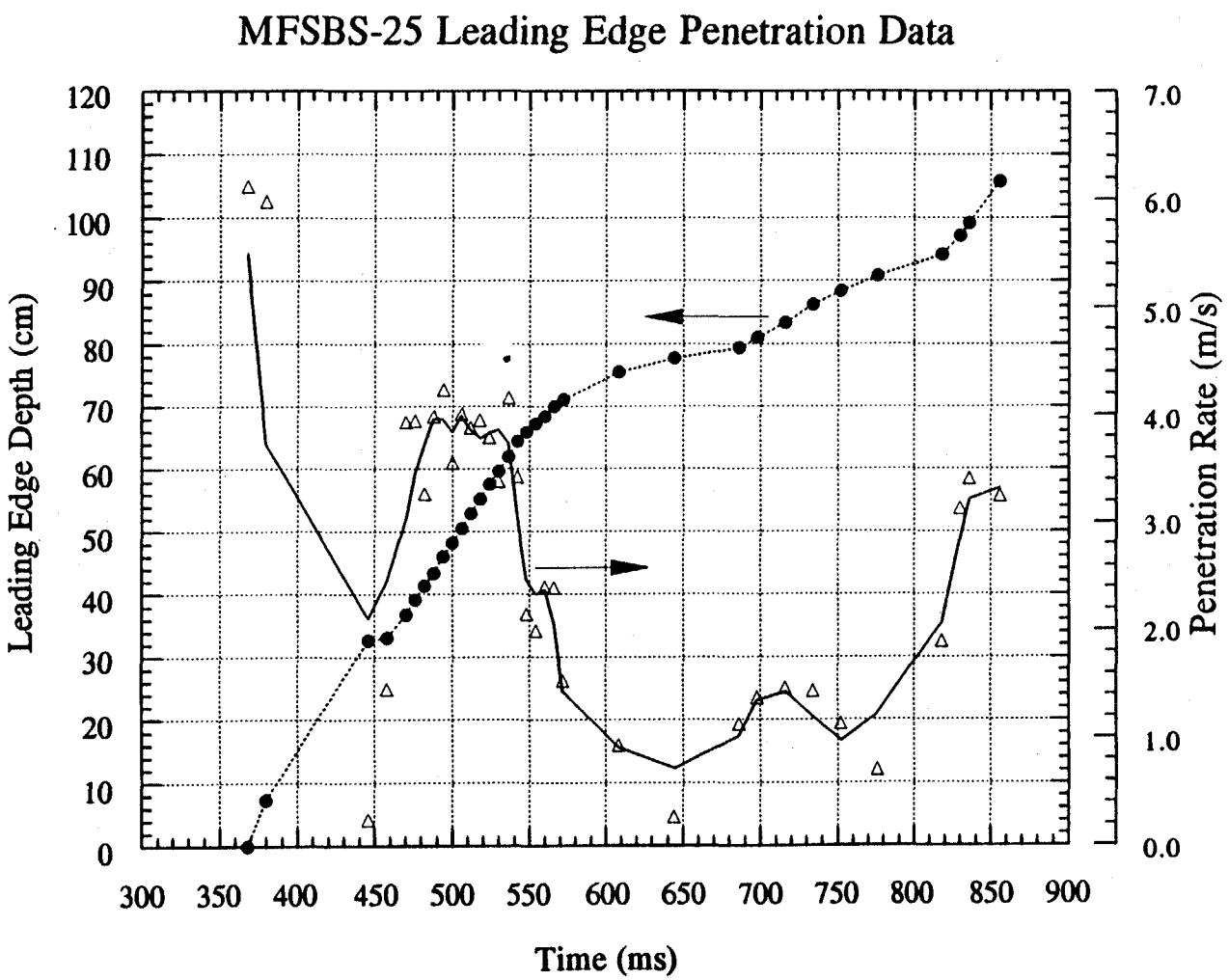
MFSBS-25 Leading Edge Penetration Data
Leading Edge Depth (cm)
Penetration Rate (m/s)
Time (ms)
0
10
20
30
40
50
60
70
80
90
100
110
120
0.0
1.0
2.0
3.0
4.0
5.0
6.0
7.0
300
350
400
450
500
550
600
650
700
750
800
850
900

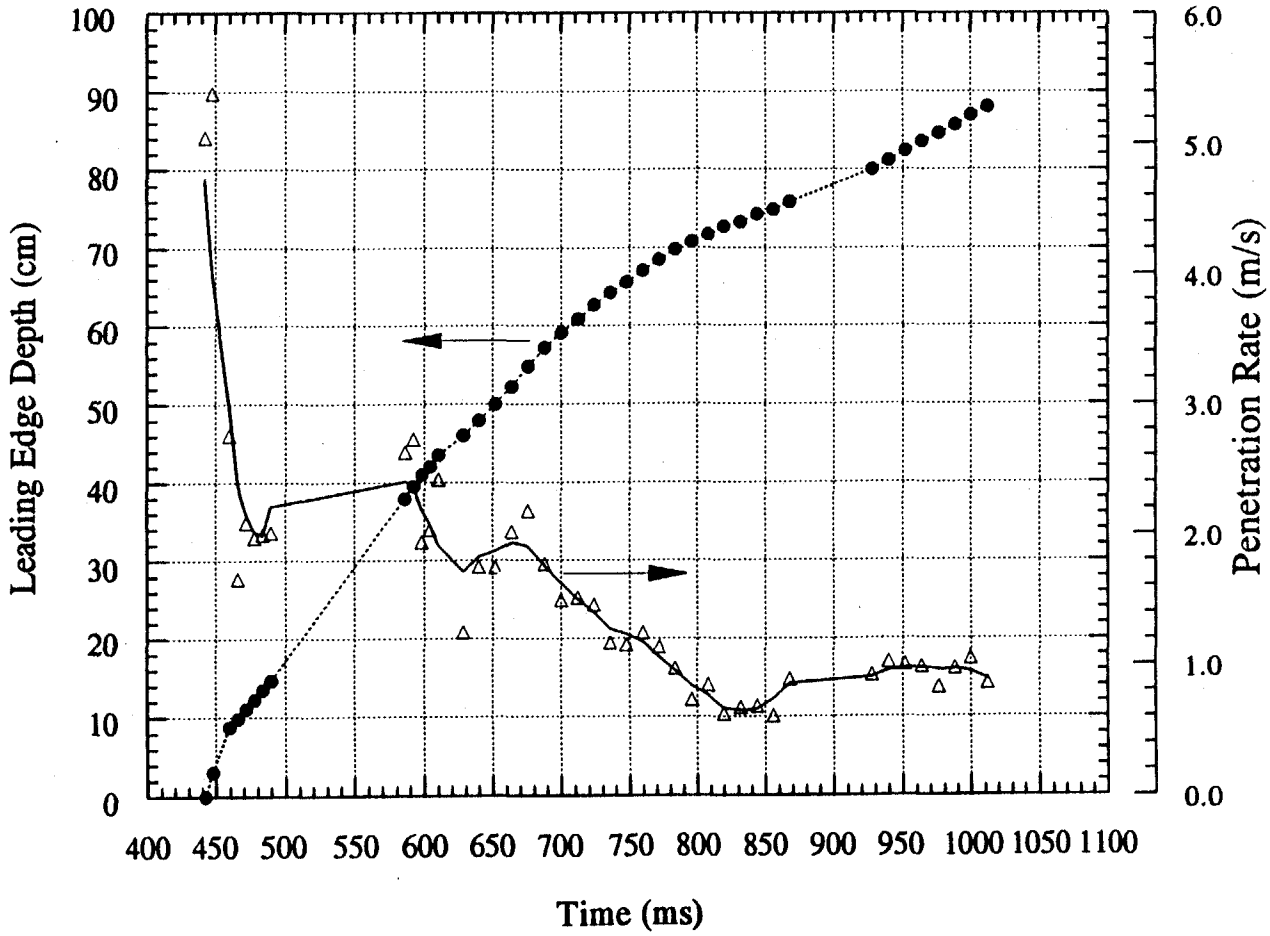
MFSBS-26 Leading Edge Penetration Data
Leading Edge Depth (cm)
Penetration Rate (m/s)
Time (ms)
0
10
20
30
40
50
60
70
80
90
100
0.0
1.0
2.0
3.0
4.0
5.0
6.0
400 450 500 550 600 650 700 750 800 850 900 950 1000 1050 1100

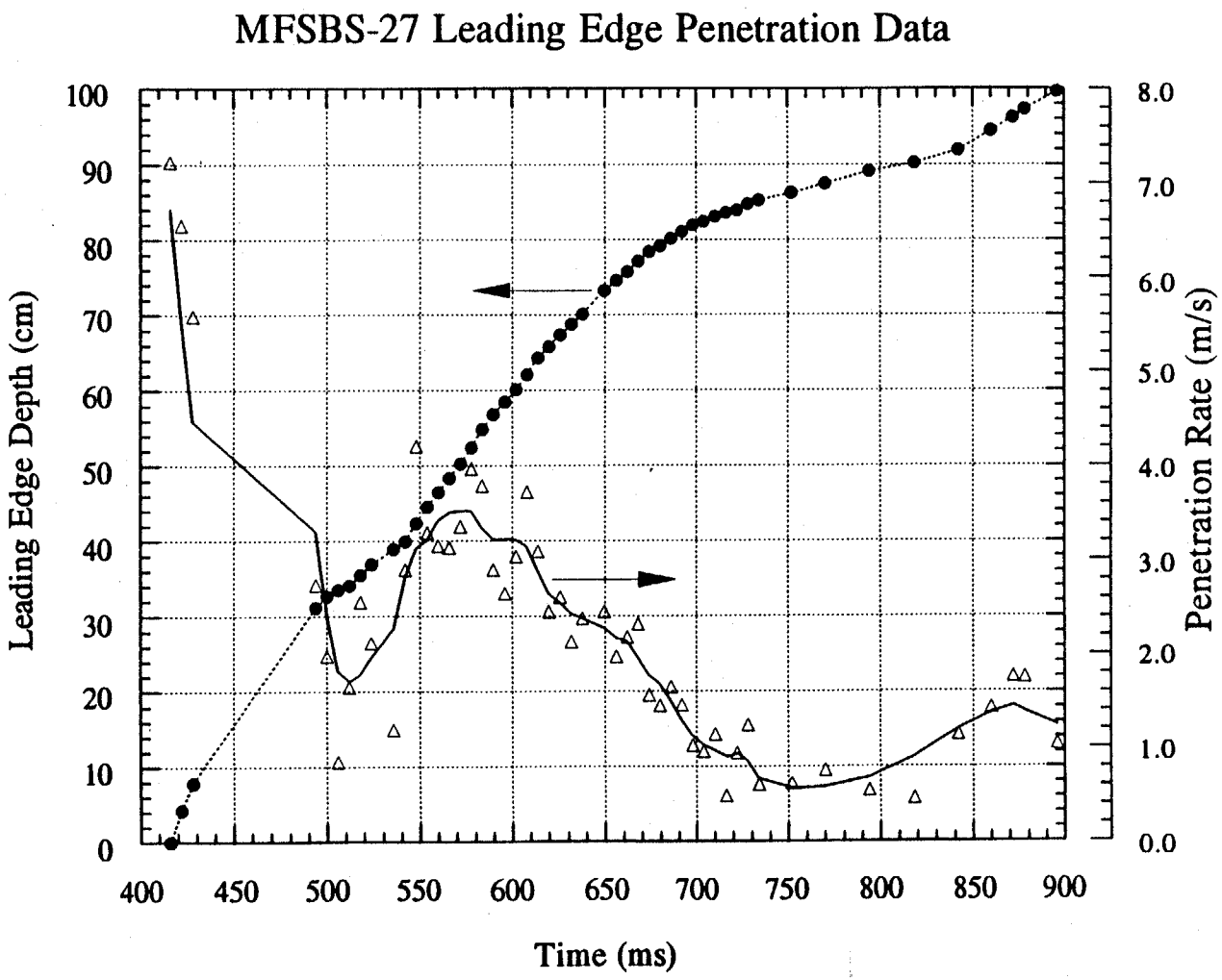
MFSBS-27 Leading Edge Penetration Data
Leading Edge Depth (cm)
Penetration Rate (m/s)
Time (ms)
0
10
20
30
40
50
60
70
80
90
100
0.0
1.0
2.0
3.0
4.0
5.0
6.0
7.0
8.0
400
450
500
550
600
650
700
750
800
850
900

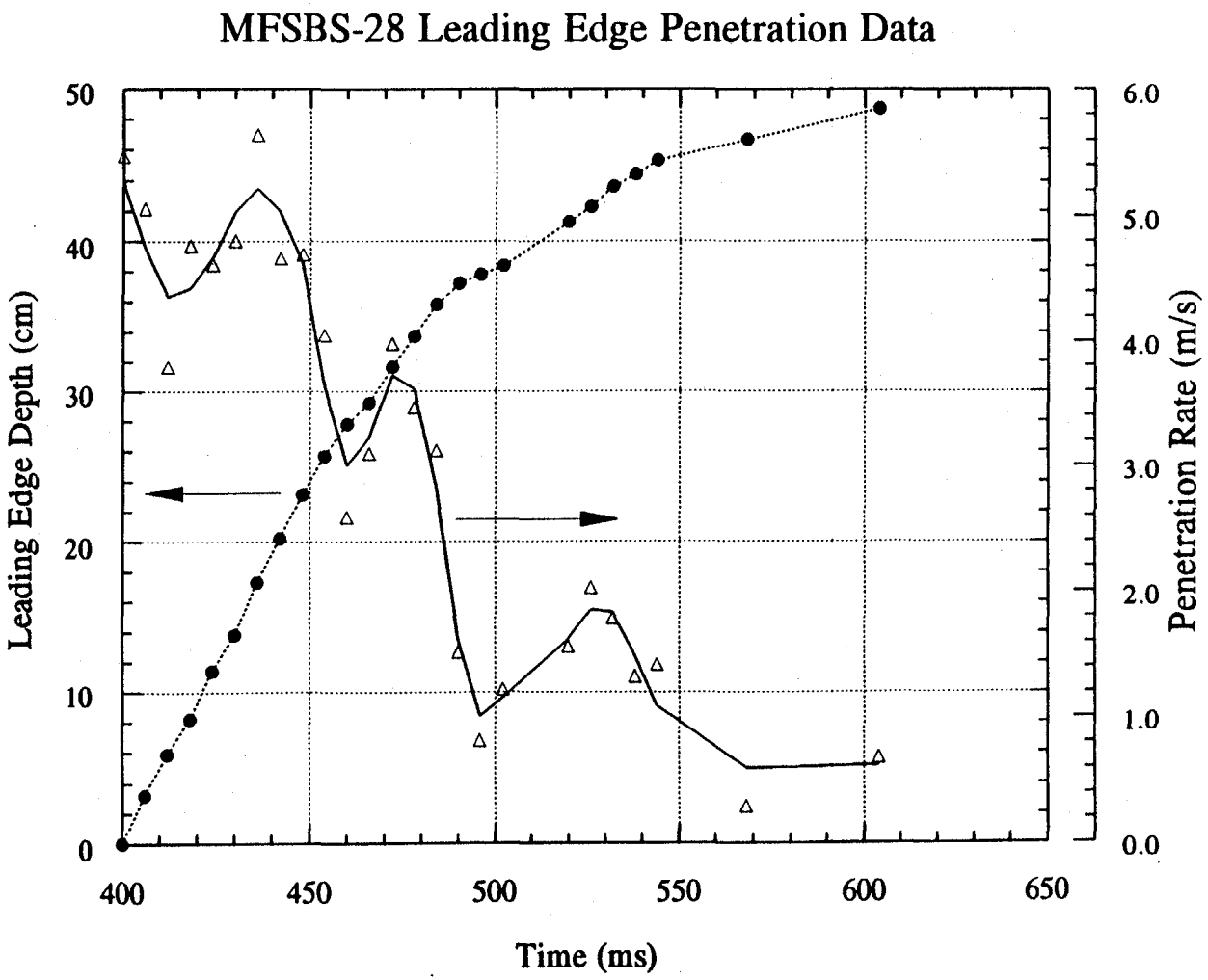
MFSBS-28 Leading Edge Penetration Data
Leading Edge Depth (cm)
Penetration Rate (m/s)
Time (ms)
0
10
20
30
40
50
0.0
1.0
2.0
3.0
4.0
5.0
6.0
400
450
500
550
600
650

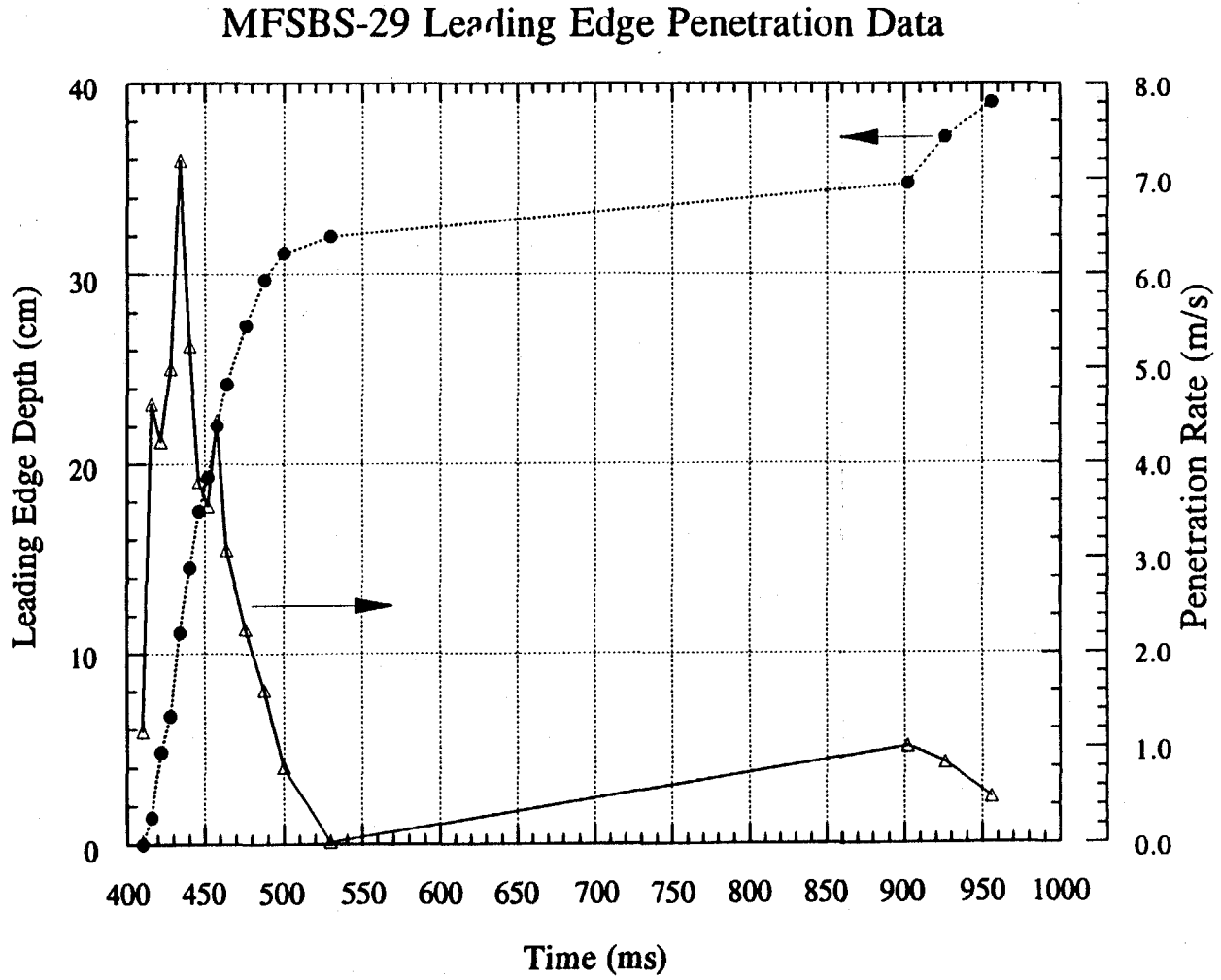
MFSBS-29 Leading Edge Penetration Data
Leading Edge Depth (cm)
Penetration Rate (m/s)
Time (ms)
0
10
20
30
40
0.0
1.0
2.0
3.0
4.0
5.0
6.0
7.0
8.0
400
450
500
550
600
650
700
750
800
850
900
950
1000

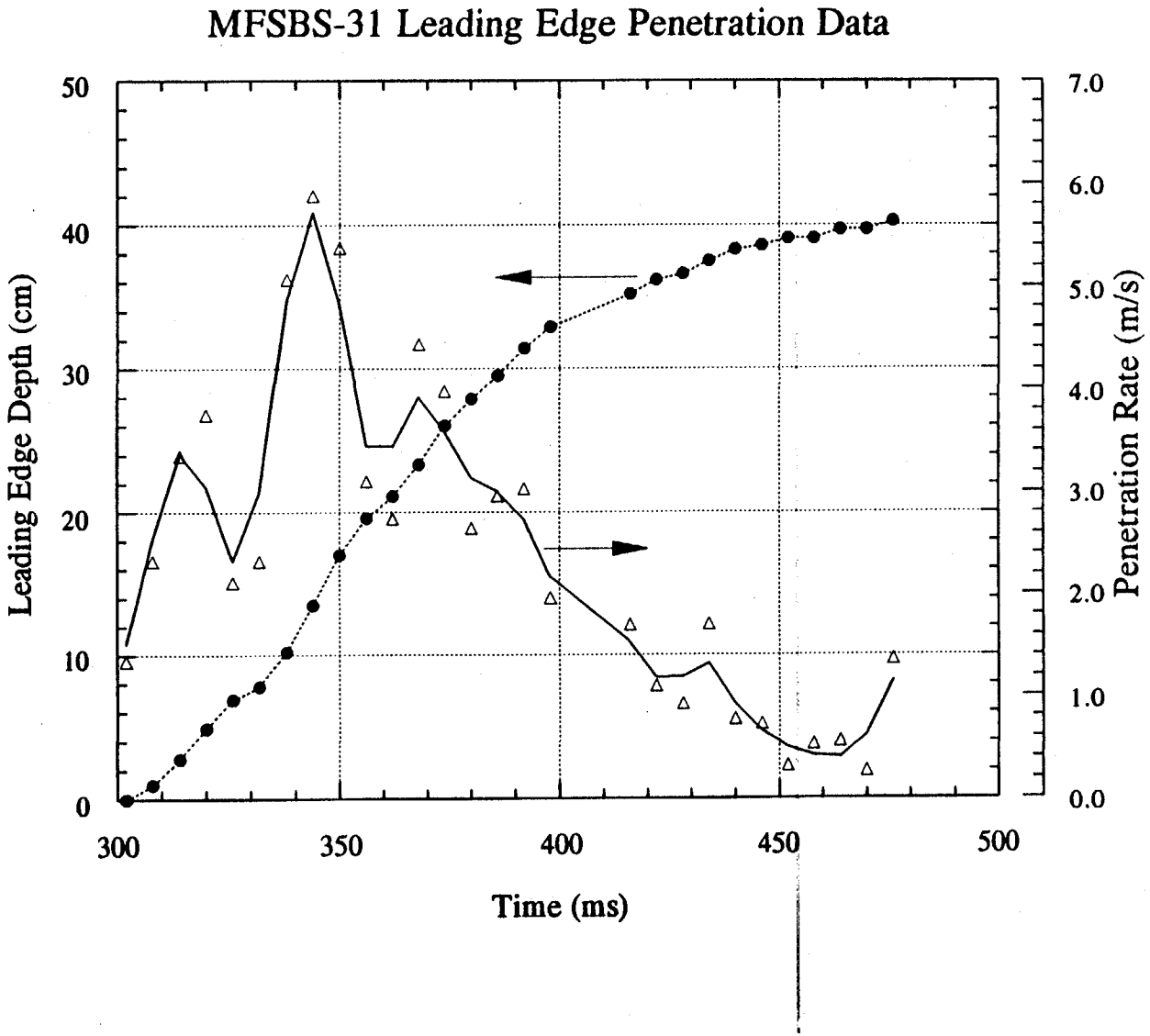
MFSBS-31 Leading Edge Penetration Data
Leading Edge Depth (cm)
Penetration Rate (m/s)
Time (ms)
0
10
20
30
40
50
0.0
1.0
2.0
3.0
4.0
5.0
6.0
7.0
300
350
400
450
500

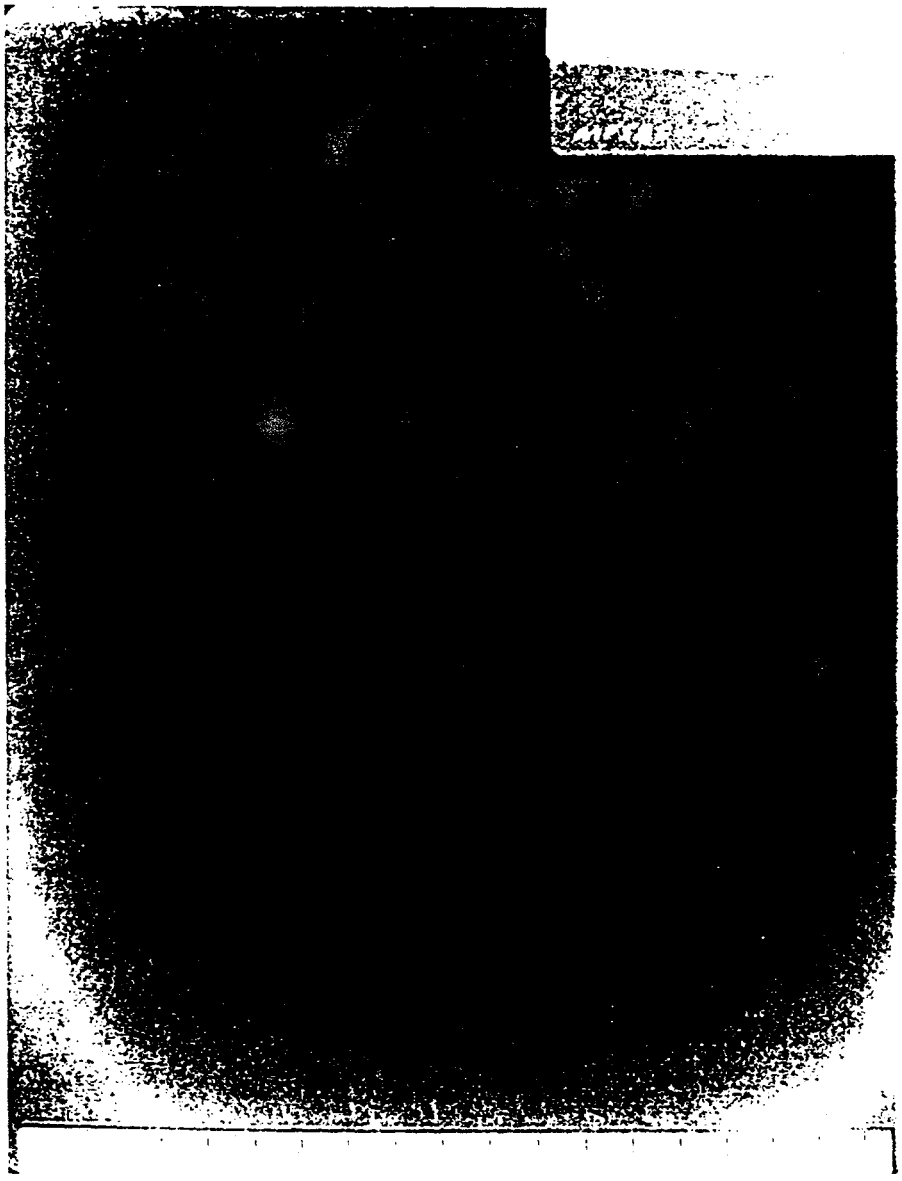

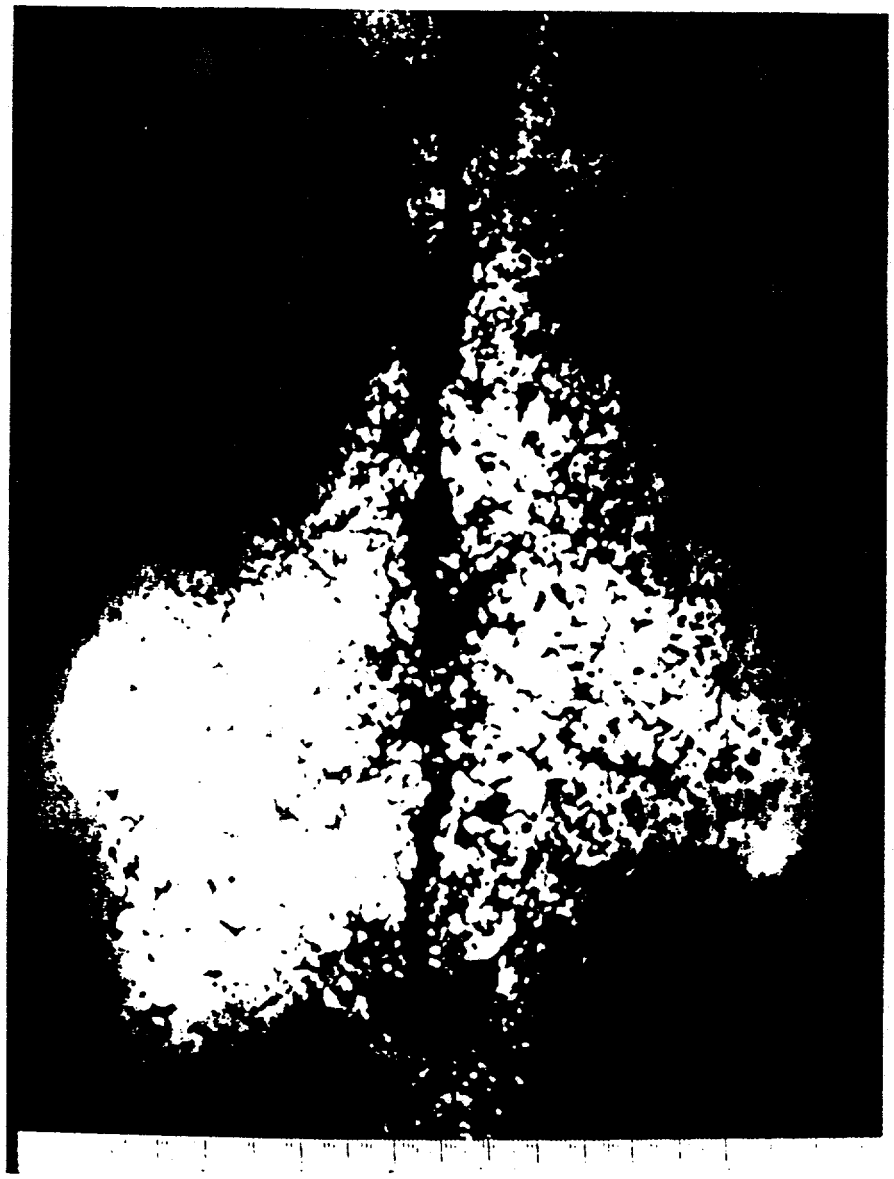

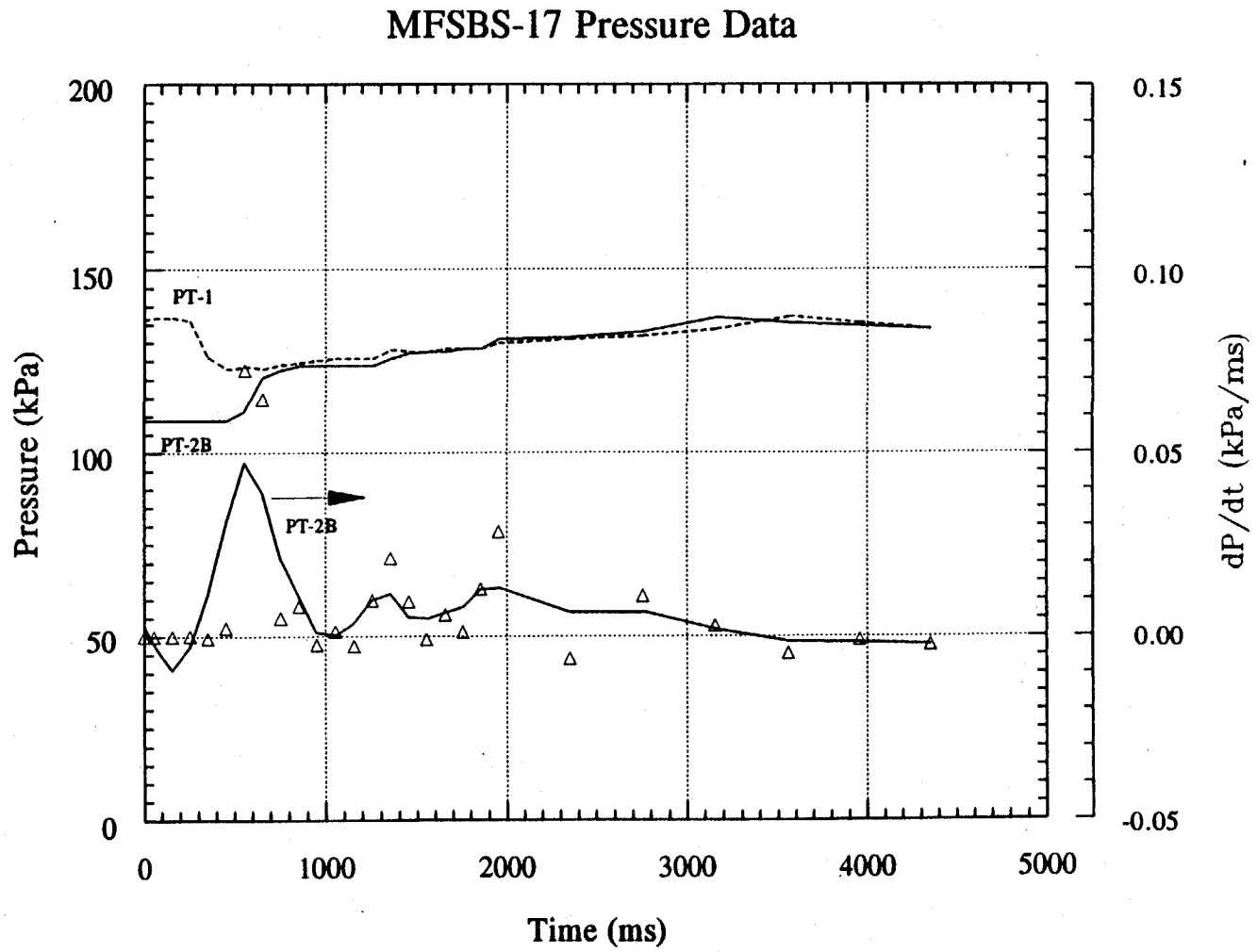
MFSBS-17 Pressure Data
Pressure (kPa)
200
150
100
50
0
PT-1
PT-2B
PT-2B
0
1000
2000
3000
4000
5000
Time (ms)
0.15
0.10
0.05
0.00
-0.05
dP/dt (kPa/ms)

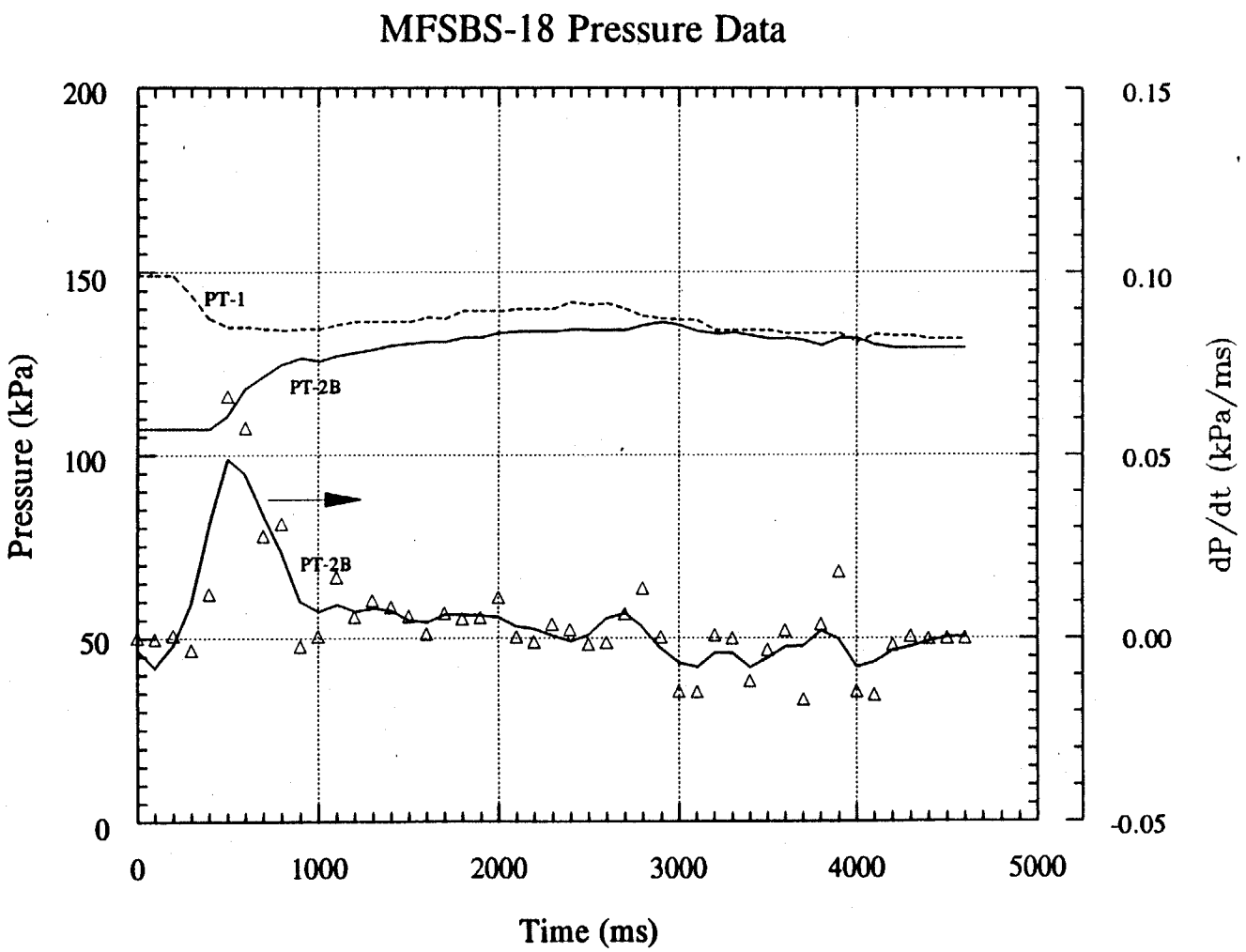
MFSBS-18 Pressure Data
Pressure (kPa)
dP/dt (kPa/ms)
Time (ms)
PT-1
PT-2B
PT-2B
200
150
100
50
0
0.15
0.10
0.05
0.00
-0.05
0
1000
2000
3000
4000
5000

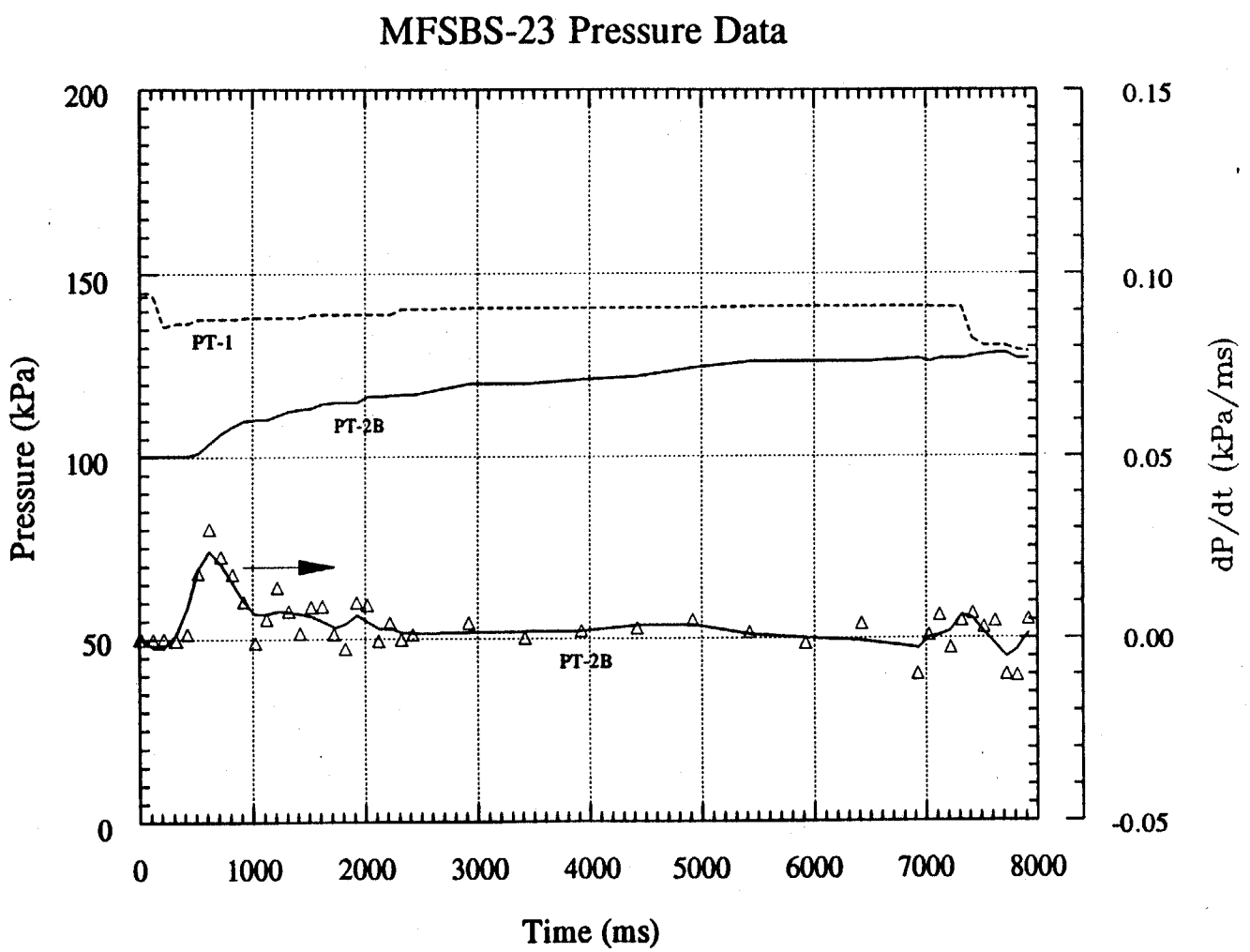
MFSBS-23 Pressure Data
Pressure (kPa)
dP/dt (kPa/ms)
Time (ms)
PT-1
PT-2B
PT-2B
200
150
100
50
0
0.15
0.10
0.05
0.00
-0.05
0
1000
2000
3000
4000
5000
6000
7000
8000

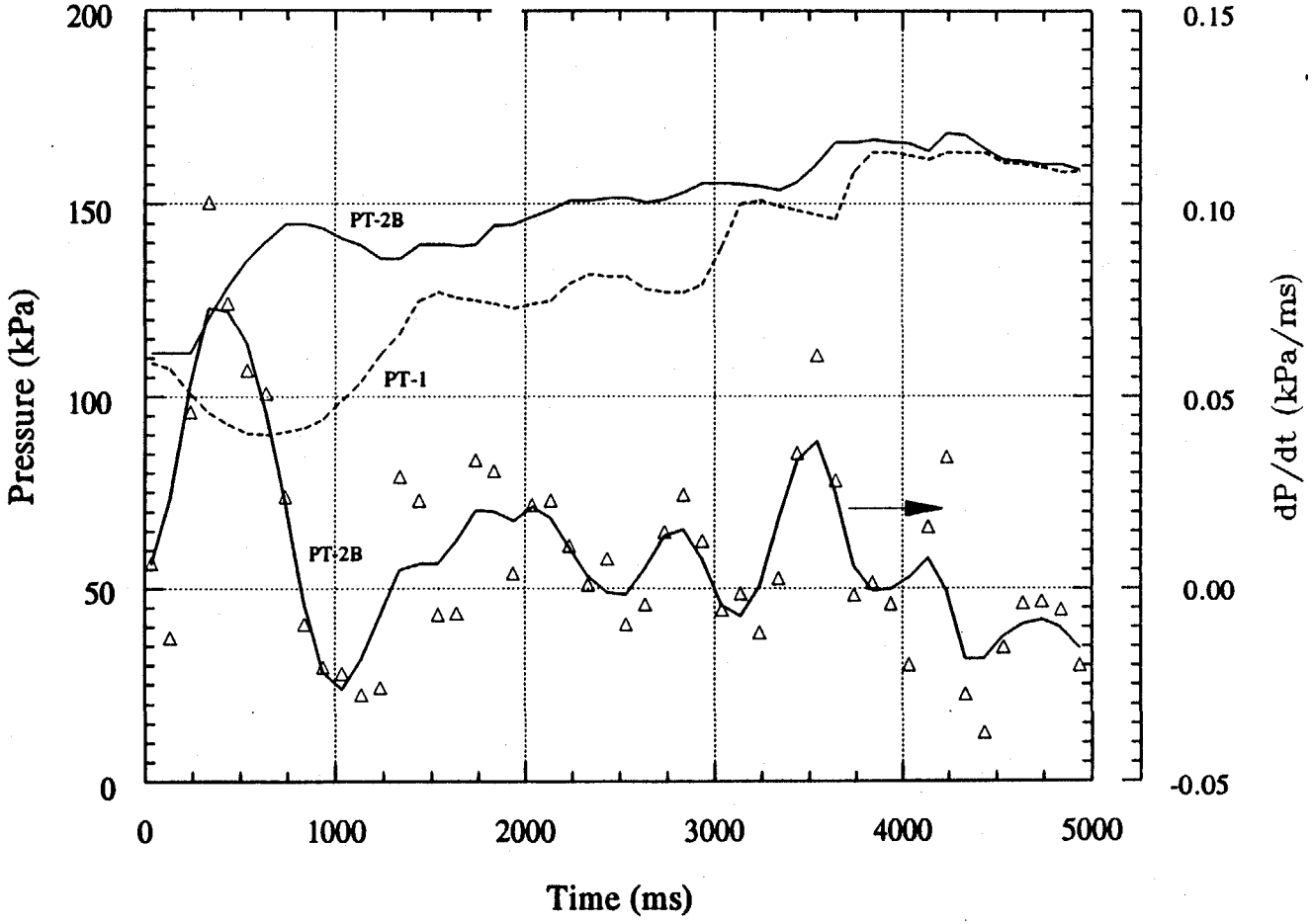
MFSBS-24 Pressure Data
Pressure (kPa)
dP/dt (kPa/ms)
Time (ms)
PT-2B
PT-1
PT-2B
200
150
100
50
0
0.15
0.10
0.05
0.00
-0.05
0
1000
2000
3000
4000
5000

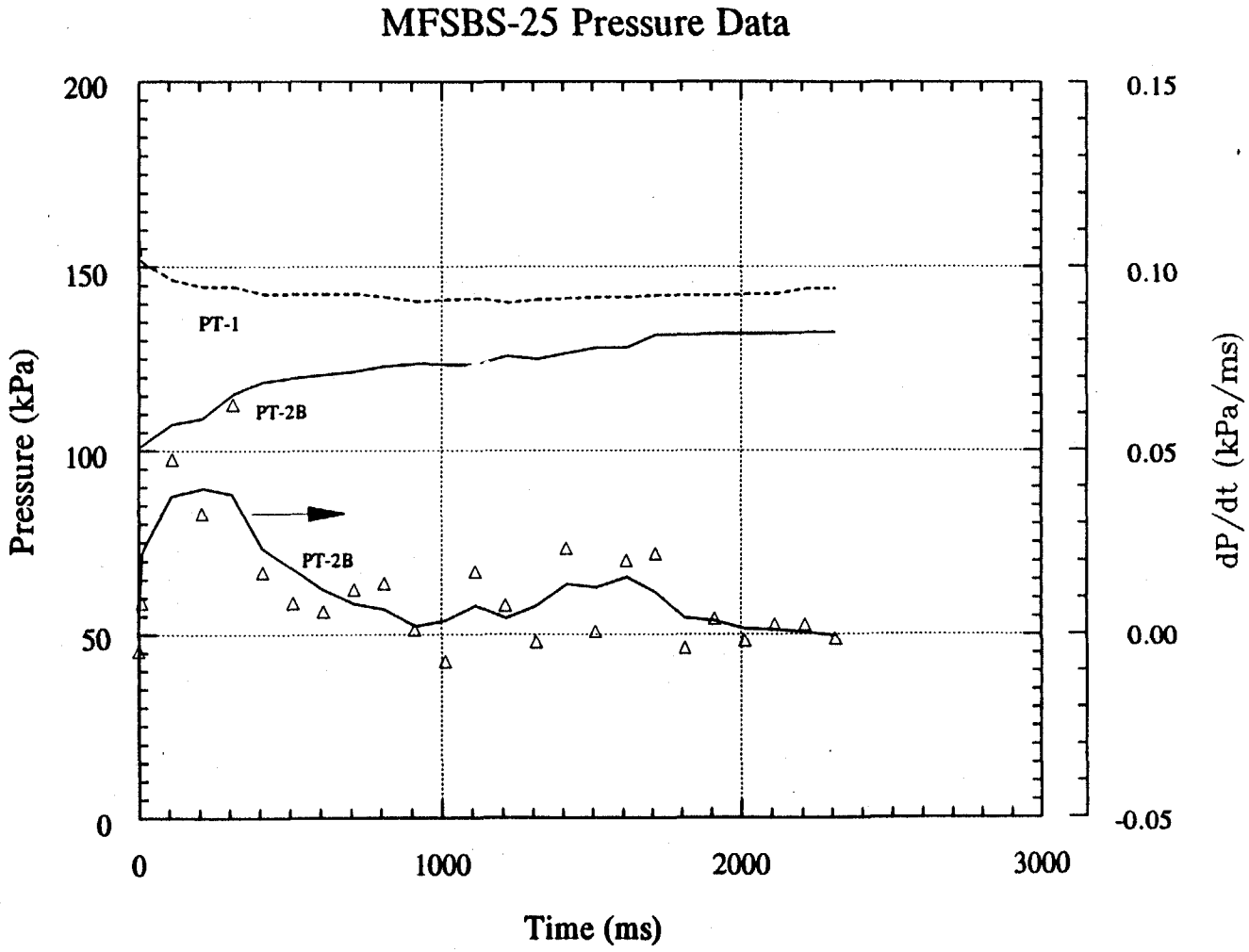
MFSBS-25 Pressure Data
Pressure (kPa)
dP/dt (kPa/ms)
Time (ms)
PT-1
PT-2B
PT-2B
200
150
100
50
0
0.15
0.10
0.05
0.00
-0.05
0
1000
2000
3000

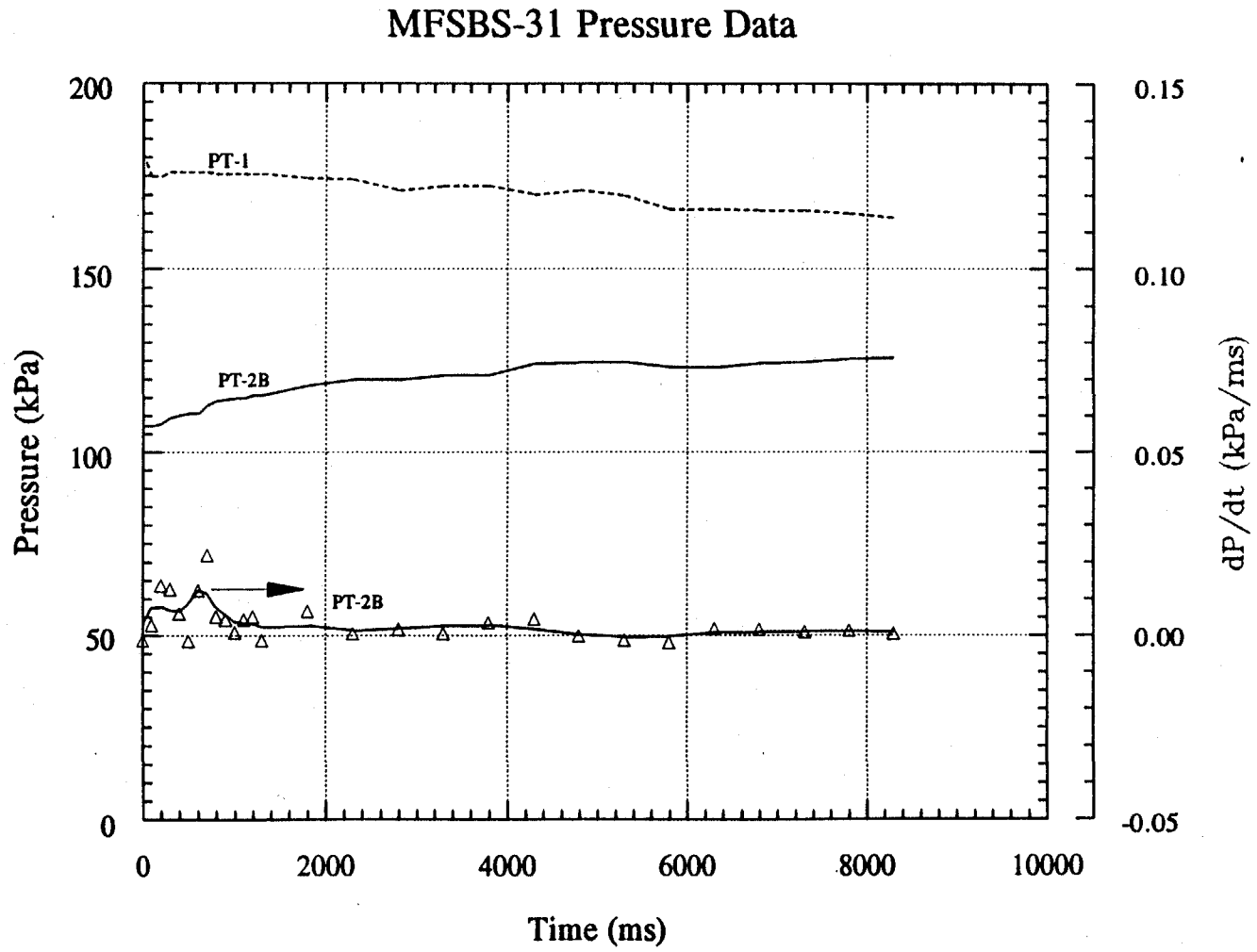
MFSBS-31 Pressure Data
200
150
100
50
0
Pressure (kPa)
PT-1
PT-2B
PT-2B
0.15
0.10
0.05
0.00
-0.05
dP/dt (kPa/ms)
0
2000
4000
6000
8000
10000
Time (ms)

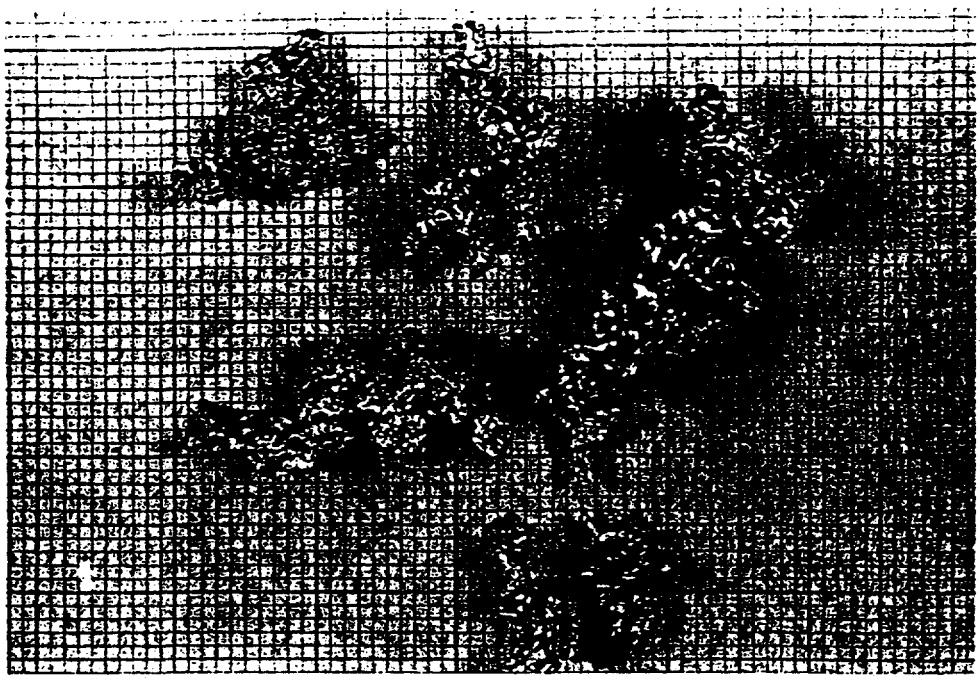

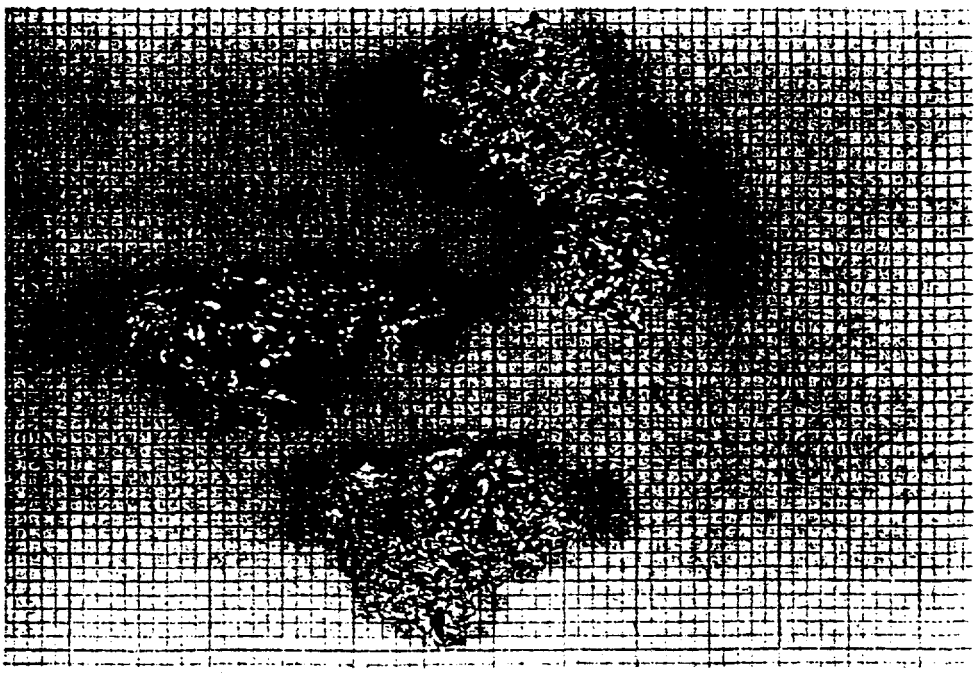

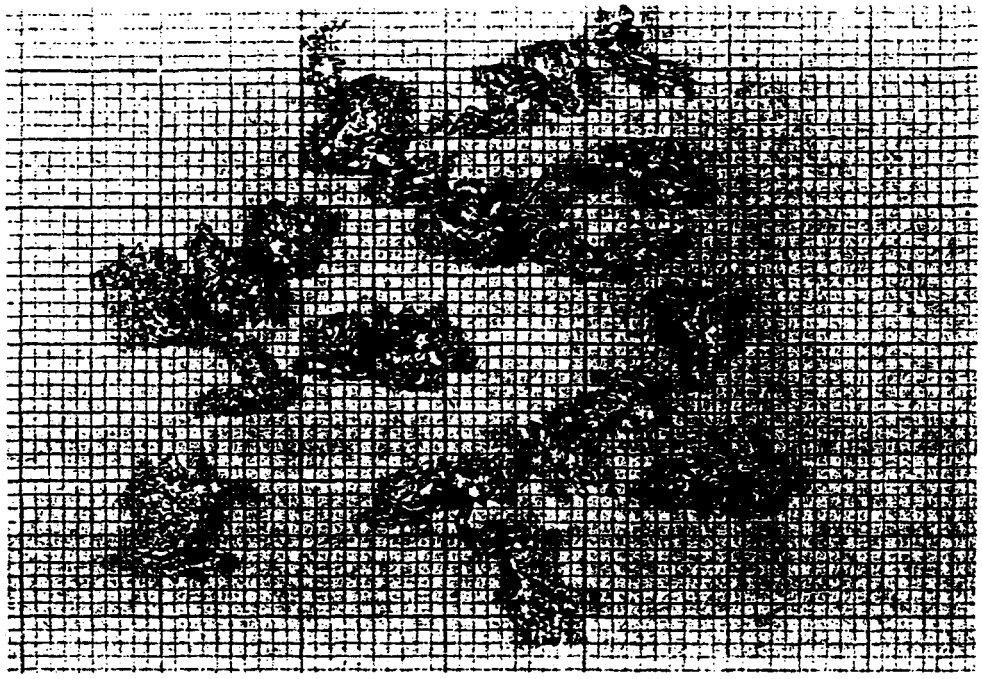

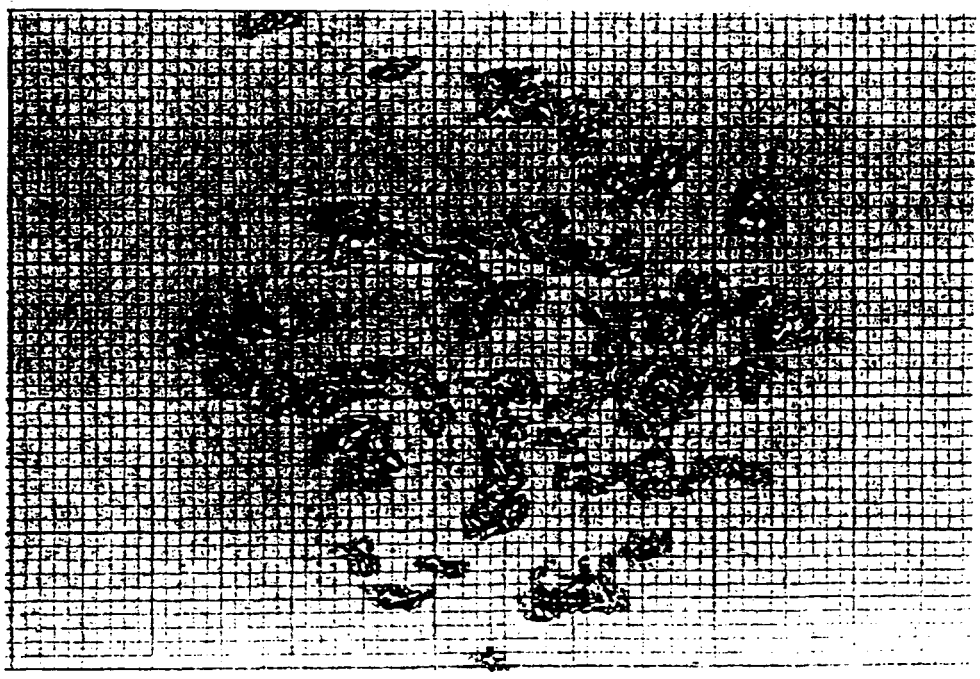

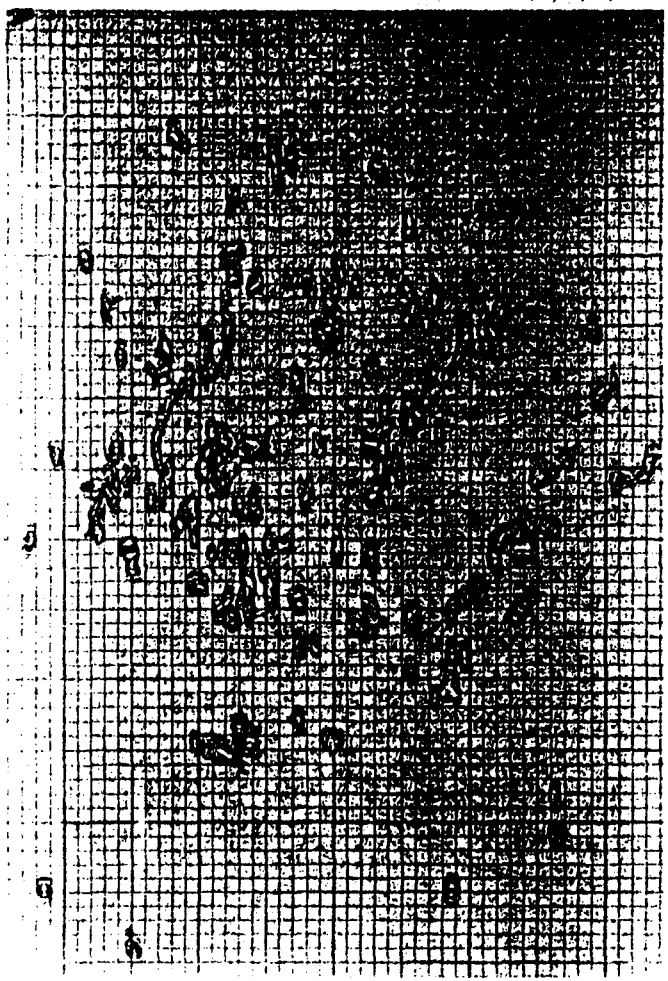

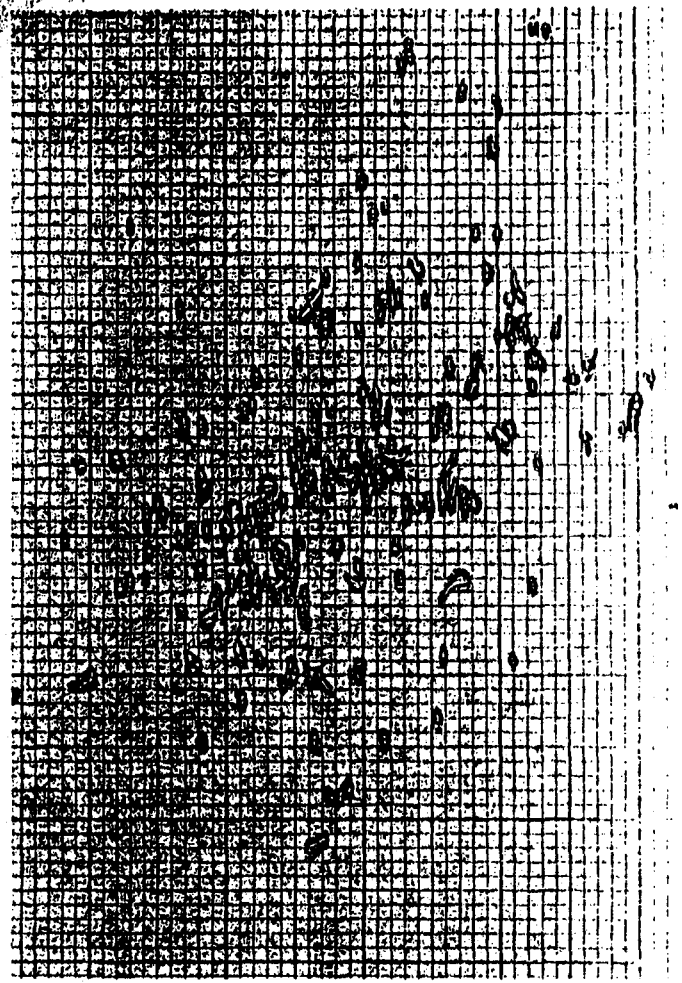

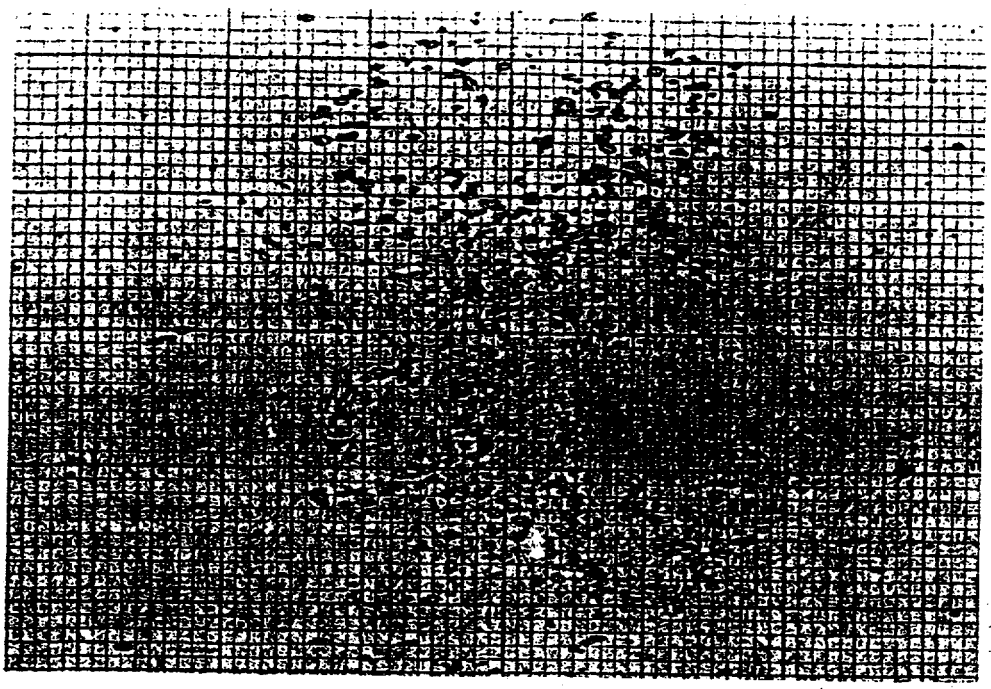

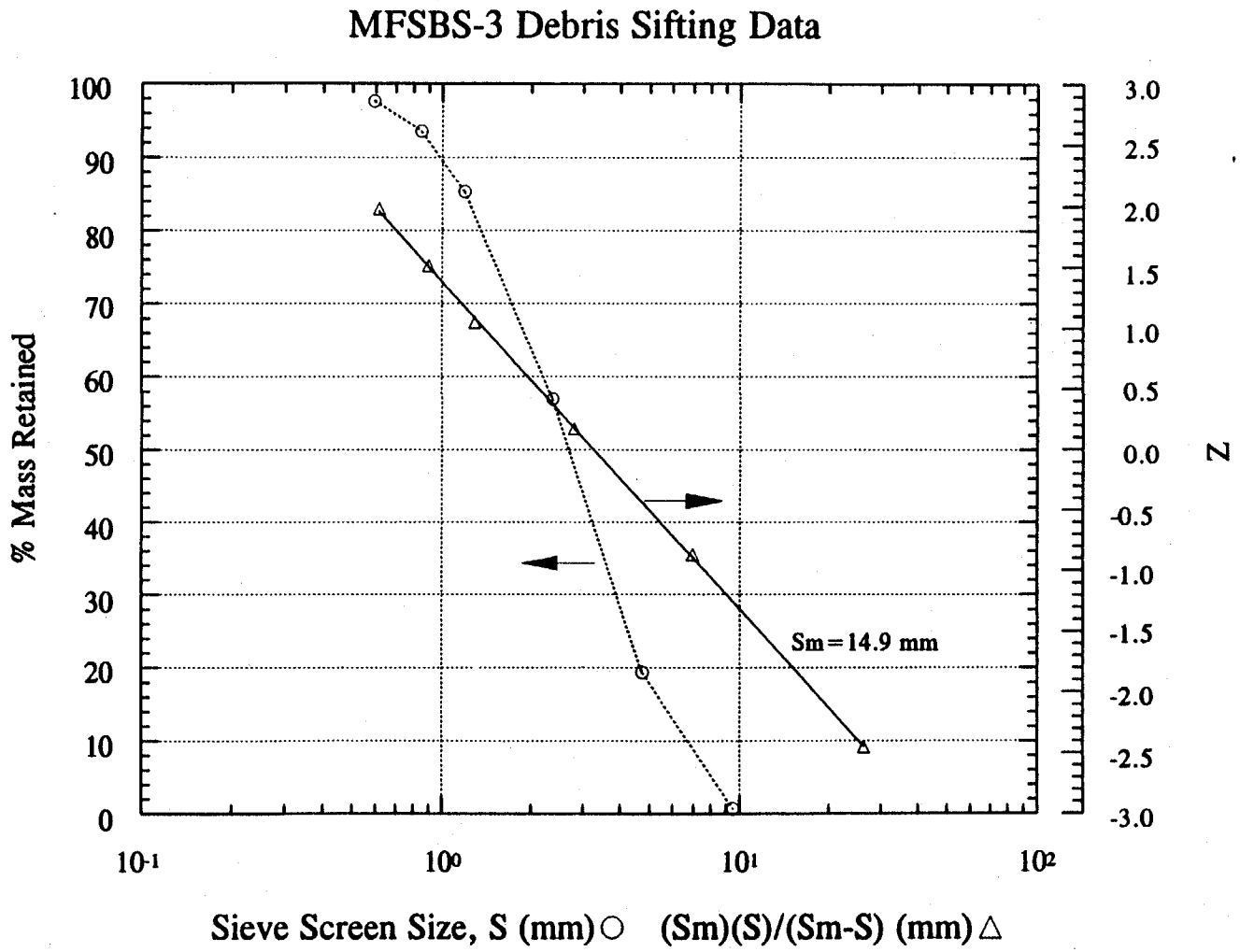
MFSBS-3 Debris Sifting Data
% Mass Retained
100
90
80
70
60
50
40
30
20
10
0
10-1
100
101
102
3.0
2.5
2.0
1.5
1.0
0.5
0.0
-0.5
-1.0
-1.5
-2.0
-2.5
-3.0
Z
Sm=14.9 mm
Sieve Screen Size, S (mm)○ (Sm)(S)/(Sm-S) (mm)△

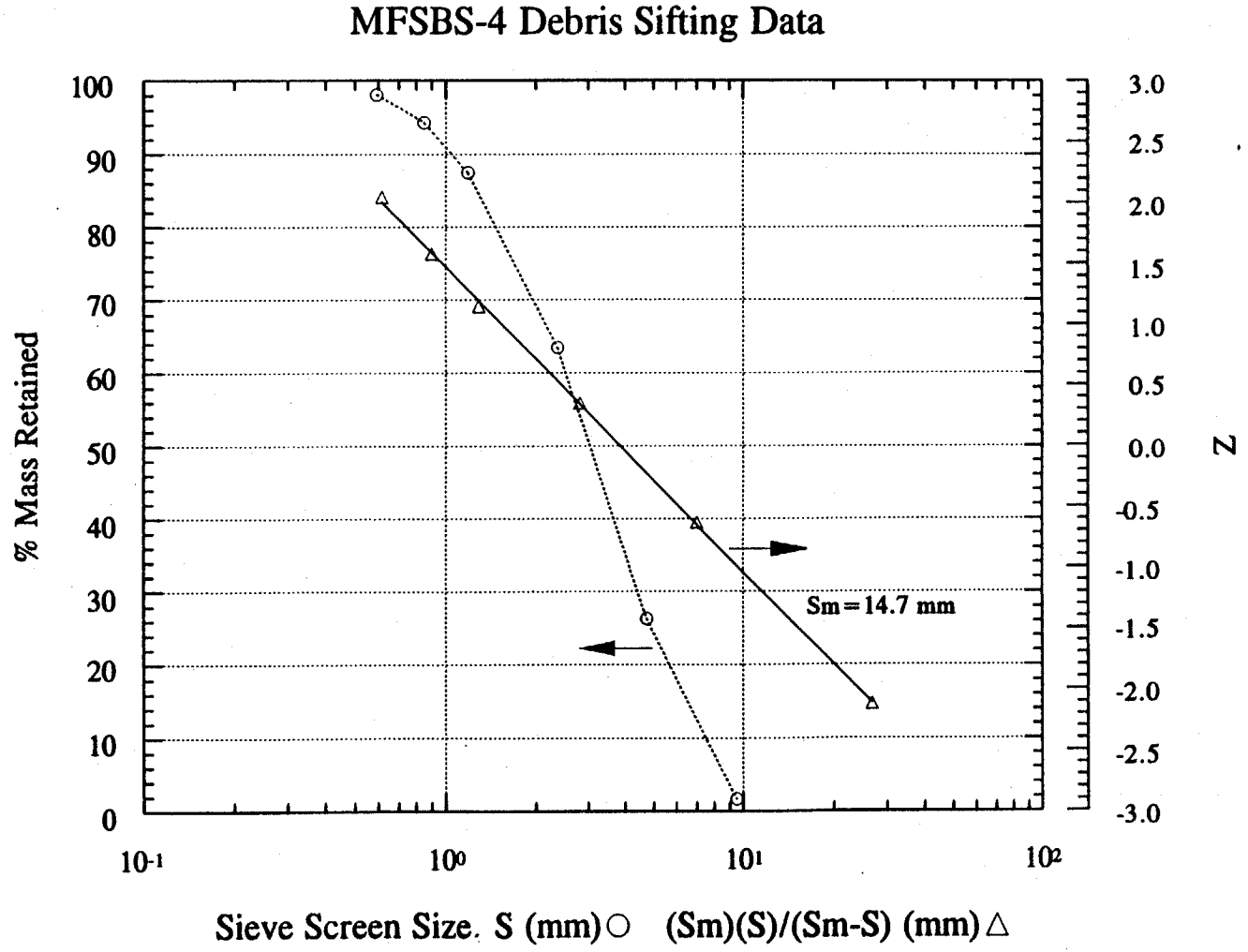
MFSBS-4 Debris Sifting Data
% Mass Retained
100
90
80
70
60
50
40
30
20
10
0
10-1
100
101
102
3.0
2.5
2.0
1.5
1.0
0.5
0.0
-0.5
-1.0
-1.5
-2.0
-2.5
-3.0
Z
Sm=14.7 mm
Sieve Screen Size. S (mm)○ (Sm)(S)/(Sm-S) (mm)△

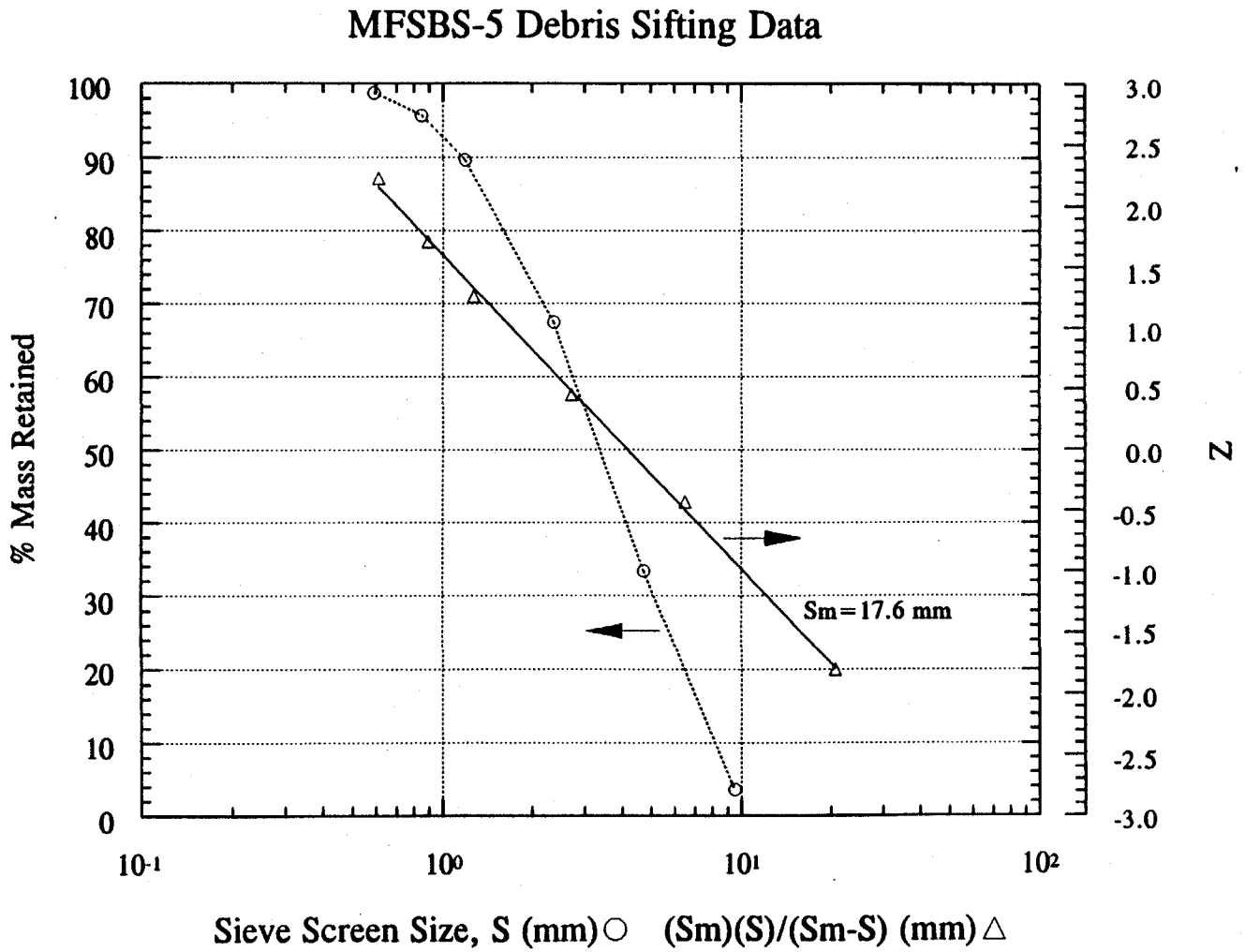
MFSBS-5 Debris Sifting Data
% Mass Retained
100
90
80
70
60
50
40
30
20
10
0
10-1
100
101
102
3.0
2.5
2.0
1.5
1.0
0.5
0.0
-0.5
-1.0
-1.5
-2.0
-2.5
-3.0
Z
Sm=17.6 mm
Sieve Screen Size, S (mm)○ (Sm)(S)/(Sm-S) (mm)△

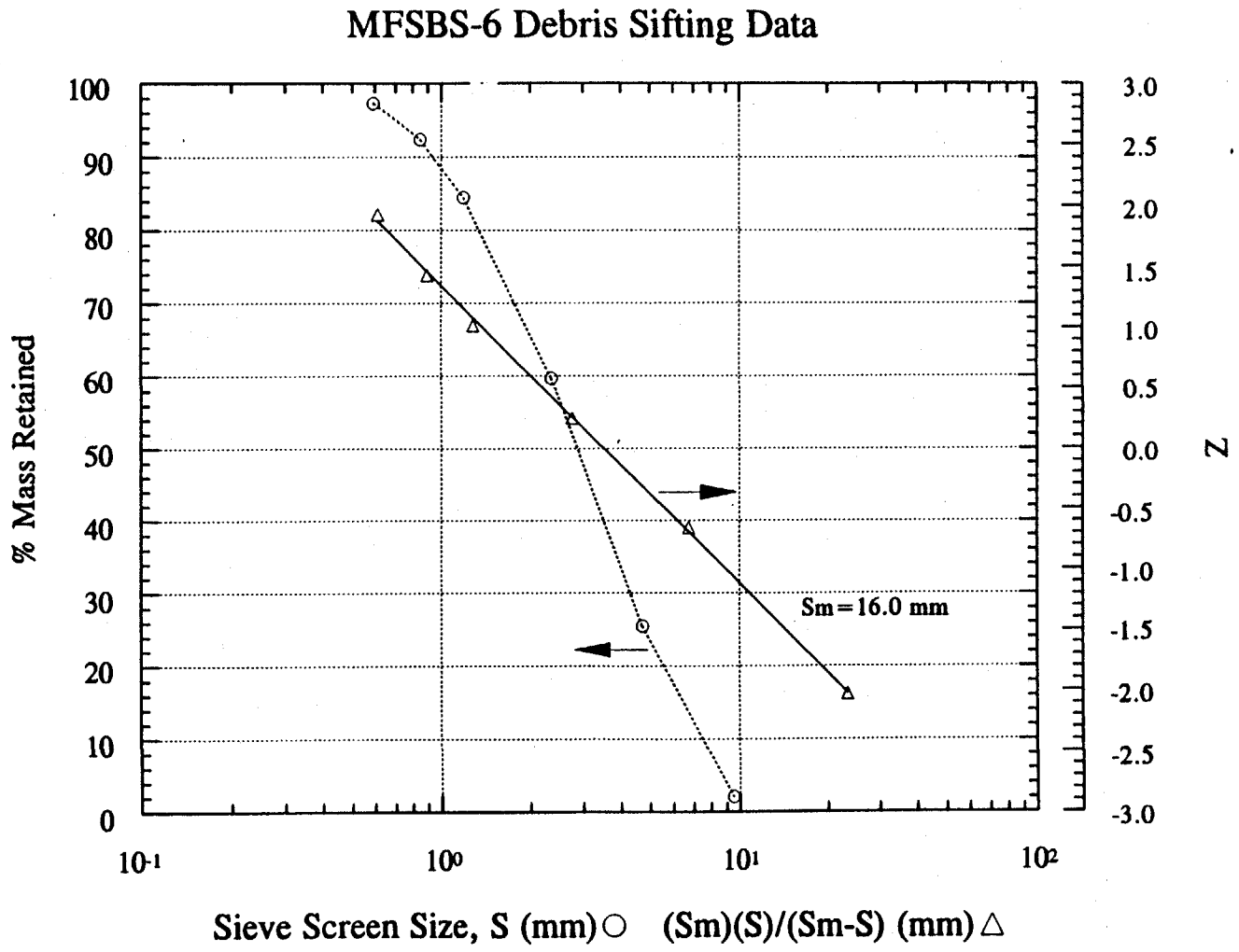
MFSBS-6 Debris Sifting Data
% Mass Retained
100
90
80
70
60
50
40
30
20
10
0
10-1
100
101
102
3.0
2.5
2.0
1.5
1.0
0.5
0.0
-0.5
-1.0
-1.5
-2.0
-2.5
-3.0
Z
Sm=16.0 mm
Sieve Screen Size, S (mm)○ (Sm)(S)/(Sm-S) (mm)△

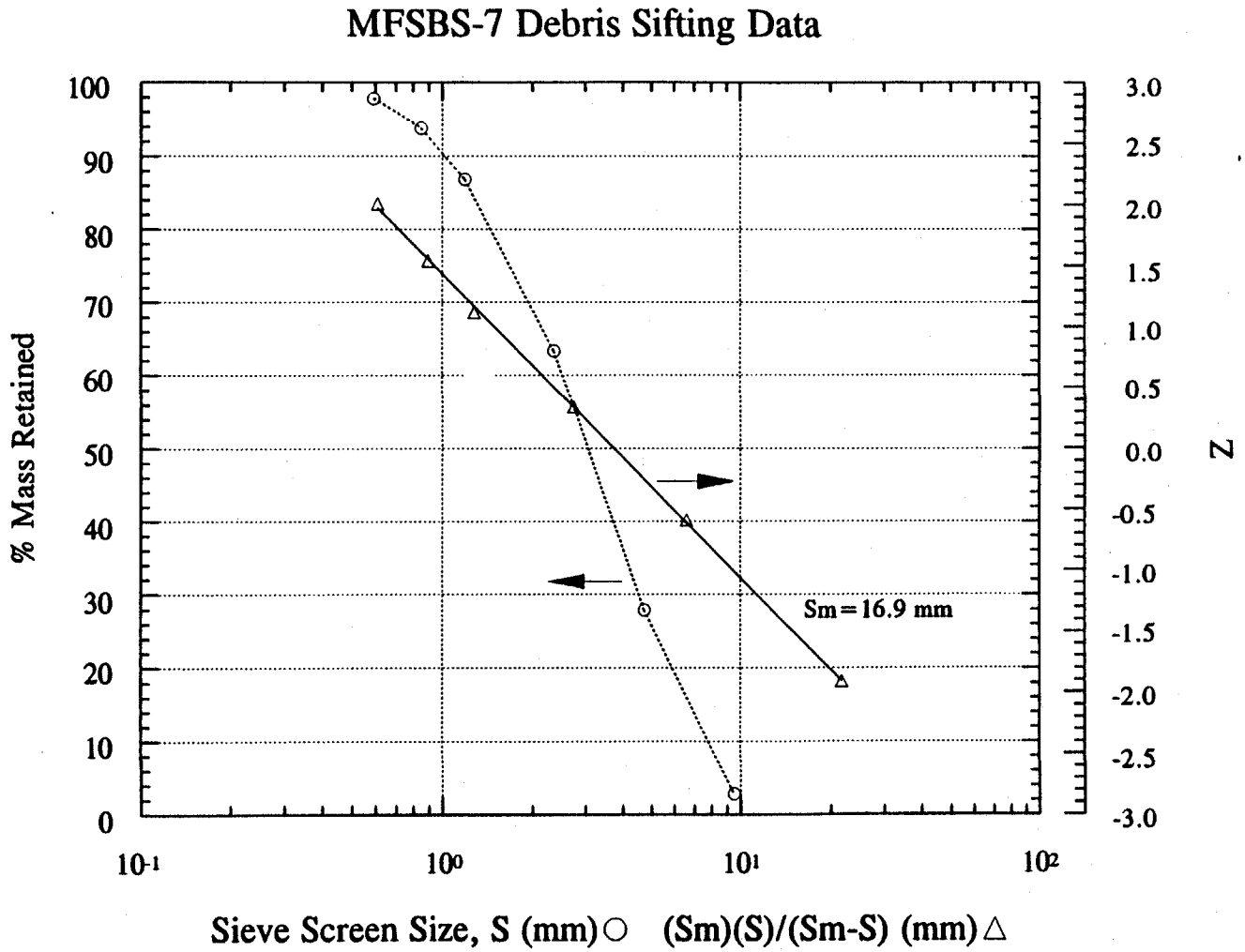
MFSBS-7 Debris Sifting Data
% Mass Retained
100
90
80
70
60
50
40
30
20
10
0
10-1
100
101
102
3.0
2.5
2.0
1.5
1.0
0.5
0.0
-0.5
-1.0
-1.5
-2.0
-2.5
-3.0
Z
Sm = 16.9 mm
Sieve Screen Size, S (mm)○ (Sm)(S)/(Sm-S) (mm)△

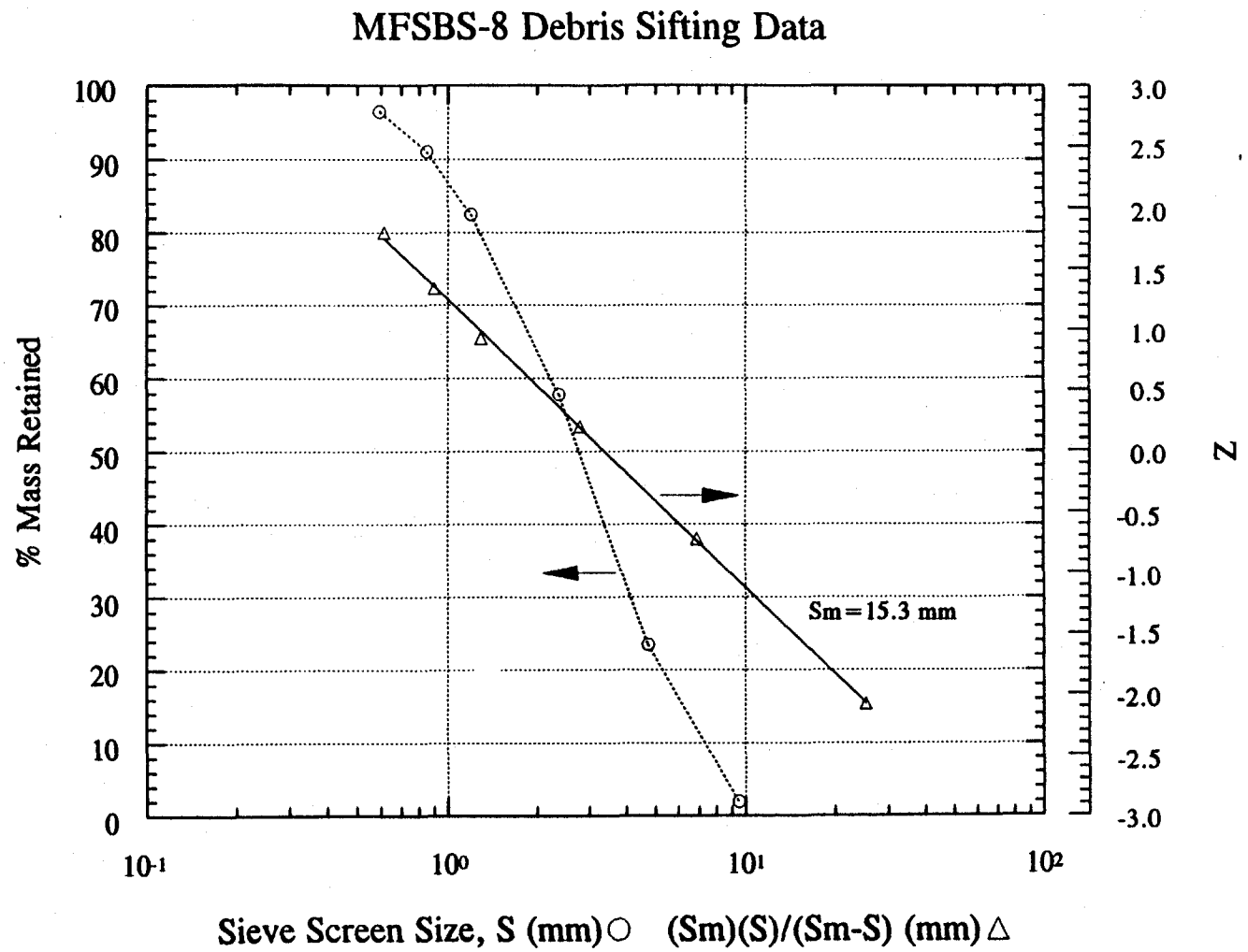
MFSBS-8 Debris Sifting Data
% Mass Retained
100
90
80
70
60
50
40
30
20
10
0
10-1
100
101
102
3.0
2.5
2.0
1.5
1.0
0.5
0.0
-0.5
-1.0
-1.5
-2.0
-2.5
-3.0
Z
Sm=15.3 mm
Sieve Screen Size, S (mm)○ (Sm)(S)/(Sm-S) (mm)△

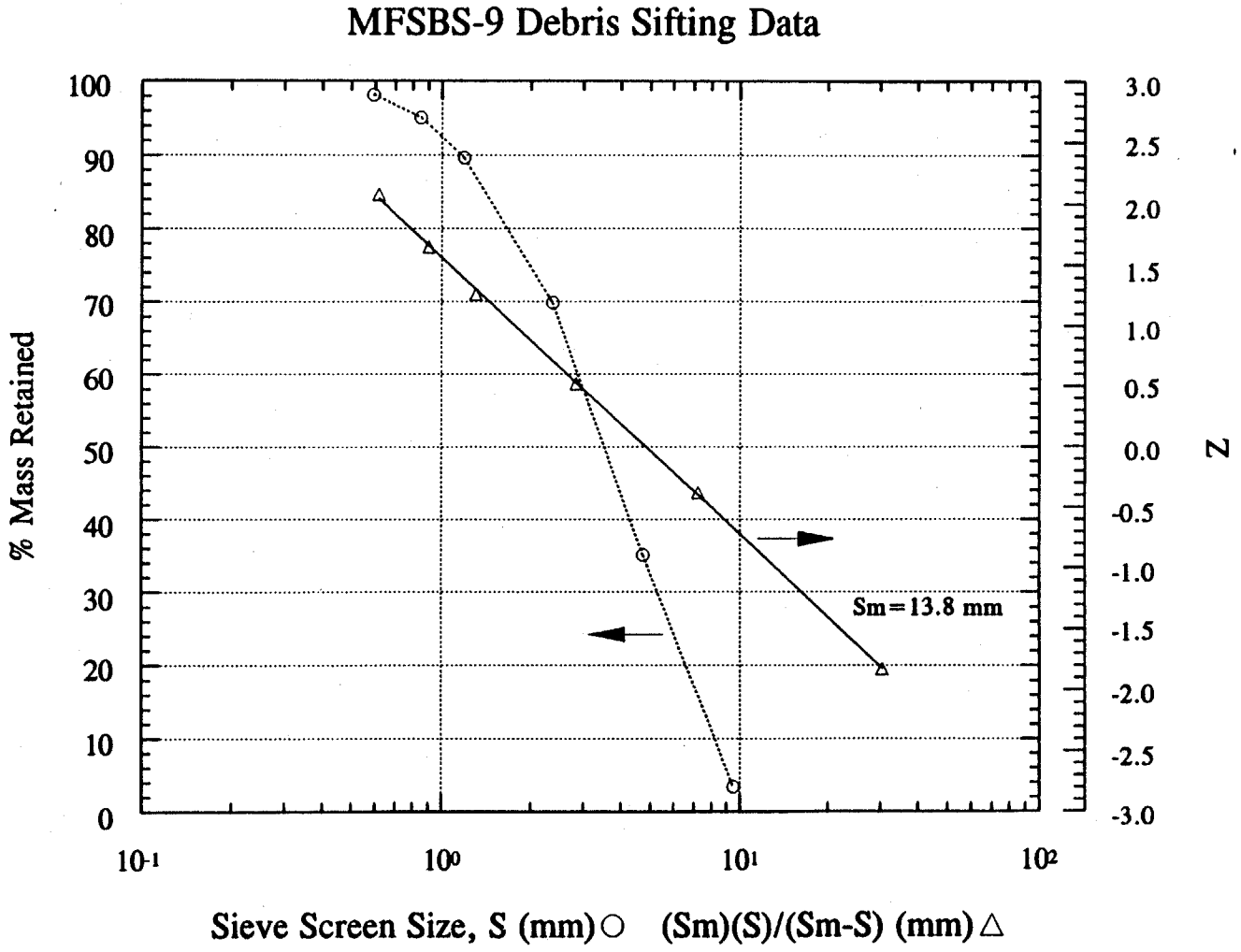
MFSBS-9 Debris Sifting Data
% Mass Retained
100
90
80
70
60
50
40
30
20
10
0
10-1
100
101
102
3.0
2.5
2.0
1.5
1.0
0.5
0.0
-0.5
-1.0
-1.5
-2.0
-2.5
-3.0
Z
Sm=13.8 mm
Sieve Screen Size, S (mm)○ (Sm)(S)/(Sm-S) (mm)△

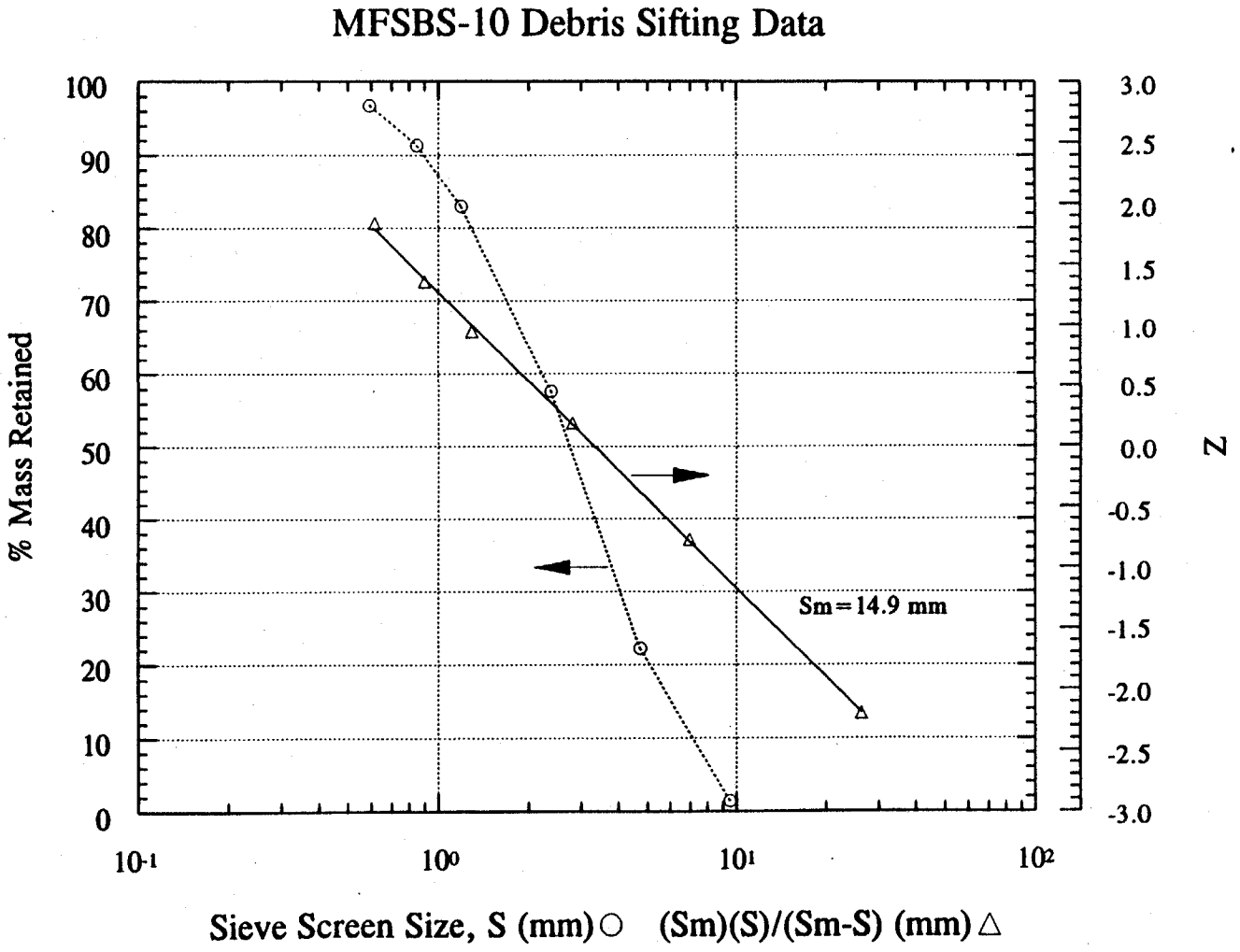
MFSBS-10 Debris Sifting Data
% Mass Retained
100
90
80
70
60
50
40
30
20
10
0
10-1
100
101
102
3.0
2.5
2.0
1.5
1.0
0.5
0.0
-0.5
-1.0
-1.5
-2.0
-2.5
-3.0
Z
Sm=14.9 mm
Sieve Screen Size, S (mm)○ (Sm)(S)/(Sm-S) (mm)△

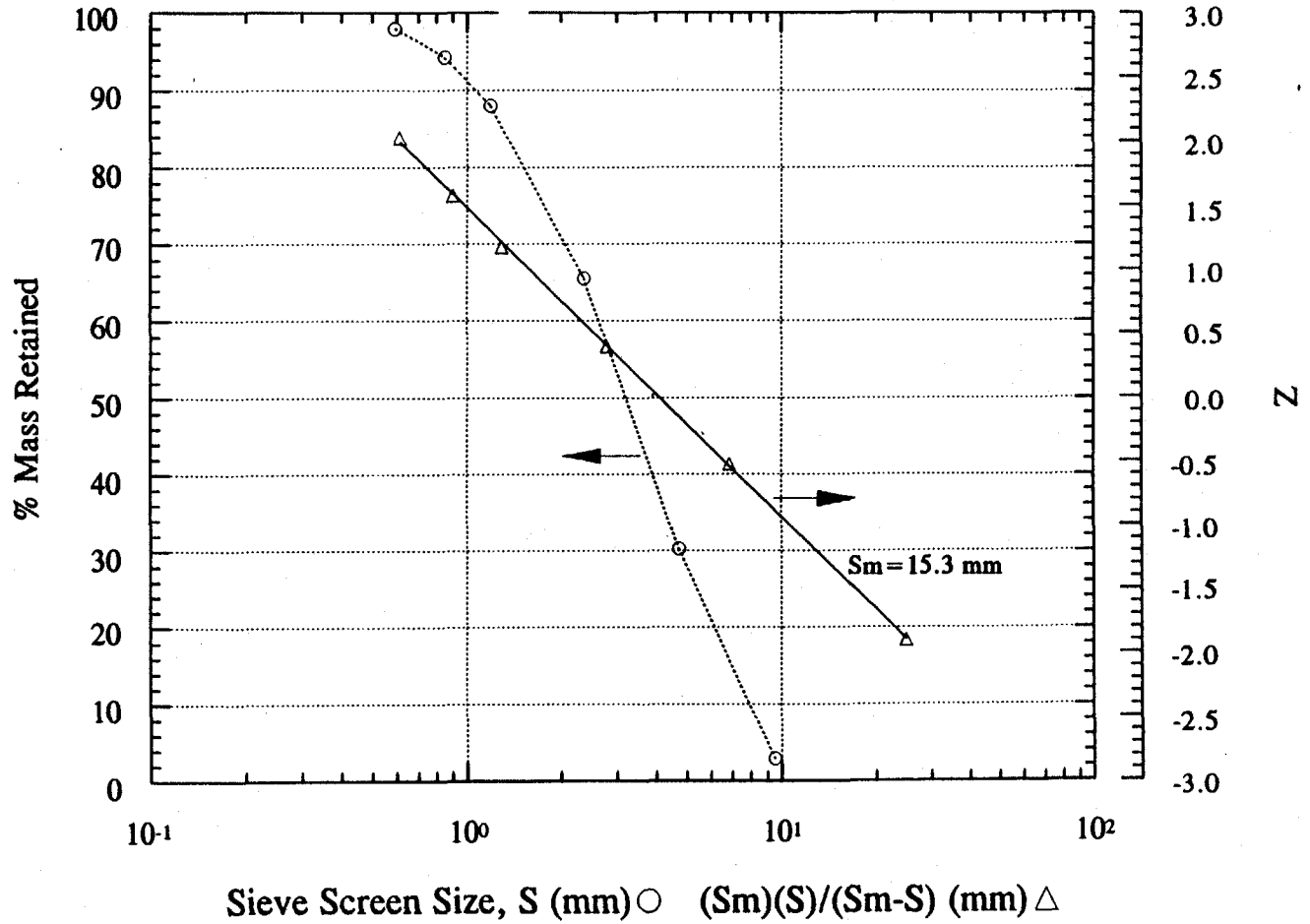
MFSBS-11 Debris Sifting Data
% Mass Retained
100
90
80
70
60
50
40
30
20
10
0
10-1
100
101
102
3.0
2.5
2.0
1.5
1.0
0.5
0.0
-0.5
-1.0
-1.5
-2.0
-2.5
-3.0
Z
Sm=15.3 mm
Sieve Screen Size, S (mm)○ (Sm)(S)/(Sm-S) (mm)△

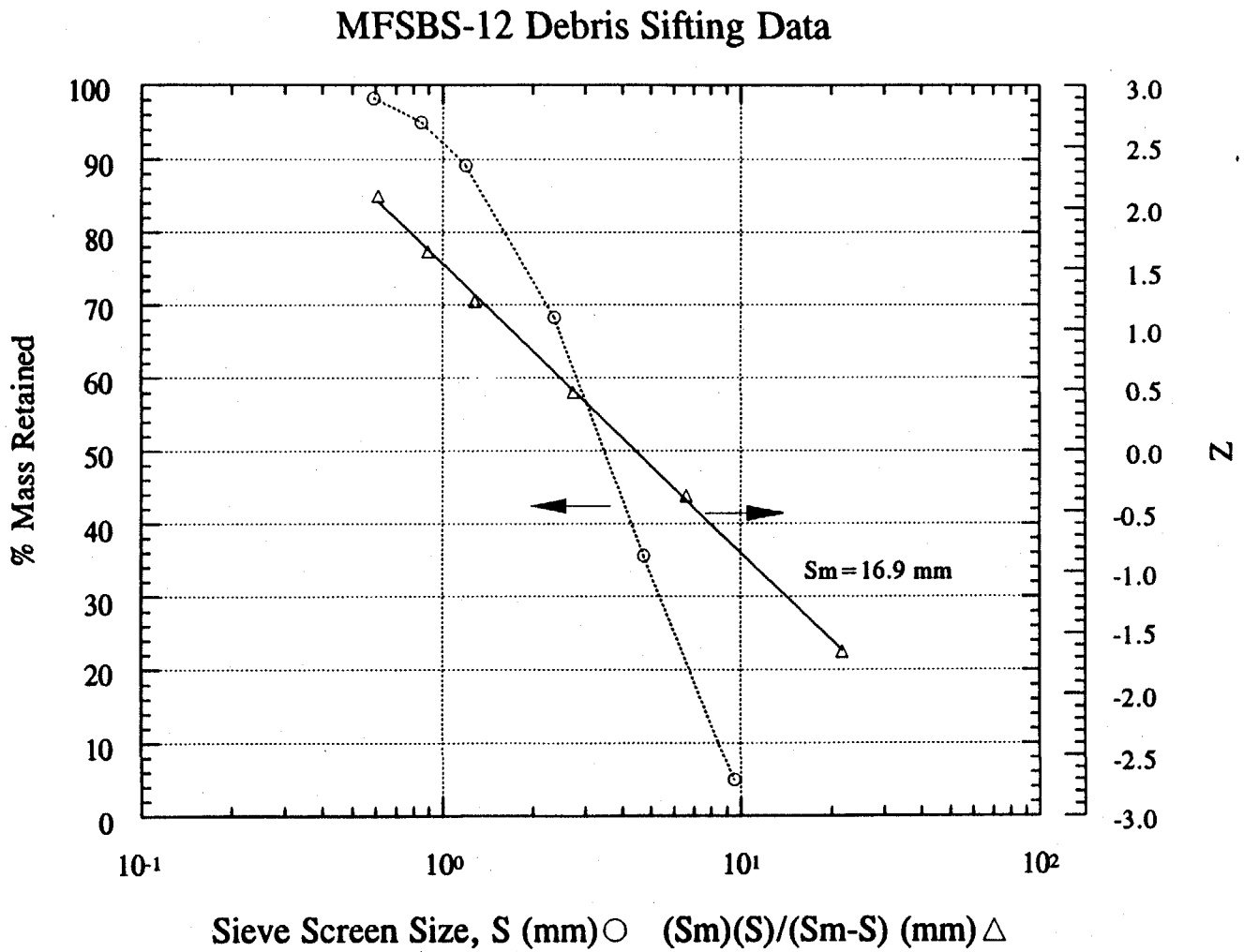
MFSBS-12 Debris Sifting Data
% Mass Retained
100
90
80
70
60
50
40
30
20
10
0
10-1
100
101
102
3.0
2.5
2.0
1.5
1.0
0.5
0.0
-0.5
-1.0
-1.5
-2.0
-2.5
-3.0
Z
Sm=16.9 mm
Sieve Screen Size, S (mm)○ (Sm)(S)/(Sm-S) (mm)△

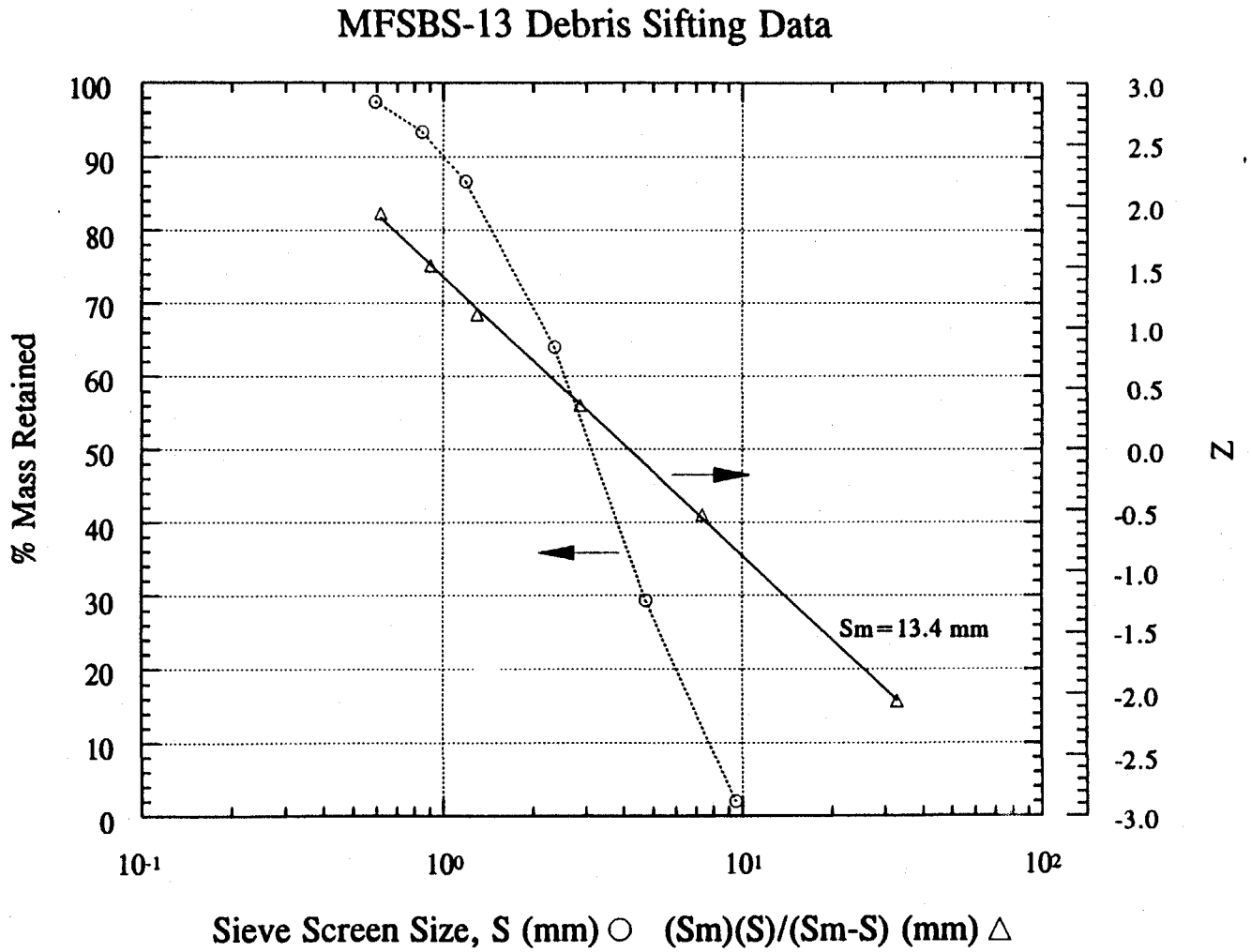
MFSBS-13 Debris Sifting Data
% Mass Retained
100
90
80
70
60
50
40
30
20
10
0
10-1
100
101
102
3.0
2.5
2.0
1.5
1.0
0.5
0.0
-0.5
-1.0
-1.5
-2.0
-2.5
-3.0
Z
Sm=13.4 mm
Sieve Screen Size, S (mm) ○ (Sm)(S)/(Sm-S) (mm) △

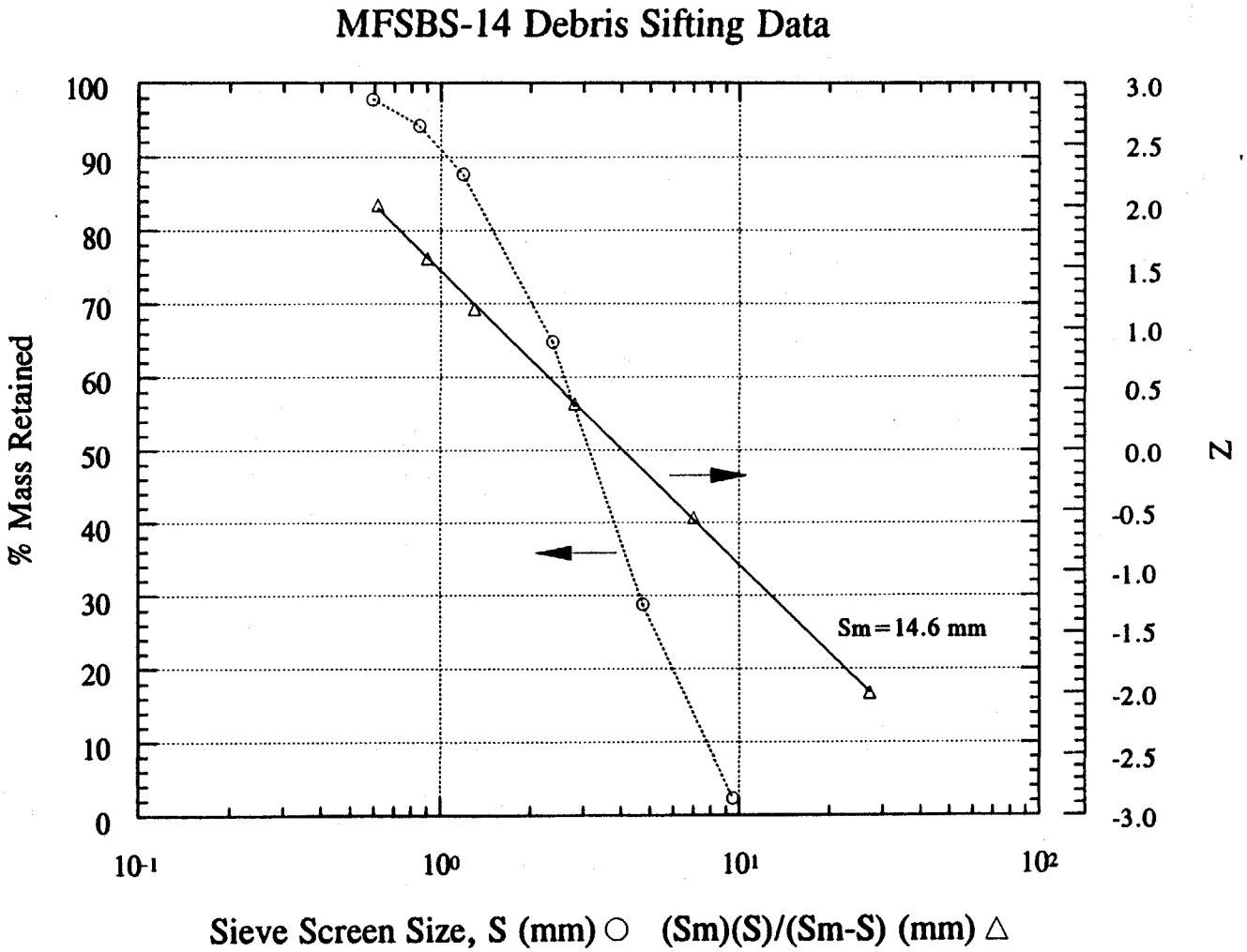
MFSBS-14 Debris Sifting Data
% Mass Retained
100
90
80
70
60
50
40
30
20
10
0
10-1
100
101
102
3.0
2.5
2.0
1.5
1.0
0.5
0.0
-0.5
-1.0
-1.5
-2.0
-2.5
-3.0
Z
Sm = 14.6 mm
Sieve Screen Size, S (mm) ○ (Sm)(S)/(Sm-S) (mm) △

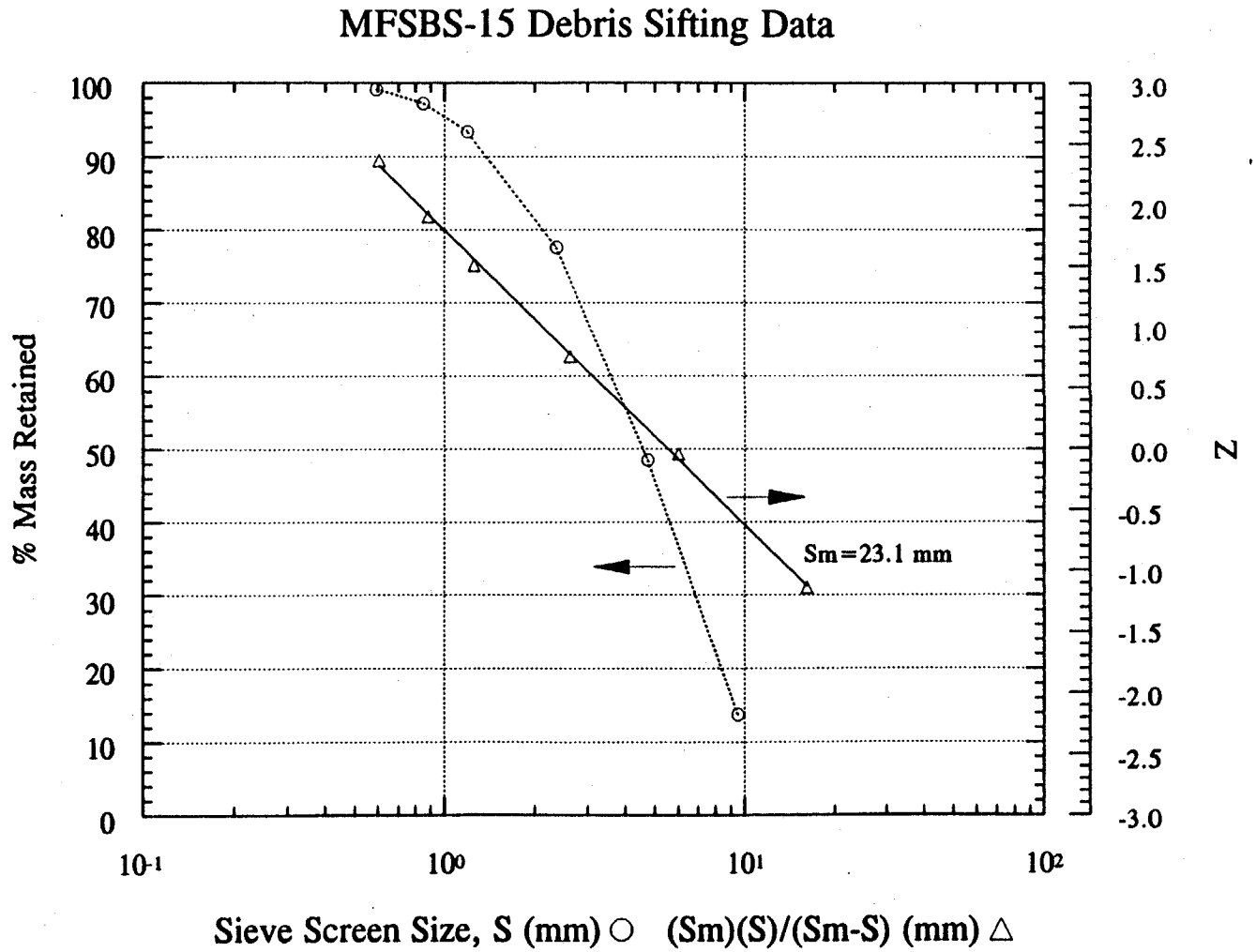
MFSBS-15 Debris Sifting Data
% Mass Retained
100
90
80
70
60
50
40
30
20
10
0
10-1
100
101
102
3.0
2.5
2.0
1.5
1.0
0.5
0.0
-0.5
-1.0
-1.5
-2.0
-2.5
-3.0
Z
Sm=23.1 mm
Sieve Screen Size, S (mm) ○ (Sm)(S)/(Sm-S) (mm) △

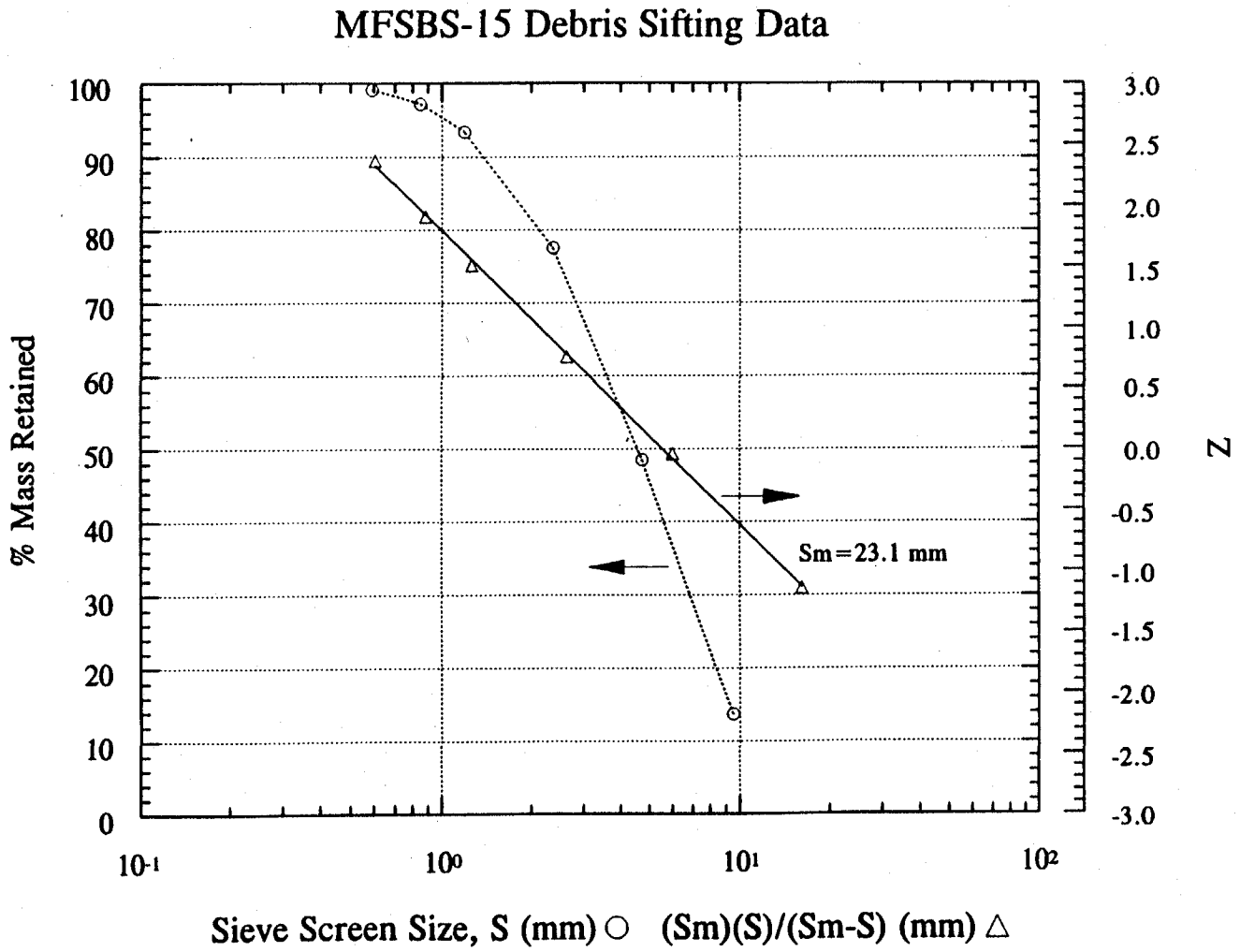
MFSBS-15 Debris Sifting Data
% Mass Retained
100
90
80
70
60
50
40
30
20
10
0
10-1
100
101
102
3.0
2.5
2.0
1.5
1.0
0.5
0.0
-0.5
-1.0
-1.5
-2.0
-2.5
-3.0
Z
Sm=23.1 mm
Sieve Screen Size, S (mm) ○ (Sm)(S)/(Sm-S) (mm) △

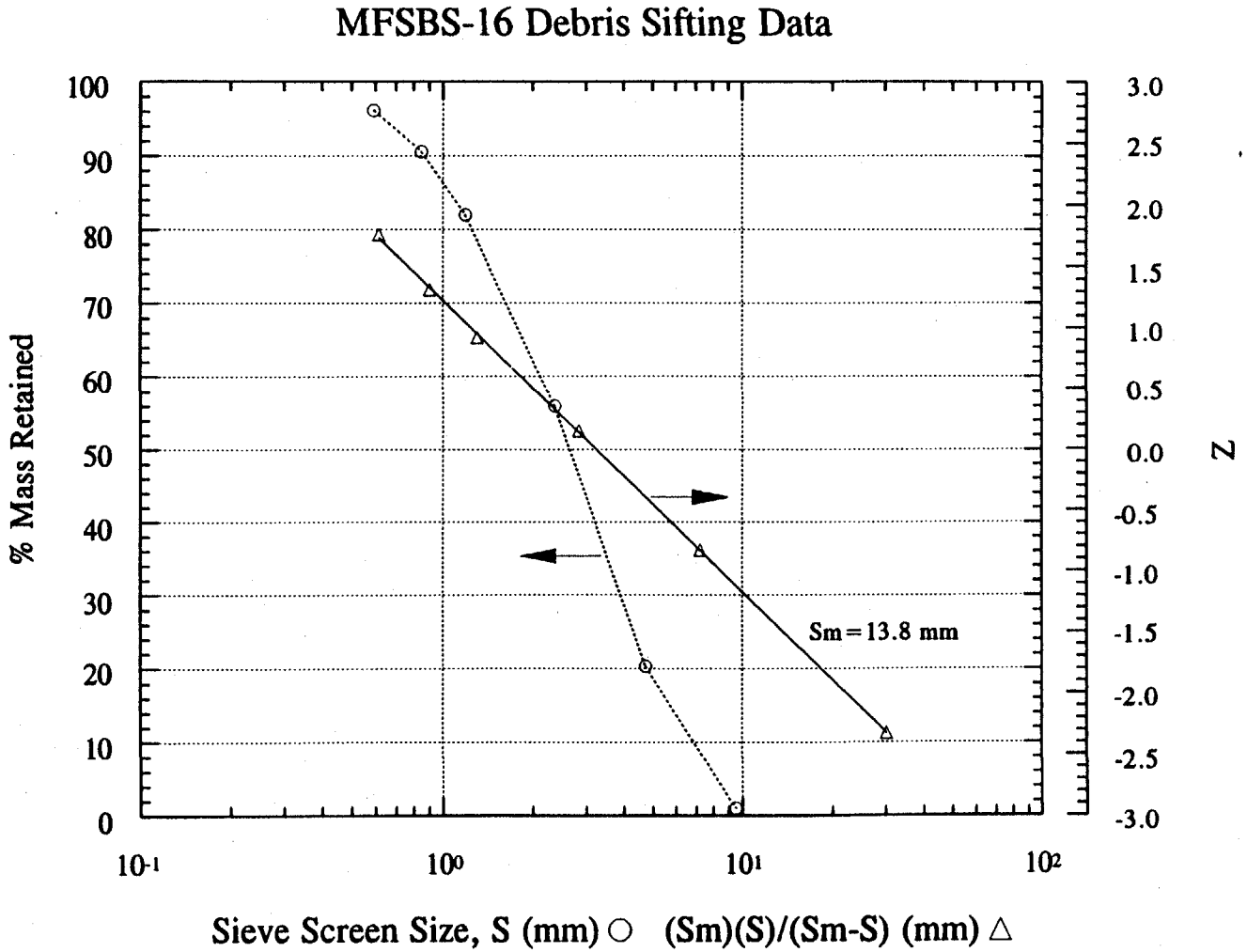
MFSBS-16 Debris Sifting Data
% Mass Retained
100
90
80
70
60
50
40
30
20
10
0
10-1
100
101
102
3.0
2.5
2.0
1.5
1.0
0.5
0.0
-0.5
-1.0
-1.5
-2.0
-2.5
-3.0
Z
Sm = 13.8 mm
Sieve Screen Size, S (mm) ○ (Sm)(S)/(Sm-S) (mm) △

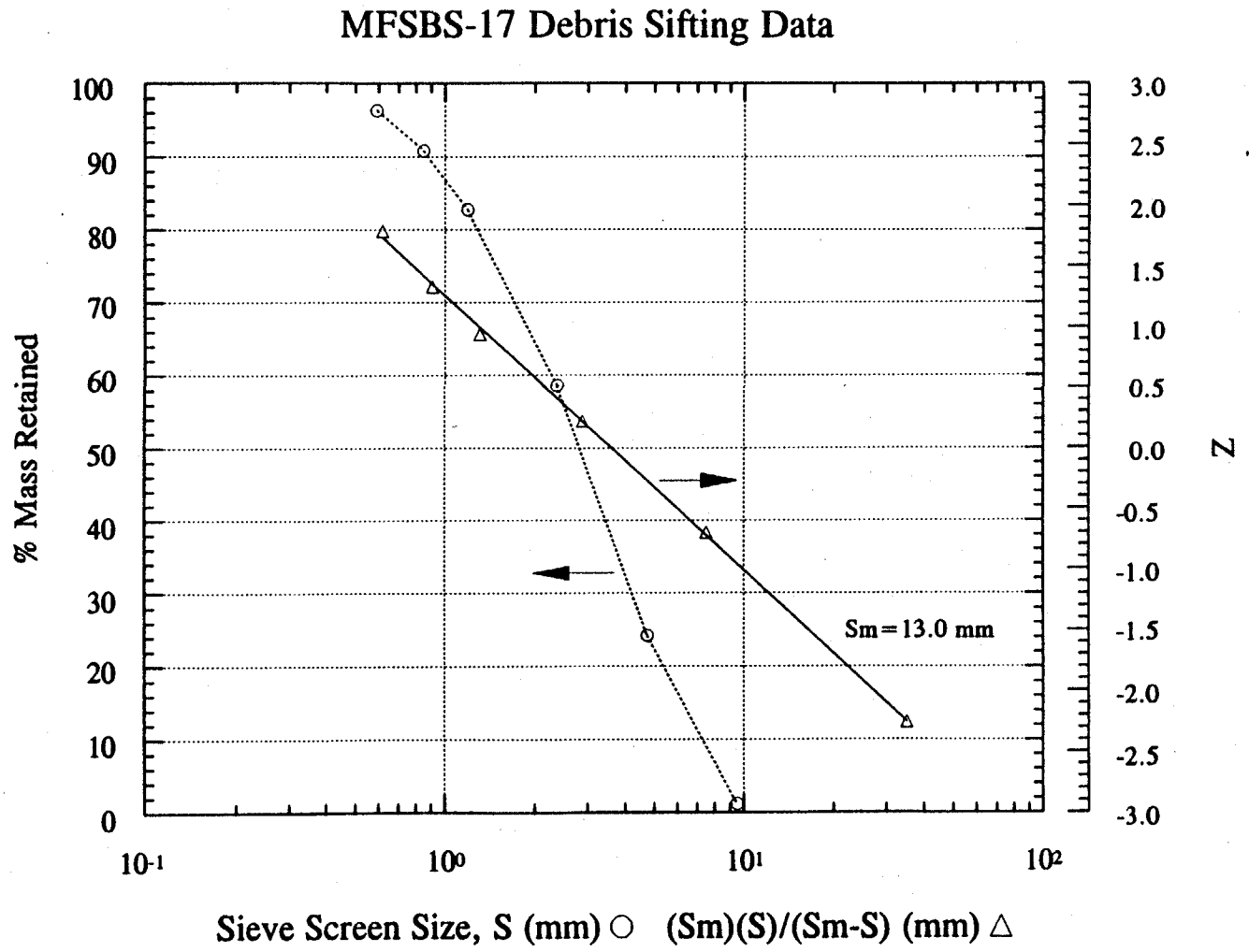
MFSBS-17 Debris Sifting Data
% Mass Retained
100
90
80
70
60
50
40
30
20
10
0
10-1
100
101
102
3.0
2.5
2.0
1.5
1.0
0.5
0.0
-0.5
-1.0
-1.5
-2.0
-2.5
-3.0
Z
Sm = 13.0 mm
Sieve Screen Size, S (mm) ○ (Sm)(S)/(Sm-S) (mm) △

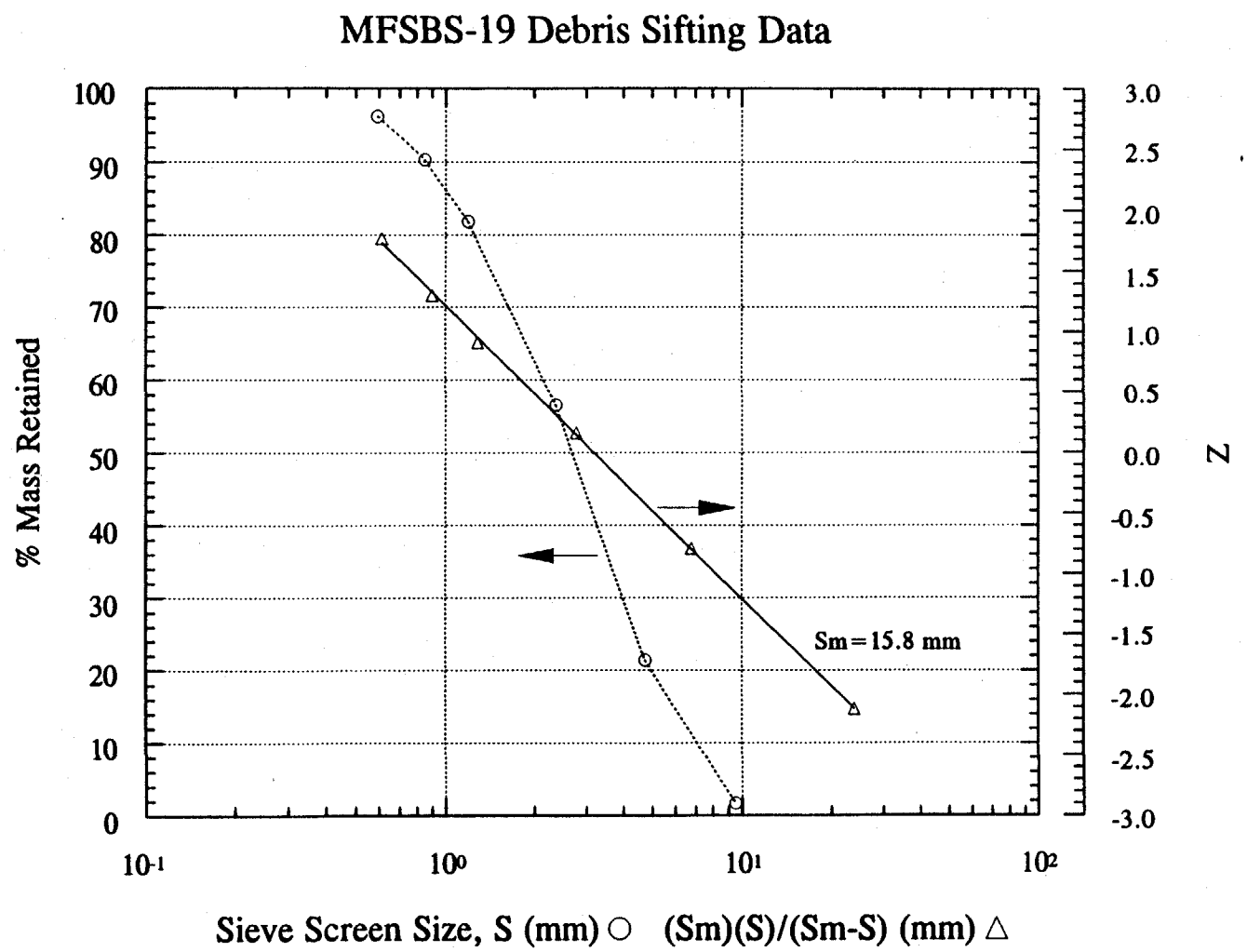
MFSBS-19 Debris Sifting Data
% Mass Retained
100
90
80
70
60
50
40
30
20
10
0
10-1
100
101
102
3.0
2.5
2.0
1.5
1.0
0.5
0.0
-0.5
-1.0
-1.5
-2.0
-2.5
-3.0
Z
Sm=15.8 mm
Sieve Screen Size, S (mm) ○ (Sm)(S)/(Sm-S) (mm) △

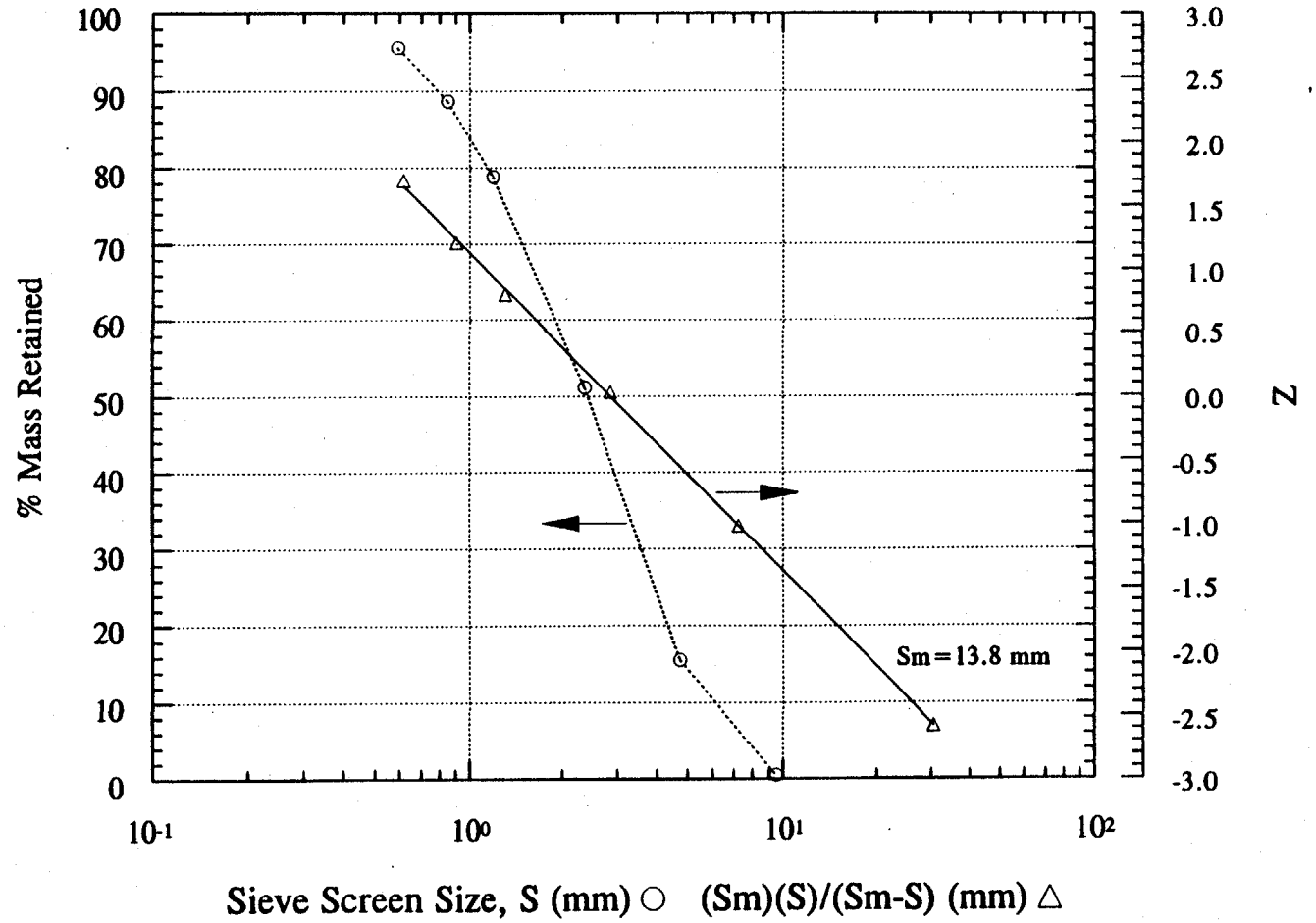
MFSBS-20 Debris Sifting Data
% Mass Retained
100
90
80
70
60
50
40
30
20
10
0
10-1
100
101
102
3.0
2.5
2.0
1.5
1.0
0.5
0.0
-0.5
-1.0
-1.5
-2.0
-2.5
-3.0
Z
Sm=13.8 mm
Sieve Screen Size, S (mm) ○ (Sm)(S)/(Sm-S) (mm) △

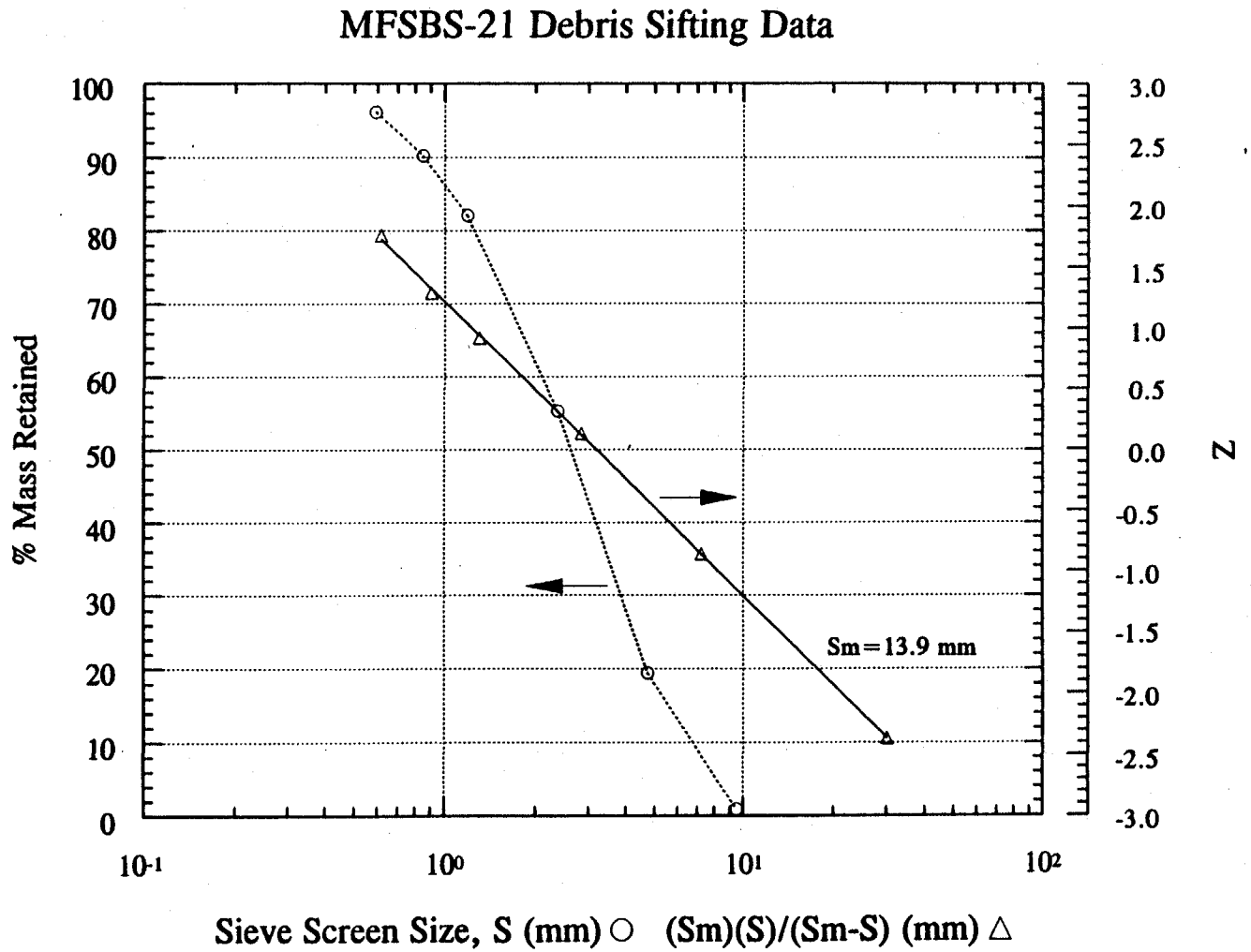
MFSBS-21 Debris Sifting Data
% Mass Retained
100
90
80
70
60
50
40
30
20
10
0
10-1
100
101
102
3.0
2.5
2.0
1.5
1.0
0.5
0.0
-0.5
-1.0
-1.5
-2.0
-2.5
-3.0
Z
Sm=13.9 mm
Sieve Screen Size, S (mm) ○ (Sm)(S)/(Sm-S) (mm) △

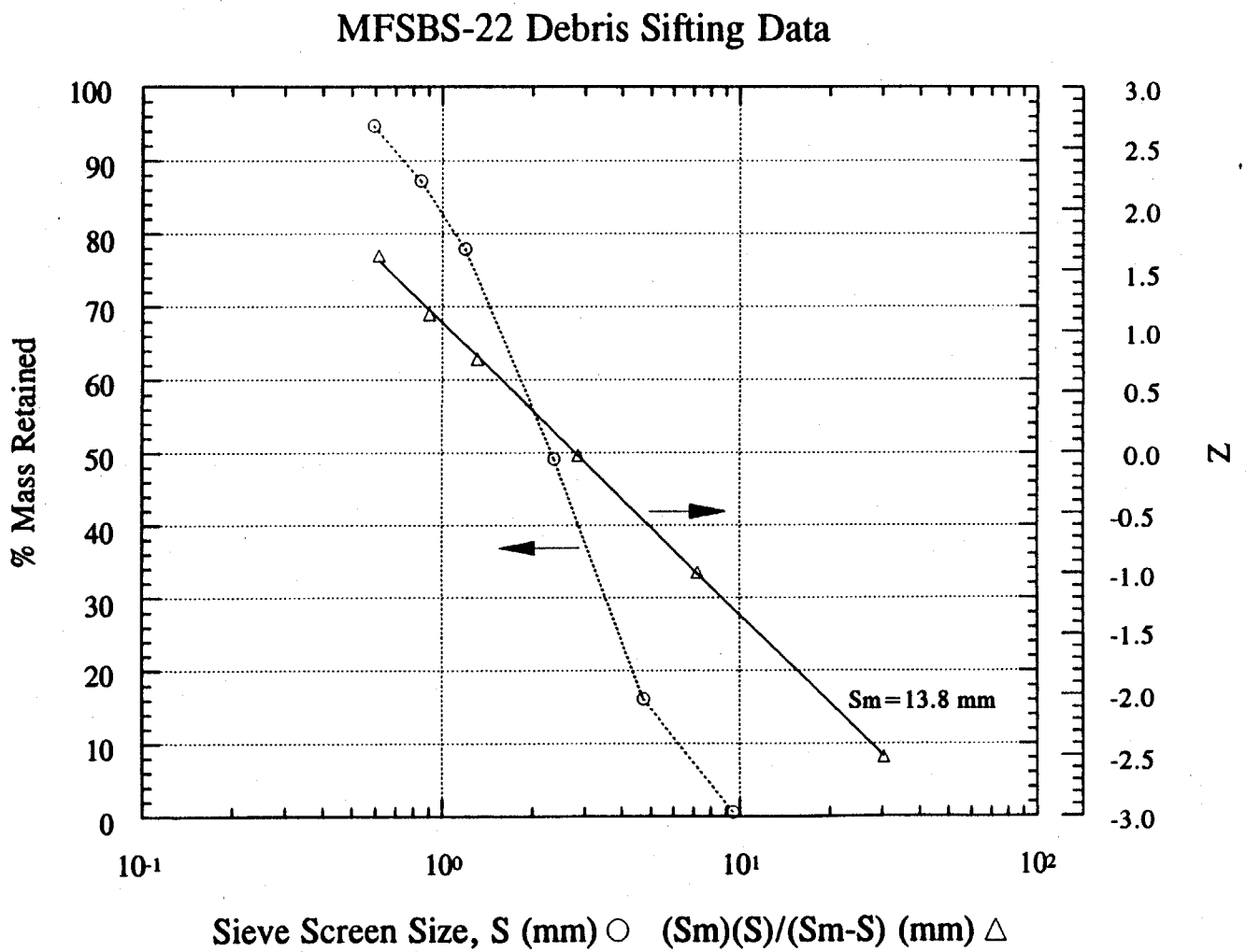
MFSBS-22 Debris Sifting Data
% Mass Retained
100
90
80
70
60
50
40
30
20
10
0
10-1
100
101
102
3.0
2.5
2.0
1.5
1.0
0.5
0.0
-0.5
-1.0
-1.5
-2.0
-2.5
-3.0
Z
Sm = 13.8 mm
Sieve Screen Size, S (mm) ○ (Sm)(S)/(Sm-S) (mm) △

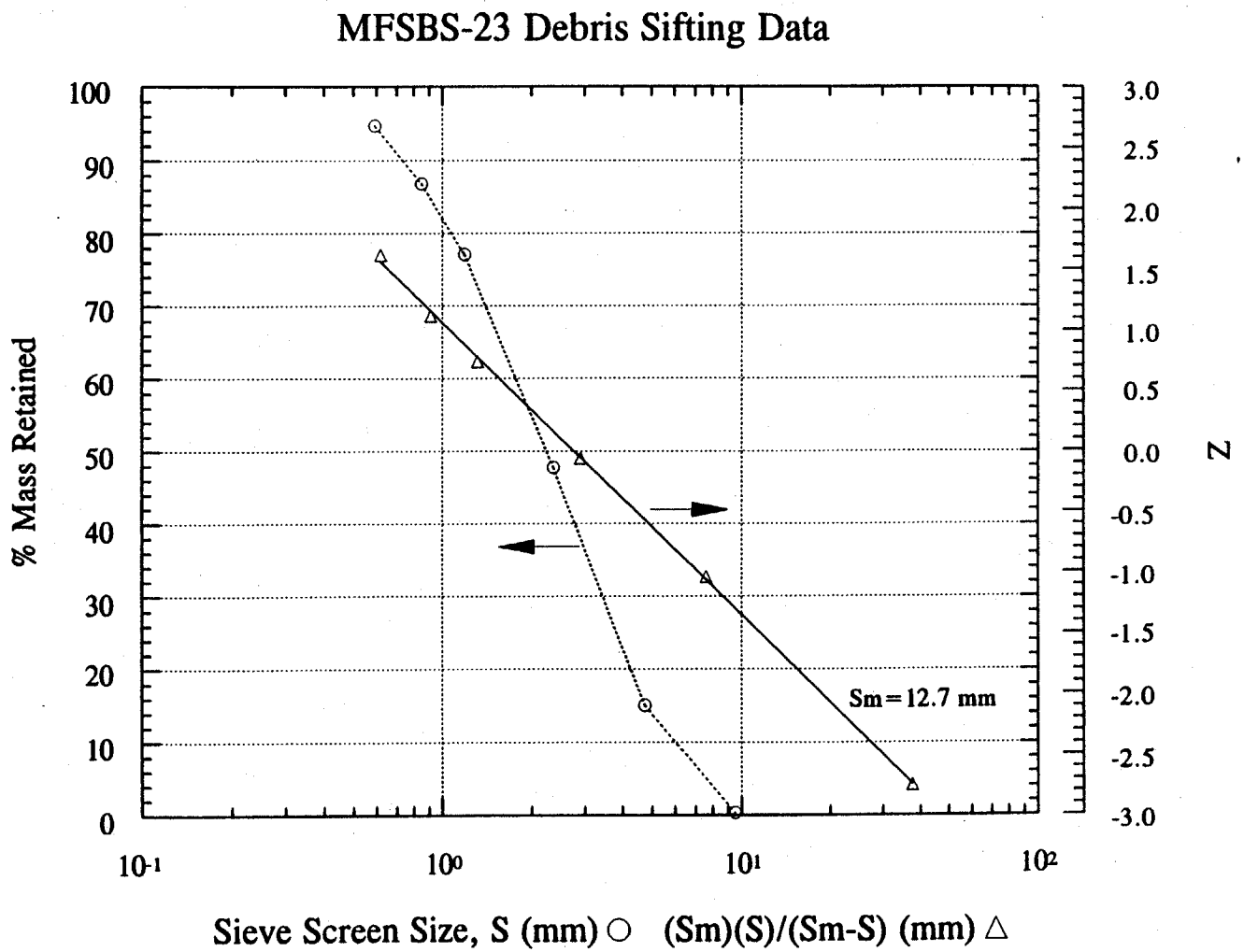
MFSBS-23 Debris Sifting Data
% Mass Retained
100
90
80
70
60
50
40
30
20
10
0
10-1
100
101
102
3.0
2.5
2.0
1.5
1.0
0.5
0.0
-0.5
-1.0
-1.5
-2.0
-2.5
-3.0
Z
Sm=12.7 mm
Sieve Screen Size, S (mm) ○ (Sm)(S)/(Sm-S) (mm) △

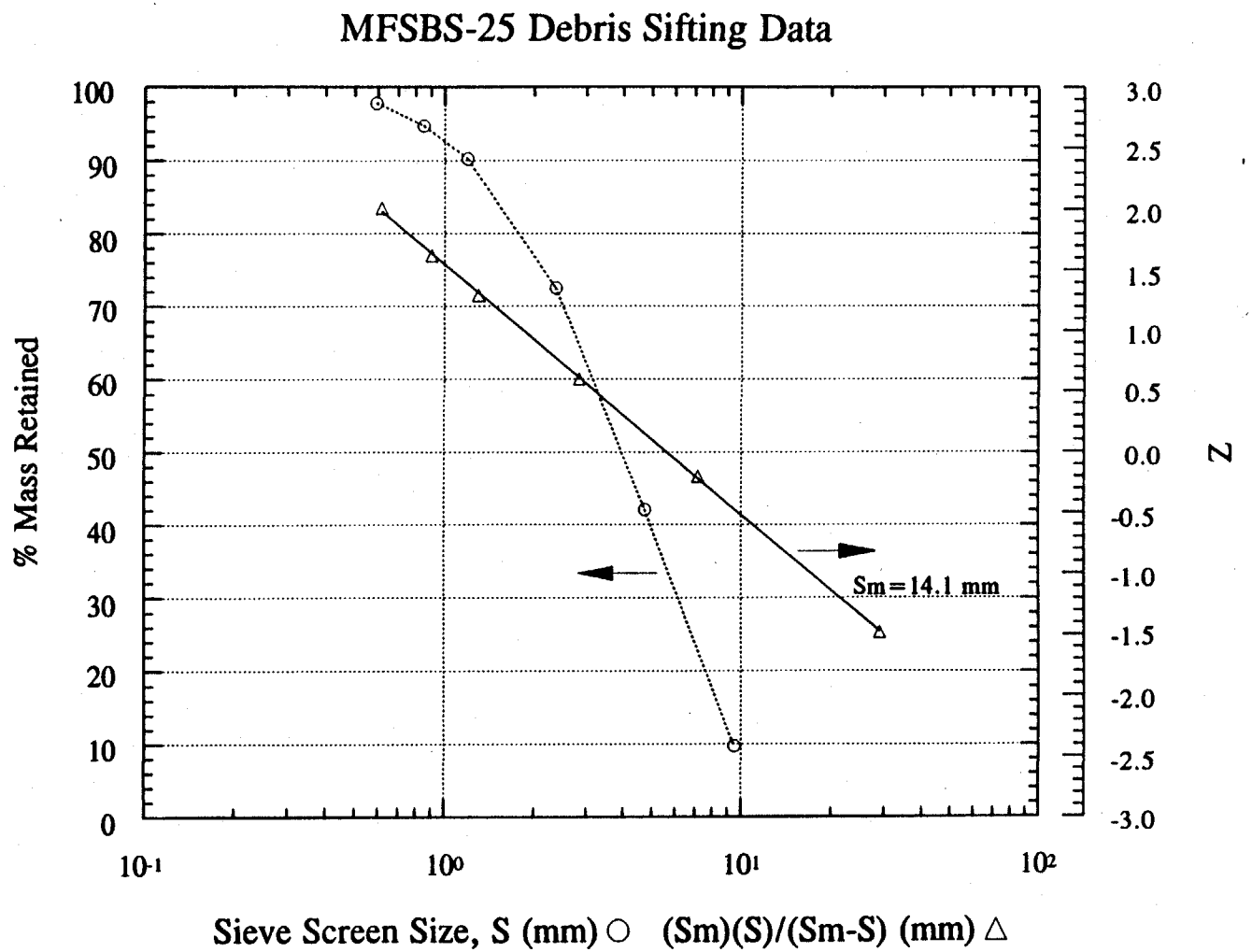
MFSBS-25 Debris Sifting Data
% Mass Retained
100
90
80
70
60
50
40
30
20
10
0
10-1
100
101
102
3.0
2.5
2.0
1.5
1.0
0.5
0.0
-0.5
-1.0
-1.5
-2.0
-2.5
-3.0
Z
Sm = 14.1 mm
Sieve Screen Size, S (mm) ○ (Sm)(S)/(Sm-S) (mm) △

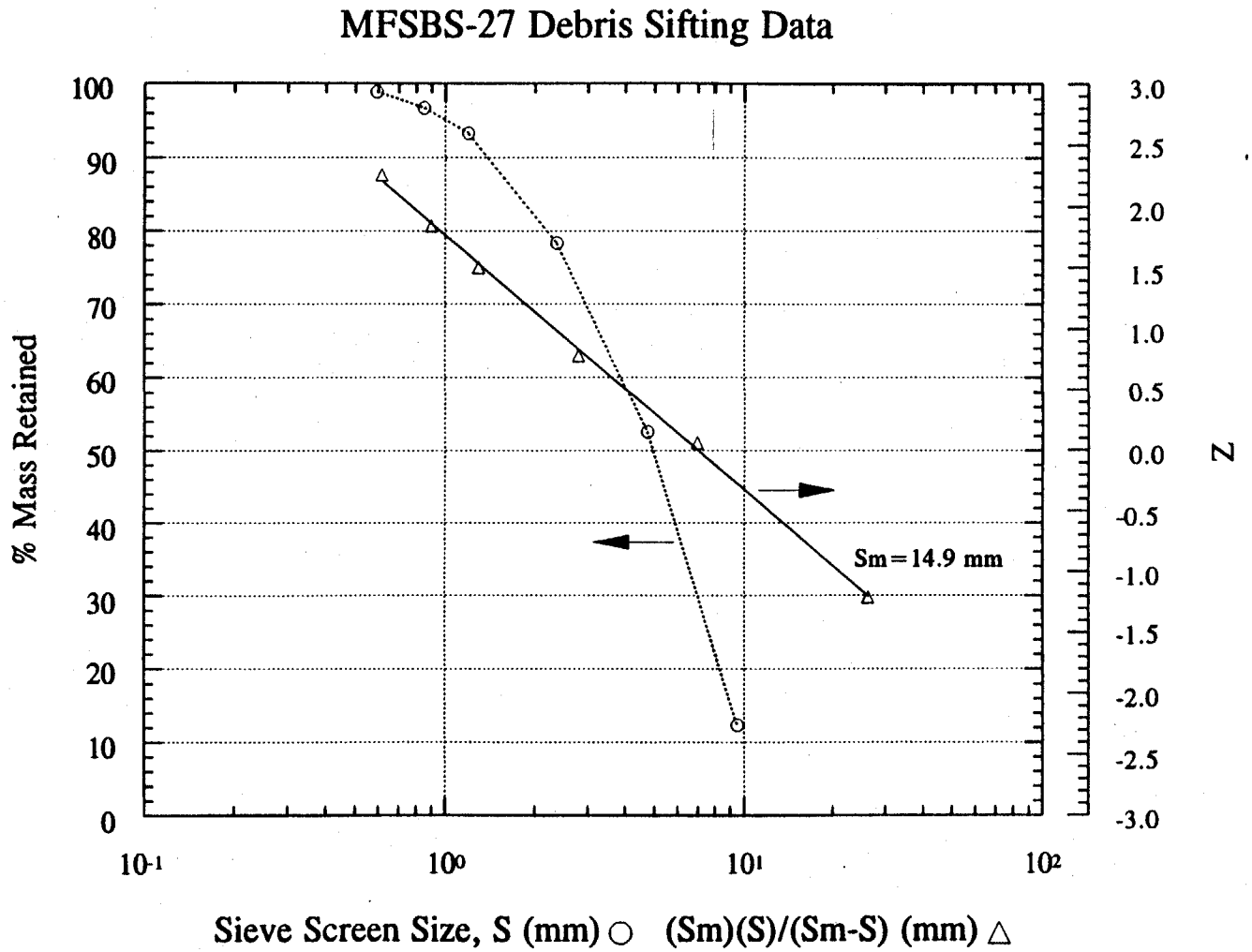
MFSBS-27 Debris Sifting Data
% Mass Retained
100
90
80
70
60
50
40
30
20
10
0
10-1
100
101
102
3.0
2.5
2.0
1.5
1.0
0.5
0.0
-0.5
-1.0
-1.5
-2.0
-2.5
-3.0
Z
Sm = 14.9 mm
Sieve Screen Size, S (mm) ○ (Sm)(S)/(Sm-S) (mm) △

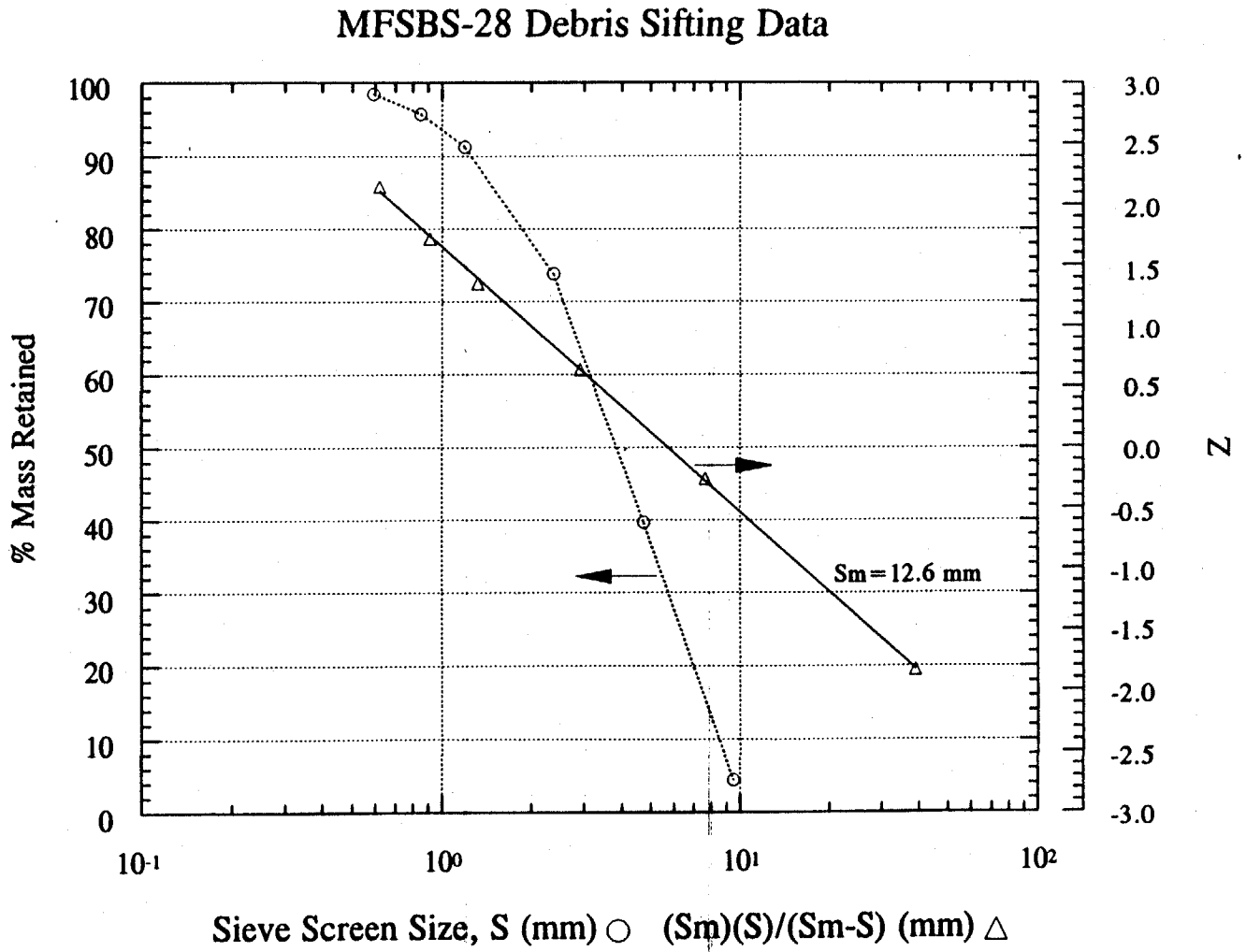
MFSBS-28 Debris Sifting Data
% Mass Retained
100
90
80
70
60
50
40
30
20
10
0
10-1
100
101
102
3.0
2.5
2.0
1.5
1.0
0.5
0.0
-0.5
-1.0
-1.5
-2.0
-2.5
-3.0
Z
Sm = 12.6 mm
Sieve Screen Size, S (mm) ○ (Sm)(S)/(Sm-S) (mm) △

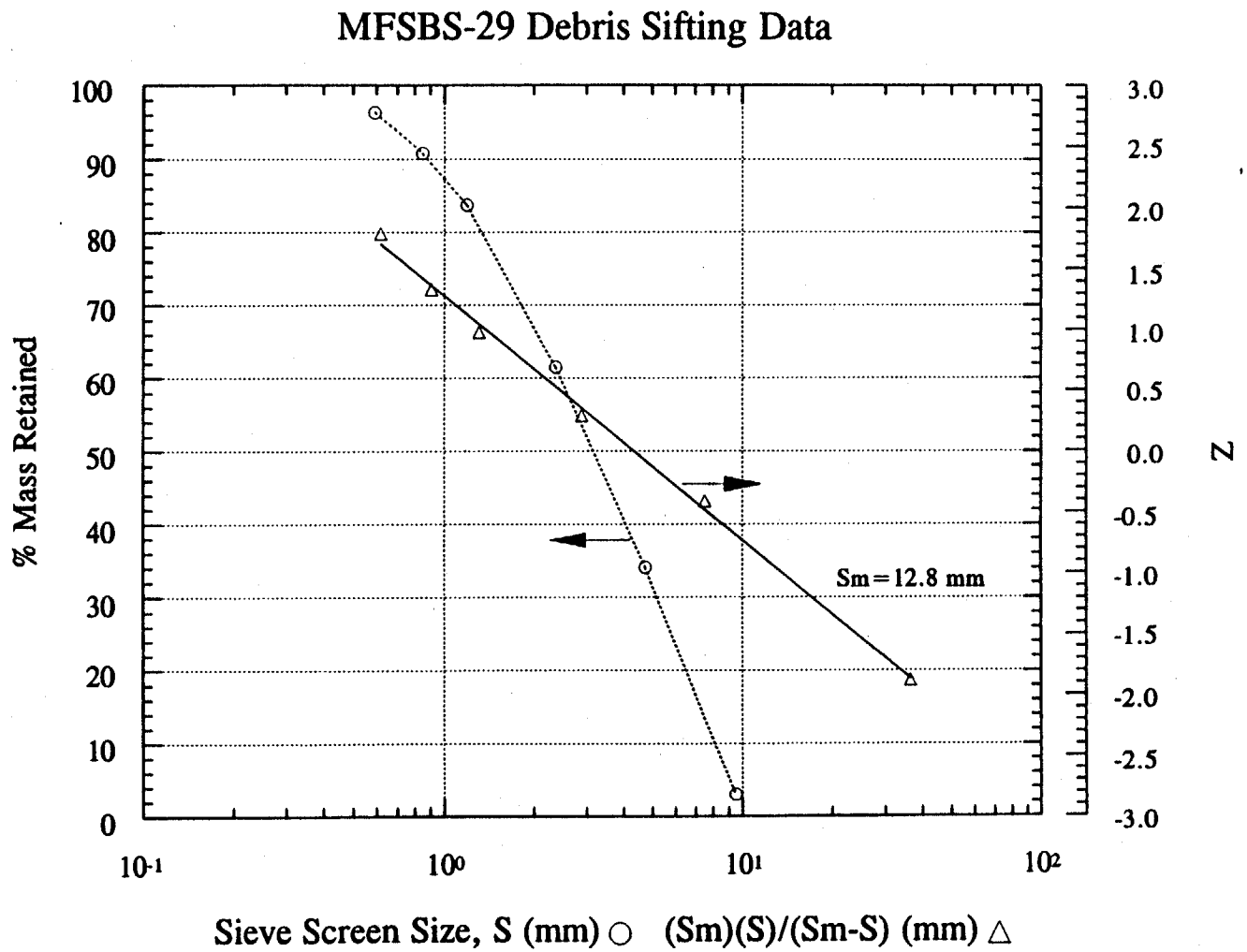
MFSBS-29 Debris Sifting Data
% Mass Retained
100
90
80
70
60
50
40
30
20
10
0
10-1
100
101
102
3.0
2.5
2.0
1.5
1.0
0.5
0.0
-0.5
-1.0
-1.5
-2.0
-2.5
-3.0
Z
Sm = 12.8 mm
Sieve Screen Size, S (mm) ○ (Sm)(S)/(Sm-S) (mm) △

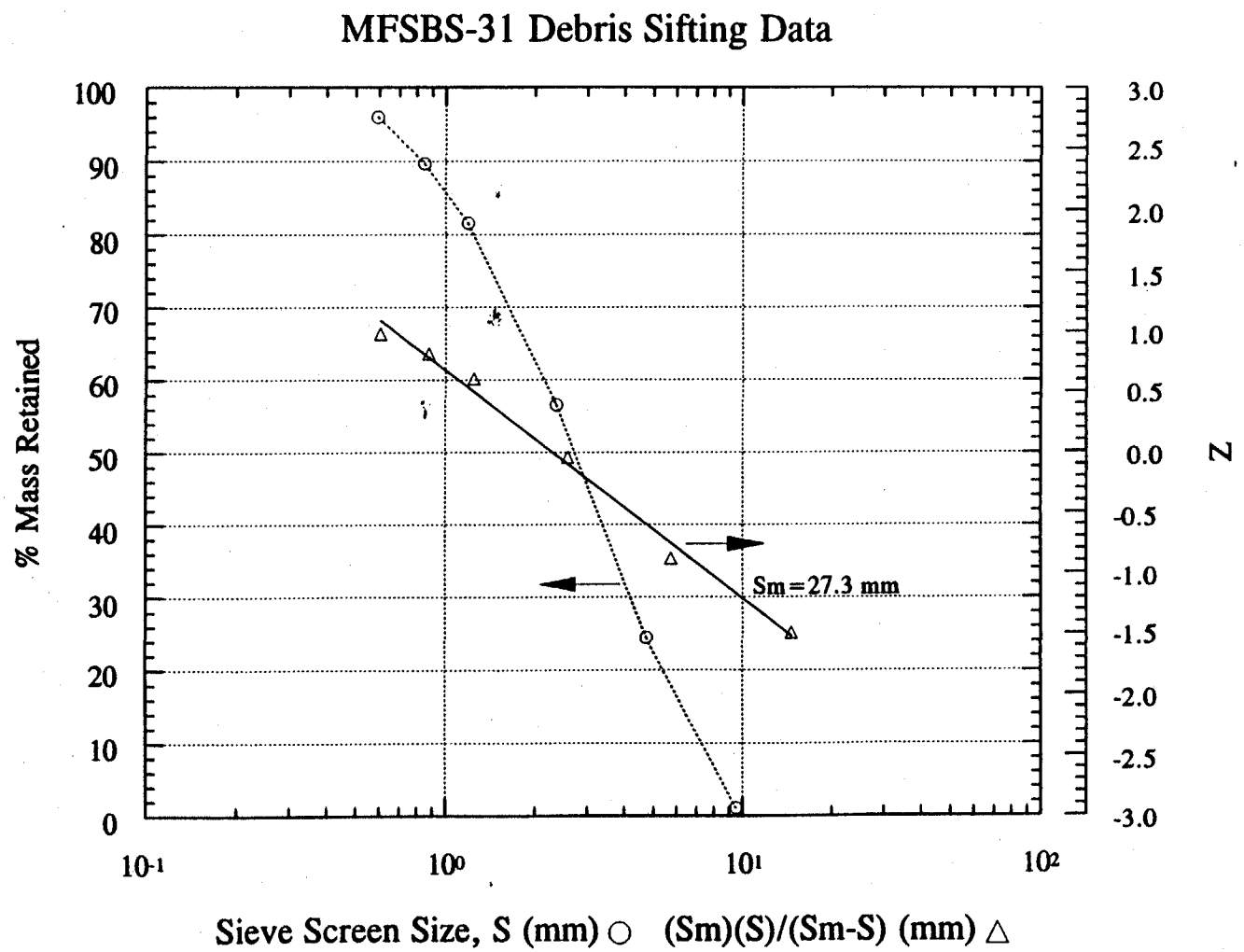
MFSBS-31 Debris Sifting Data
% Mass Retained
100
90
80
70
60
50
40
30
20
10
0
10-1
100
101
102
3.0
2.5
2.0
1.5
1.0
0.5
0.0
-0.5
-1.0
-1.5
-2.0
-2.5
-3.0
Z
Sm = 27.3 mm
Sieve Screen Size, S (mm) ○ (Sm)(S)/(Sm-S) (mm) △

462 ms 620 ms 796 ms 1496 ms

368 ms 524 ms 855 ms 1998 ms

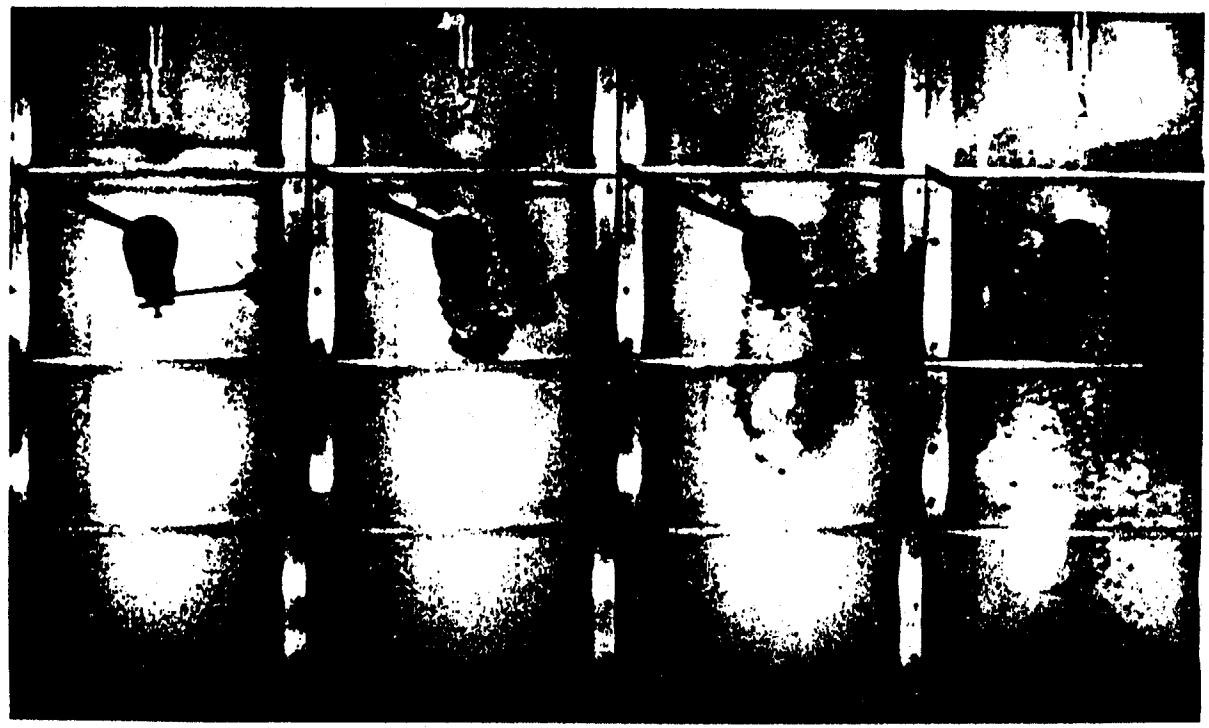

442 ms 610 ms 760 ms 2026 ms

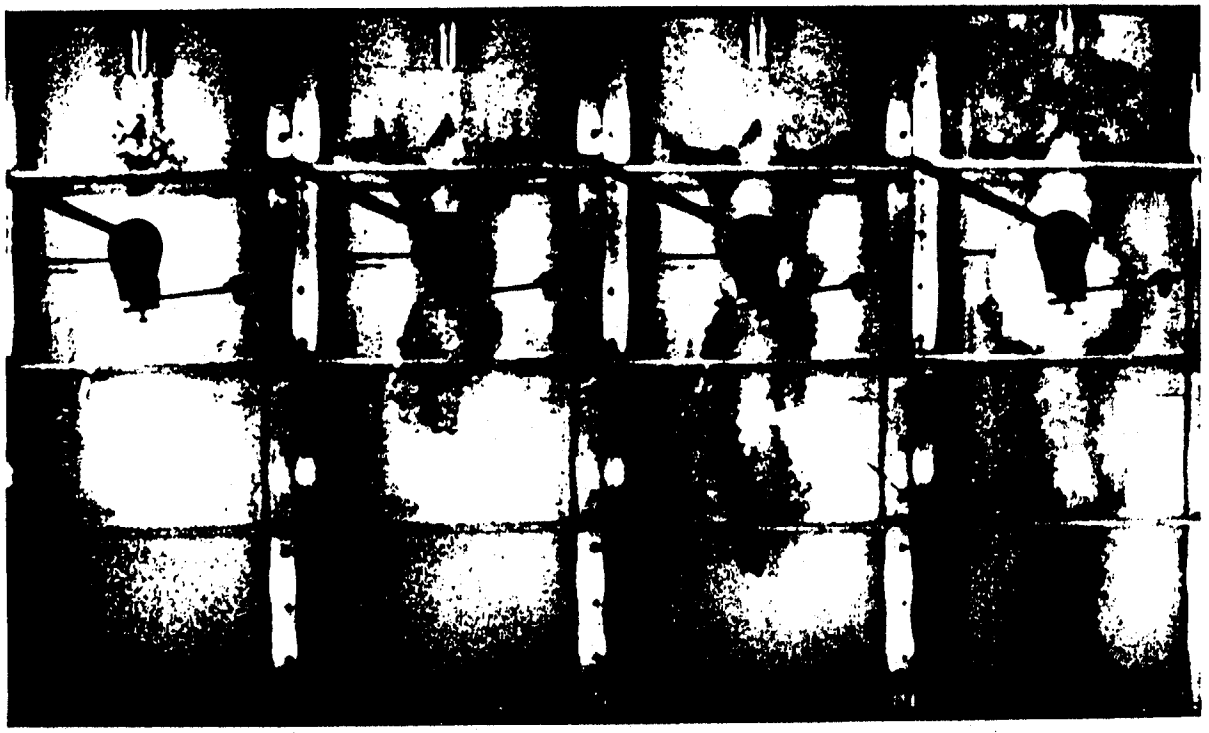

416 ms 588 ms 700 ms 1116 ms

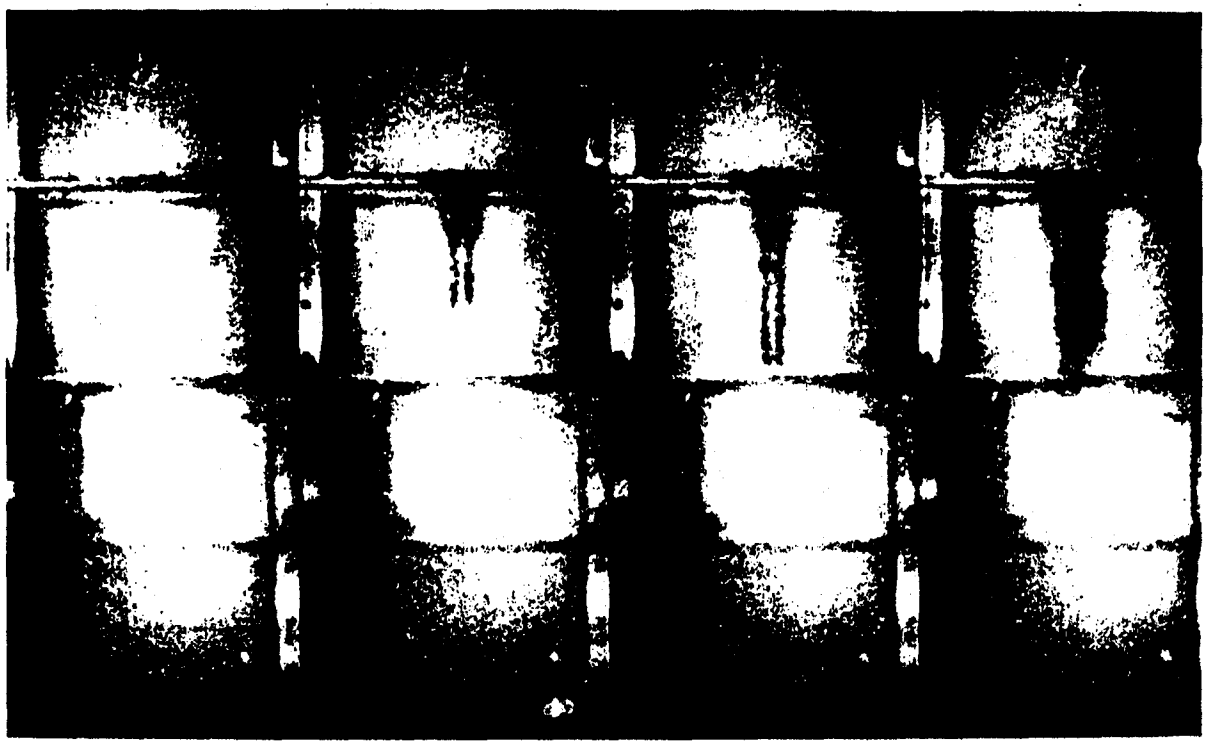

400 ms 460 ms 495 ms 968 ms

410 ms 460 ms 495 ms 1398 ms

302 ms 386 ms 420 ms 1158 ms

NSMHDXX.PSC

FILENAME

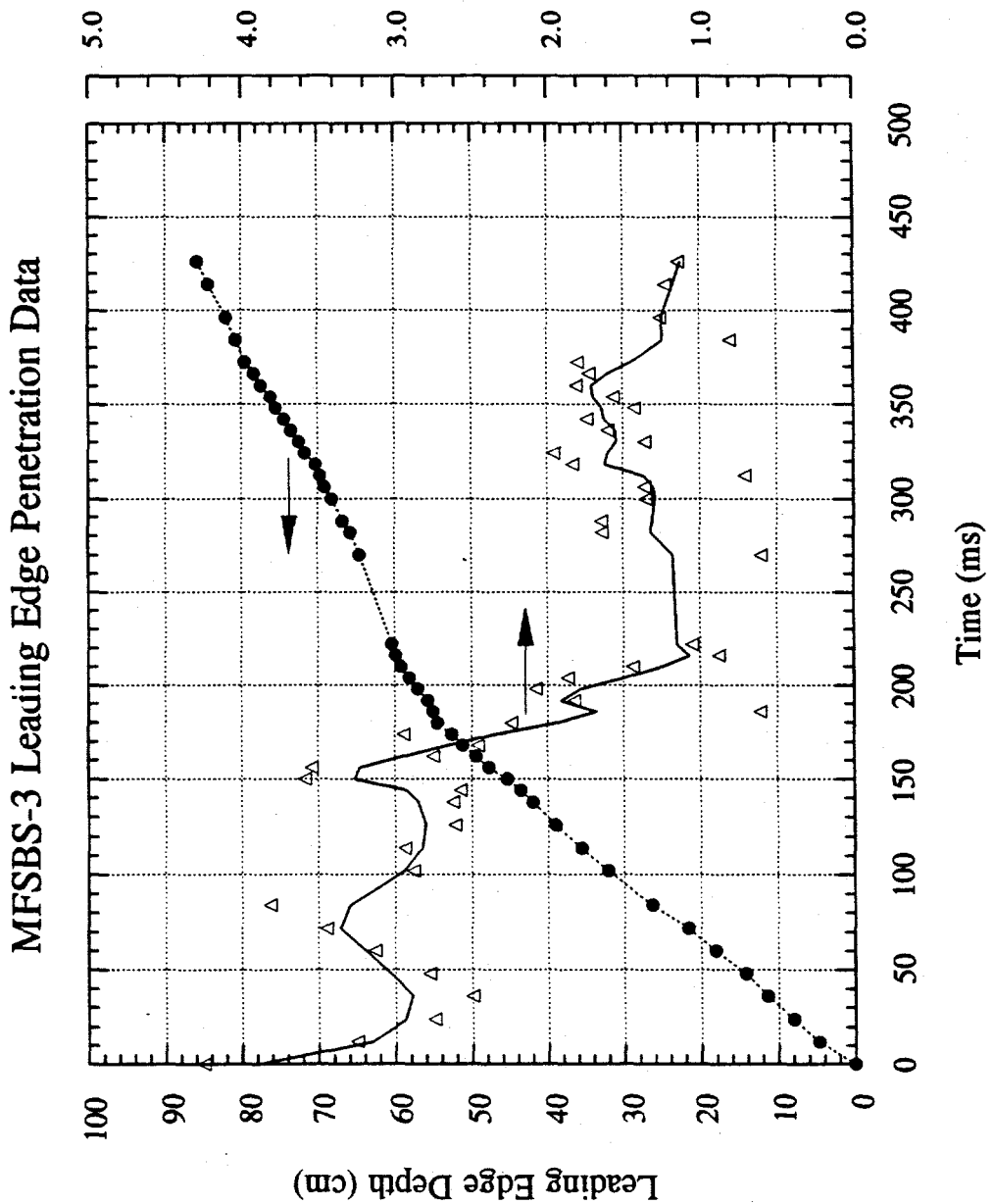

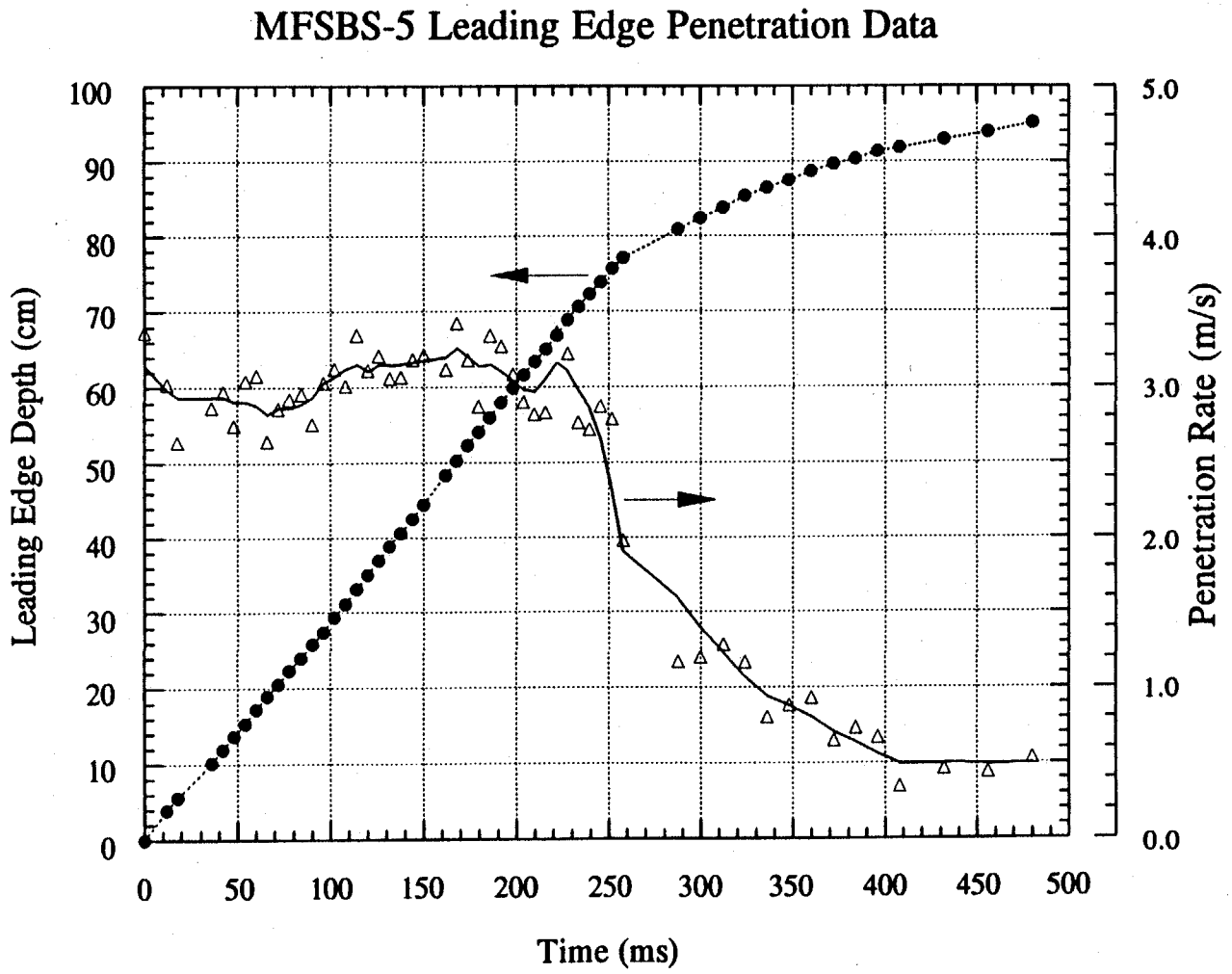
MFSBS-5 Leading Edge Penetration Data
Leading Edge Depth (cm)
Penetration Rate (m/s)
Time (ms)
0
10
20
30
40
50
60
70
80
90
100
0.0
1.0
2.0
3.0
4.0
5.0
0
50
100
150
200
250
300
350
400
450
500

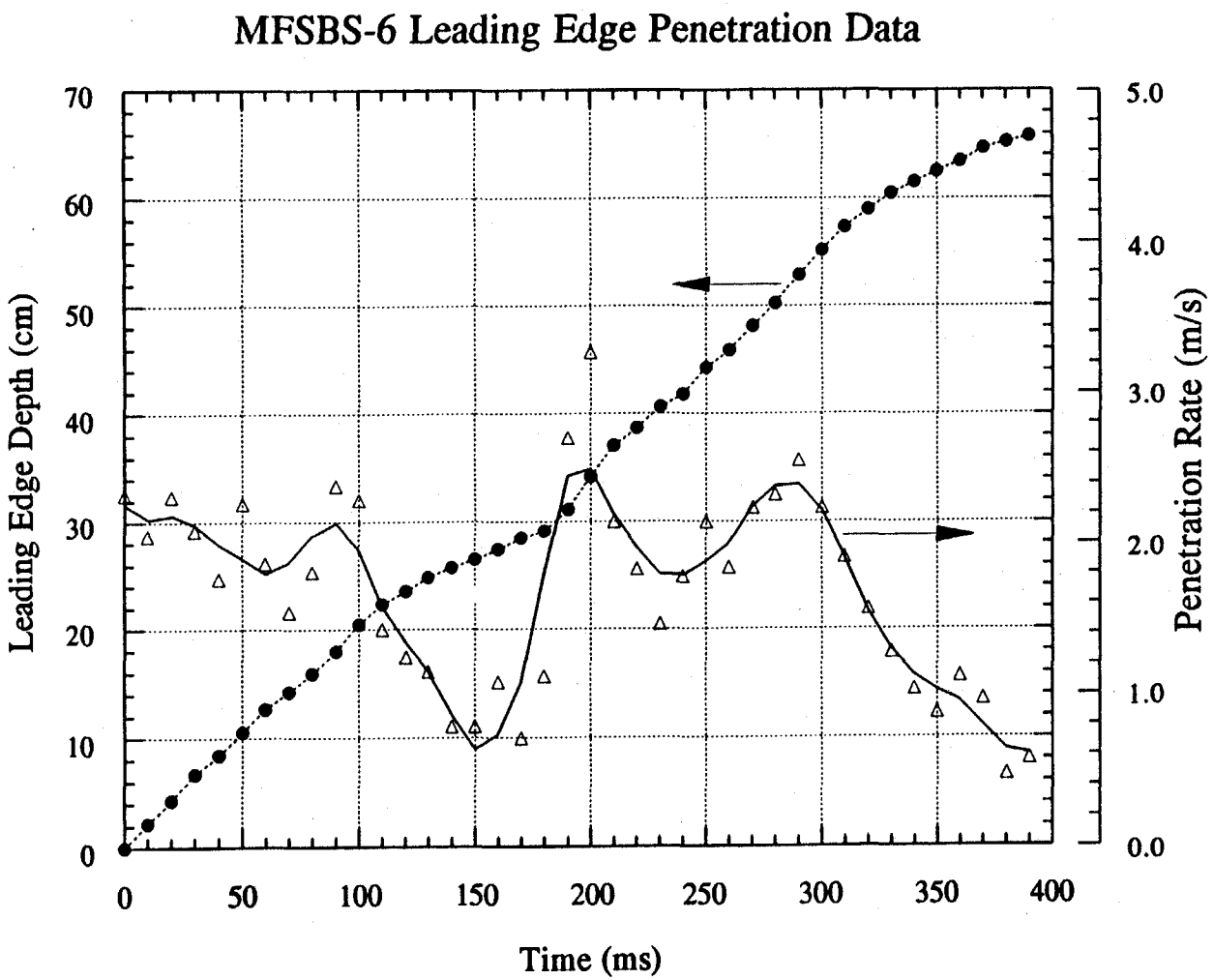
MFSBS-6 Leading Edge Penetration Data
Leading Edge Depth (cm)
Penetration Rate (m/s)
Time (ms)
0
10
20
30
40
50
60
70
0.0
1.0
2.0
3.0
4.0
5.0
0
50
100
150
200
250
300
350
400

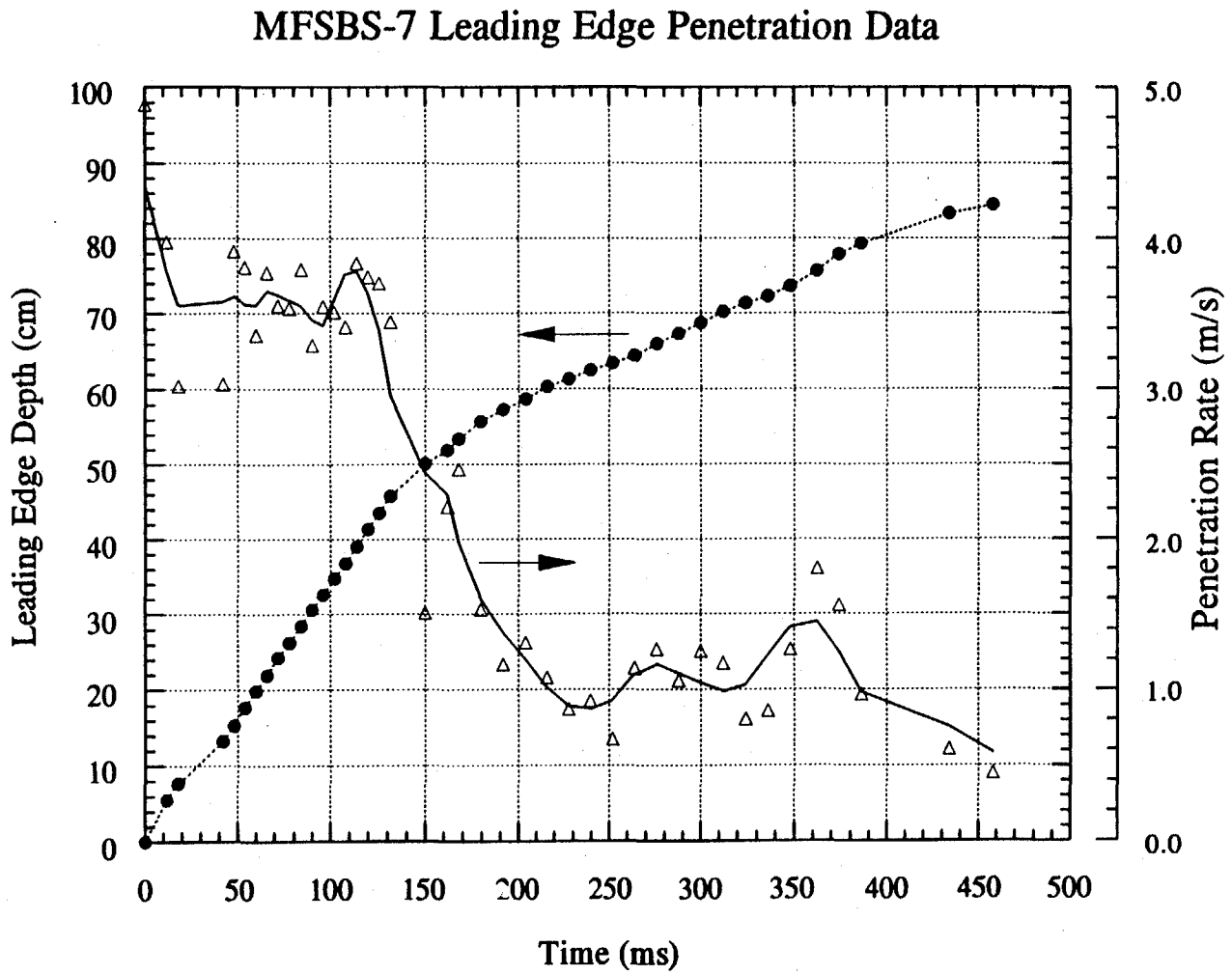
MFSBS-7 Leading Edge Penetration Data
Leading Edge Depth (cm)
Penetration Rate (m/s)
Time (ms)
0
10
20
30
40
50
60
70
80
90
100
0.0
1.0
2.0
3.0
4.0
5.0
0
50
100
150
200
250
300
350
400
450
500

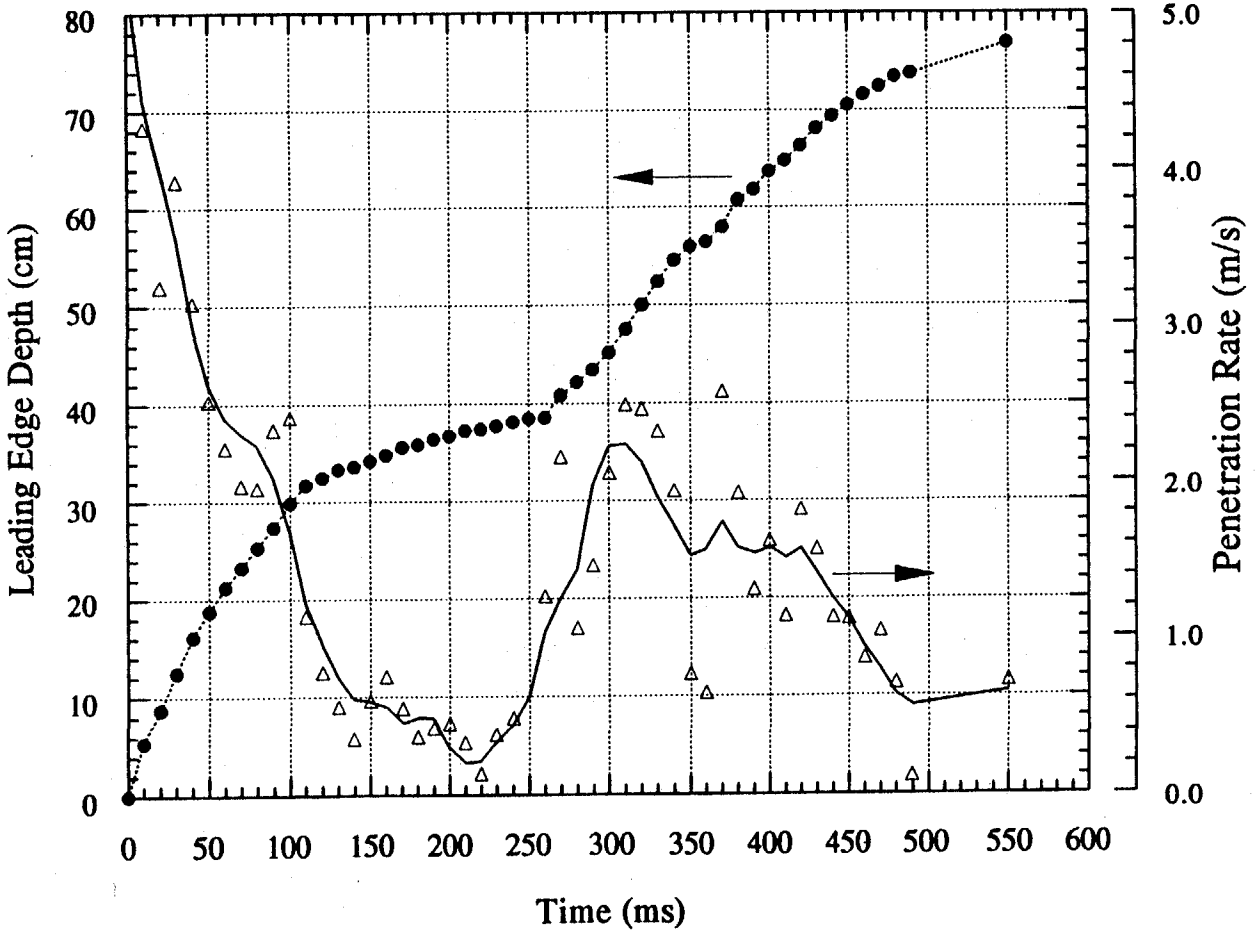
MFSBS-8 Leading Edge Penetration Data
Leading Edge Depth (cm)
Penetration Rate (m/s)
Time (ms)
0
10
20
30
40
50
60
70
80
0.0
1.0
2.0
3.0
4.0
5.0
0
50
100
150
200
250
300
350
400
450
500
550
600

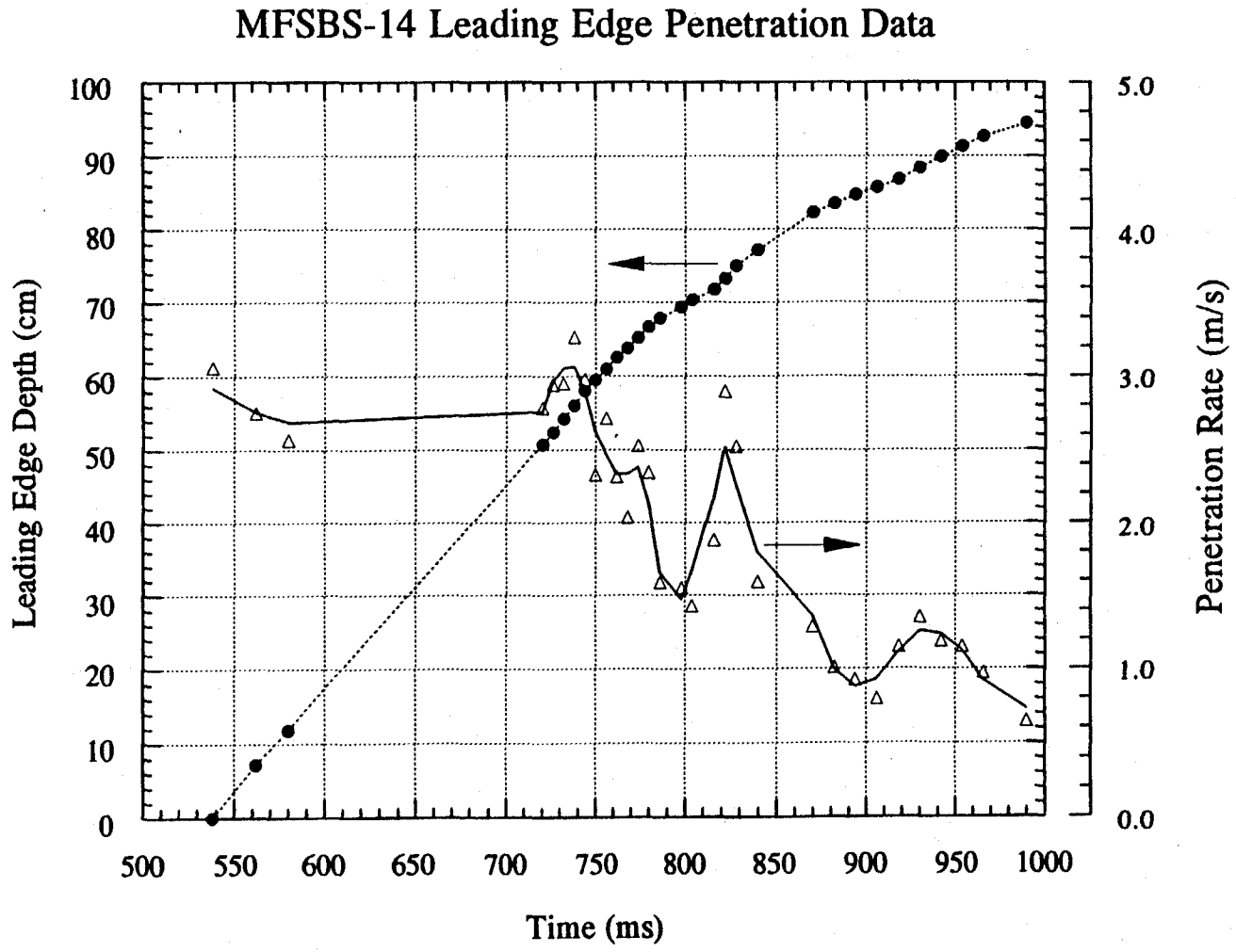
MFSBS-14 Leading Edge Penetration Data
Leading Edge Depth (cm)
Penetration Rate (m/s)
Time (ms)
0
10
20
30
40
50
60
70
80
90
100
0.0
1.0
2.0
3.0
4.0
5.0
500
550
600
650
700
750
800
850
900
950
1000

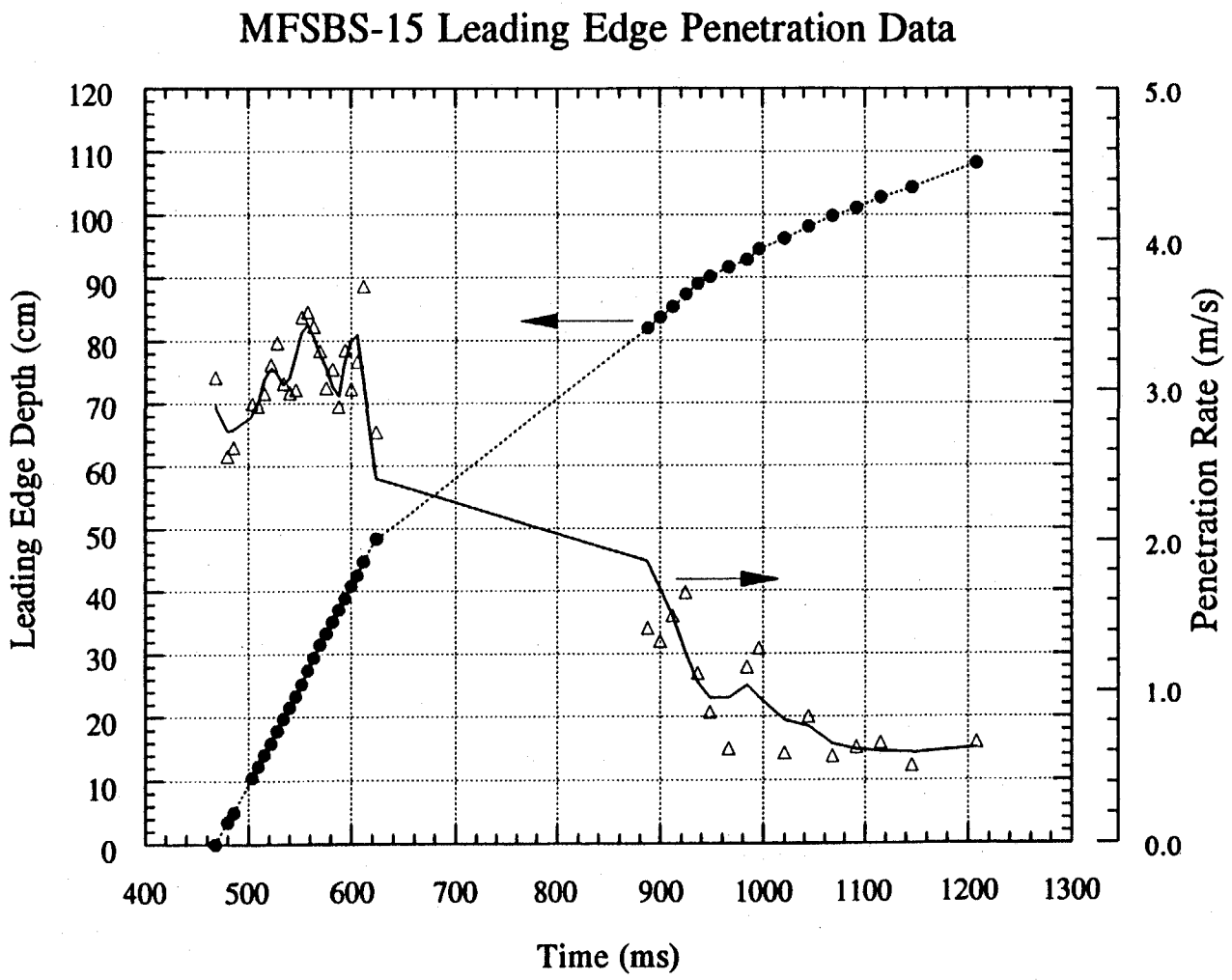
MFSBS-15 Leading Edge Penetration Data
Leading Edge Depth (cm)
Penetration Rate (m/s)
Time (ms)
0
10
20
30
40
50
60
70
80
90
100
110
120
0.0
1.0
2.0
3.0
4.0
5.0
400
500
600
700
800
900
1000
1100
1200
1300

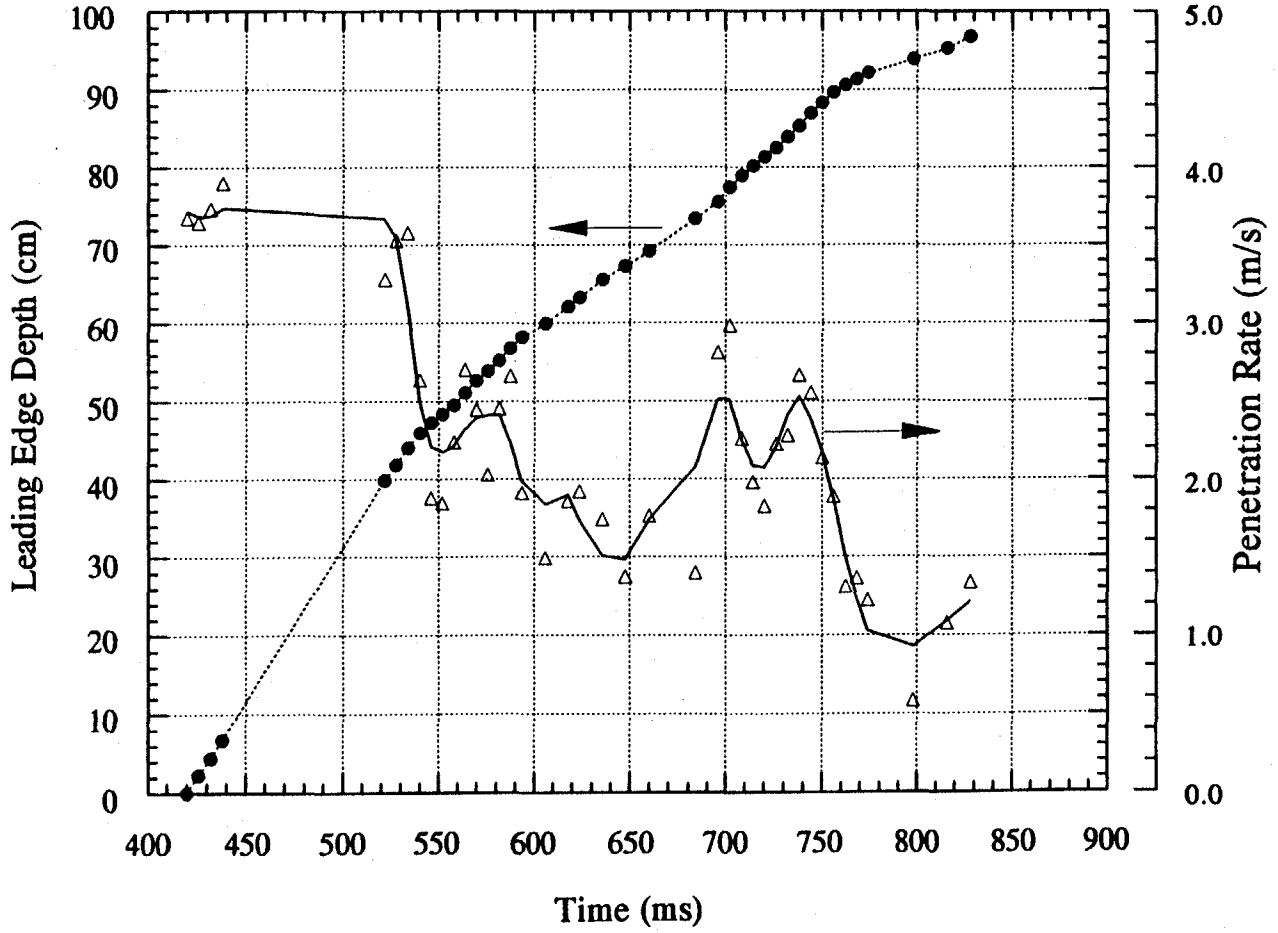
MFSBS-16 Leading Edge Penetration Data
Leading Edge Depth (cm)
Penetration Rate (m/s)
Time (ms)
0
10
20
30
40
50
60
70
80
90
100
0.0
1.0
2.0
3.0
4.0
5.0
400
450
500
550
600
650
700
750
800
850
900

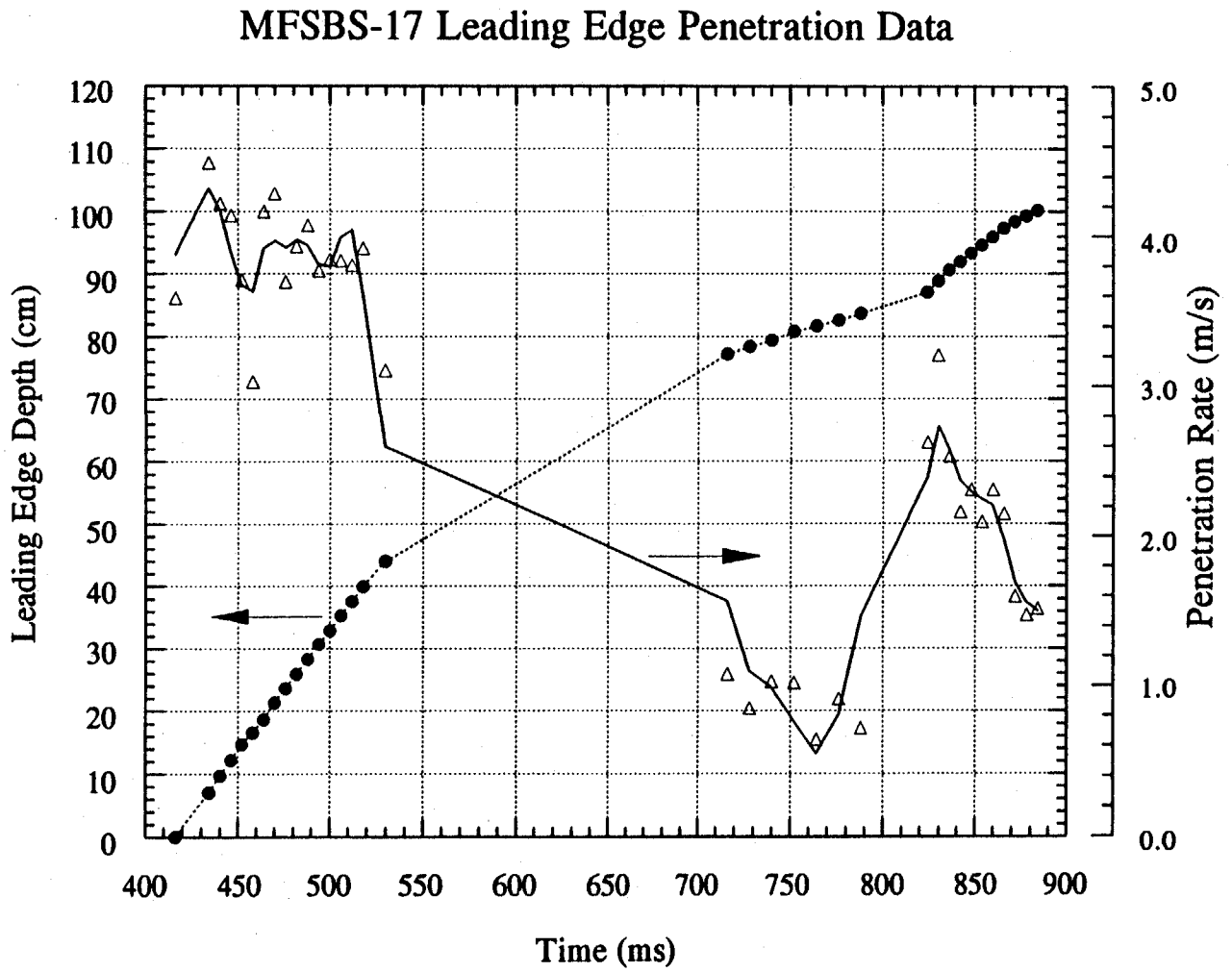
MFSBS-17 Leading Edge Penetration Data
Leading Edge Depth (cm)
Penetration Rate (m/s)
Time (ms)
120
110
100
90
80
70
60
50
40
30
20
10
0
5.0
4.0
3.0
2.0
1.0
0.0
400
450
500
550
600
650
700
750
800
850
900

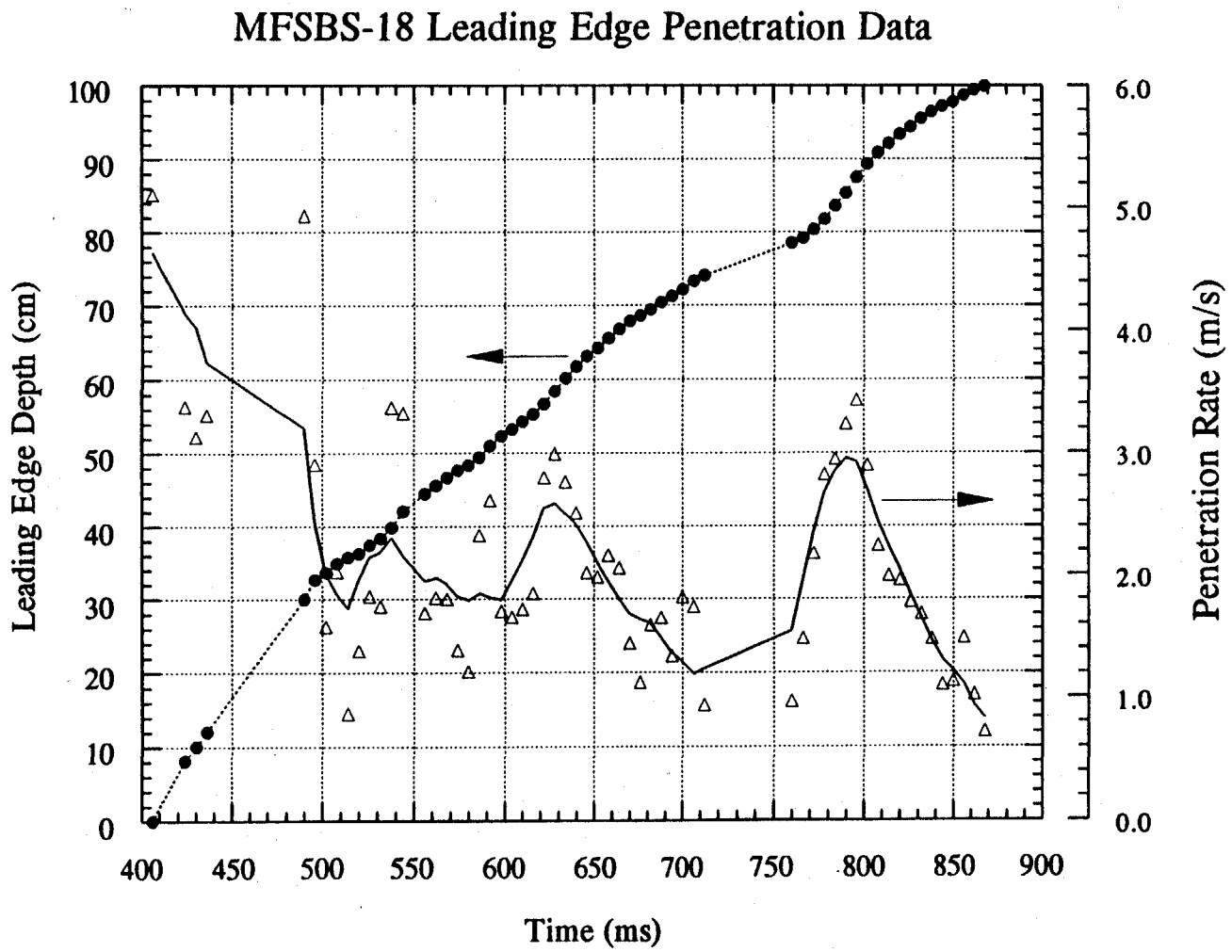
MFSBS-18 Leading Edge Penetration Data
Leading Edge Depth (cm)
Penetration Rate (m/s)
Time (ms)
0
10
20
30
40
50
60
70
80
90
100
0.0
1.0
2.0
3.0
4.0
5.0
6.0
400
450
500
550
600
650
700
750
800
850
900

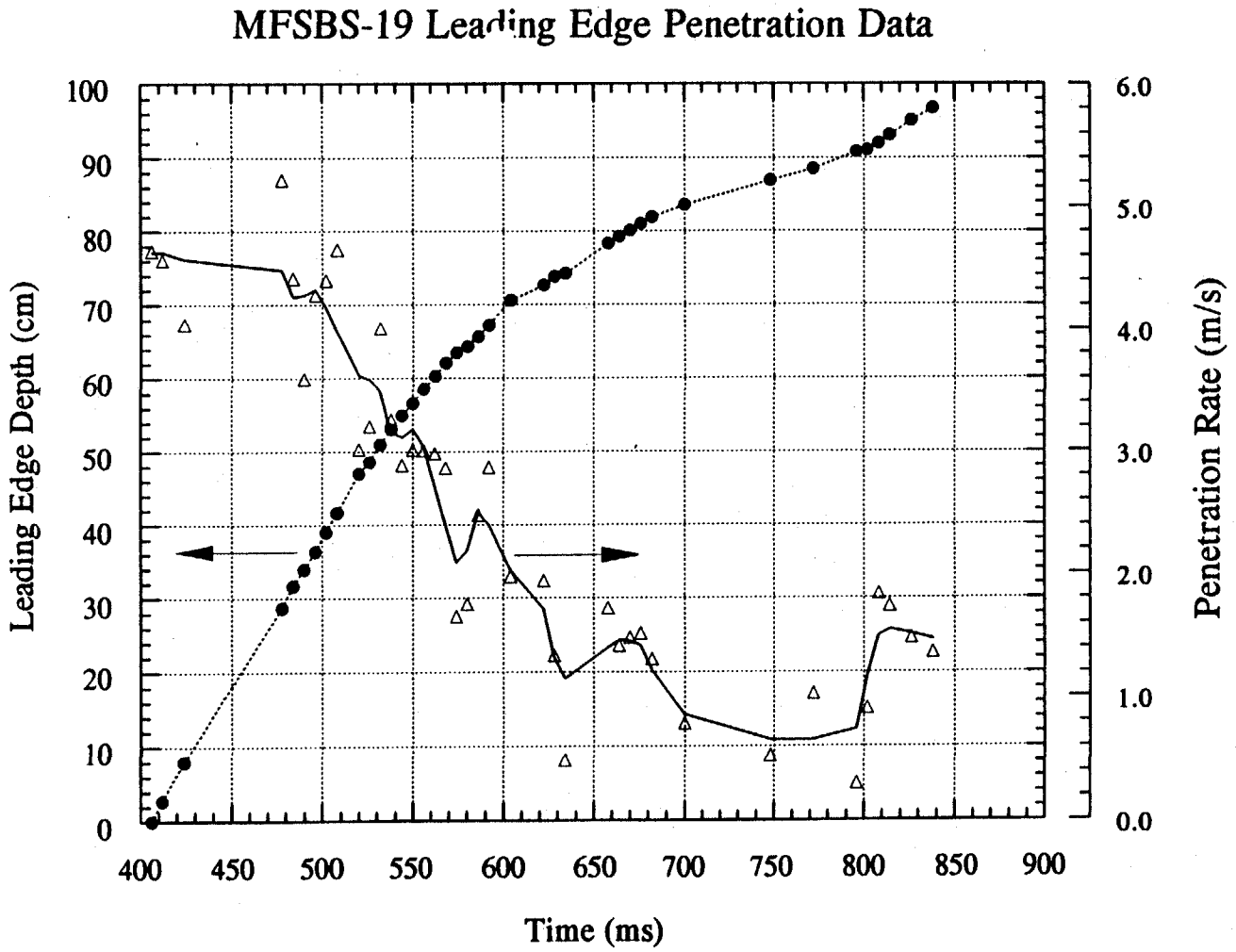
MFSBS-19 Leading Edge Penetration Data
Leading Edge Depth (cm)
Penetration Rate (m/s)
Time (ms)
0
10
20
30
40
50
60
70
80
90
100
0.0
1.0
2.0
3.0
4.0
5.0
6.0
400
450
500
550
600
650
700
750
800
850
900

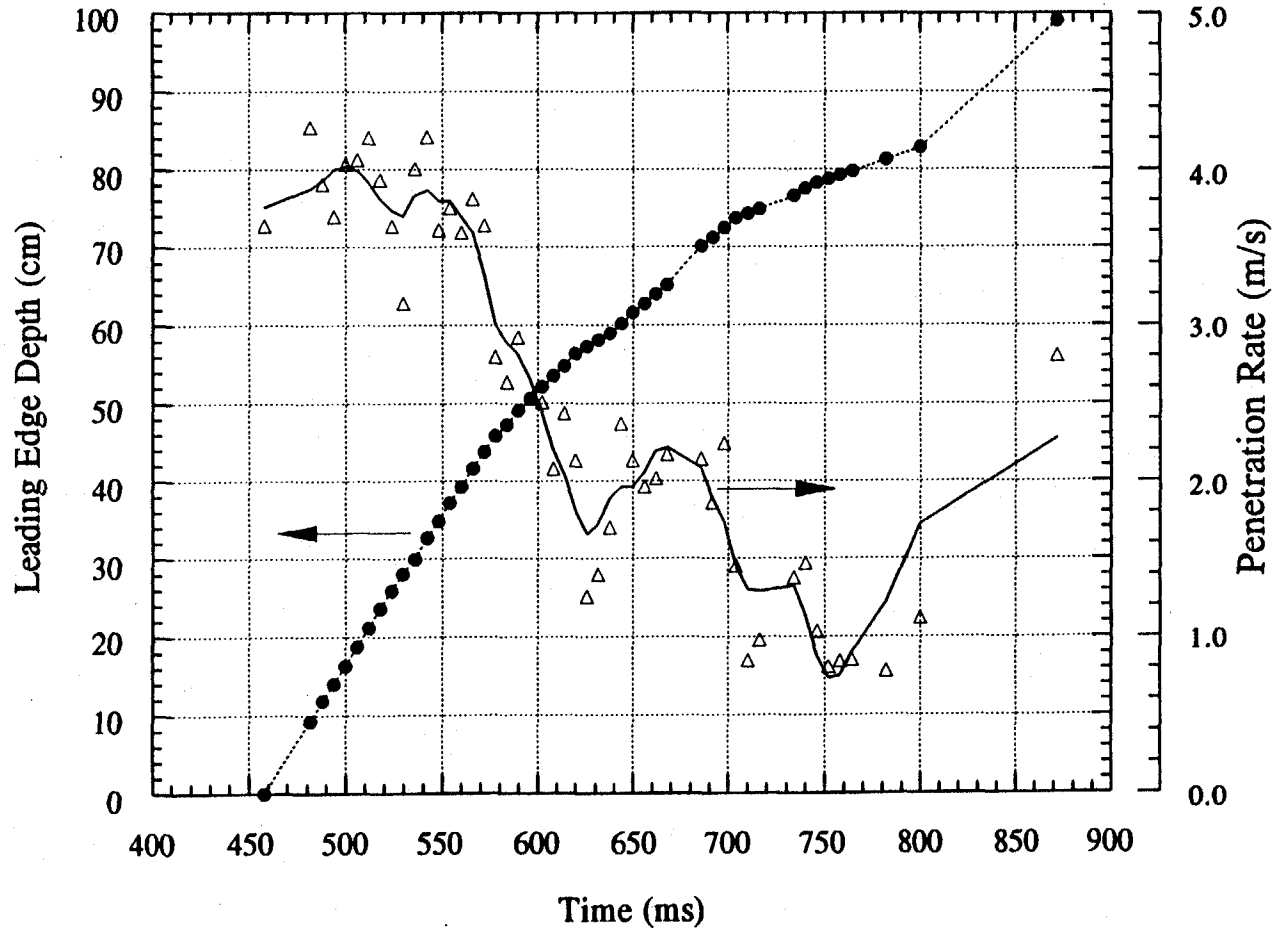
MFSBS-20 Leading Edge Penetration Data
Leading Edge Depth (cm)
Penetration Rate (m/s)
Time (ms)
0
10
20
30
40
50
60
70
80
90
100
0.0
1.0
2.0
3.0
4.0
5.0
400
450
500
550
600
650
700
750
800
850
900

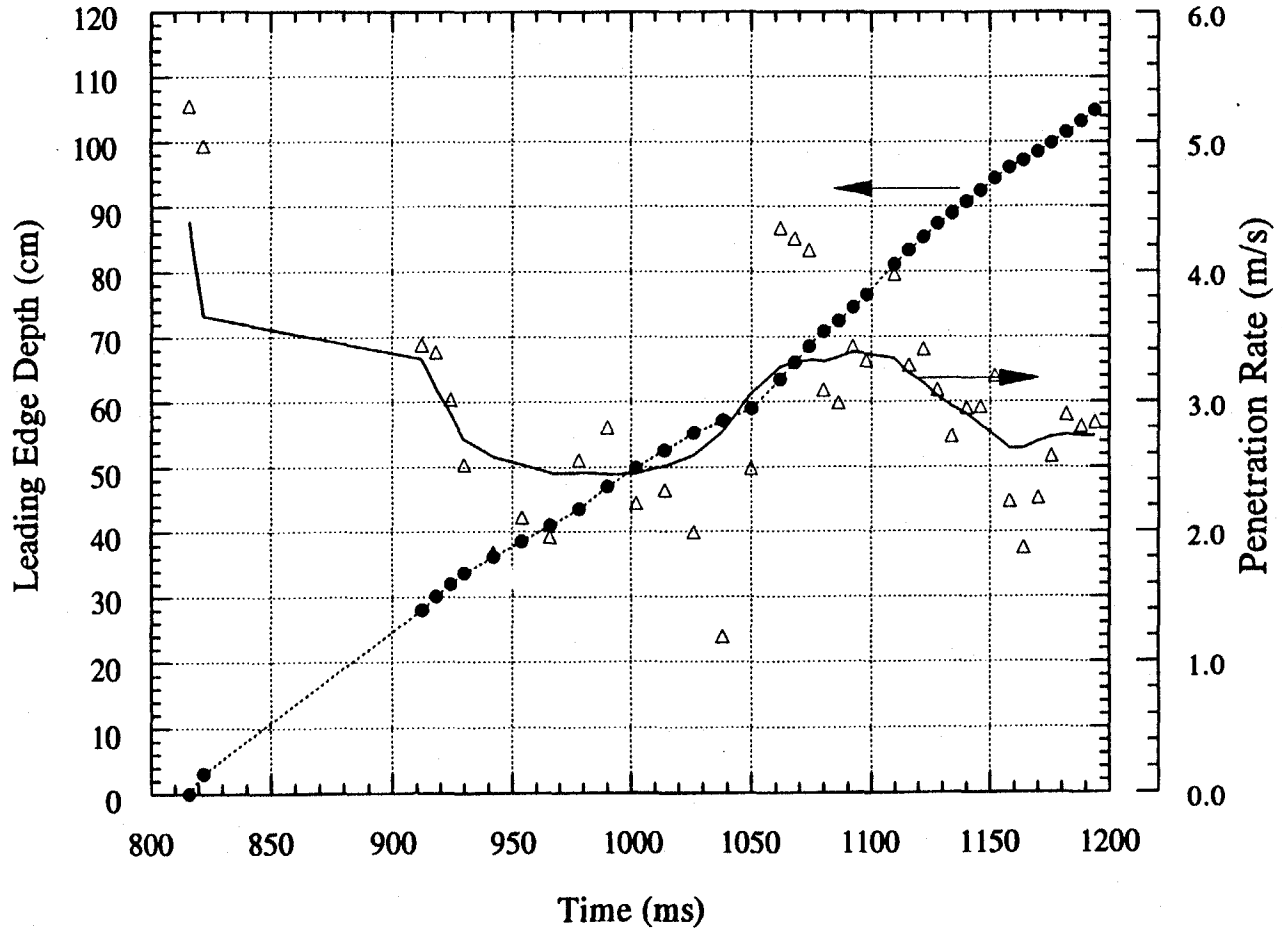
MFSBS-21 Leading Edge Penetration Data
Leading Edge Depth (cm)
Penetration Rate (m/s)
Time (ms)
0
10
20
30
40
50
60
70
80
90
100
110
120
0.0
1.0
2.0
3.0
4.0
5.0
6.0
800
850
900
950
1000
1050
1100
1150
1200

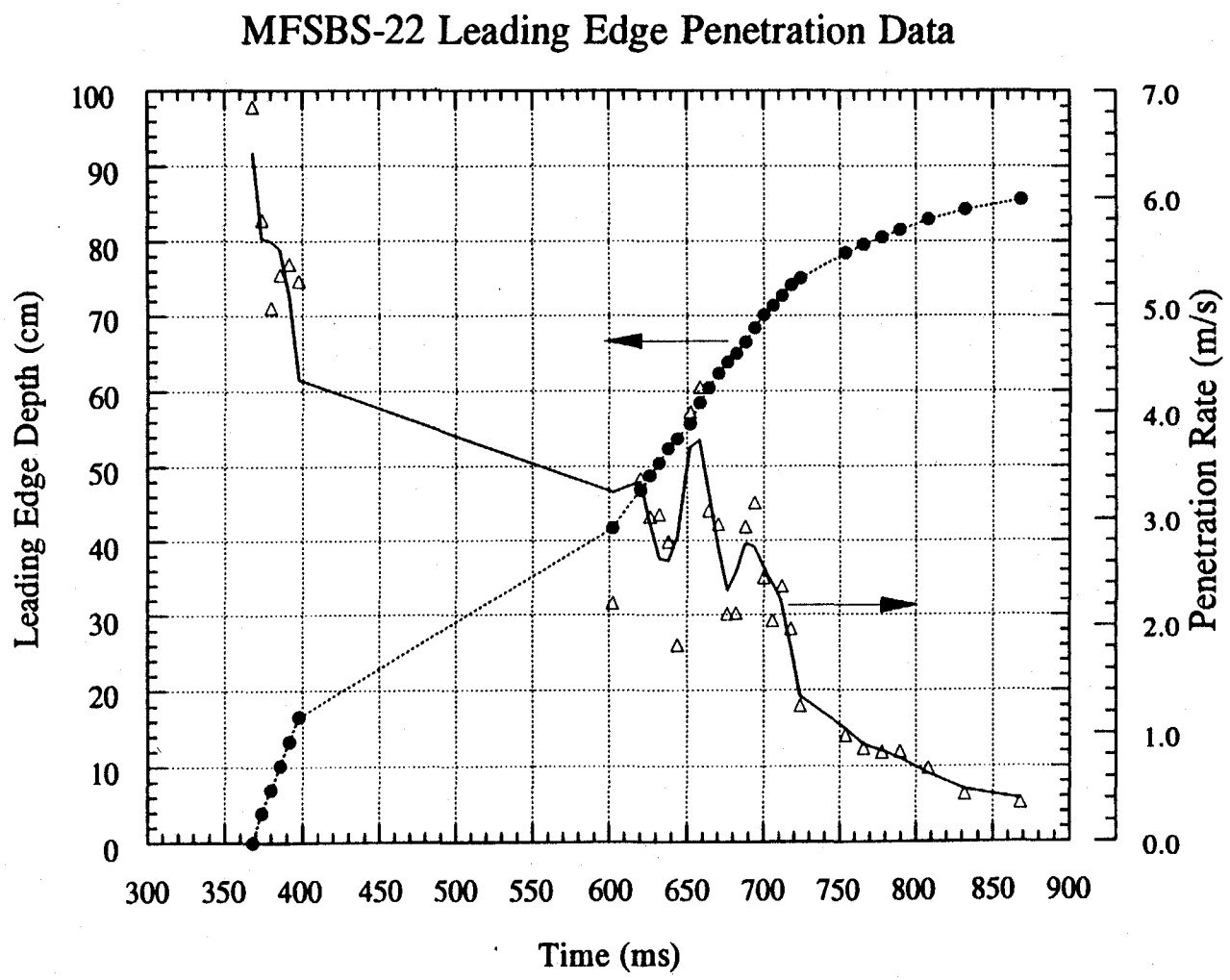
MFSBS-22 Leading Edge Penetration Data
Leading Edge Depth (cm)
Penetration Rate (m/s)
Time (ms)
0
10
20
30
40
50
60
70
80
90
100
0.0
1.0
2.0
3.0
4.0
5.0
6.0
7.0
300
350
400
450
500
550
600
650
700
750
800
850
900

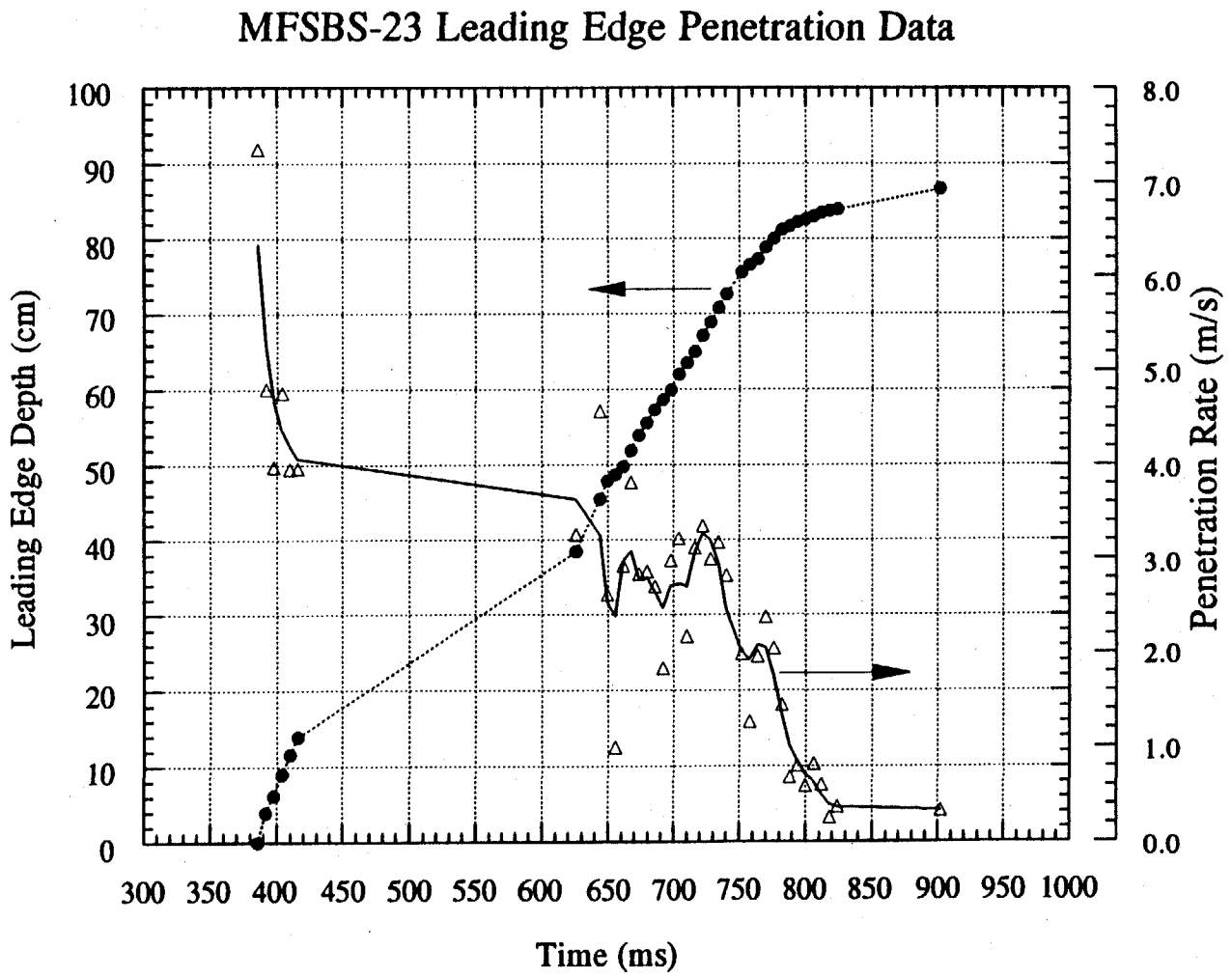
MFSBS-23 Leading Edge Penetration Data
Leading Edge Depth (cm)
Penetration Rate (m/s)
Time (ms)
0
10
20
30
40
50
60
70
80
90
100
0.0
1.0
2.0
3.0
4.0
5.0
6.0
7.0
8.0
300 350 400 450 500 550 600 650 700 750 800 850 900 950 1000

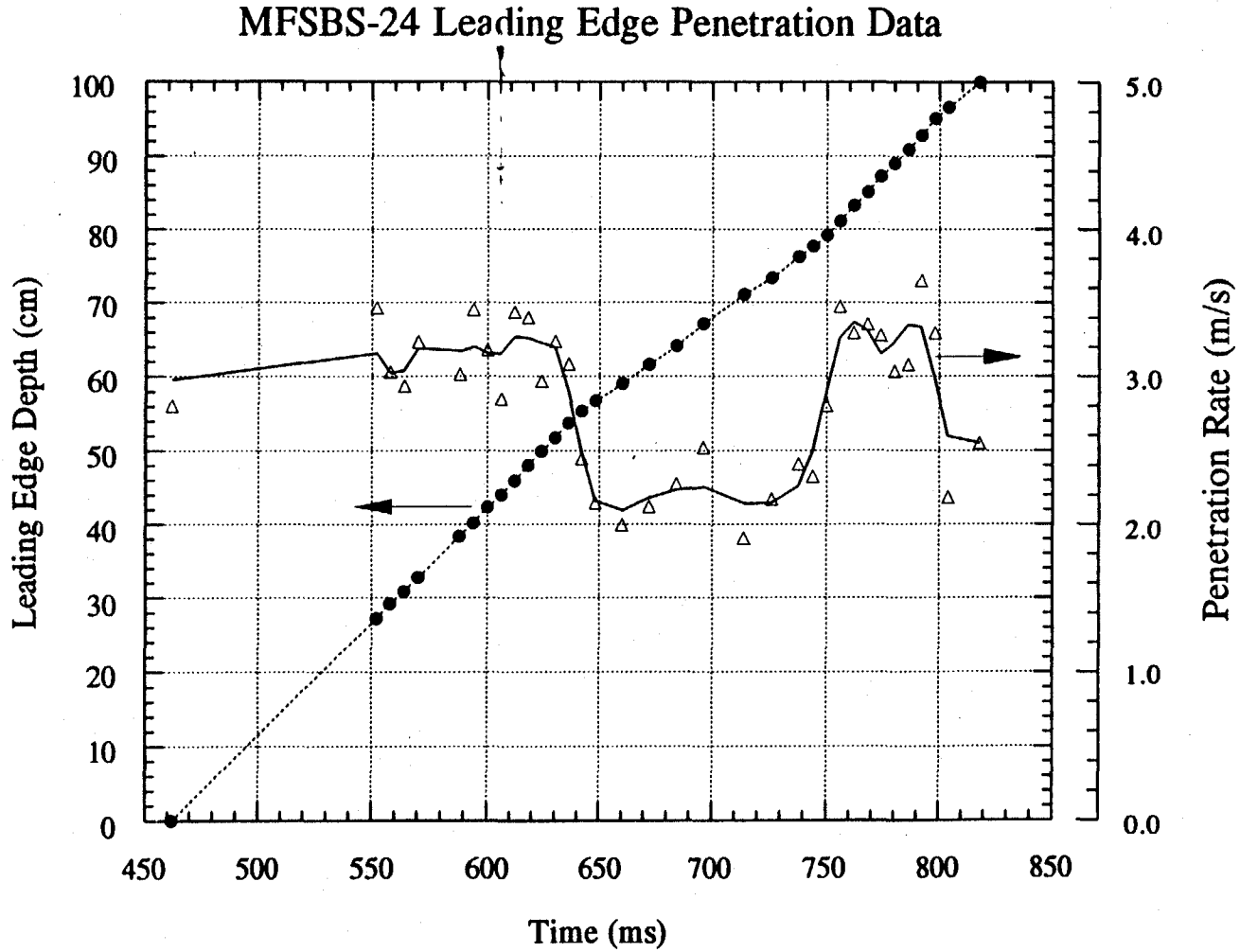
MFSBS-24 Leading Edge Penetration Data
Leading Edge Depth (cm)
Penetration Rate (m/s)
Time (ms)
0
10
20
30
40
50
60
70
80
90
100
0.0
1.0
2.0
3.0
4.0
5.0
450
500
550
600
650
700
750
800
850

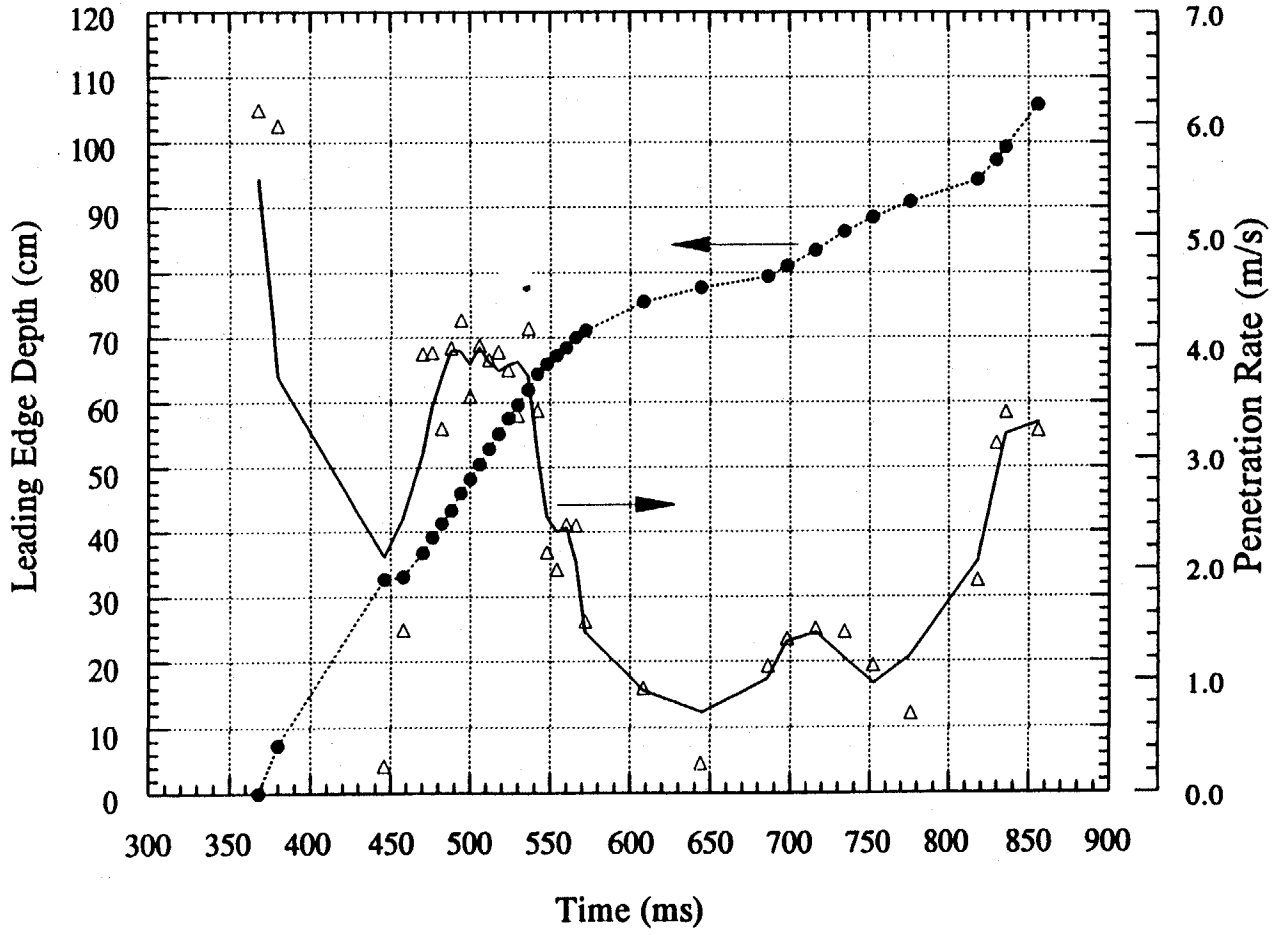
MFSBS-25 Leading Edge Penetration Data
Leading Edge Depth (cm)
Penetration Rate (m/s)
Time (ms)
0
10
20
30
40
50
60
70
80
90
100
110
120
0.0
1.0
2.0
3.0
4.0
5.0
6.0
7.0
300
350
400
450
500
550
600
650
700
750
800
850
900

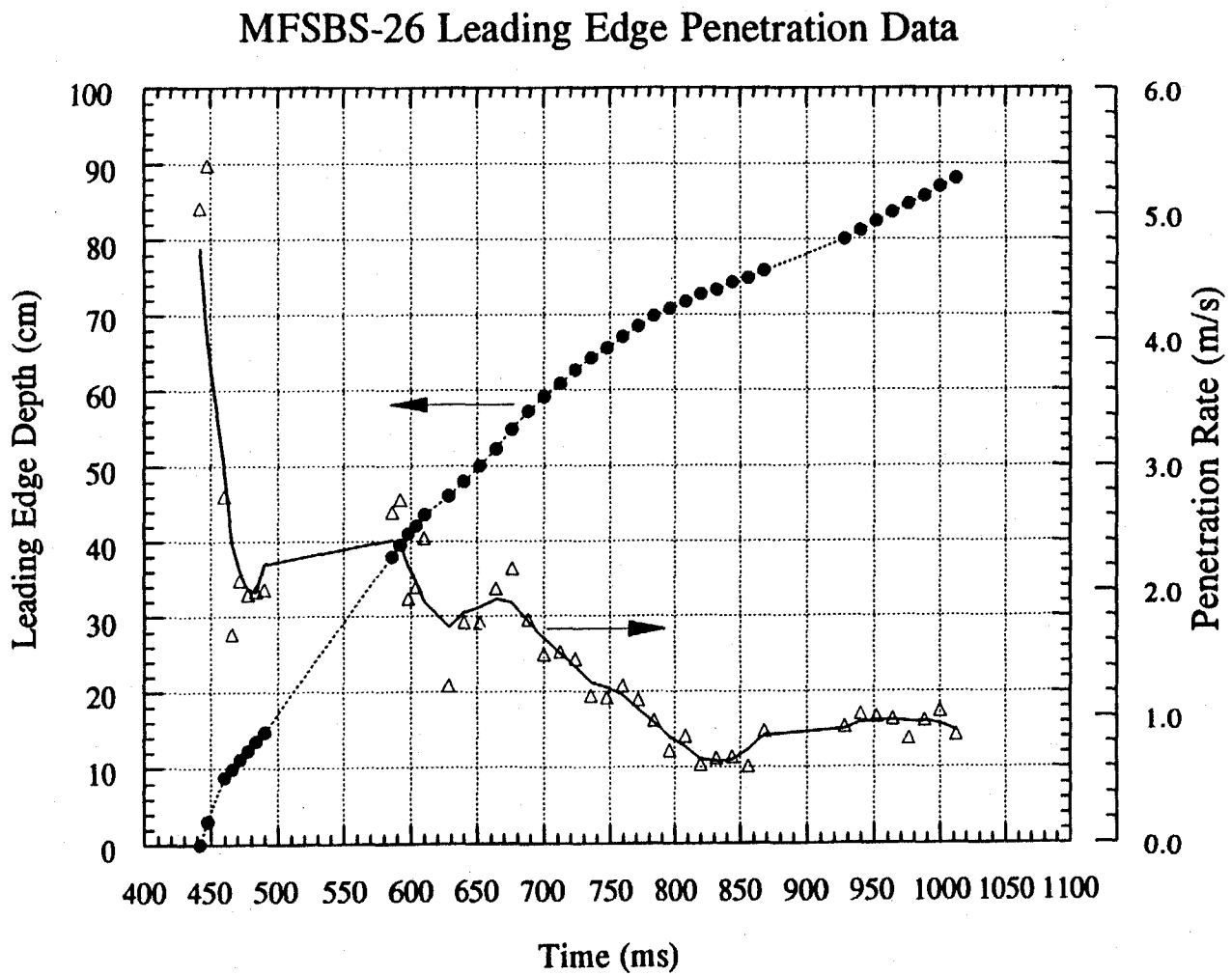
MFSBS-26 Leading Edge Penetration Data
Leading Edge Depth (cm)
Penetration Rate (m/s)
Time (ms)
0
10
20
30
40
50
60
70
80
90
100
0.0
1.0
2.0
3.0
4.0
5.0
6.0
400 450 500 550 600 650 700 750 800 850 900 950 1000 1050 1100

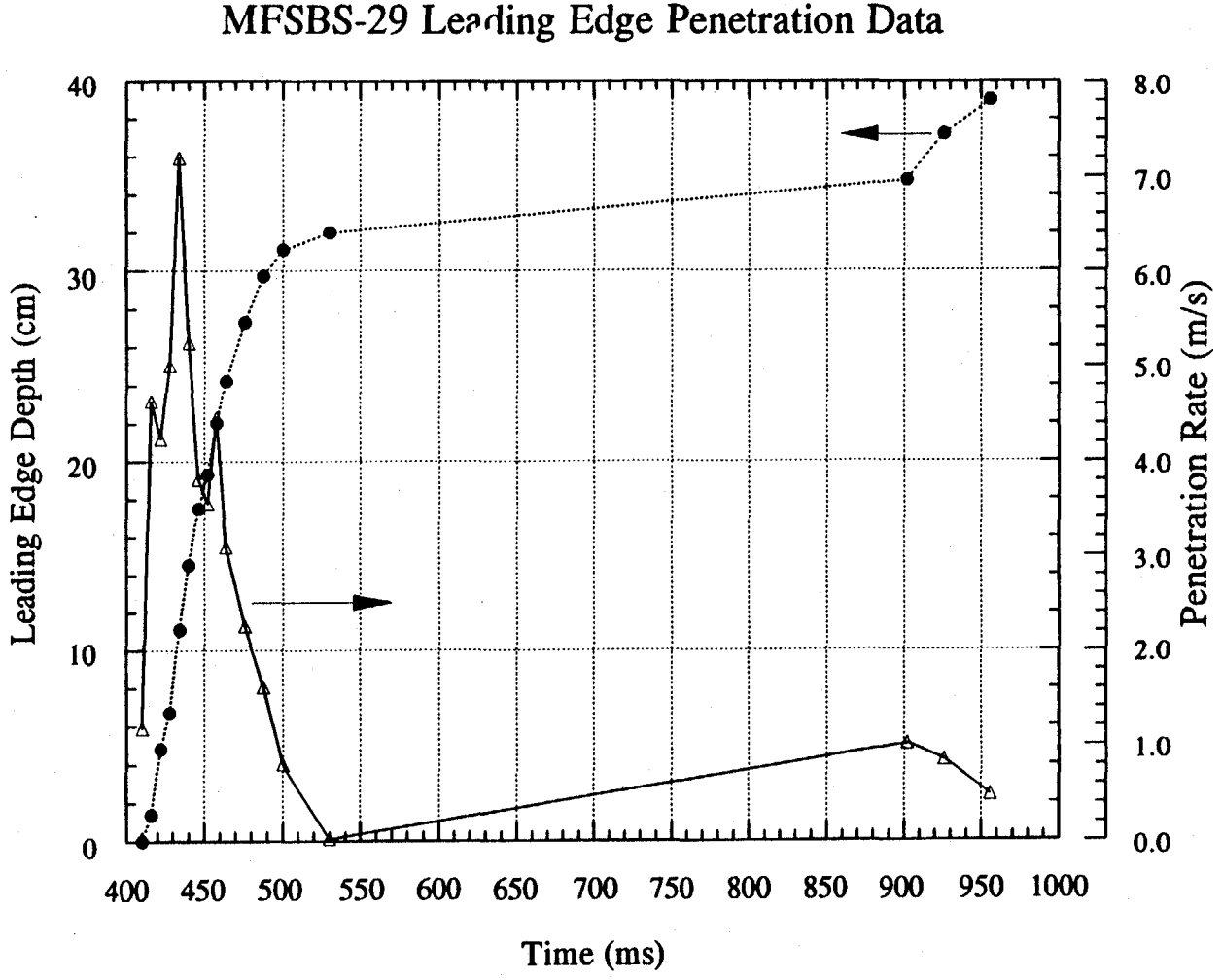
MFSBS-29 Leading Edge Penetration Data
Leading Edge Depth (cm)
Penetration Rate (m/s)
Time (ms)
0
10
20
30
40
0.0
1.0
2.0
3.0
4.0
5.0
6.0
7.0
8.0
400
450
500
550
600
650
700
750
800
850
900
950
1000

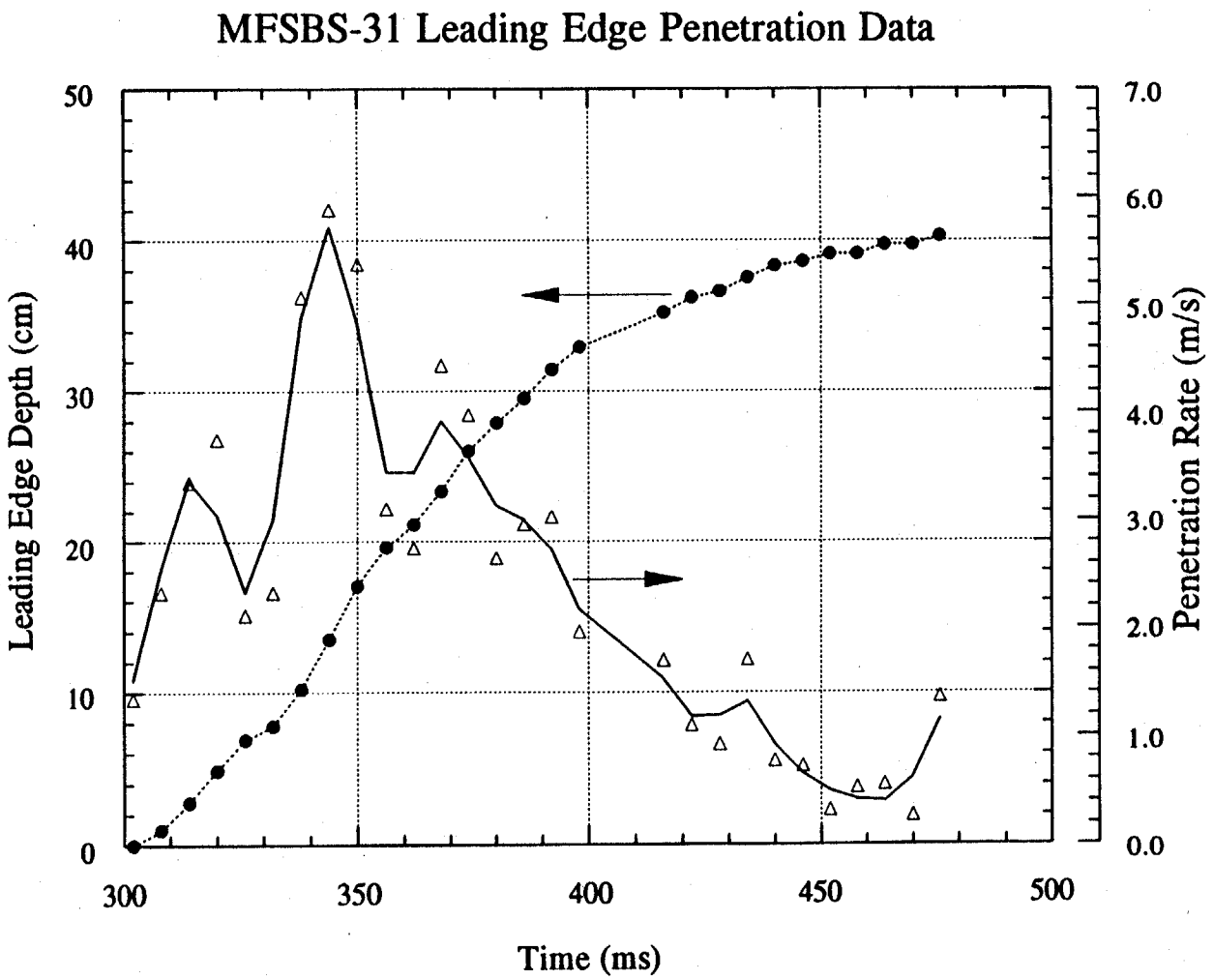
MFSBS-31 Leading Edge Penetration Data
Leading Edge Depth (cm)
Penetration Rate (m/s)
Time (ms)
0
10
20
30
40
50
0.0
1.0
2.0
3.0
4.0
5.0
6.0
7.0
300
350
400
450
500